A THEORETICAL ANALYSIS OF SPINAL CORD STIMULATION WITH PARTICULAR REFERENCE TO MYELINATED FIBRES

W. K. SIN

THESIS PRESENTED FOR THE DEGREE OF

DOCTOR OF PHILOSOPHY

DEPARTMENT OF MECHANICAL ENGINEERING

BRUNEL UNIVERSITY, UXBRIDGE, MIDDLESEX

ENGLAND

FEBRUARY 1984

ABSTRACT

This thesis describes extensive development, and validation by experiment, of theoretical methods for the bioengineering analysis of electrical stimulation of spinal cord.

Two-dimensional finite element methods are used to survey certain crucial geometrical and tissue property aspects, but the stimulus field analyses are centred on full three-dimensional representations.

The three-dimensional models are validated by comparing results with published data from the monkey, and original work with both patients and cadaver material. A definitive finite element model is presented.

An existing computer simulation of the myelinated nerve fibre, especially suitable for use with finite element field solutions, is tested experimentally using an in-vitro preparation from the chick. Further developments for branched and bending fibres, and stimulus field interaction with normal ongoing nerve impulses are examined theoretically.

The two essential aspects, field analysis and neural modelling, are shown to be sufficiently well-developed to allow confident application in spinal cord stimulation studies.

ACKNOWLEDGEMENTS

I wish to express my gratitude to Dr B Coburn for his invaluable guidance and encouragement throughout the work.

At Brunel, I wish to thank Dr R C Elliott, Lecturer in Applied Biology, Mr R C Pank, Senior programmer, and Dr A L Yettram, Reader in Mechanical Engineering, for their assistance in their respective areas of expertise.

Special thanks go to Dr E M Sedgwick, Consultant in Clinical Neurophysiology, and Mr R Hunt, Chief Technician at the Wessex Neurological Centre, for much help throughout the work.

I am also grateful to Neuromed, 5000A Oakes Road. Fort Lauderdale, Florida for financial and technical support. Part of the work was carried out during a visit to the Institute for Rehabilitation and Research, Texas Medical Centre, Houston, and I wish to thank Dr A M Sherwood, Director of Research at that establishment, for considerable hospitality and kind provision of facilities.

CONTENTS

APPENDICES

NOMENCLATURE

$[A]$	square matrix
An	area of tissue n
a	tendon wall thickness
b	tendon wall thickness
C_ℓ	terminal capacitance
Cm	lumped nodal capacitance
d	axon diameter (internal myelin diameter)
D	fibre diameter (external myelin diameter)
E	membrane depolarisation
$\dot{E}$	rate of membrane depolarisation
Em	membrane potential Vi-Ve
Er	resting potential
G_ℓ	terminal conductance
Ga	axial internodal conductance
Ge	external condutance
Gm	nodal membrane conductance
Gs	external conductance
Θ	conduction velocity
i	ionic current
$\underline{I}i$	total ionic current vector
Is	stimulus current
It	threshold current
$\{I\}^e$	current at one node of element e
J	current density vector

$[K]^e$	stiffness matrix for element e
l	nodal gap width
L	myelinated internodal spacing
λ	equivalent characteristic length for myelinated fibre
[L],[M].[N],[P]	square matrices
n	total number of node of Ranvier total number of finite element nodes
Rn	impedance of tissue n
ρ_i	axoplasm resistivity
ρ_e	specific resistivity of external medium
ρ_x ρ_y ρ_z	specific resistivity in x-, y- and z- direction
ρ_n	specific resistivity of tissue n
ø	bending angle
T	temperature
τ	constant
[U]	square matrix
V	potential
Ve	extracellular potential
$\underline{V}e$	external potential vector
Vi	intracellular potential
$\{V\}^e$	potential at node of element e
Vs	stimulator voltage
x	measured distance
y	electrode distance from fibre
Z	lumped impedance

CHAPTER 1 INTRODUCTION

1.1 CLINICAL BACKGROUND

Electrical stimulation of spinal cord continues to attract widespread interest since the report by SHEALY et al (1967) on the relief of intractable pain. The technique has , since then, been used for the treatment of many neurological disorders, including multiple sclerosis (ILLIS et al,1983), spinal cord injury (CAMPOS et al,1978), peripheral vascular disease (ROSEN and BARSOUM,1979), cerebral palsy (WALTZ and PANI,1978) and spasmodic torticollis (GILDENBERG, 1977).

Historically, the practice was called dorsal column stimulation as stimulating electrodes were placed in 'direct' contact with the dorsal surface of spinal cord, separated only by one or two membranes (pia and arachnoid). The method was later modified, with a great increase in surgical safety and simplicity, by inserting electrodes into the epidural space percutaneously, using local anaesthesia (ILLIS et al,1976). Figure 1.1 shows the use of a multi-pole electrode. Electrical stimulation may be carried out with equipment connected via the percutaneous leads. Unless otherwise stated, the analysis in the thesis is related to electrical stimulation by such epidural electrodes (EDS). If satisfactory clinical results are obtained during an assessment period (ILLIS et

FIGURE 1.1 ANTERIOR-POSTERIOR X-RAY SHOWING POSITION OF A MULTI-SITE ELECTRODE (4 POLES) IN EPIDURAL SPACE.

al, 1980), then permanent implantation is carried out. Electronic aspects of the stimulating system can be found in JOBLING et al (1980), but typical stimulating parameters are 10mA square pulses of 0.2ms duration at 33 Hz.

Stylised computer models indicating the location of electrodes in the epidural space, and the general anatomy of the region may be seen in Figures 2.1-2.3.

1.2 THEORETICAL BACKGROUND

A theoretical analysis of spinal cord stimulation needs to draw on different disciplines, from biophysics and engineering sciences. A first step is the finite element technique for the numerical solutions of potential field distributions . Formulation of potential field theory is well catered for in standard texts (for example JEANS, 1925; SMYTHE, 1968). By treating the human body as a volume conductor, the analysis can equally be applied in electrophysiological problems (e.g., PLONSEY, 1969; HERINGA et al, 1982).

Essentially, the equation governing the electric potential, V, in a three-dimensional domain is

$$\frac{\partial}{\partial x}\left(\frac{1}{\rho_x}\frac{\partial V}{\partial x}\right)+\frac{\partial}{\partial y}\left(\frac{1}{\rho_y}\frac{\partial V}{\partial y}\right)+\frac{\partial}{\partial z}\left(\frac{1}{\rho_z}\frac{\partial V}{\partial z}\right)=0$$

where ρ_x, ρ_y, ρ_z are corresponding specific resistivities in the direction of the principal coordinates.

A second topic concerns the physiological properties of excitable nerve membrane of nerve fibre. The voltage clamp studies on squid giant axon by HODGKIN and HUXLEY (1952) formed a starting point for modelling other excitable membranes. The work that is directly relevant to this thesis is the modelling of node of Ranvier by FRANKENHAEUSER and HUXLEY (1964); the model by HODGKIN and HUXLEY (1952) being modified to describe the nodal membrane behaviour of myelinated axon of frog.

The third aspect is the representation of the whole myelinated nerve fibre, including the internodal sections, in terms of electrical networks. A profusion of work exists in this area, but the approach by McNEAL (1976) is especially useful when used in conjuction with finite element analyses of stimulus fields.

1.3 PRINCIPAL PROBLEMS AND AIMS

In spite of the clinical trials cited above, the complete mechanism underlying the success of spinal cord stimulation remains unknown. Activation of nerve cells in the cord is the obvious central phenomenon. The Gate Theory (MELZACK and WALL, 1965) can be used to explain inhibition of pain due to the excitation of large fibres in the dorsal column, and hypotheses concerning the mechanisms of long-term motor improvement in other

disorders also exist (ILLIS et al, 1976). The intention of this work is to provide a biophysical contribution and it must suffice to say that purely clinical and neurophysiological theories are agreed to be inadequate.

The idea of electrical stimulation is to set up electrical fields, or apply current, within the spinal cord so as to affect the neurophysiological state of neuron structures. From the analytical veiwpoint, relevant data on the strength and orientation of these fields are surprisingly rare. The only published data available are the current density measurements made in vivo with monkey and in fresh human cadaver spinal cord (SWIONTEK et al,1976). Theoretical studies of these fields has also been carried out in a two-dimensional approach (COBURN,1980) , which was later extended to three-dimensional studies (COBURN, 1981).

On the other hand, estimation of these fields within the neuron structure is only the first stage. The next step is to investigate the immediate effects of these fields with biophysical neuron models. This two-stage approach allows, in principle, the predictions of the theoretical threshold of any myelinated nerve fibre system, as first demonstrated by COBURN (1981).

The primary aim of this present work was to further develop and rigorously validate the essential field analysis methods and biophysical models to provide a reliable and routine set of 'tool' for the analysis of spinal cord stimulation.

First, the problems with the finite element model do not lie on the techniques of numerical solution . In fact, with the availability of software packages, numerical solution using the finite element method has become fairly standard. The problems are the poorly-defined anatomical structures of the human body and the electrical properties of certain biological tissues. Many assumptions are made and a rigorous validation on the model is required. Second, in parallel with the finite element model verification, there is also the need for a searching validation of the mathematical model of McNeal nerve fibre to which field solution will be applied. In this case, the area to be validated is its ability to predict fibre threshold for a given applied field.

1.4 GUIDE TO THE THESIS

1.4.1 Content Layout

As the format of the thesis is not entirely conventional, it is worth describing the layout of the content. The reason for this unusual presentation is that a number of disciplines are drawn upon and each of them requires separate background introduction. For the ease of reference these introductory materials are better distributed in the thesis closest to the relevant subjects. Thus many chapters will begin with a section describing some background information. In addition, any

short discussion which is of direct relevance to the work will be presented in the same chapter.

The thesis can be considered in two main sections. Chapters 2-6 are concerned with potential field analysis at a macroscopic level. An introduction to finite element method and models used in this thesis are presented in Chapter 2. Some interesting field solutions completed in the early stage of the work will also be included. As mentioned before, anatomical factors and electrical properties are two major difficulties encountered in finite element modelling, and Chapter 3 investigates these aspects using a two-dimensional model.

Chapter 4 is the first part of the three-dimensional model validation, comparing data from existing literature with computer-generated solutions. Chapter 5 is the second part of the 3-D validation : the main issue being the use of clinical measurements to provide some verifications of the computed solutions for electrode fields.

The final development of a finite element model from the original one is presented in Chapter 6. Modified features include finer meshing in the vertebral canal, a better geometrical approximation and a change in node and element numbering systems. In addition, the mesh in the spinal cord is specially re-designed for further theoretical studies.

The second part of the thesis extends from Chapter 7 to 9 and deals with studies on myelinated nerve fibre models at the single cell level. Chapter 7 covers the

fundamental formulation of the fibre model and also considers two possible applications of the model. Chapter 8 is a validation study of the model by comparing experimental data on chicks with theoretical predictions. A further theoretical study of the fibre model is presented in Chapter 9. This involves development of the model to study the effects of external fields on already excited fibres.

Finally, the whole work ends with a general discussion and recommendation in Chapter 10.

1.4.2 Omission of Materials

Many relevant and background materials used in this thesis have been omitted. First, the general anatomy and neurophysiology are left to standard texts (for example WARWICK and WILLIAMS,1973; KATZ,1966; TALBOT and GESSNER, 1973). Full comprehensive anatomical data concerned can also be found in COBURN (1981).

Second, practical aspects of data preparations for the computer packages will not be presented here, and the information must also be left to the appropriate user's manuals (HENSHELL,1978; KOHNKE,1979).

Third, although computer programming is indispensable to the modelling of myelinated fibre, these programs (at least five have been used) will not be listed. Instead, the programming aspects of these programs are given in the appropriate sections.

1.4.3 A Note on Sign Convention

In clinical and neurophysiological practices, cathodic field generators and the subsequent electrical potentials are often presented in terms of positive values, while anodic sources are taken as negative.

On the other hand, finite element analyses of potential fields in Chapters 2-6 use the usual mathematical practices, where the absolute values of fields are presented together with the polarity sign. An upright ordinate in a graph would therefore represent a positive (anodic) source.

When these two disciplines are brought together, confusion concerning the sign notation may occur. One example is the graphically presentation of strength-duration and strength-distance relationships. In the former practices, the ordinate representing the cathodic current is drawn upright showing only the absolute values. The mathematical practice would imply that the current is an anode.

In this thesis, the mathematical practice will be used.

Another sign convention is that of the direction of current, presented as an arrow in drawings. The practice adopted here is that a point cathode will have an arrow indicating the flow of positive charge being extracted from the medium at that point.

CHAPTER 2 FIELD ANALYSIS USING FINITE ELEMENT METHOD

2.1 METHOD OF FIELD SOLUTION

2.1.1 Finite Element Method

Numerical analysis of potential field problems in physiology has aroused a lot of interest. The concepts are used widely, from general field analyses (for example, KINNEN,1966; GUHA et al,1973; KIM et al,1981; HERINGA et al, 1982) to specialised areas like electrocardiographic potentials (SILVESTER and TYMCHYSHYN,1974; HORACEK,1974; MILLER and GESELOWITZ, 1978). The most relevant work here, of course, is the analyses of potential distributions within human body due to epidural stimulating electrodes (COBURN,1980; RUSINKO et al, 1981).

As mentioned in Chapter 1, the equation to be solved in order to obtain the three-dimensional potential distribution is

$$\frac{\partial}{\partial x}\left(\frac{1}{\rho_x}\frac{\partial V}{\partial x}\right)+\frac{\partial}{\partial y}\left(\frac{1}{\rho_y}\frac{\partial V}{\partial y}\right)+\frac{\partial}{\partial z}\left(\frac{1}{\rho_z}\frac{\partial V}{\partial z}\right)=0 \qquad (2.1)$$

subjected to certain boundary conditions.

A full description of the finite element technique is now textbook material (ZIENKIEWICZ,1977), but the overall concept can be summarised in the following seven steps.

Note that some of the accepted terms arise from the original application of the method in stress analysis.

(1) select element and node representations of the structure

(2) define material properties used in the structure

(3) define boundary conditions

(4) derive element "stiffness" matrices $[K]^e$ based on element type, geometry, material properties and assumed polynomial function. For each element, the solution to equation (2.1) may be expressed as

$$\{I\}^e = [K]^e \{V\}^e \qquad (2.2)$$

where $\{I\}^e$ and $\{V\}^e$ are the currents and potentials at the nodes of element 'e' respectively.

(5) assemble system "stiffness" matrix $[K]$ for the entire structure where

$$[K] = \Sigma \{K\}^e \qquad (2.3)$$

so that a complete set of n linear equations is formed by suitable combination of eqn. (2.2) from every element, i.e.

$$\{I\} = [K] \{V\} \qquad (2.4)$$

(6) formulate "load" vector $\{I\}$ from boundary conditions. External applied electrode currents determine some of the elements in $\{I\}$, but most will be zero. Such

specified values of current correspond to unknown Values of potenial V. On the other hand, when nodal potentials are specified as boundary conditions, the corresponding currents are unknown.

(7) calculate unknowns by solving $\{I\} = [K]\{V\}$.

It must be pointed out that the above procedures are only a general guide to finite element method. The use of frontal technique (IRONS, 1970) in the equation-solving process, for example, means that the complete set of equations $\{I\}=[K]\{V\}$ will never be formed.

2.1.2 Analysis Software

Two commercial suites of programs were used throughout the study : PAFEC 75 (HENSHELL, 1978) and ANSYS (KOHNKE,1979). PAFEC 75, based in University of London Computer Centre (ULCC) , was used extensively in this thesis and the work by COBURN (1980,1981). ANSYS, on the other hand , was mainly used for the model validation study to be described in Chapter 4. A few general aspects of field distributions are also studied using ANSYS, these being part of the present chapter. Both packages, incidentally, were run on CDC7600 computers. PAFEC 75 has also begun to be run on a CRAY-1S which has just replaced the CDC machine in ULCC during the closing stage of the work. Data file preparation and post-processing for PAFEC was accomplished locally on a HONEYWELL MULTICS system.

Each package has its strong and weak features. The

major weak point in PAFEC 75 is the output plotting routine, where the classical isopotential plots are restricted to two-dimensional (2-D) solution. In other words, solutions from three-dimensional (3-D) domain cannot be presented graphically in PAFEC. Nevertheless,the strong point of the package is the ability to generate small elements within a pre-defined element . This feature, called PAFBLOCK, is particular useful for generating 'localised' fine elements in the neighbourhood of, say, applied current source, where the voltage gradient will be steep.

The useful feature of ANSYS lies on the graphics facility, where contour plots on defined surfaces through 3-D meshes can be produced. Other useful facilities include direct computation of current density at element centroids, extented range of boundary conditions enabling better modelling of electrode currents.

With the availability of these packages, solving any field problem is straightforward. The 'user' only need to carry out steps (1) -(3) mentioned in the last section, these being called data preparation. Steps (4)-(7) are then performed automatically by programs in the packages.

The solution printout from an execution run consists of calculated potentials at each node, which can be used for further analysis.

2.2 FINITE ELEMENT MODELS OF HUMAN THORAX

This section describes the general and common features of finite element models used in the thesis. Detailed descriptions of particular features used for solving a specified problem will be presented in the relevant chapter.

2.2.1 Three-dimensional Model of Human Thorax

Figure 2.1 shows the outline of the 3-D model relative to the global coordinated system used in this thesis, where the concept of symmetry is also illustrated. Sections of transverse plane (X-Y) at z=0mm are shown in Figures 2.2-2.3, and the whole model is built prismatically from the transverse plane. Thus the structure consists of rectangular bricks and triangular wedges, and element heights are therefore equal within any layer. Owing to the fact that symmetry has been exploited, only electrode arrays symmetrical about the mid-sagittal plane can be studied.

Figure 2.1(a) illustrates a bipolar case, where the transverse plane at z=0mm may be set at zero potential due to electrical symmetry. Moreover, the electrical field generated from mid-line electrodes will also be symmetrical about the mid-sagittal plane (x=0mm plane). It is only necessary to apply an electrode current of Is/2 to

the single-sided representation. In other words, the solid boundary drawing in Figure 2.1(a) represents one-quarter of the effective model of thoracic region. The nature of the known symmetry for the monopolar case, shown in Fig. 2.1(b), is slightly different, however. Here no current flows across the z=0 plane, a condition automatically catered for by the model bounda ry. Note that the applied current in this case needs to be Is/4 where Is is the current applied in the real case.

On the other hand, the model in Figure 2.1(c) represents one-half of the thorax, where the model is no longer symmetrical about the transverse (z=0.0mm) plane. This feature is introduced so that a single 'remote' indifferent can be modelled; it is the least desirable case from the point of view of computing economy.

Figure 2.1(a) also illustrates that the 3-D model has different element heights. First, element heights have to be small at levels near that of the electrode, where the voltage gradient would be steep. On the other hand, the total height of the model (in other words total volume) must also be large enough so that the ultimate truncation does not significantly influence the electrical fields in the operating region of the electrodes. One way is to increase the height of successive layers at increasing distance from the electrode to represent a reasonable volume of thorax.

The 3-D model used in PAFEC 75 consists of eight layers, a total of 760 elements and about 2500 nodes.

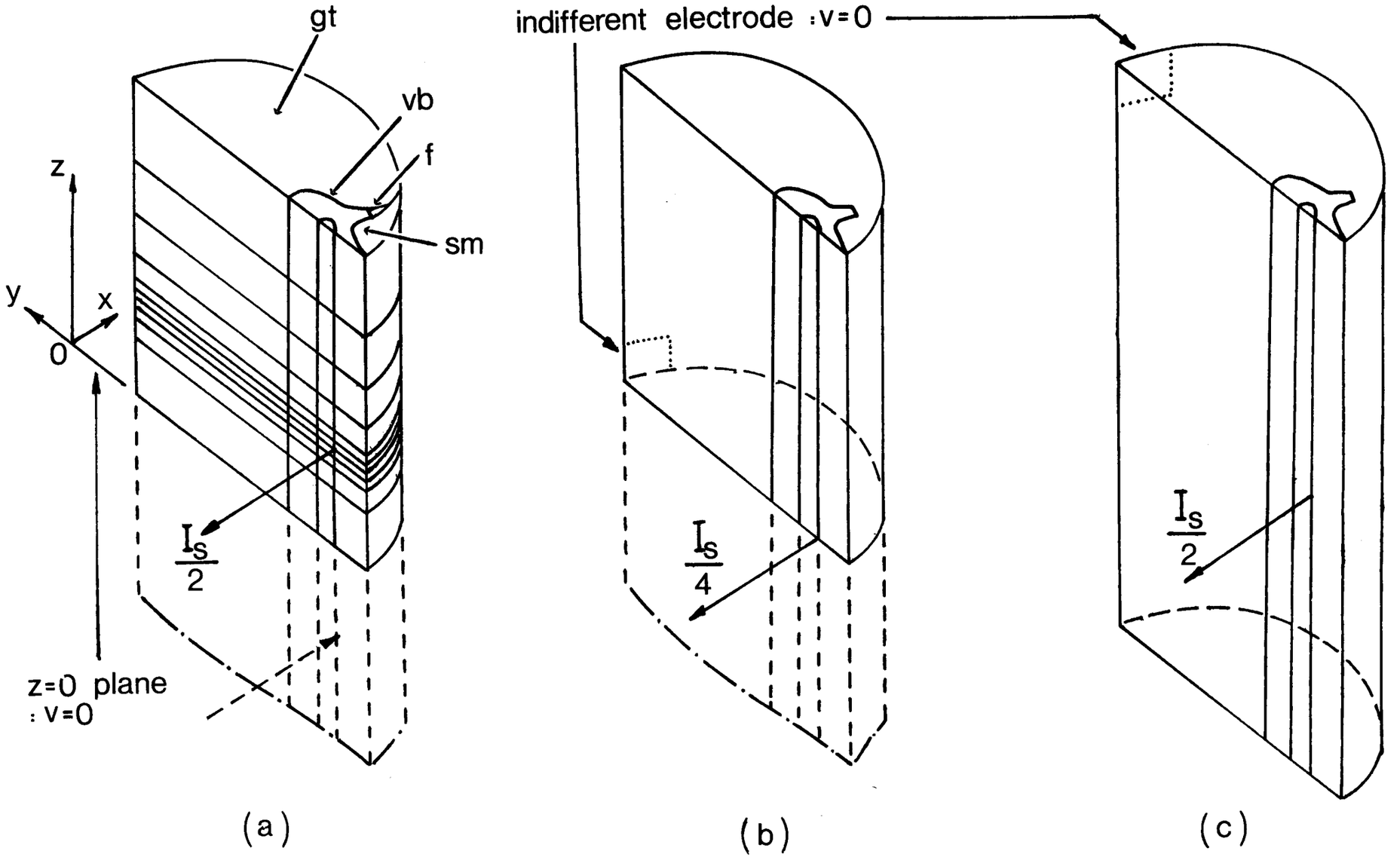

FIGURE 2.1 GENERAL SCHEME OF THREE-DIMENSIONAL FINITE ELEMENT MODELS

(a) bipolar epidural electrodes with cathode at upper half.
(b) monopolar epidural electrode with ventral surface indifferent.
(c) monopolar epidural electrode with 'remote' surface indifferent.
See text for details

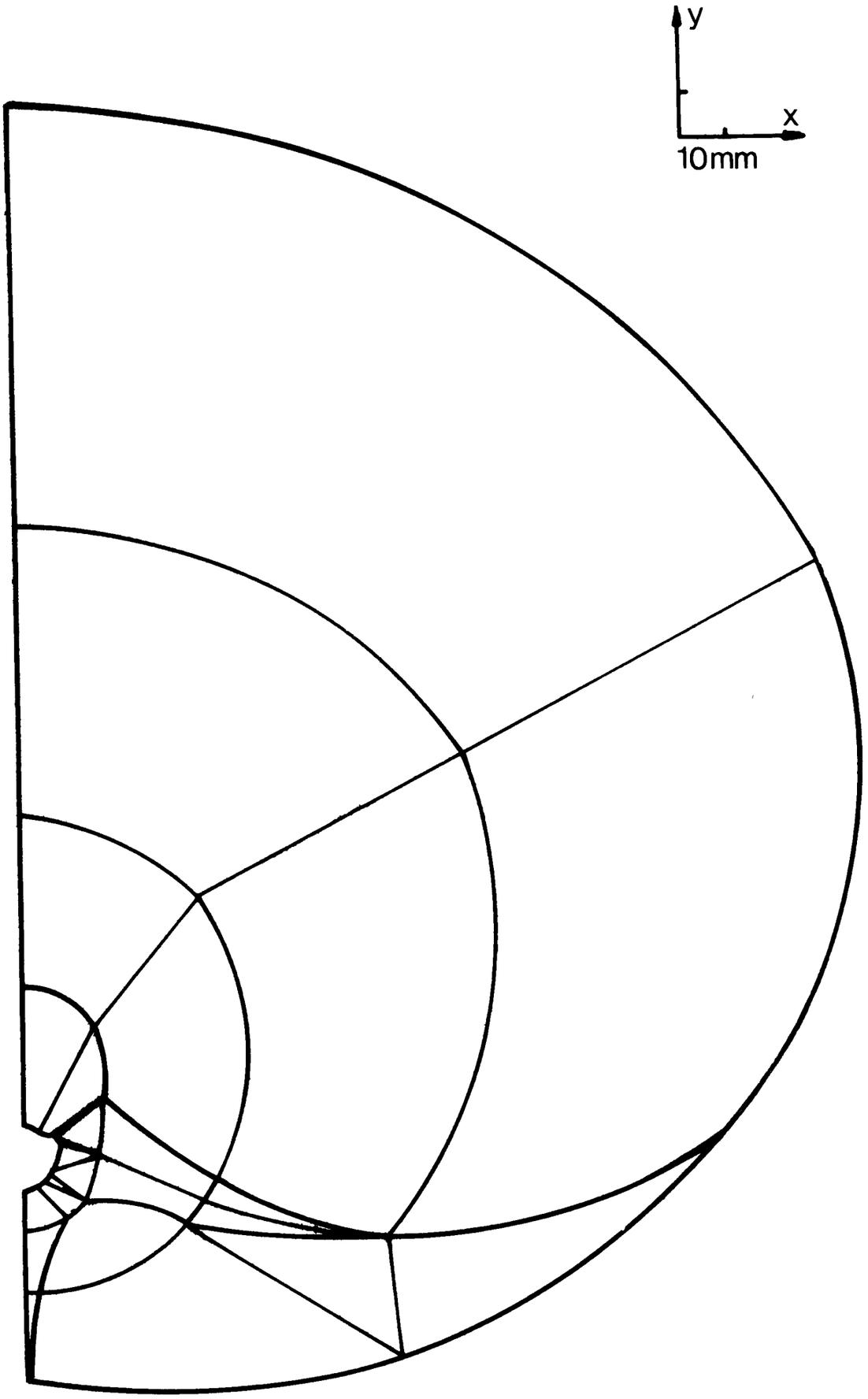

FIGURE 2.2 FINITE ELEMENT MESH OF TRANSVERSE SECTION THROUGH HUMAN THORAX AND VERTEBRA (PAFEC MODEL)

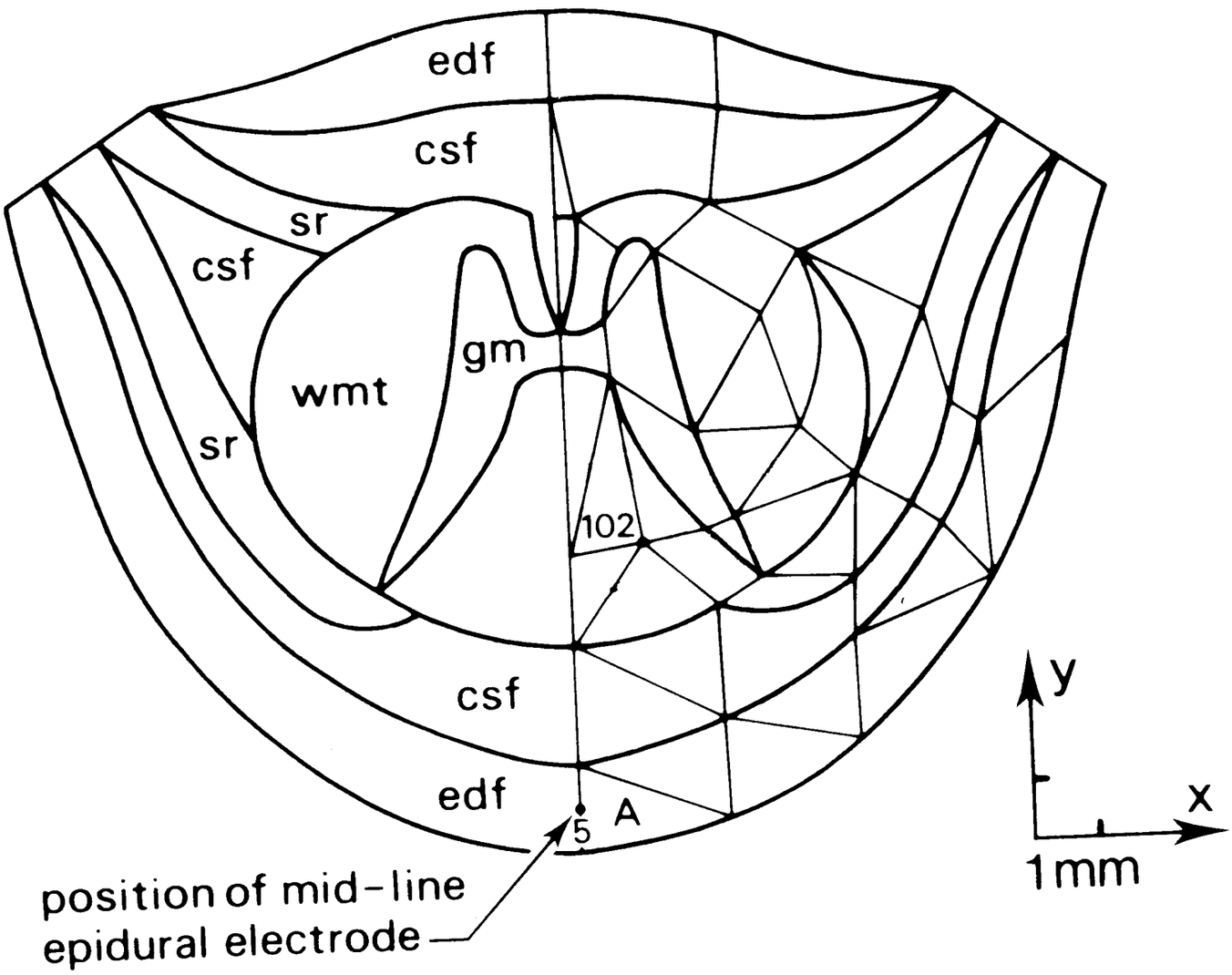

FIGURE 2.3 FINITE ELEMENT MESH OF TRANSVERSE SECTION THROUGH VERTEBRAL CANAL (PAFEC MODEL)

See Table 2.1 for abbreviations.

The 3-D ANSYS models had a similar structure, although straight-sided elements (8-noded brick and 6-noded wedge) were used, as shown in Figures 2.4-2.6.

2.2.2 Anatomy

Many assumptions have to be made in modelling the human thorax, partly because the degree of mesh fineness is restricted by computer memory size, and partly because the anatomy of many body tissues, from an engineering veiwpoint, are poorly defined. A glance at Figures 2.1 and 2.3 reveals that there are nine different tissues in the 3-D model, five of them are within the vertebral canal. It goes without saying that the boundaries between tissues in the model are exceedingly well-defined and stylised in relation to the biological reality.

While the geometry of the outer thorax and vertebrae can be developed from sources like computer tomography and standard texts (MORTON et al,1941), tissues within the vertebral canal present difficulties. In this model, the sizes of spinal cord, epidural and subarachnoid spaces in the vertebral canal were approximated from serial sections of fresh human spinal column (COBURN, 1980). Nevertheless, the dimensions of grey matter and spinal roots still had to be estimated. Variations of tissue geometry in the vertical (z-axis) direction are also neglected, since the model is a prismatic structure. Features like the curvatures of vertebral column are, necessarily, neglected.

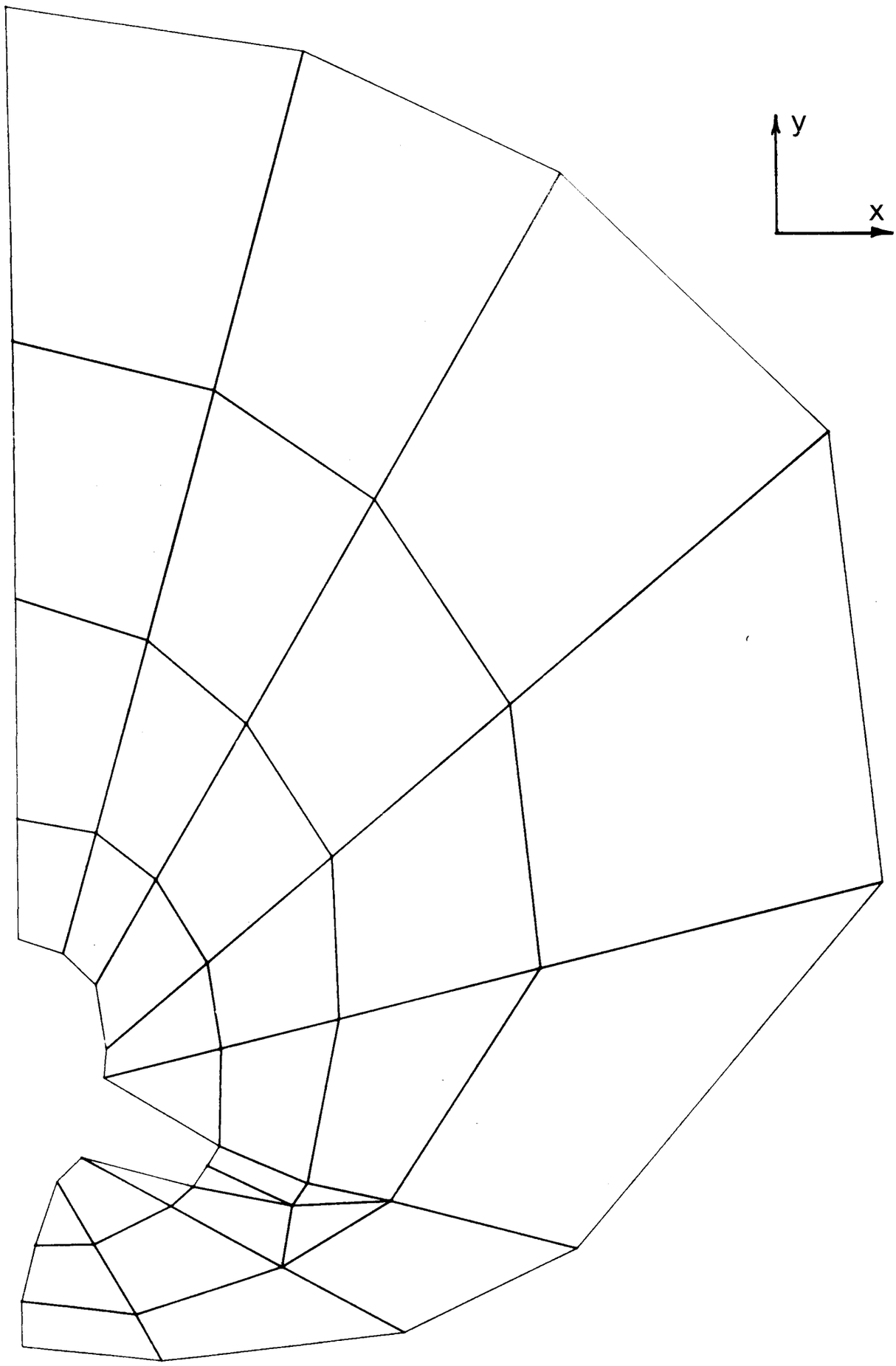

FIGURE 2.4 FINITE ELEMENT MESH OF TRANSVERSE SECTION THROUGH HUMAN THORAX (ANSYS MODEL)

Approx. scale 0.775

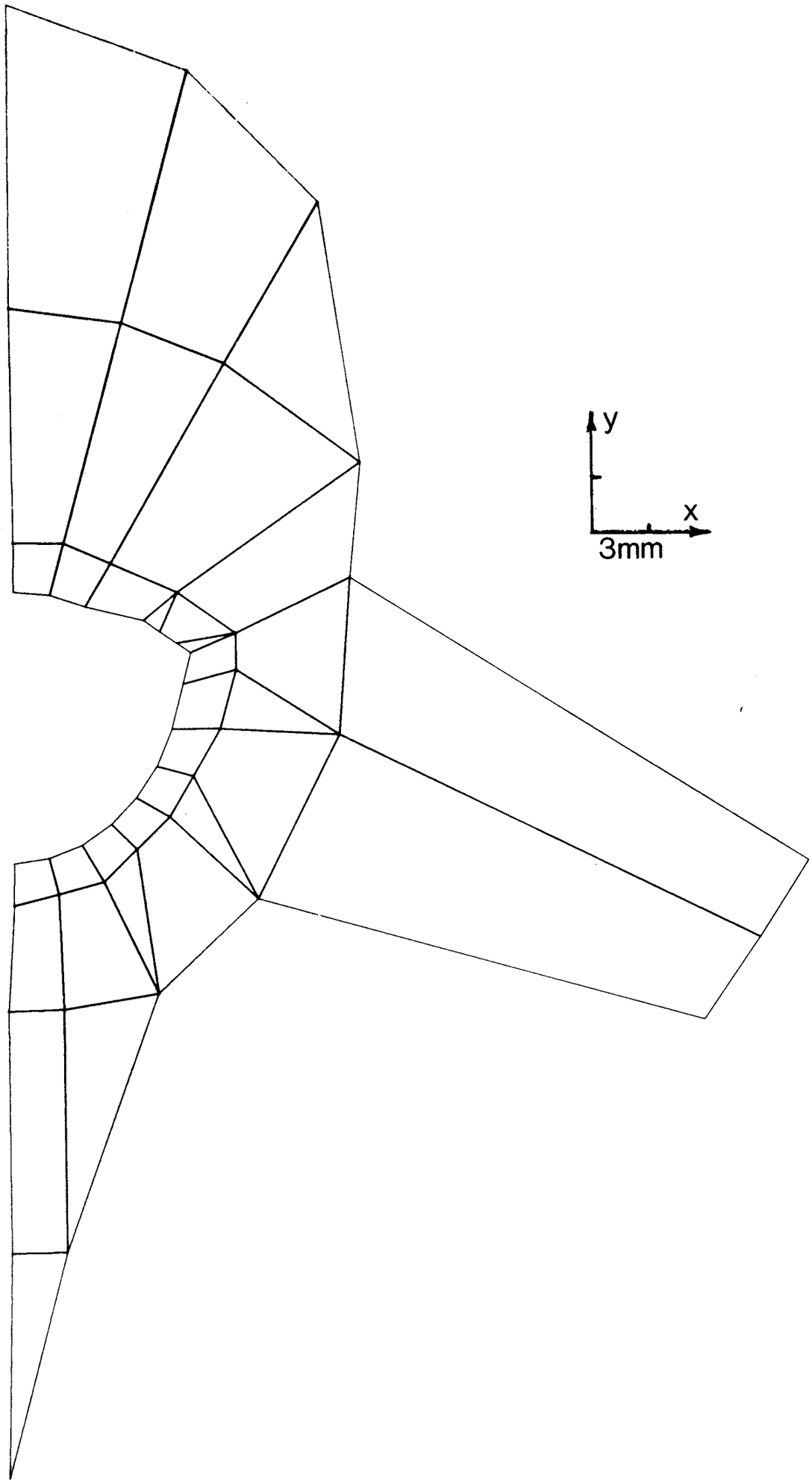

FIGURE 2.5 FINITE ELEMENT MESH OF TRANSVERSE SECTION THROUGH VERTEBRAL COLUMN (ANSYS MODEL)

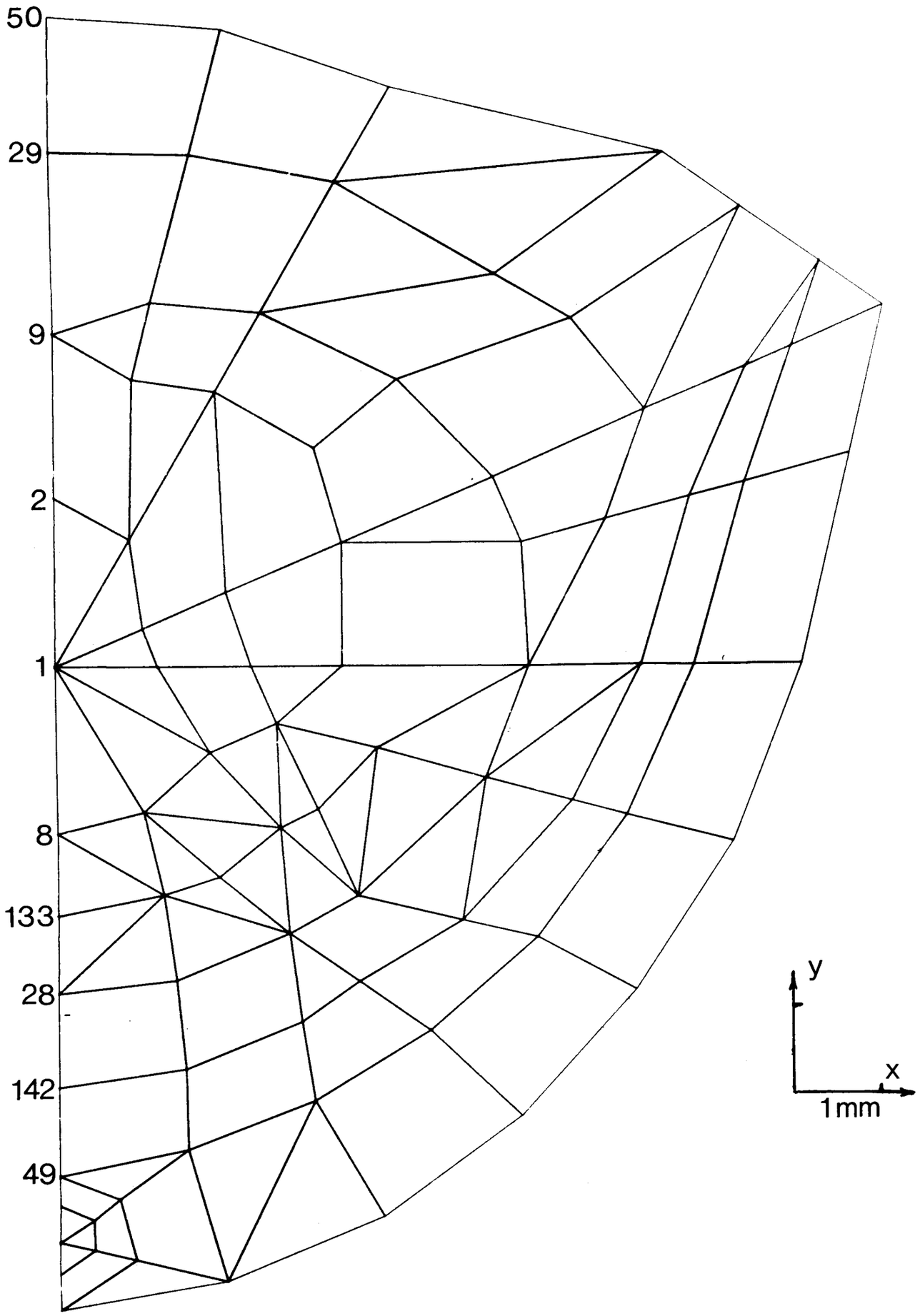

FIGURE 2.6 FINITE ELEMENT MESH OF TRANSVERSE SECTION THROUGH VERTEBRAL CANAL (ANSYS MODEL)

In general, the whole model consists of four main sections : general thorax, dorsal skeletal muscle , vertebral column and canal. Inhomogeneities in the general thorax such as lungs, ribs, sternum, blood masses and subcutaneous fat are all omitted; instead the region is represented by a single homogeneous tissue.

The vertebral column is also simplified by a single homogeneous material representing the bony body, intervertebral discs, ligaments and the like.

In the vertebral canal, the three membranes (meninges) are all omitted. The pairs of spinal roots are modelled, although they are also running vertically along the subarachnoid space, dividing it into three compartments.

2.2.3 Electrical Properties of Tissues

Table 2.1 contains the values of specific resistivities (and abbreviations) assumed for the tissues. These values, with the exception of metal electrode, are based on the compendium of GEDDES and BAKER (1967), and have been used in the early work (COBURN, 1980,1981) , the work in this chapter and validation study to be described in Chapter 4. This set of values will be referred in the future as 'standard' or 'nominal'.

TABLE 2.1

Material	Abbreviation	Assumed resistivity (ohm-cm)
Grey matter	gm	400
White matter, transverse	wmt	1211
White matter, longitudunal	wml	138
Cerebrospinal fluid	csf	60
Fat in epidural space	edf	2000
Vertebral column	vb	4000
General thorax	gt	400
Skeletal muscle	sm	950
Spinal roots	sr	675
Fillers	f	1066
Metal electrode	--	1

The value of bone, vb, is uncertain, although a general range of 2000-6000 ohm-cm was suggested by GEDDES and BAKER (1967). A survey of texts on subjects like

"electrical impedance measurement of physiological systems" (NYOBER,1959; ALLISON,1970; MARKOVICH, 1970) and "electrical properties of bone" (BRIGHTON et al, 1979; ERIKSSON, 1976) failed to reveal any measurements made on bones. Early investigators (BURGER and VAN MILAAN, 1943; SCHWAN and KAY, 1957) even suggested that bone could be considered as a non-conductor. Recently, CHAKKALAKAL et al (1980) and ROSTERICH et al (1983) experimentally determined the properties of fluid-saturated bone, and the range of values were 4000-160000 ohm-cm !

Owing to such a wide range of resistivity values, a nominal value of 4000 ohm-cm was chosen initally (COBURN, 1980).

Anisotropic properties of some tissues also present difficulties in the modelling. Spinal roots and skeletal muscle are two examples, as the orientation of these fibrous tissues lie in neither sagittal nor transverse planes. Average values have to be used.

A value of 1 ohm-cm has to be used to represent the resistivity of metal electrode. It is appreciated that this value is 10^6 times higher than platinum, but unless the mesh is exceptionally fine, numerical inaccuracy arises due to the great difference in values between the metal and the surrounding tissues. A check of computer solution on the electrode itself showed, nevertheless, that there was a constant potential within the region. Note that only ANSYS models used finite size electrode. Point sources were used for all other 3-D models .

2.3 EFFECTS OF SURFACE INDIFFERENT POSITIONS : A MONOPOLAR STUDIES

The significance of surface stimulating indifferent positions on field solutions aroused interest during the development of the finite element model.

The investigation was conducted by a 3-D ANSYS model, where the stimulating condition was a monopolar epidural electrode, similar to the one shown in Figure 2.1(b).

Figure 2.7 shows contour plots on a transverse section through the thorax at the level of a monopolar epidural cathode. Electrode current, Is, in each case is a nominal 1 mA.

Three positions of surface indifferent electrode are shown : dorsal, lateral and anterior. It should be noted that in the lateral case the symmetrical (mirror-image) modelling technique implies two lateral indifferent electrodes electrically common at zero voltage, one on each side.

The general field shapes are as expected with the zero voltage indifferent in each case distorting the field contours in its locality. However, although the thorax fields vary in outer regions, when moving in towards the epidural electrode and reaching the boundary of the vertebra, the differences between the plots become only slight. Although not shown on the figure, the positions at which the minimum potentials occur have the values varying

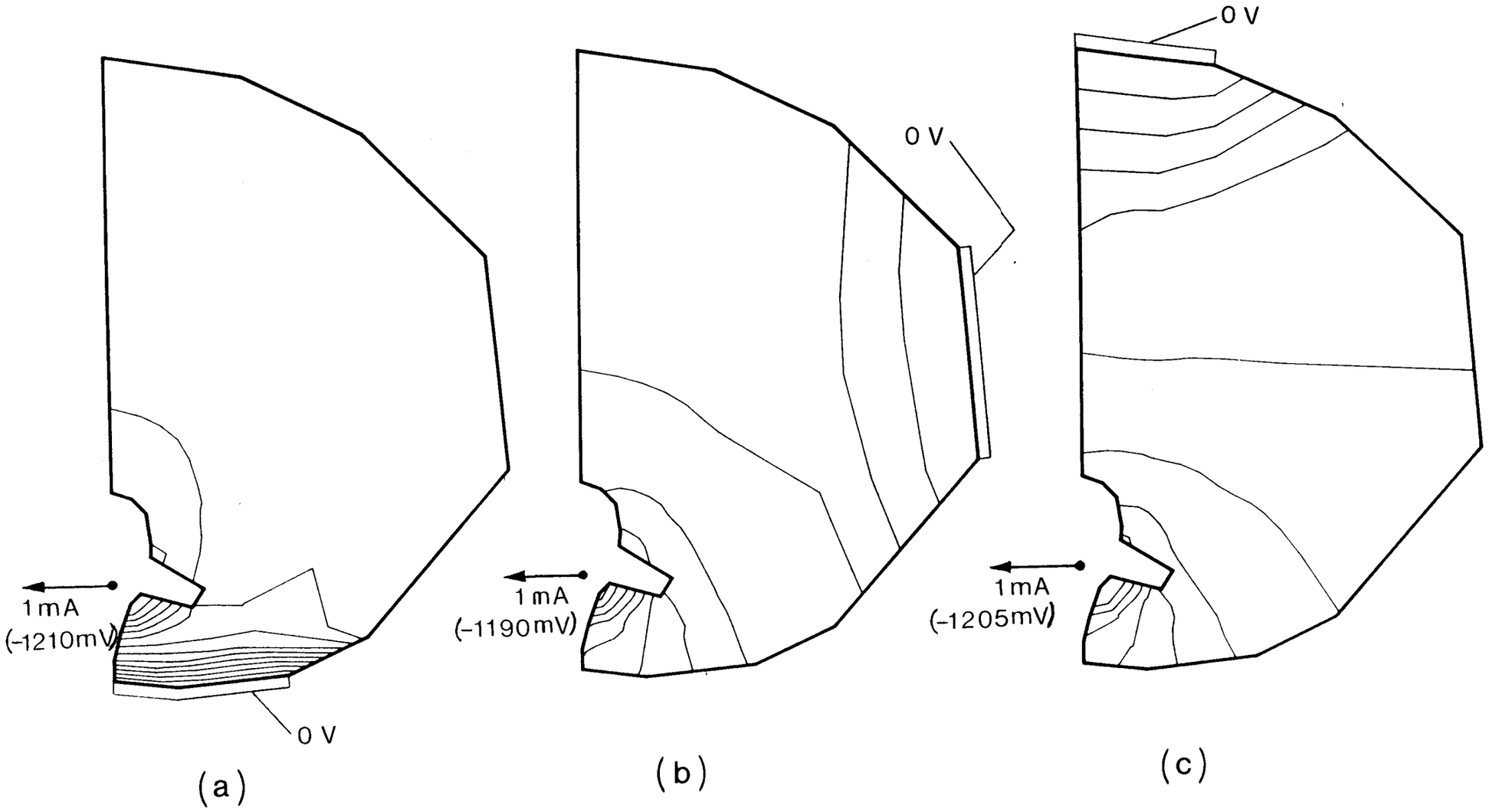

FIGURE 2.7 THORAX ISOPOTENTIALS FOR MONOPOLAR CATHODE WITH DIFFERENT PLACEMENTS OF SURFACE STIMULATING INDIFFERENT.

(a) dorsal (b) lateral (two) (c) anterior
Level of transverse plane is z=0mm plane. Contour spacing 5mV.
Electrode potential bracketed.

between -59 mV to -72 mV

Figure 2.8 shows the field within the vertebra which was corresponding to Figure 2.7(b). Other cases for Figures 2.7(a) and (c) will not be shown as the pattern are virtually indistinguishable. A further 'enlargement' of the solution within the vertebral canal is shown in Figure 2.9. Another illustration of the same monopolar field is given in Figure 2.10, showing the field in the mid-sagittal plane. Note that the plot is slightly (0.1mm) off the mid-plane, as the graphics routine would not permit plotting at the element boundaries.

The model gave a better results when viewed on the sagittal plane, mainly because the mesh was built up in relatively fine vertically-stacked layers. Reasons for this stacking technique have already been explained in Section 2.2.1. In the transverse plane, however, the disadvantage of straight-sided elements shows up. Nevertheless, the plots within the spinal cord are not disappointing, with only a few obvious solution-discontinuities near the electrode being evident.

The major issue is, of course, the effects on potential distribution within the spinal cord due to the alternative placements of surface indifferents. The mid-line potentials, forward from the electrode through the spinal cord, have been plotted for the three cases and are illustrated in Figure 2.11. There are ten data points in each curve, corresponding to the nodal points shown in Figure 2.6 (node 49 to node 50). Although the absolute

values of the potentials vary slightly, the general shapes of these profiles, clearly shown here by using point-to-point drawing technique, are essentially the same.

Another illustration shown in Figure 2.12 is the potential variations vertically along the white matter (along node number 133 in figure 2.6). These profiles of potential, which again have similar shapes, can be considered to coincide with the pathway of a fibre running vertically in the dorsal column.

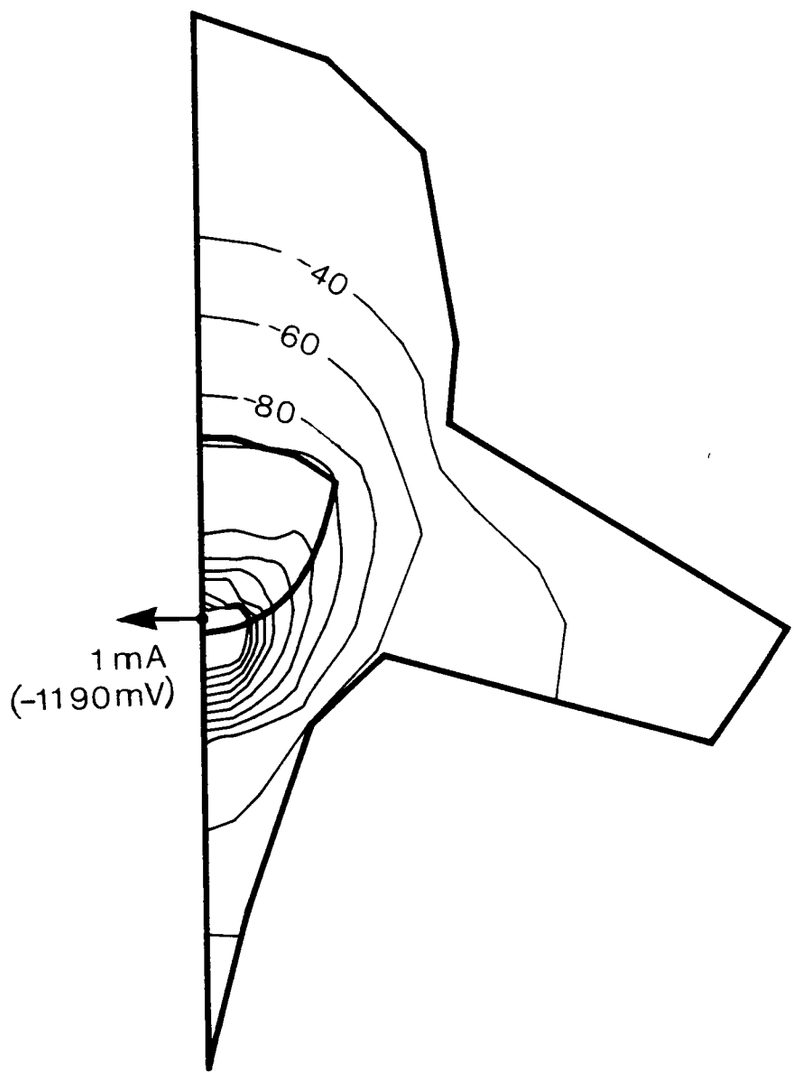

FIGURE 2.8 VERTEBRAL ISOPOTENTIAL FOR MONOPOLAR CATHODE WITH LATERAL SURFACE INDIFFERENT (TWO).

Contour spacing 20mV. Other remarks as Fig. 2.7.

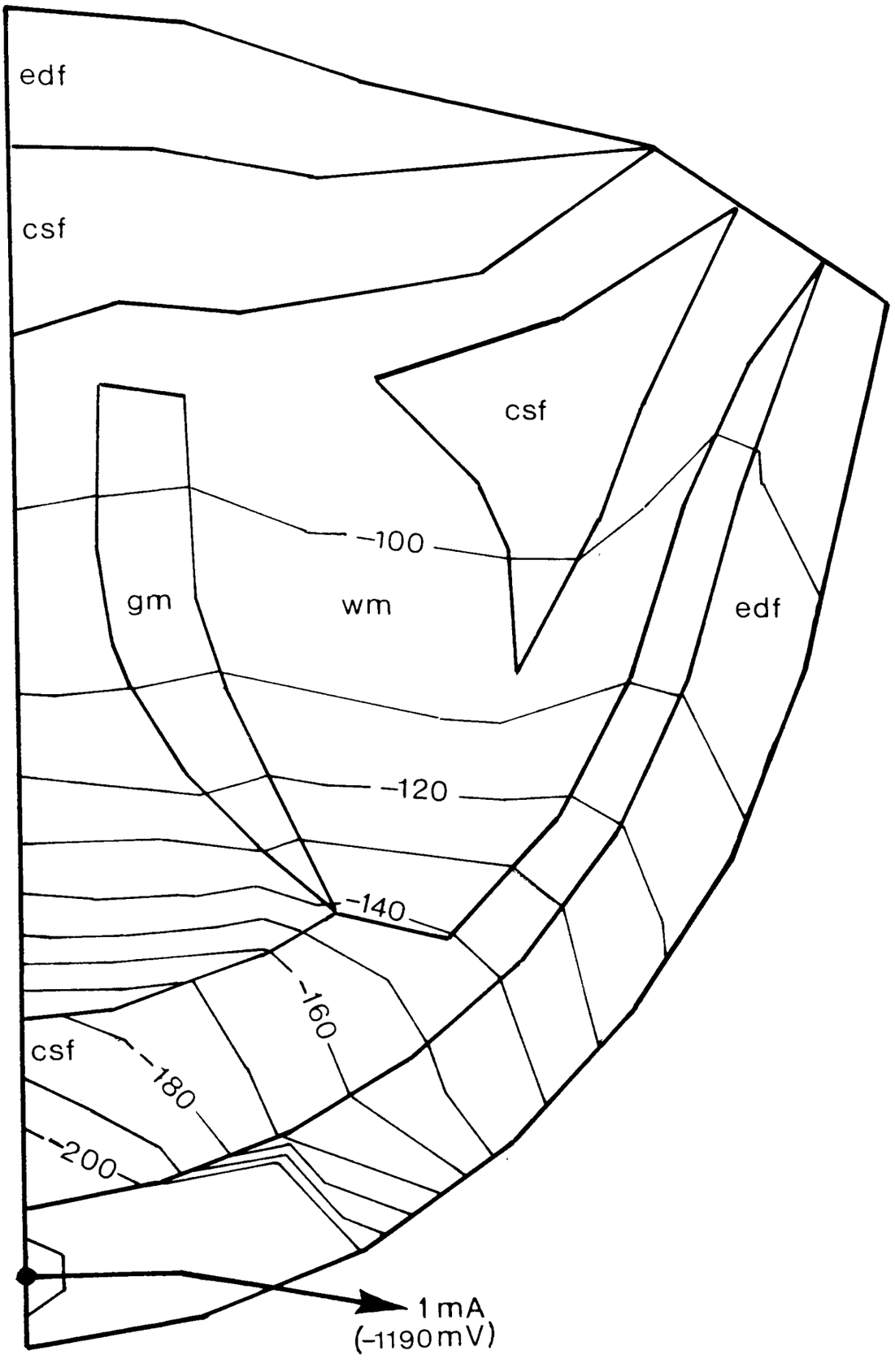

FIGURE 2.9 ISOPOTENTIAL THROUGH THE VERTEBRAL CANAL WITH LATERAL SURFACE INDIFFERENT (TWO).

Contour spacing 10mV. Other remarks as Figure 2.7.

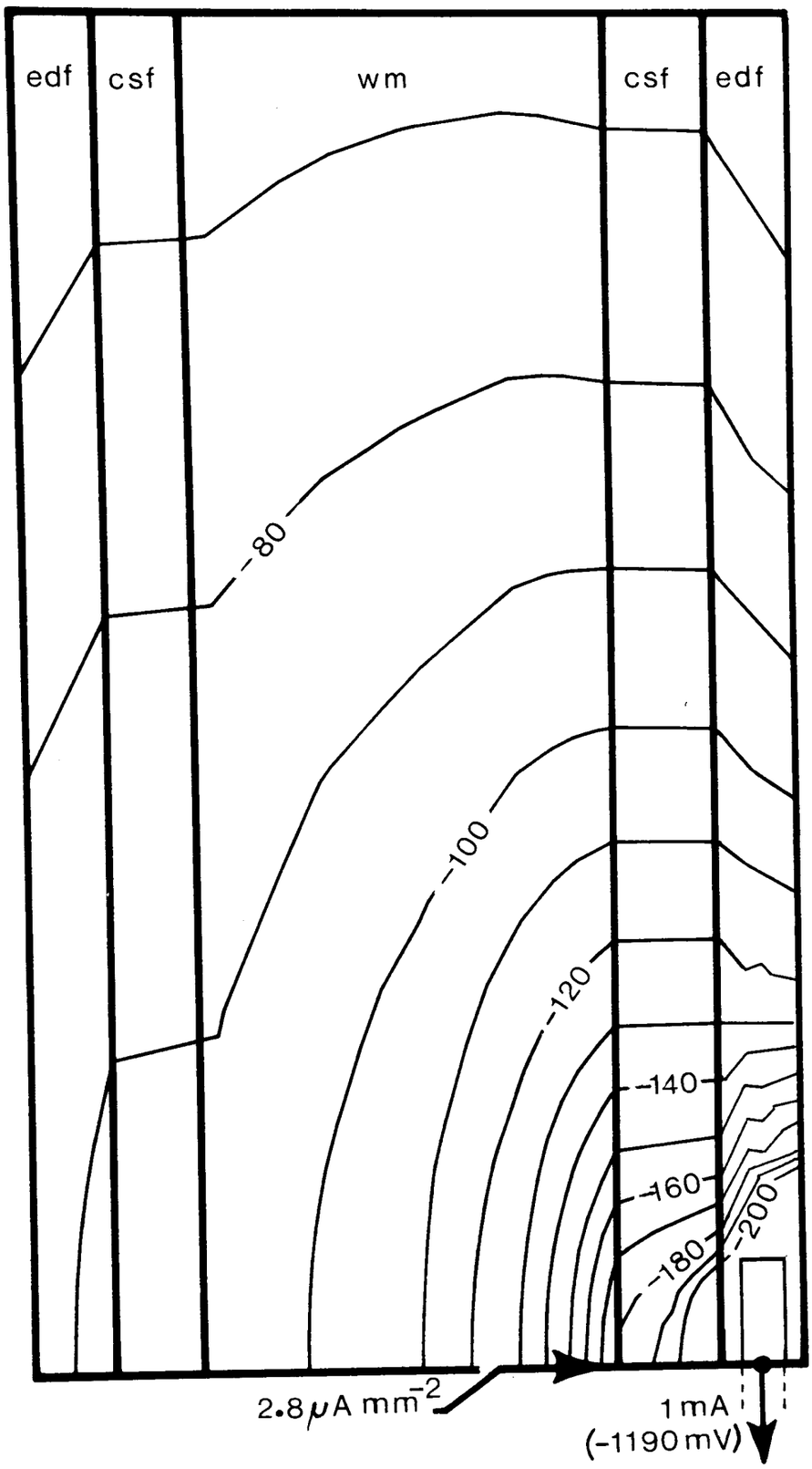

FIGURE 2.10 MID-SAGITTAL ISOPOTENTIAL IN THE VERTEBRAL CANAL FOR LATERAL SURFACE INDIFFERENT

Upper half of fields shown. Peak current density also indicated. Electrode potential bracketed

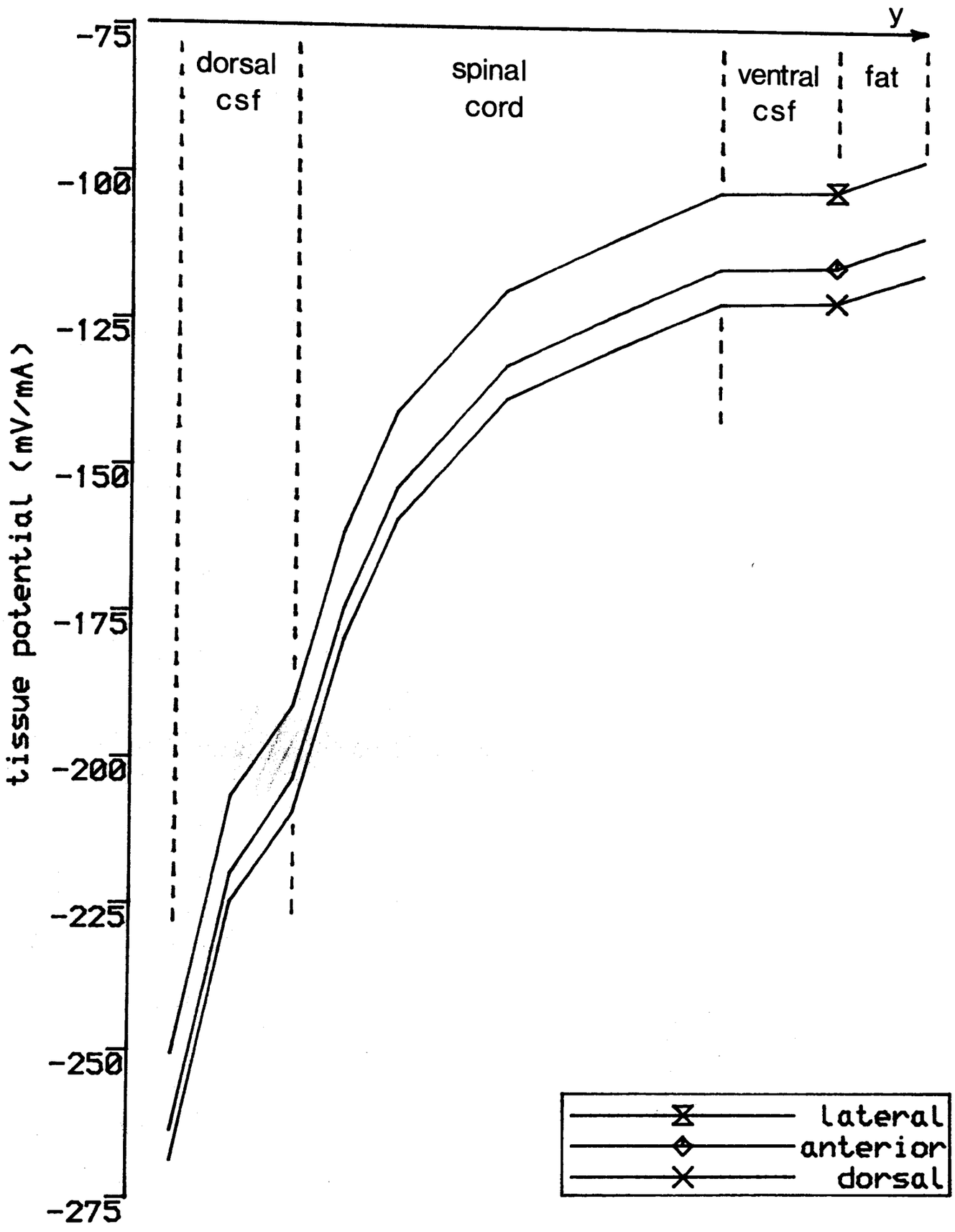

FIGURE 2.11 : VARIATION OF TISSUE POTENTIALS : EFFECTS OF POSITION OF SURFACE INDIFFERENT.

Potential is plotted on the mid-line forward from the cathode and at the same level.

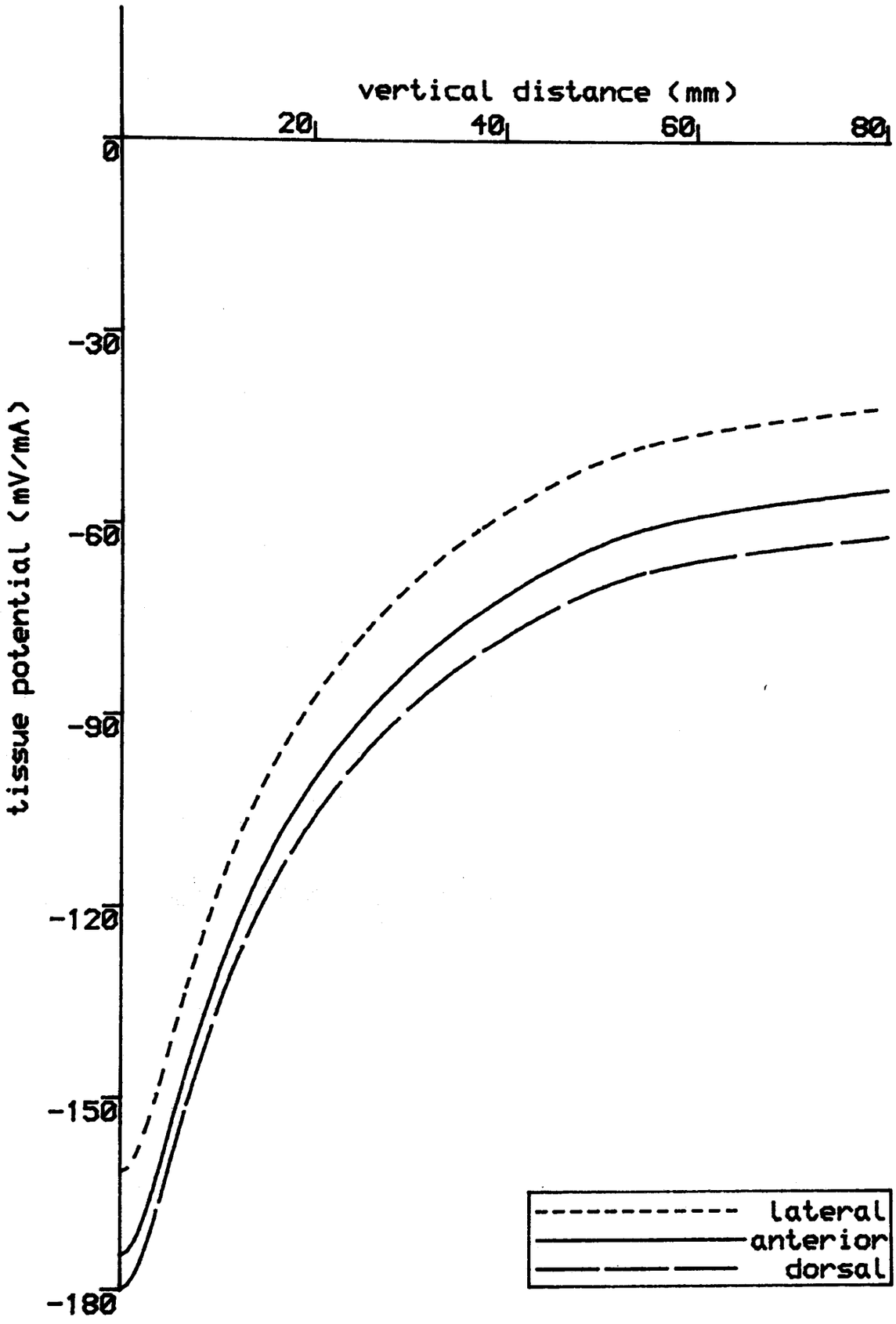

FIGURE 2.12 VARIATION OF POTENTIAL ALONG PATH REPRESENTING DORSAL COLUMN FIBRE.

Potential plotted vertically along node 133 shown in Figure 2.6

2.4 THREE-DIMENSIONAL FIELD SOLUTIONS FOR MULTI-SITE ELECTRODE

This section presents the field characteristics from different electrode configurations. Owing to the use of mirror-image modelling, only electrode configurations symmetrical about the transverse and mid-sagittal planes can be modelled. Using the numbering notation (given in Appendix 1) for a multi-site electrode, they are 0-3 (bipolar), 1-20 and 12-30 (multi-poles) configurations. Figure 2.13 relates to the configuration 0-3, and shows the upper half of the field. Note the important point that the peak dorsal column current density for the bipolar configuration of Figures 2.13 is similar to that for the monopolar field of Figure 2.10. The assumption that equivalent current density implies equivalent neurostimulation, however, should not be made.

Turning finally to configurations 1-20 and 12-30, Figures 2.14 and 2.15 unfortunately show the limitations of the ANSYS model. The choices of contour values do especially highlight solution discontinuities near electrodes. The solutions within the spinal cord, which another set of contours would better demonstrate, are quite smooth and certainly acceptable for use in the required biophysical analysis of nerve thresholds.

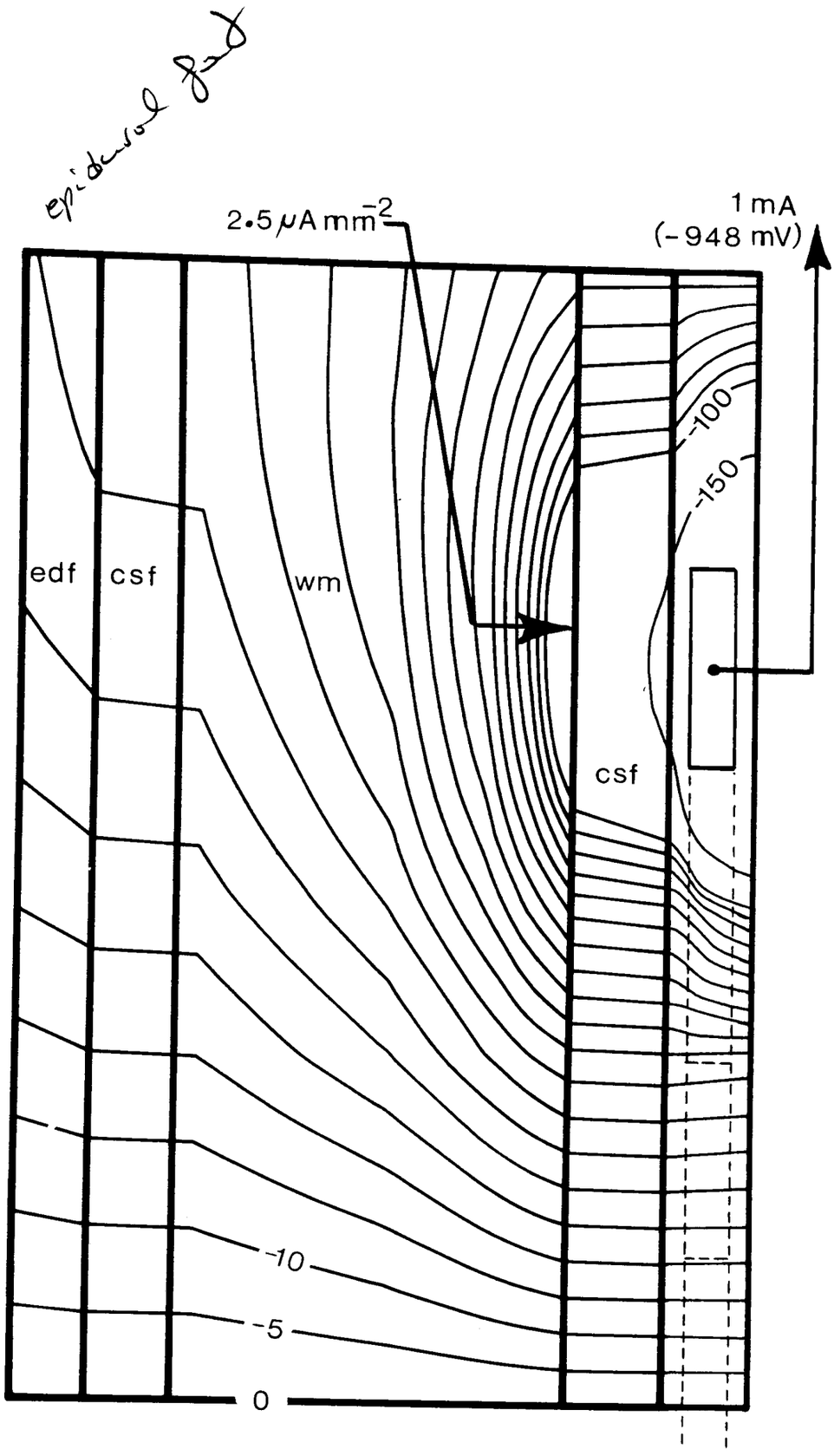

FIGURE 2.13 MID-SAGITTAL ISOPOTENTIAL IN THE VERTEBRAL CANAL : ELECTRODE CONFIGURATION 0-3

contour spacing 5mV. Other remarks as Figure 2.10

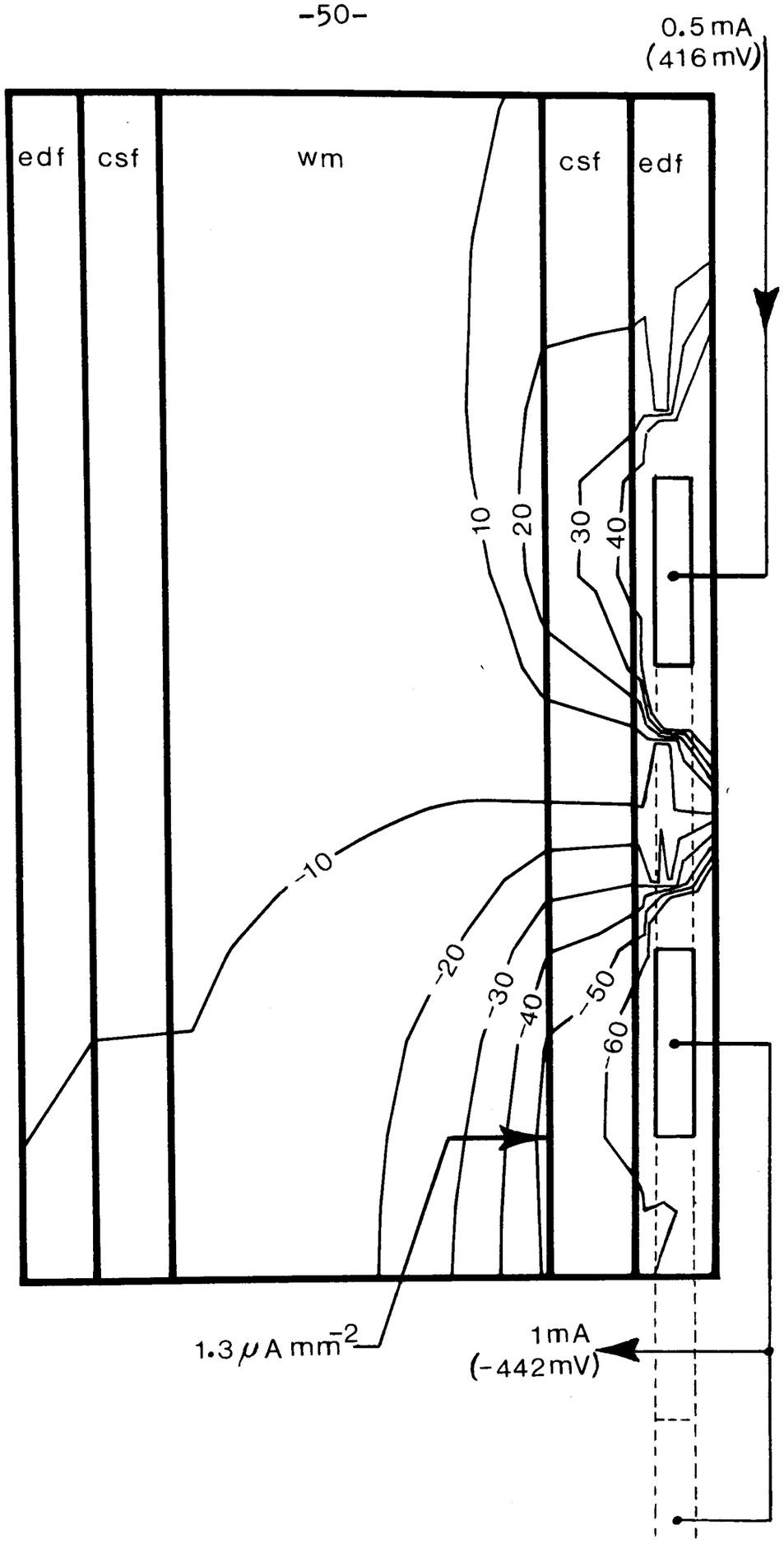

FIGURE 2.14 MID-SAGITTAL ISOPOTENTIAL IN THE VERTEBRAL CANAL : ELECTRODE CONFIGURATION 12-30

Poles 1 & 2 sharing 1mA (cathode), Poles 3 & 0 sharing 1mA (anode)
Other remarks as Figure 2.10

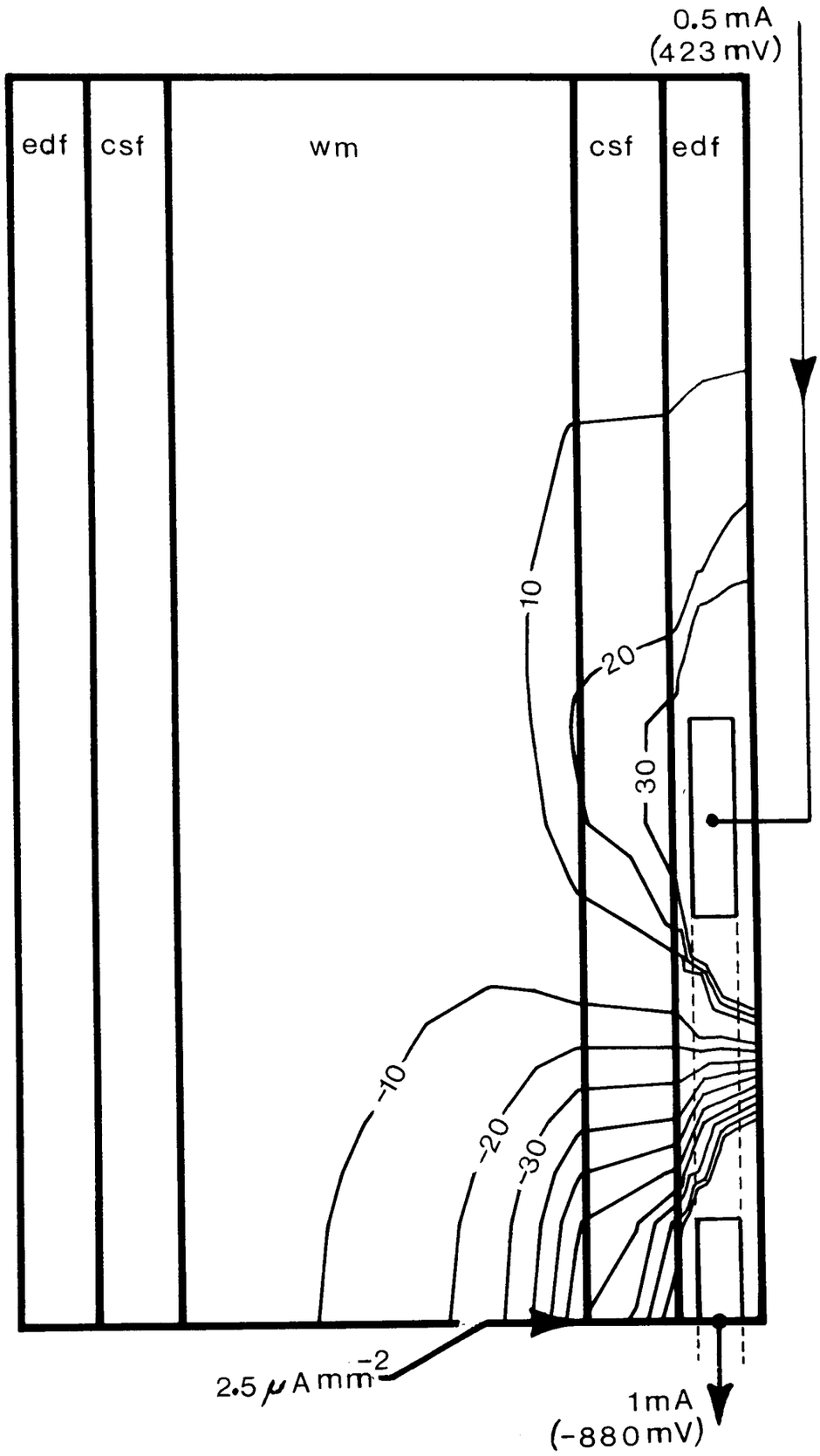

FIGURE 2.15 MID-SAGITTAL ISOPOTENTIAL IN THE VERTEBRAL CANAL : ELECTRODE CONFIGURATION 1-20

Zero potential omitted. Poles 0 & 2 sharing 1mA (anode)
Other remarks as Figure 2.10

CHAPTER 3 EFFECTS OF VARIATIONS IN TISSUE PROPERTIES AND ANATOMICAL FACTORS : A TWO-DIMENSIONAL STUDY

3.1 INTRODUCTION

Theoretical insights of stimulus fields generated by epidural electrode were presented in the last chapter. Central to the problem of solving for the field is specifying the electrical properties of the human model. Moreover, the geometry of the human thorax is another important factor affecting the current flow. For the present work to be described, current density J within the spinal cord will be of interest. Sensitivity of theoretical solutions to variations in assumed tissue properties is a vital issue. For example, this has been the subject of research in electrocardiography for many years (BAYLEY et al, 1969; RUDY et al,1979; RUDY and PLONSEY, 1980; GULRANJANI and MAILLOUX, 1983). A more relevant work is that of RUSINKO et al (1981), who suggested that dura mater, through which current must pass from an epidural electrode to reach the spinal canal, might have a crucial influence on the effective stimulus intensity.

This chapter therefore explores the effects of tissue properties and basic anatomical factors using a simple two-dimensional finite element model. Essentially, the study includes comparisons of current densities due to

variations in

(1) dura mater resistivity ,

(2) vertebral bone resistivity and

(3) geometrical factors of epidural and subarachnoid spaces.

Although proper field analysis requires three-dimensional modelling, solutions from 2-D domains are still of considerable importance. Computer storage on even the CDC7600 machine is a problem for 3-D models, restricting the number of elements being used.

Two-dimensional approaches, on the contrary, permit a high degree of mesh fineness. In addition, isopotential contours from 2-D model solutions can indicate some qualitative differences among different field distributions.

3.2 DESCRIPTION OF THE TWO-DIMENSIONAL MODEL

The simple representation in Figure 3.1 has been derived from one of the models described by COBURN (1980). Finite element computation was, as before, accomplished using PAFEC 75 on a CDC7600 computer.

Finer meshing of the spinal cord, especially in the region of an electrode, is the further development here. Details are given in Figure 3.2. Eight groups of elements (A B C D W X Y Z), four posterior and four anterior, have been used in various combinations to represent the epidural fat (edf), the electrode and the subarachnoid

space containing cerebrospinal fluid (csf).

Although not the arrangement shown in Figure 3.2, the mesh also enabled element groups BY and/or CX to be specified with resistivity values intended to represent the dura mater separating regions of edf and csf. Body tissues were, as before, idealised into distinct groups with isotropoic properties. Unless stated here, assumptions are as described by COBURN (1980). Values of resistivity chosen for the model can also be found in Table 2.1. Relevant low-frequency resistivity measurements on dura mater do not seem to be in the literature and, in any case, one of the present aims was to assess the sensitivity of results to the assumed resistivity of this material. To give the study direct practical relevance, electrode size and spacing relate to a commercially available multi-site electrode system. In fact the bipolar configuration chosen, i.e. 1mm diameter cylindrical electrodes of length 4 mm, spaced 20 mm between centres, is typical of clinical practice even when bipolar stimulation is accomplished using two separately inserted single-pole electrodes.

Electrical symmetry of bipolar fields has also been exploited, with only the upper half of each field being determined. This point is illustrated by the solution shown in Figure 3.3. It must be emphasised that the model is two dimensional in concept. No current flows at right angles to the plane of the section, which is taken to be of unit (1mm) thickness.

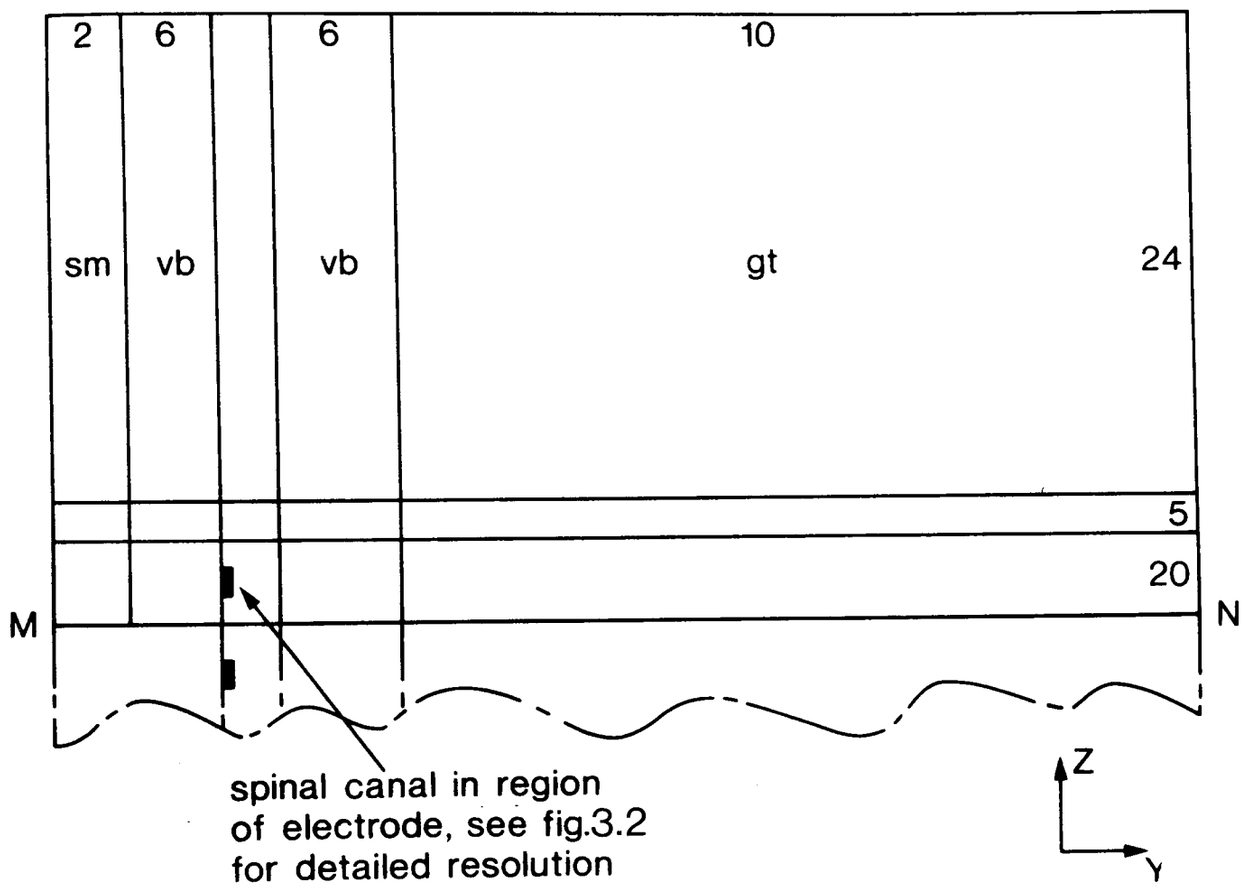

FIGURE 3.1 GUIDE TO FINITE ELEMENT RECTANGULAR MESH USED FOR MID-SAGITTAL SECTION THROUGH HUMAN THORAX.

Numerals indicate number of element divisions per side Abbreviation defined in Table 2.1. Dura mater is not shown. MN at zero potential.

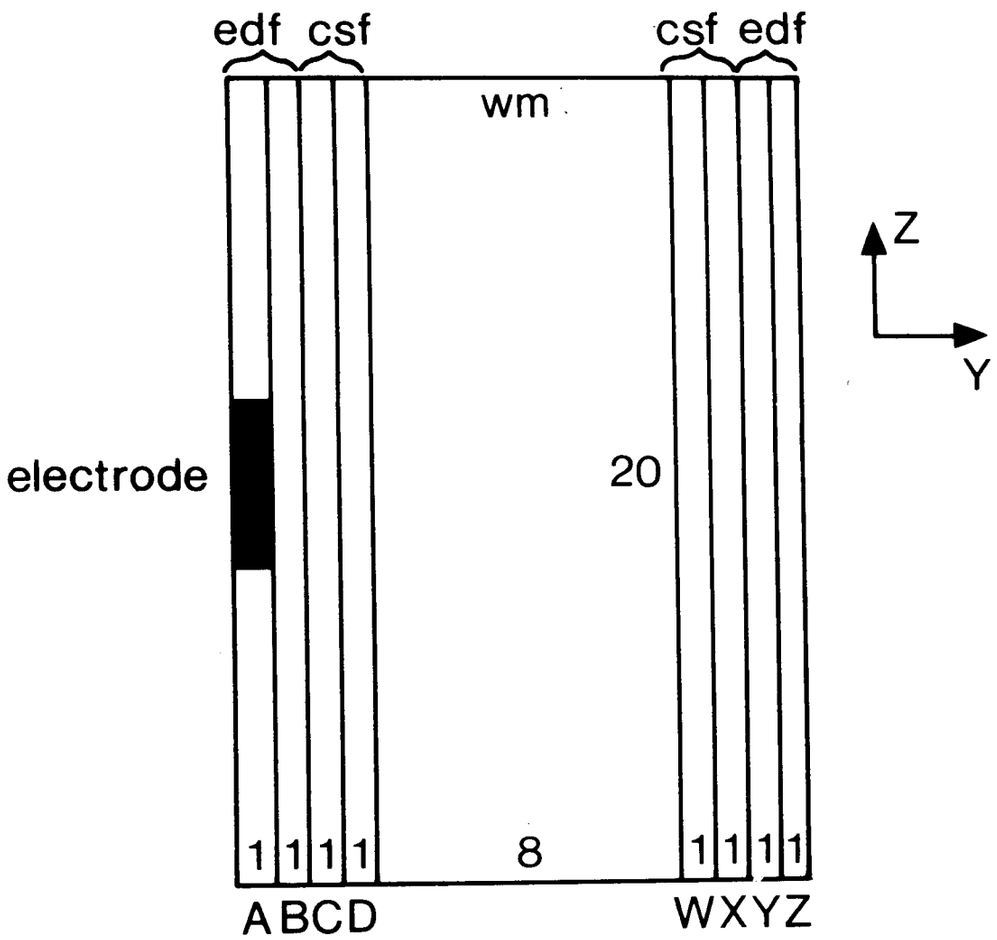

FIGURE 3.2 DETAILED RESOLUTION OF THE FINITE ELEMENT MESH USED FOR MID-SAGITTAL SECTION THROUGH THE SPINAL CANAL IN THE REGION OF AN ELECTRODE.

Combinations in the choice of resistivities for layers A B C D. W X Y Z permit dura mater to be represented between edf and csf. Other remarks as Figure 3.1

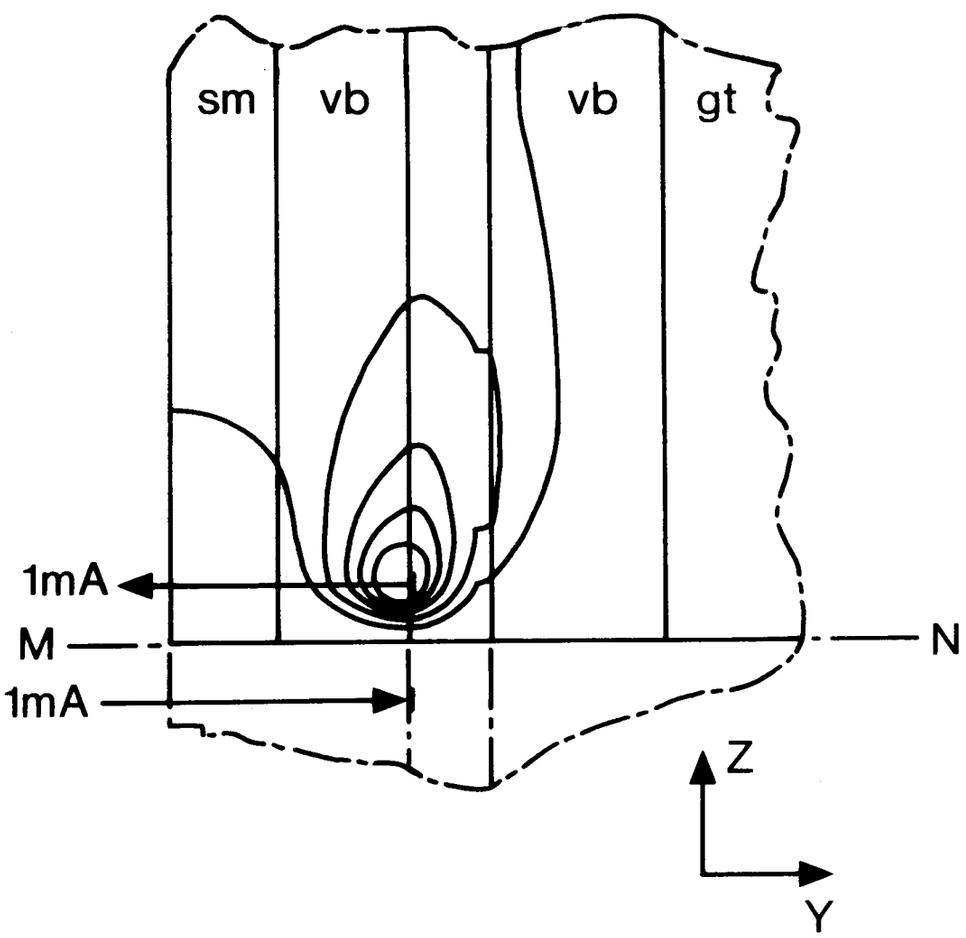

FIGURE 3.3 GENERAL PATTERN OF ISOPOTENTIALS IN MID-SAGITTAL PLANE

Contour spacing 0.26V. minimum (inner) -1.6V.
Artifical boundary condition of zero potential is on line MN.
Electrode spacing 20mm between centres.

3.3 RESULTS

3.3.1 Standard Solution

The general distribution of the potential created by the bipolar epidural electrodes may be seen in Figure 3.3. An applied stimulus current of 1mA is used throughout this study. Greater detail relating to the spinal canal, generated from the same computer output data, is shown in Figure 3.4, The maximum current density within the cord has also been indicated.

This field solution is similar to one of those presented by COBURN (1980), with the exception of the changes in electrode size and spacing. It is included here, for convenience, as it will be taken as the 'standard' solution with which other results in this study will be compared. Although the isopotential contour plots give a useful visual picture of the field, comparisons will be made also in terms of current density, which is widely assumed to be the fundamental parameter that depolarises nerve fibres.

3.3.2 Effects of Dura Mater Resistivity

Element groups B and Y in Figure 3.2 were, in this case, regarded as dura mater separating the epidural and subarachnoid spaces. Effects have been explored over a wide range, 60-10000 ohm-cm, of assumed resistivity values for the dura. Field distributions and maximum current density vectors for differing dura resistivities in this

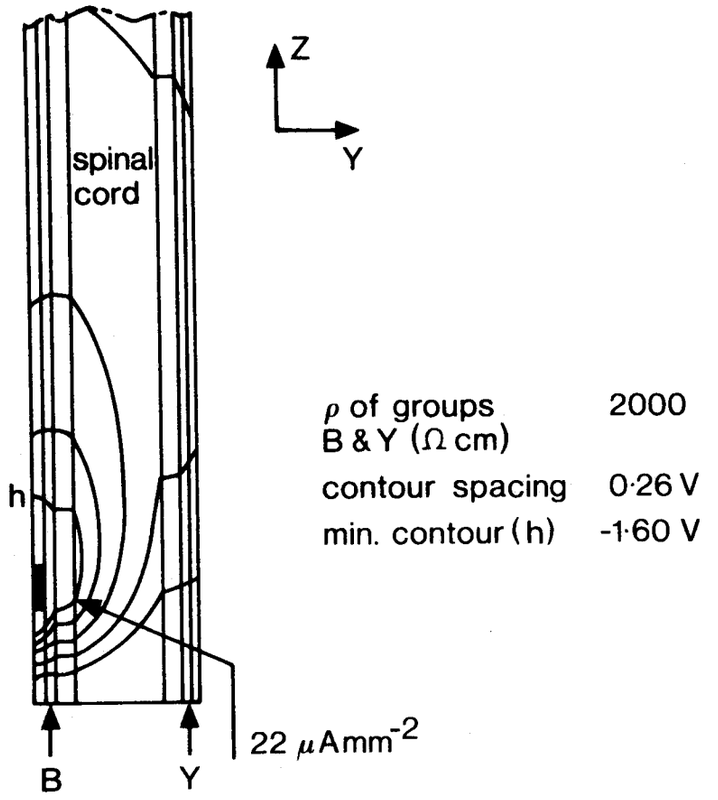

FIGURE 3.4 DETAILS OF ISOPOTENTIALS AND MAXIMUM CURRENT DENSITY FOR THE SOLUTION OF FIG. 3.3 WITHIN THE SPINAL CANAL

Upper half of field shown (5 contours) with cathodic current 1mA.
resistivity of groups B and Y = 2000 ohm-cm
contour spacing = 0.26V
minimum contour (h) = -1.6V

range are shown in Figure 3.5. The solution of Figure 3.4 is also relevant, since it could be considered to represent a dura mater with 2000 ohm-cm resistivity. Maximum current density values may be seen plotted against dura resistivity in Figure 3.6.

3.3.3 Effects of Bone Resistivity

Apart from dura mater, bone is another biological material having highly uncertain resistivity, as described in Section 2.2.4. A range of 1000-8000 ohm-cm for bone is examined in this study. In the same manner as described above for dura mater, the variation of current density with bone resistivity is shown in Figure 3.6. While the properties of the bone were varied, the resistivity of the element groups B and Y were held at the nominal standard of 2000 ohm-cm.

3.3.4 Effects of Epidural and Subarachnoid Spaces

The effects of geometric changes in the dorsal epidural and subarachnoid spaces have been studied by varying the tissue properties of element groups A, B, C and D. Isopotential contour plots and current density vectors need not be shown as their shapes and orientations are similar to those shown in Figure 3.5. Instead, a diagrammatic summary of all the geometric configurations and the corresponding maximum current densities within the cord is given in Figure 3.7.

Figure 3.7(a) illustrates the effect of subarachnoid

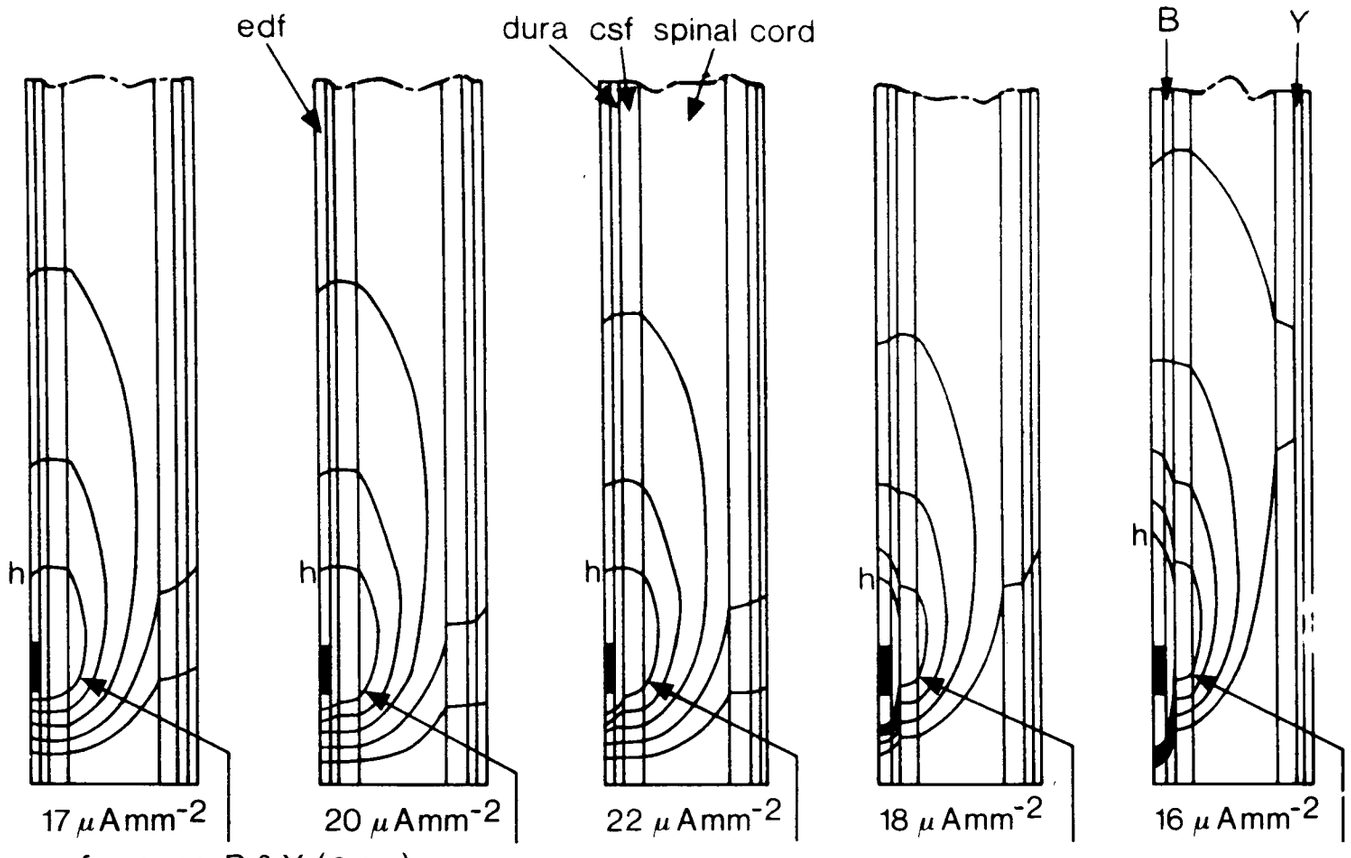

ρ of groups B & Y (Ω cm)				
60	500	1000	5000	10000
contour spacing				
0·21V	0·27V	0·27V	0·27V	0·19V
minimum contour (h)				
-1·22V	-1·48V	-1·53V	-1·83V	-1·61V

FIGURE 3.5 ISOPOTENTIALS AND MAXIMUM CURRENT DENSITIES WITHIN THE SPINAL CANAL FOR DIFFERENT DURA RESISTIVITIES

Upper half of fields shown (5 contours) with cathodic current 1mA. Electrode potentials are half the stimulator voltage Vs plotted in Figure 3.8(a)

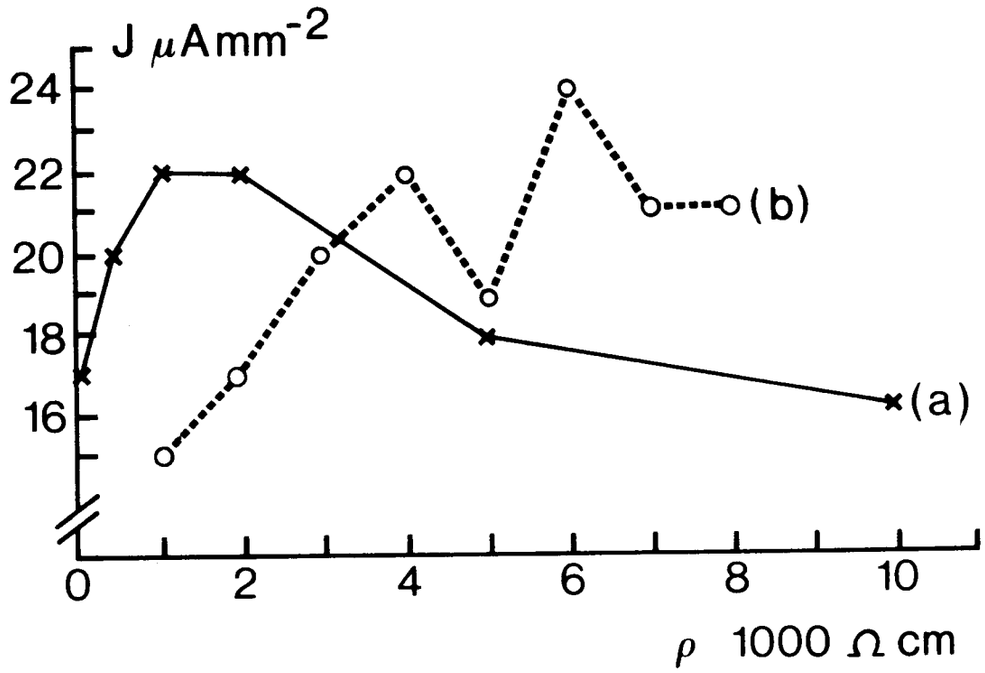

FIGURE 3.6 VARIATION OF MAXIMUM CURRENT DENSITY J IN THE SPINAL CORD AS FUNCTION OF ASSUMED SPECIFIED RESISTIVITY FOR DURA MATER AND BONE

(a) dura varied with bone constant at 4000 ohm-cm
(b) bone varied with dura constant at 2000 ohm-cm
All other resistivities are as Table 2.1

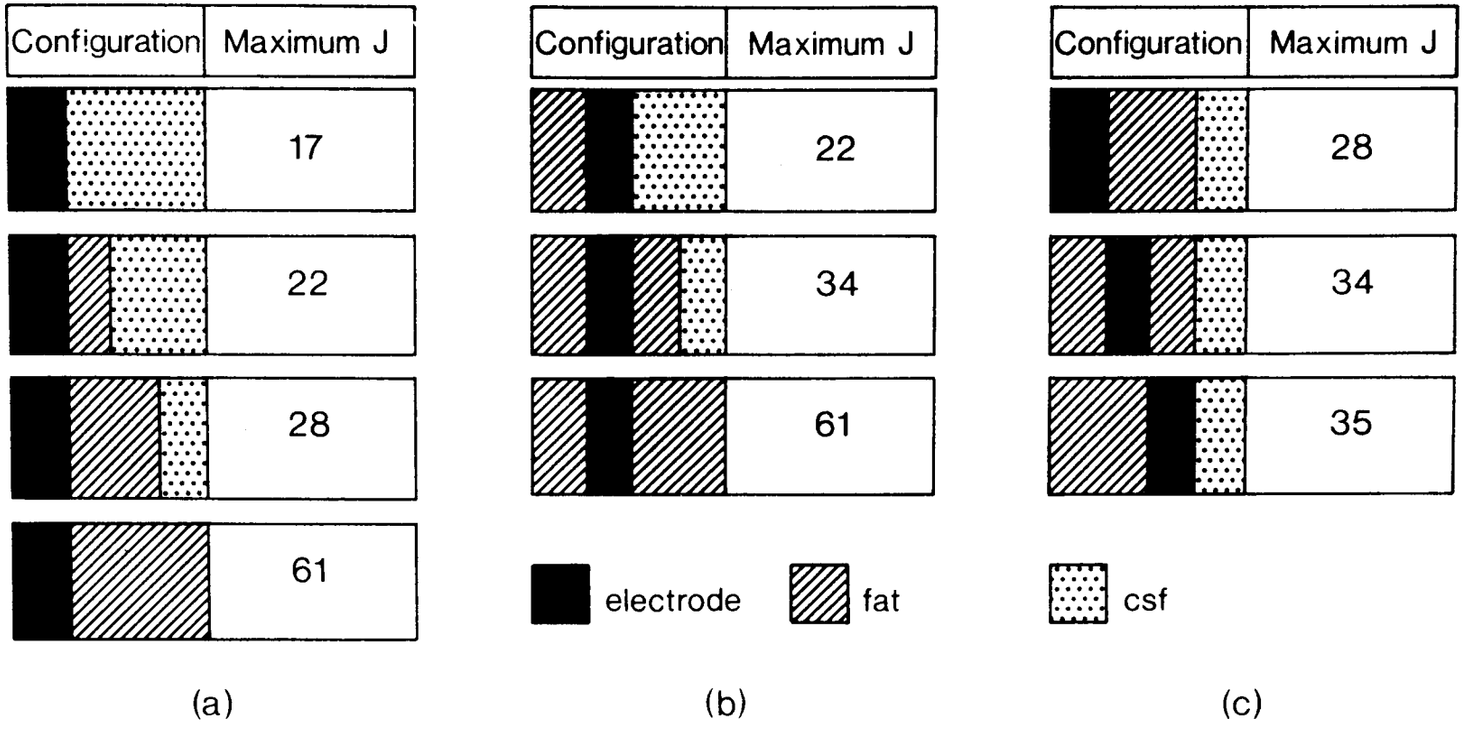

FIGURE 3.7 MAXIMUM CURRENT DENSITIES J IN THE SPINAL CORD FOR VARIOUS GEOMETRICAL RELATIONSHIPS BETWEEN ELECTRODE. EPIDURAL FAT AND SUBARACHNOID SPACE (CSF)

Unit of J in $\mu A.mm^{-2}$. For details see text 3.4

space (in other words csf) thickness on the current density for a fixed electrode position. It may be seen that the maximum csf thickness was three element layers. In each case, a reduction in csf thickness has been assumed to be accompanied by an increase of epidural fat.

Figure 3.7(b) serves the same purpose as Figure 3.7(a) but the electrode is one layer closer towards the dorsal surface of the cord.

The influence of a 2000 ohm-cm epidural fat barrier separating the electrode and csf is shown in Figure 3.7(c). The subarachnoid space (csf) was maintained at a constant thickness.

3.4 DISCUSSION

It must be emphasised again that the results from this two-dimensional study are useful only for comparative purposes. The limitation of two-dimensional analyses, fully discussed in the earlier paper (COBURN,1980), make it quite inappropriate to take, for example, the absolute values of current density to be at all representative of values likely to be encountered clinically.

The series of results shown in Figs. 3.4 and 3.5, where the assumed resistivity of dura mater was varied over a wide range, shows surprising uniformity in the patterns and magnitudes of isopotentials generated within the spinal cord. Figure 3.6 shows clearly that it is only for the extreme, somewhat academic, values of dura

resistivity of 60 and 10000 ohm-cm that reductions in spinal cord current densities in the order of 30% were achieved. The lower value of 60 ohm-cm is equivalent to that for csf so that, in effect, the dura is not present; the upper value is 2.5 times higher than the resistivity assumed for vertebral bone in Table 2.1.

The reductions of stimulus intensity for both high and low values of dura resistivity need to be explained. It is to be expected that, for sufficiently high values of assumed resistivity, the dura might form an effective insulator around the spinal cord. At the other extreme, a highly conductive dura would provide a direct shunt path for current between the electrodes.

The importance of data on the likely influence of bone resistivity is not due simply to uncertainty in the resistivity value itself; it arises also from the geometrical complexity of the spinal vertebrae. It is hard to see how any theoretical model could take full account of the complex anatomy of the bony structures of the spine, not to mention the labyrinthine possibilities for current leakage through foramina and intervertebral connective tissue. Thus, even if an accurate resistivity value for vertebral bone were available, any model would probably need to be based on a simplified anatomy and an effective overall resistivity for the combinations of structures and tissue type forming the column. A step in assessing the extent to which such simplifications can continue to be justified is to assess the sensitivity of

results to the general insulating effect of an idealised spinal column. Bearing in mind the earlier remarks on the effect of the resistivity assumed for the thin dura membrane, Figure 3.6 indicates unexpectedly that variation in the resistivity of vertebral bone, with its far greater volume, has only the same order of effect. No special significance can be proposed for the discontinuities. The general indications are that current leakage through spaces in the bony structures would need to be sufficiently great to reduce the effective resistivity of the spinal column to below 1000 ohm-cm before current densities in the cord fell significantly.

Turning now to the results of Figure 3.7, it will be noted that the dura does not appear explicitly in the various configurations which are shown. Results already described, however, would justify the assumption of a nominal resistivity for dura of 2000 ohm-cm. This would be the same as that specified for fat. Hence configurations in Figure 3.7 specifying a layer of fat between the electrode and the cord would, if so desired, reasonably be taken to approximate also to the presence of a dura membrane. Figures 3.7(a) and (b) illustrate the effect of csf thickness. When the width of subarachnoid space is decreased, current shunting through the csf is reduced, with the result that current penetration into the cord is increased. It is notably that this increase in spinal cord current density occurs in spite of the widening layer of insulating fat (or dura) between the electrode and the

cord. The point is explored further in Figure 3.7(c) , where it may be seen that the thickness of high resistance material separating the electrode and csf has little influence on the current density. This last set of results involves the assumption that the csf thickness remains constant, with anode and cathode remained vertically aligned. The slight increase of current density from top to bottom of Figure 3.7(c) is attributable to the decrease of electrode distance from the cord.

In view of the above results, it appears that high resistance materials such as bone and fat are not the major parameters influencing the current density within the cord, although they are surrounding it. Note that this is not the case when absolute potential is considered, as shown in the 3-D validation work of Chapter 5. Instead, the crucial factor is highly conductive material such as the csf surrounding the electrode. Unless the tough dura has an unlikely conductivity, outside the range of other biomaterials, then including the membrane in finite element models does not seem necessary.

Finally it is important to consider the implications of the work having been based upon constant current stimulation. This approach has the overwhelming advantage of making it unnecessary to model polarisation effects local to an electrode. However, one disadvantage may come into question with respect to practical implanted devices.

To emphasise the point the voltage Vs, representing

the stimulator output , anode to cathode, has been plotted in Figure 3.8 for the same range of dura mater and vertebral bone resistivities as in Figure 3.6. As may be seen, the stimulator voltage Vs required to provide the 1mA nominal current source, in effect the tissue impedance, rises markedly as higher values of resistivity are assumed for the dura membrane. Figure 3.8 has not been presented simply in terms of tissue impedance because the values are not at all representative of actual in vivo measurements (JOBLING et al, 1980). The limitations of a two-dimensional study need to be held in mind. The resistivity assumed for vertebral bone seems to have little influence on the required electrode voltage for 1mA current except at values below 2000 ohm-cm, but the possibility cannot be ruled out that leakage paths may reduce the effective resistivity of the vertebral column far below that generally assumed for bone. Experimental work on cadaver material is needed to resolve this issue, and this will be described in Chapter 5.

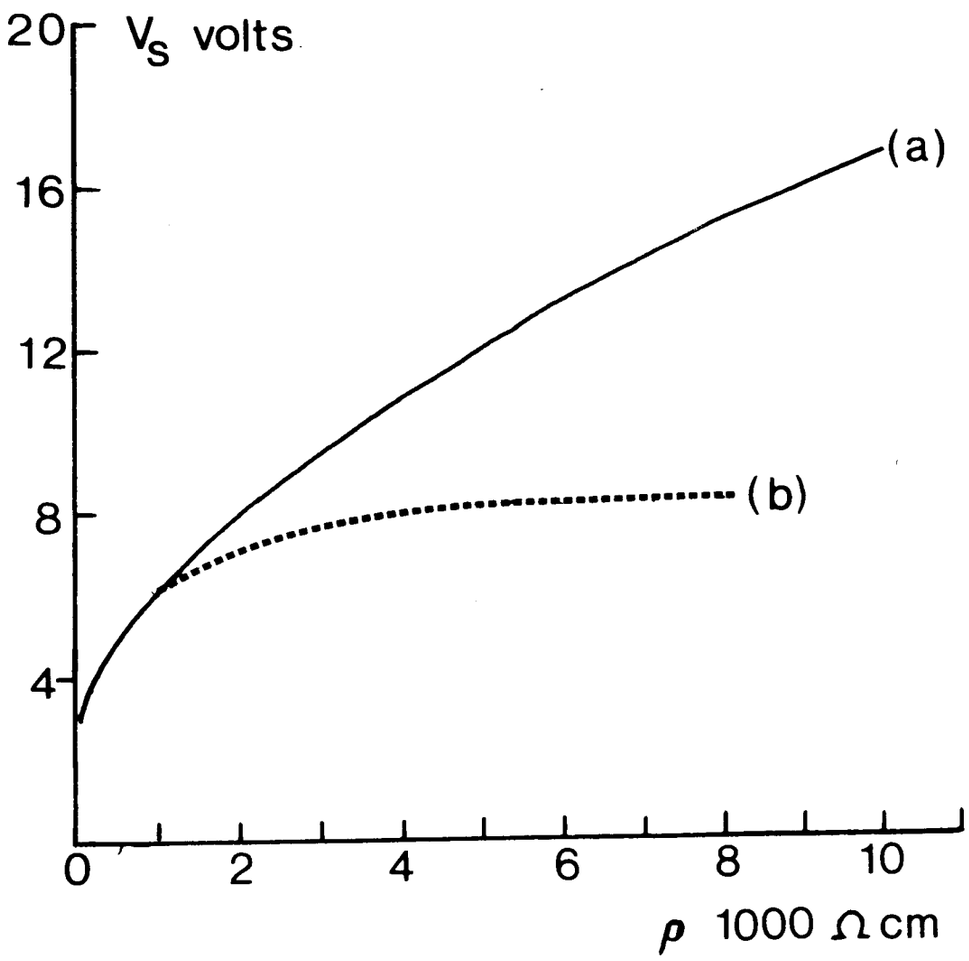

FIGURE 3.8 VARIATION OF STIMULATOR VOLTAGE Vs AS A FUNCTION OF ASSUMED SPECIFIC RESISTIVITY FOR DURA MATER AND BONE :

(a) dura varied with bone constant at 4000 ohm-cm
(b) bone varied with dura constant at 2000 ohm-cm
All other resistivities as Table 2.1.
Stimulator current 1mA (2-dimensional model)

CHAPTER 4 VALIDATION STUDY OF FINITE ELEMENT MODEL : COMPARISON WITH PUBLISHED LITERATURE

4.1 INTRODUCTION

Opportunities for a validation on the finite element model using published data are rare. The most important relevant experimental work, actually measuring fields, remains that of SWIONTEK et al (1976). No comparable work is known and the data of Swiontek, restricted as they are, has been vitally important to this study.

Full detail must be left to the authors' published report (SWIONTEK et al,1976), but the essential feature of the work was in-vivo measurement of spinal cord current density in monkey. Human cadaver material was also used but it was felt that the full thoracic anatomy was needed for a validation exercise.

An laminectomy was performed on the monkey, remaining open for the course of the work, and the dura was incised to expose the cord. Saline bath was applied to the exposed region to keep the cord warm and moisture. Applied electrode poles, connected as shown in Fig 4.1(a), were brought in contact with the cord. A measuring probe, having a 0.3 mm cubic tip, was inserted into the cord between the poles to measure current density. Note that measurements were restricted to a direction parallel to the axis of the cord and were for one plane only. The

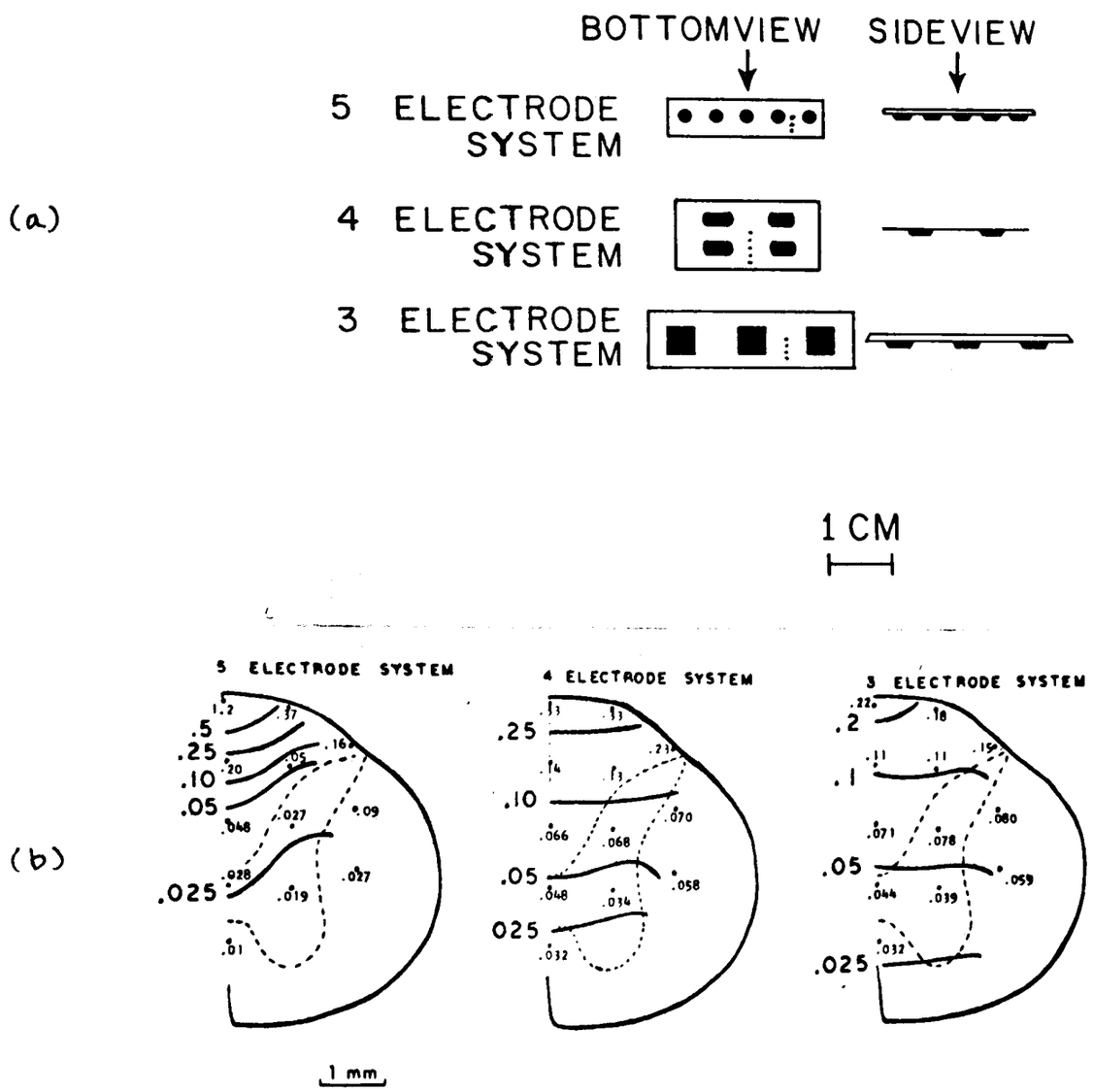

FIGURE 4.1 CURRENT DENSITY PLOTS IN MONKEY

Reproduced from SWIONTEK et al (1976).
Measured currents were orthogonal to the spinal cord section shown and are stated in $mA.cm^{-2}$. Contours were hand drawn by the originators.

Upper diagram indicates the electrode systems.
Note the different scales of electrode diagram and contour plots. Small dots (⋮) indicate position where current probe was inserted.

dotted line shown in Fig. 4.1(a) represents the plane in which current density was measured.

The reported measurements for different electrode configurations are reproduced in Fig 4.1(b). Another presentation of these data are graphs showing variation of current density with (a) depth below dorsal surface of the cord on the mid-line and (b) distance, measured from dorsal mid-line, moving laterally around the cord 'just' below the surface. These data are reproduced in Fig. 4.2 and will be used to compare with computer-generated results.

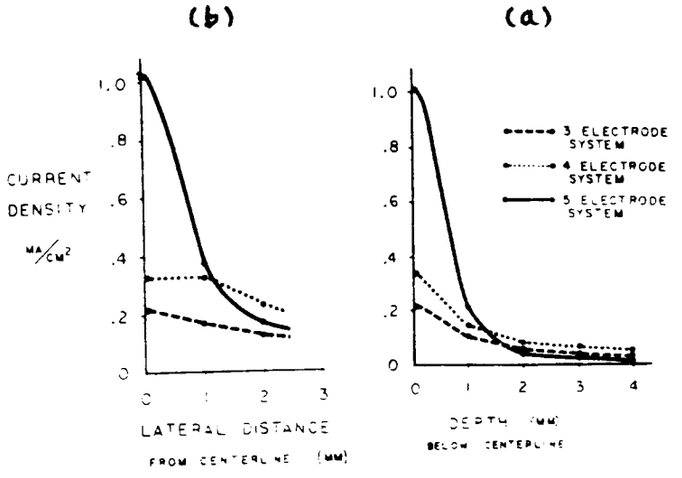

FIGURE 4.2 CURRENT FROM IN VIVO MONKEY SPINAL CORD

Reproduced from SWIONTEK et al(1976). (a) depth below the dorsal surface in the mid-sagittal plane, (b) distance lateral to mid-sagittal plane along the surface of the cord

4.2 FINITE ELEMENT MODEL

The 3-D model used to duplicate the results was based upon that shown in Figures 2.4-2.6 in Chapter 2, using the ANSYS package on a CDC7600. Special modifications, nevertheless, were required to represent the laminectomy feature in the Swiontek work.

Figure 4.3 illustrates the approach for the outer thorax mesh. Essentially, dorsal elements in the model were removed to represent the laminectomy. Removal of elements in the vertebra and spinal canal meshes followed the same pattern down to the dorsal surface of the cord, as shown in Figures 4.4 and 4.5. In a similar manner to that described in Chapter 2, symmmetry was exploited so that only one quarter of the structure needed to be modelled. The arachnoid and pia mater were ignored in the modelling so that the electrode poles were having direct contact with the dorsal surface of the cord. The finite elements had been arranged in such a way that, by defining appropriate material properties in regions A, B, C and D shown in Figure 4.5, the three different electrode systems could be represented within the single mesh design. The spaces between electrodes were specified with saline whose thickness could be varied in different computer runs. Fine meshing, as shown in Figure 4.5, had also been applied in the dorsal column region immediately under the electrode where the field gradients were likely

to be steep.

Six-noded and eight-noded straight-sided 3-D solid elements were used. The 3-D model consisted of 15 layers and represented a height of 80mm. The effective numbers of elements and nodal points in the whole model were 1845 and 1648 respectively. The standard set of material properties, as given in Table 2.1, was used.

Computer output were mainly in two forms ; a listing of electrical potential at each nodal point, and contour plots of isopotentials on defined surfaces. The latter was particularly useful as current densities along the cord could then be calculated from

$$J_z = -\text{gradient } V_z \;/\; \text{resistivity of wml}$$

where gradient Vz were approximated directly from the plots.

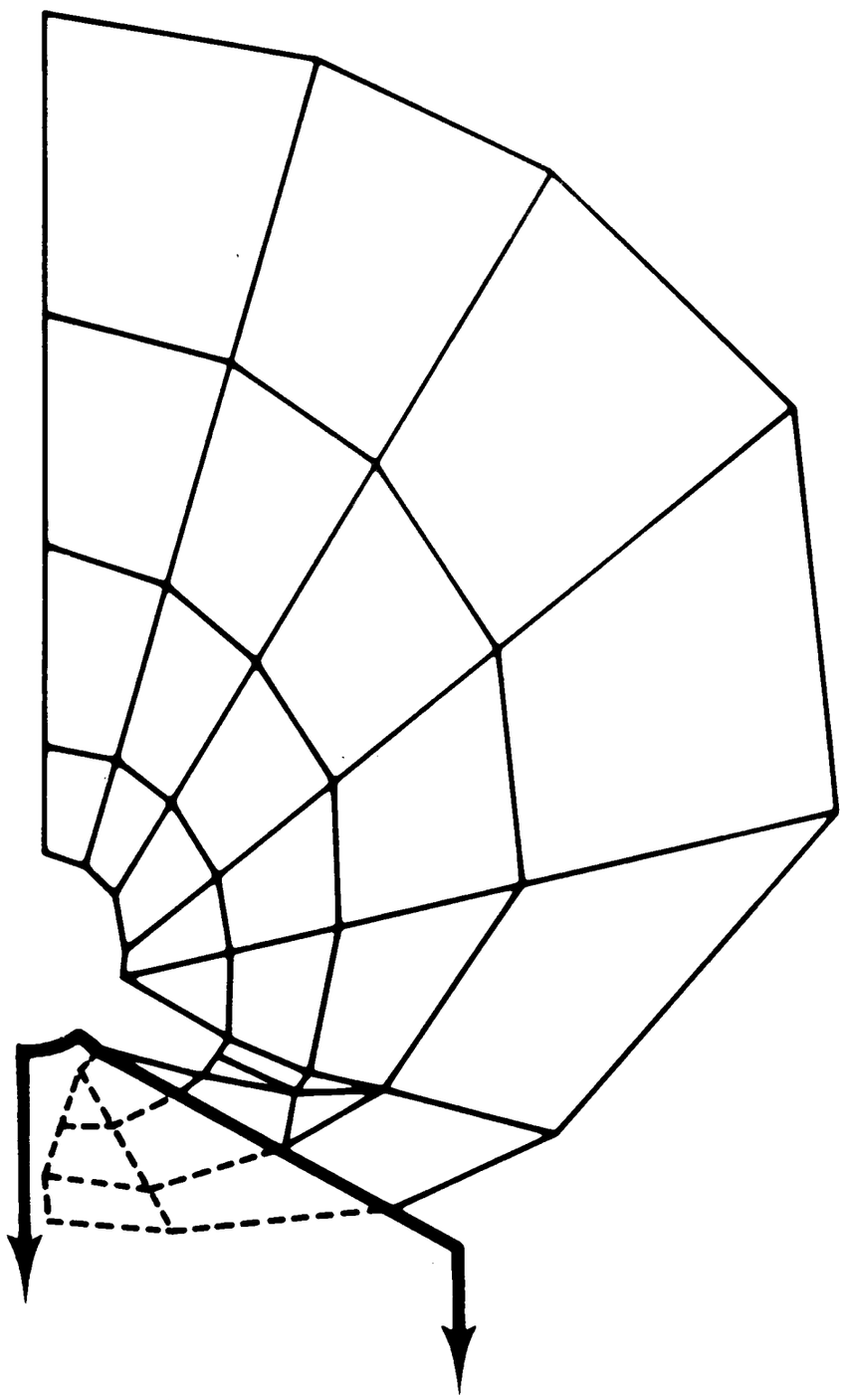

FIGURE 4.3 REMOVAL OF DORSAL ELEMENTS IN THE FINITE ELEMENT MESH OF THORAX TO REPRESENT A LAMINECTOMY

See text 4.2 for details

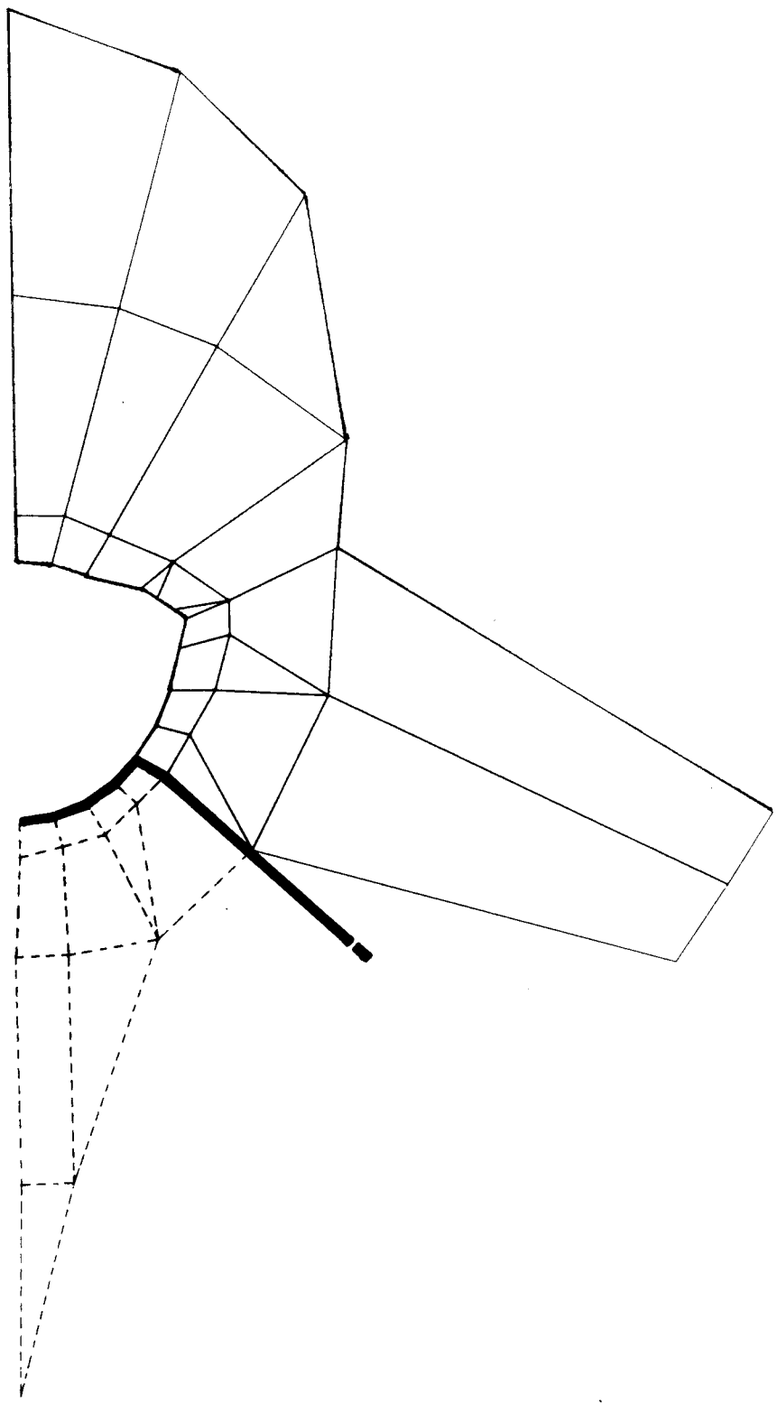

FIGURE 4.4 REMOVAL OF DORSAL ELEMENTS IN THE FINITE ELEMENT MESH OF VERTEBRA TO REPRESENT A LAMINECTOMY

See text 4.2 for details

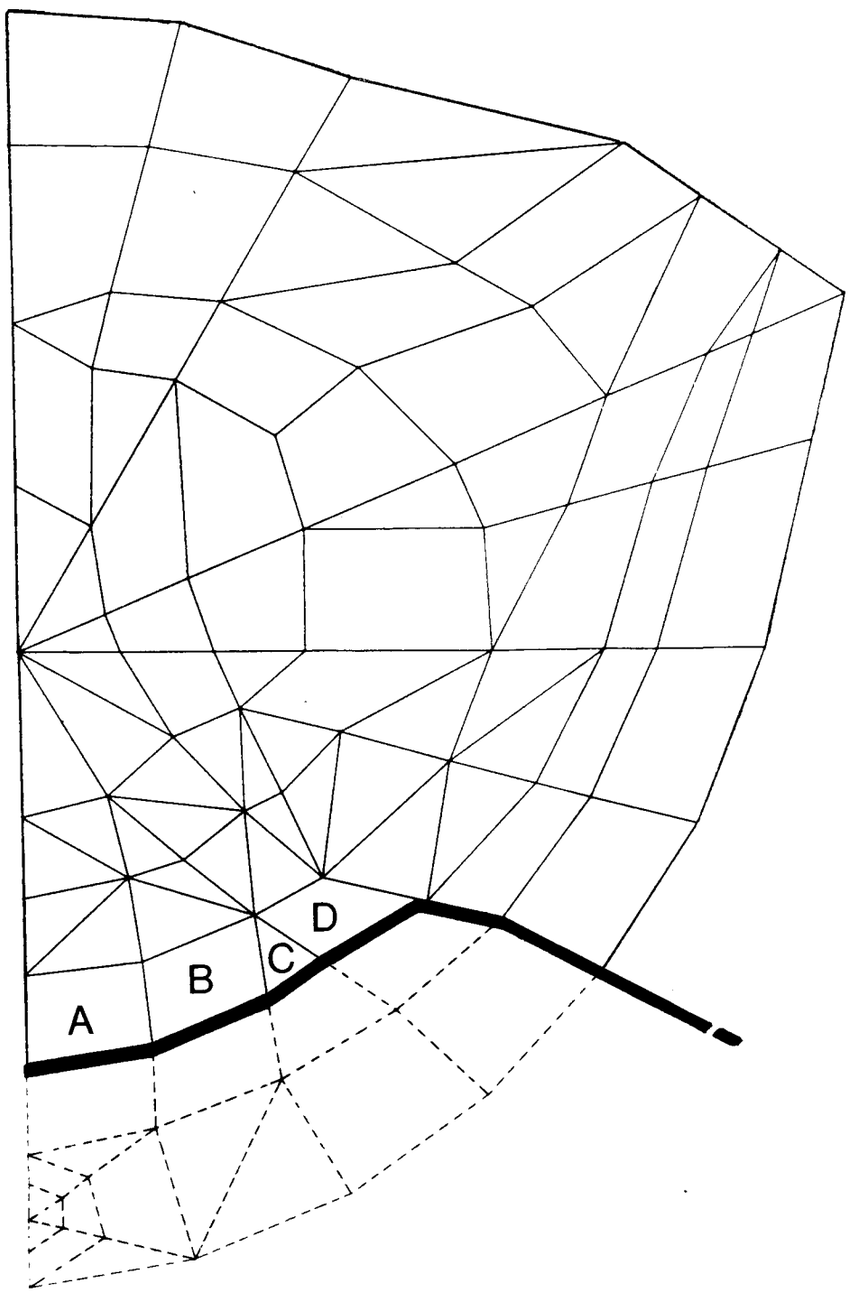

FIGURE 4.5 REMOVAL OF DORSAL ELEMENTS IN THE FINITE ELEMENT MESH OF VERTEBRAL CANAL TO REPRESENT A LAMINECTOMY

See text 4.2 for details

4.3 RESULTS

The isopotentials of the 3-electrode system in the mid-sagittal plane are shown in Fig. 4.6. The electrode array is also indicated schematically, and the dotted line between the pairs of electrode poles indicated the plane within which measurement probe was inserted in the experiment of Swiontek et al. This plot is used to evaluate current density 'just' below the cord in the z-direction . Similar plots for the 4- and 5-electrode arrays are shown in Figures 4.7 and 4.8 respectively.

Plots in other sagittal planes were also produced from the solutions to evaluate current density variation against lateral distance.

The calculated results are produced as dotted lines in Figure 4.9. Fine, intermediate and coarse dotted lines are computed results for no saline, 0.5mm depth of saline and 1.0mm depth of saline respectively. Swiontek e^{+} al results are also reproduced here as the full-line curves for comparison purposes.

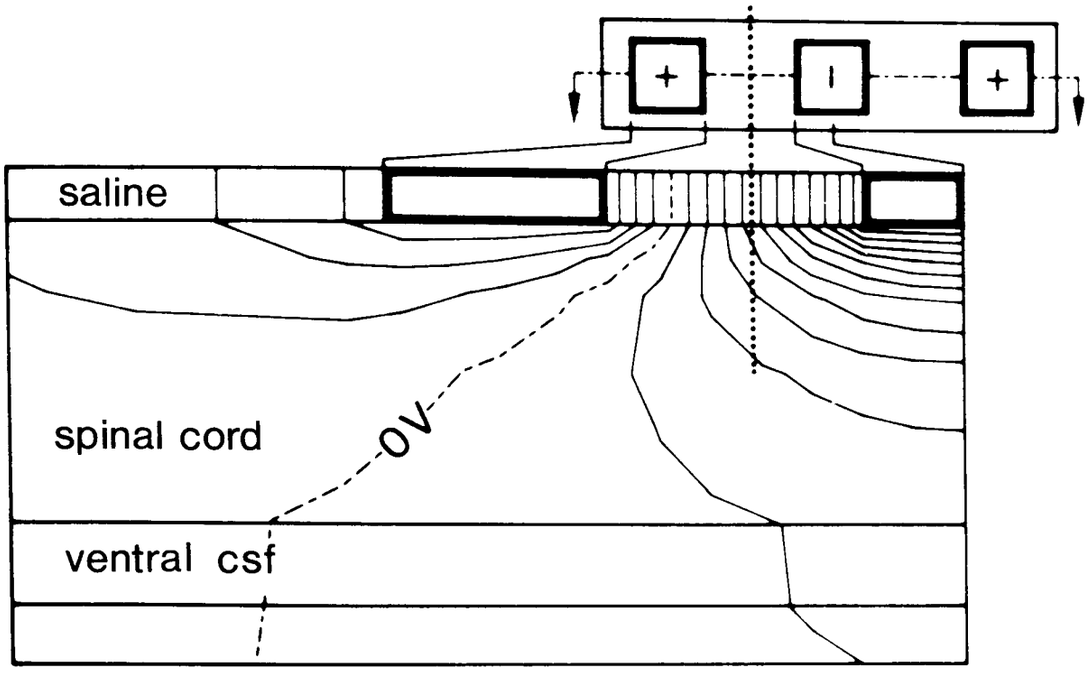

FIGURE 4.6 COMPUTED MID-SAGITTAL SPINAL CORD ISOPOTENTIALS CORRESPONDING TO THE EXPERIMENTAL SCHEMES OF SWIONTEK et al

3-electrode array. Contour spacing 2mV. Total current 250μA. Plan sketches of electrode array is drawn to a relative scale of 1/3. Further details in text 4.3

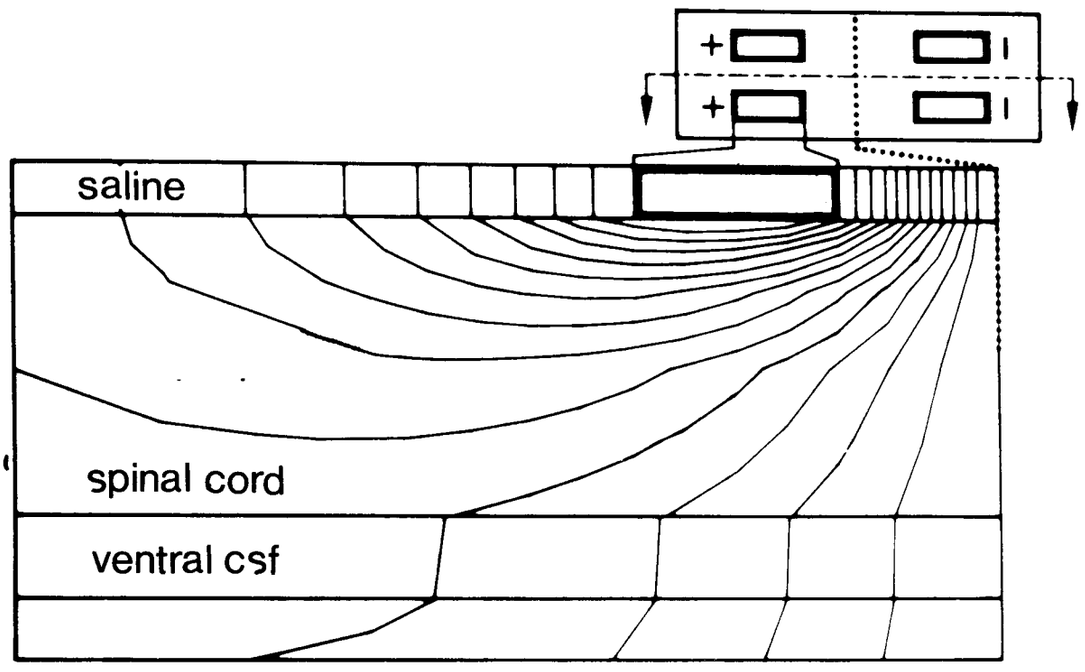

FIGURE 4.7 COMPUTED MID-SAGITTAL SPINAL CORD ISOPOTENTIALS CORRESPONDING TO THE EXPERIMENTAL SCHEMES OF SWIONTEK et al

4-electrode array. Contour spacing 1.5mv
Other remarks as Figure 4.6

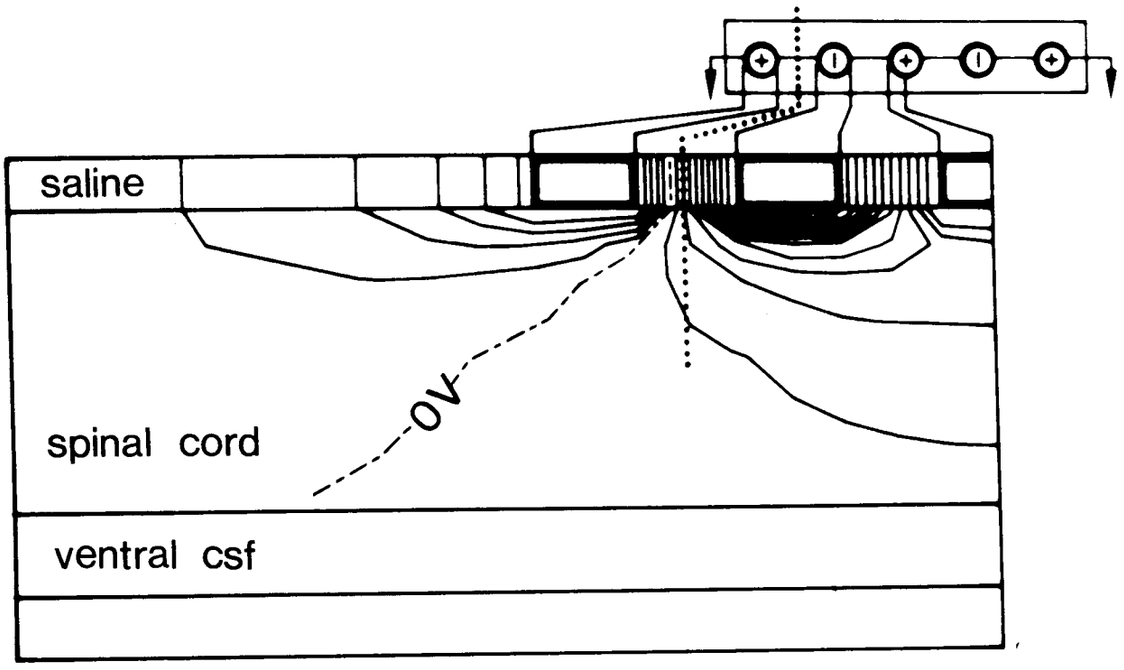

FIGURE 4.8 COMPUTED MID-SAGITTAL SPINAL CORD ISOPOTENTIALS CORRESPONDING TO THE EXPERIMENTAL SCHEMES OF SWIONTEK et al

5-electrode array. Contour spacing 1mV.
Other remarks as Figure 4.6

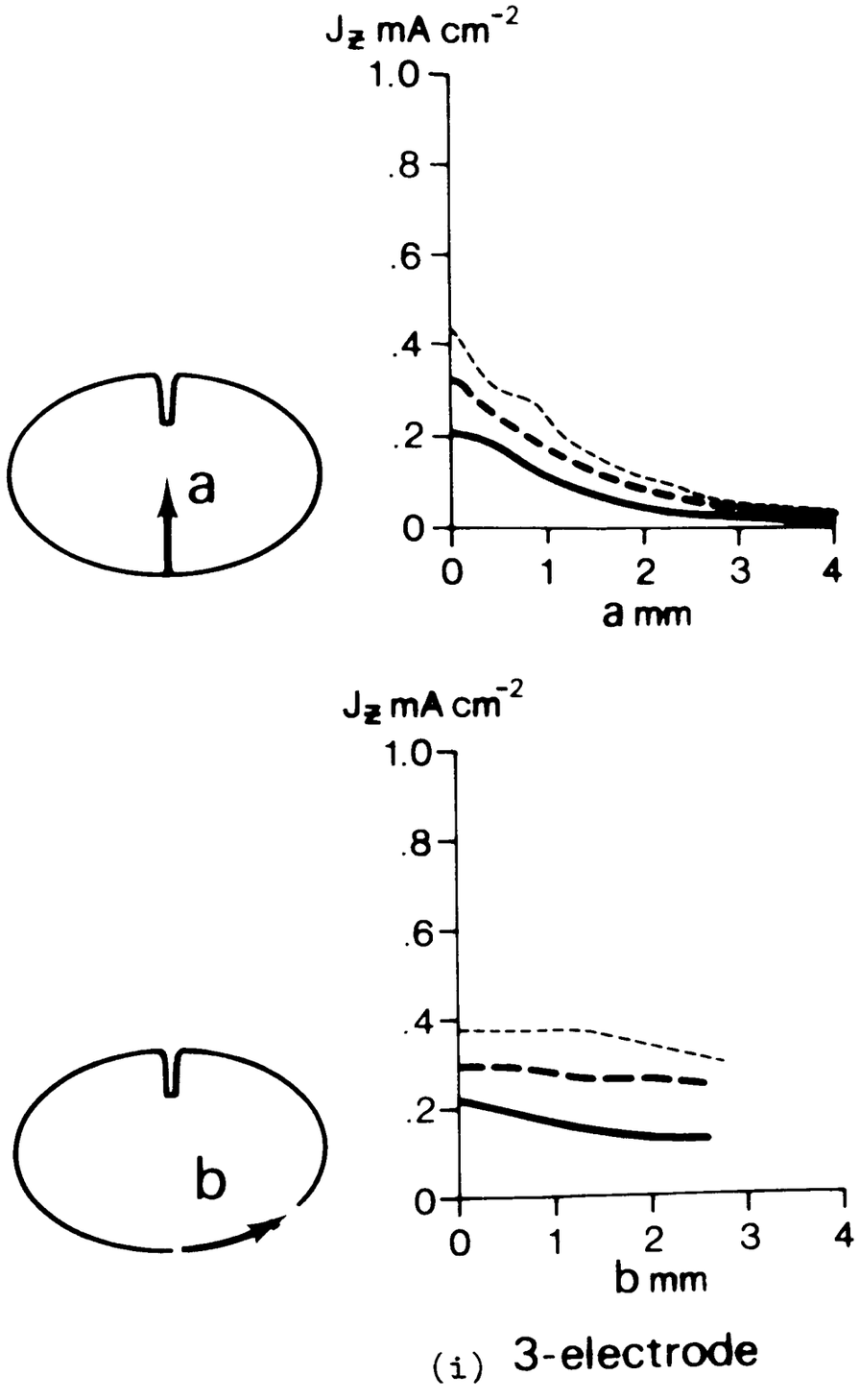

FIGURE 4.9 COMPARISONS OF SPINAL CORD CURRENT DENSITY MEASURED IN MONKEY WITH COMPUTED RESULTS FROM FINITE ELEMENT MODEL.

Full lines are experimental data from SWIONTEK et al (1976)
Fine, intermediate and coarse dotted lines are computed
results for no saline, 0.5mm depth of saline and 1mm depth
of saline. respectively, as described in text.
Total current for each electrode array is 250μA.
(ii) 4-electrode (iii) 5-electrode

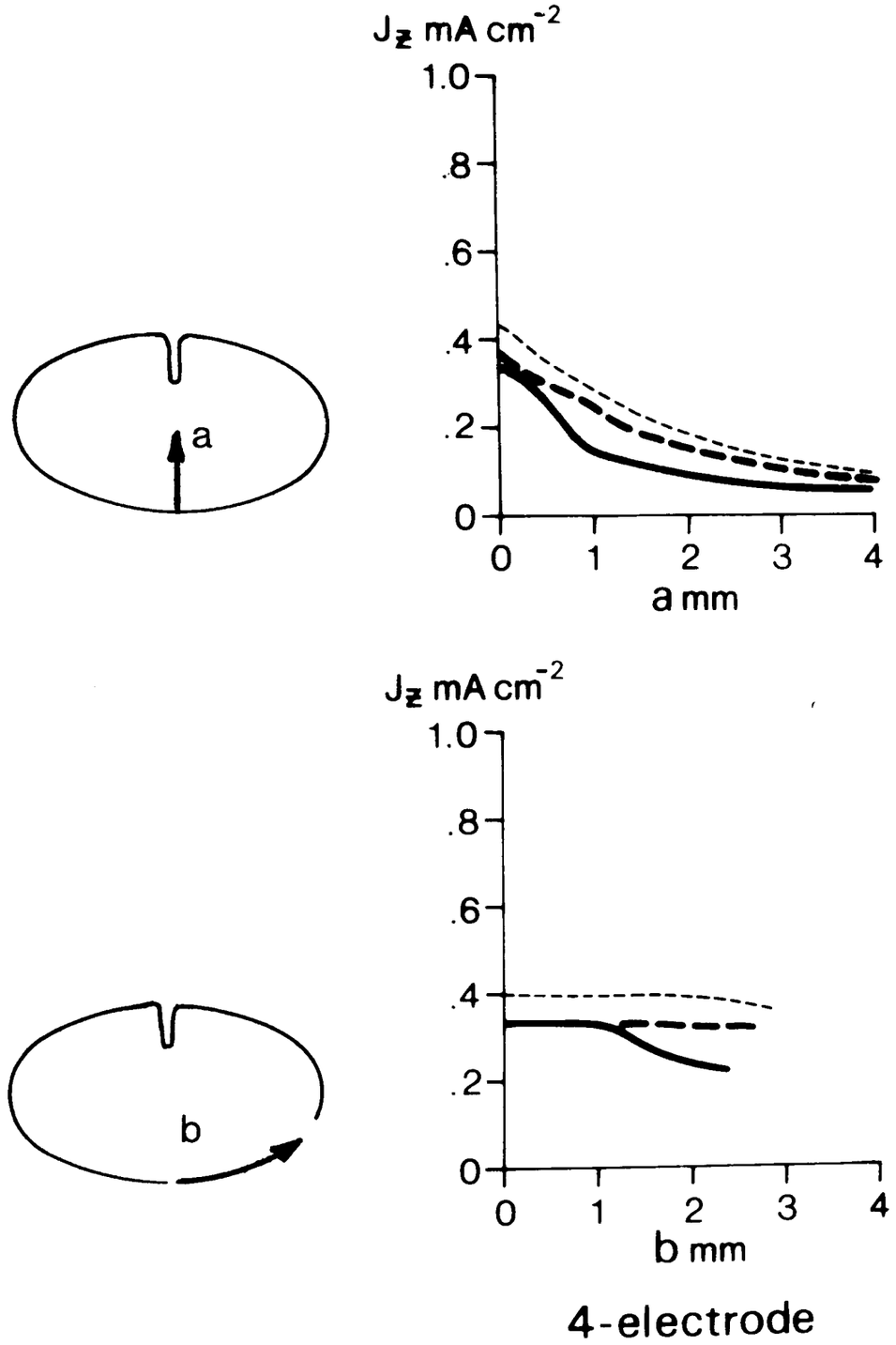
J_z mA cm^{-2}
1.0
.8
.6
.4
.2
0
0 1 2 3 4
a mm
a
J_z mA cm^{-2}
1.0
.8
.6
.4
.2
0
0 1 2 3 4
b mm
b
4-electrode

FIGURE 4.9(ii)

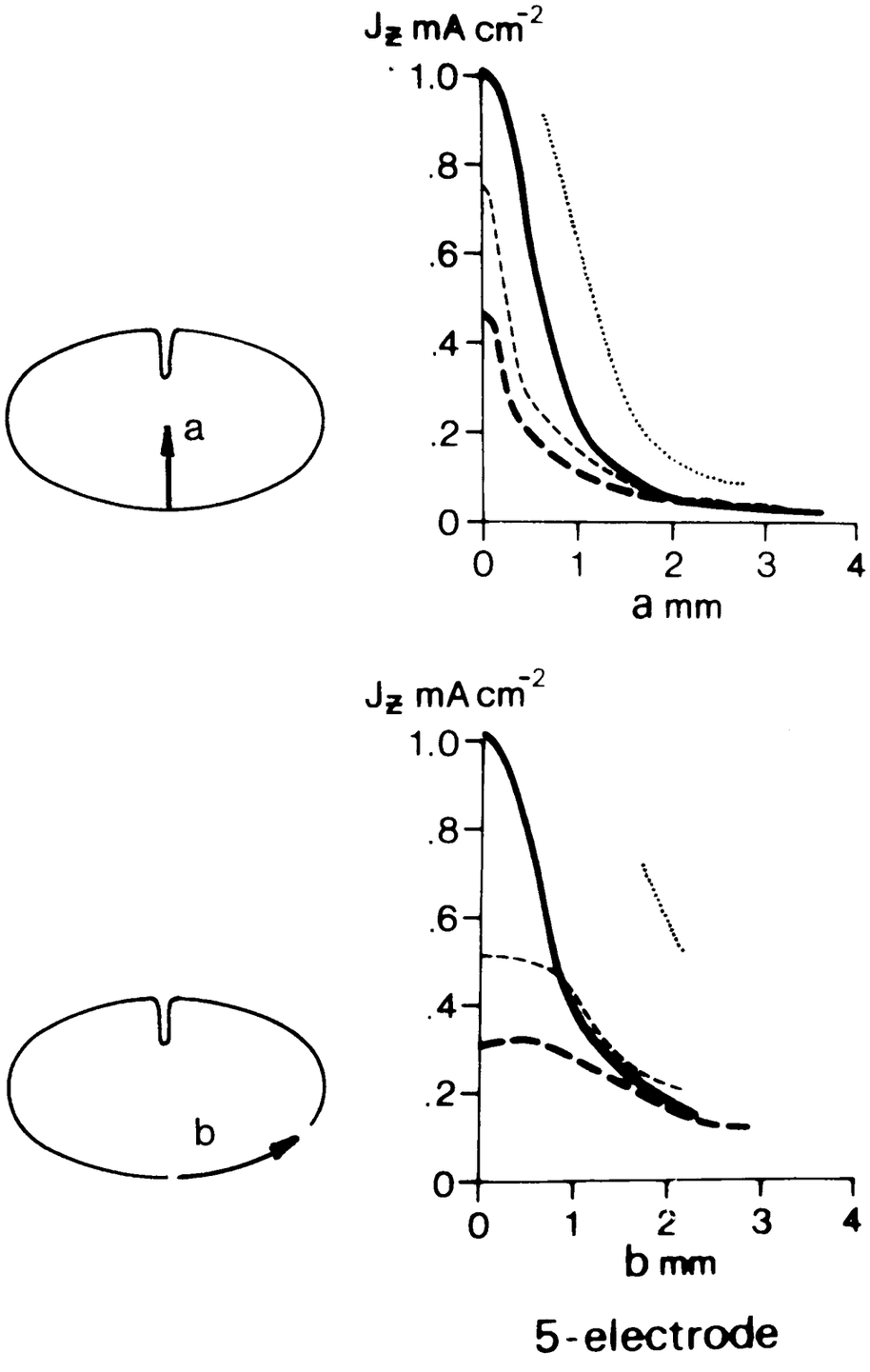

FIGURE 4.9(iii)

4.4 DISCUSSION

Each of the graphs in Figure 4.9 shows axial current density computed from the finite element model corresponding to the Swiontek's measurements. The reason why two or three sets of computed data are given in each case arises from a fundamental uncertainty in respect of the Swiontek work which concerns the depth of saline solution applied to replace the lost cerebrospinal fluid .

The monkey was assumed to be in the prone position in the experiment. The dorsal surface of the cord was, of course, upwards and electrodes were brought down to touch the cord. Although electrode configurations were similar to those shown in Figure 4.1(a), each pole, attached to the end of a copper rod, was applied individually (SWIONTEK, 1975). This was necessary to enable the current density probe to be inserted between electrodes. With the electrodes in place, saline was added to form a shallow pool around the electrodes, and the depth of this pool was subject to uncertainty.

Comparisons of the graphs in Figure 4.9 , however, show that current density values predicted by the model are in the same order of magnitude as the experimental measurememnts. Values for the 3-electrode and 4-electrode systems are lower than measurements, attributable to current shunting by the surrounding low-impedance csf. Examination of Figure 4.1 reveals the comparatively large poles in the 3- and 4-electrode systems, and it is quite

clear that the integrity of contacts between the cord and the poles were likely to be sensitive to technique.

On the other hand, in the 5-electrode system, the model predicts a higher current density distribution. Zero mm saline thickness was also modelled, which represented the extreme situation where the entire current had to be entering the cord. Results in Figure 4.9 indicate that the required saline bath thickness in order to match the experiment was between zero and 0.5mm. It should be mentioned that the Swiontek data in this case contained only 4 points.

The major difference between the model and the monkey work is the physical size, the former being based upon human body. It may be argued, however, that current flow is mainly confined within the cord and the surrounding saline due to the presence of nearby opposite poles. The physical size, in particular the general thorax, does not significantly affect the current distribution. Fortunately, this is borne out by the very similar results by SWIONTEK et al in an isolated human cadaver cord.

CHAPTER 5 VALIDATION STUDY OF FINITE ELEMENT MODEL : FIELD MEASUREMENT IN HUMAN SUBJECTS

5.1 INTRODUCTION

The use of relevant published data for model validation described in Chapter 4 is only an 'indirect' method. The most useful and direct way is to measure the fields in human subjects and compare with finite element solutions, and the implanted electrodes in epidural space provide an excellent opportunity for such a validation.

This chapter, therefore, is concerned with validation involving measurements in humans. The first section of the chapter describes the equipment and the general scheme involved , while the actual measurements conducted in patients are presented in the second section. The third part , however, is not concerned with patients but in vitro field measurements inside the canal of human vertebral column. The intention is to evaluate an effective resistivity for the spinal column which appears to be a crucial issue affecting the field distribution. Comparison of clinical measurements with computer solutions involving different programmed tissue resistivities , are given in Section 5.5.

5.2 BASIC SCHEME OF FIELD MEASUREMENT

Figure 5.1 show a general scheme of field measurements conducted in patients, where the electrode system in the figure is arbitrarily shown as a multi-site electrode. Constant current pulses are delivered at one of the poles, and the stimulated fields (artifacts) are measured at other sites. The stimulating indifferent is in a remote position, usually in one of the extremities while the recording indifferent is on the other extremity. The duration and the sign of the current pulses is not important; they may also be at very low frequency or even single-shot, and may be below sensory threshold of the patient. Stimulus current is monitored by a 1-ohm resistor connected in series with the stimulating circuit as shown, and the instantaneous current is displayed as potential difference across the resistor. Note that all potentials are measured with a differential oscilloscope.

When the electrode is a multi-site system in the epidural space, the voltage profile along the epidural space can be measured at three points (10, 20 and 30 mm from the stimulating electrode) simply by connecting the oscilloscope to each of the remaining electrode poles in turn. A note of the stimulus current and the three resulting potentials is all that is required.

It is felt that having a large separations among the two indifferents and the electrode system is the most suitable practice. There are two reasons for this.

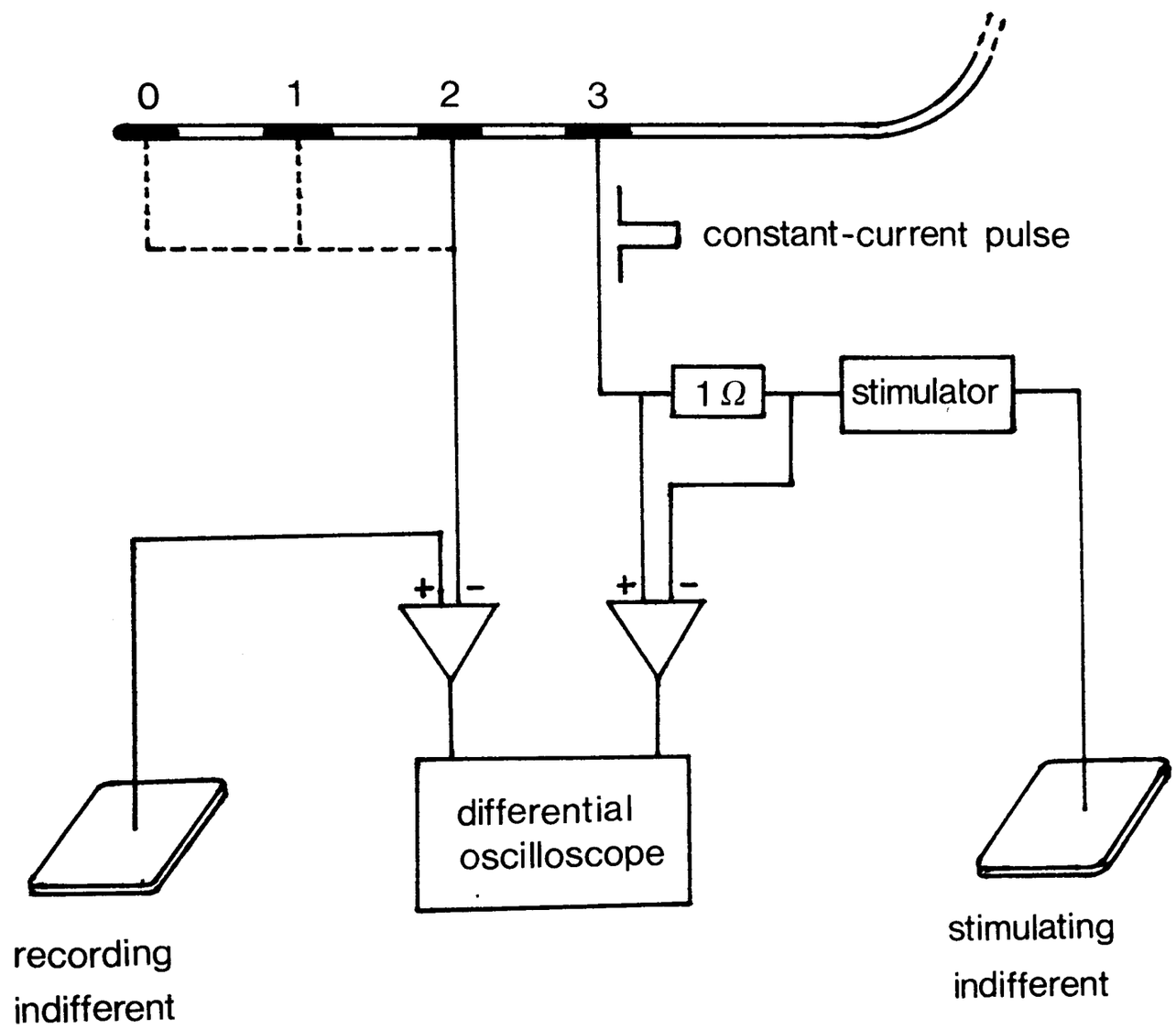

FIGURE 5.1 EXPERIMENTAL SCHEME FOE MEASURING EPIDURAL FIELDS

Details see text 5.2

First, when a large stimulating indifferent (say 50X40 mm^2) on the dorsal skin surface region is not exactly above the stimulating epidural electrode, the resulting field will not be symmetrical.

Theoretical studies in Section 2.3 show that the position of stimulating indifferent around the body at the level of the stimulating pole is immaterial; in fact placing an indifferent on the dorsal skin is an ideal arrangement as this results in a constant potential distribution on most of the model surface, and this potential will be the reference potential for recording. In practice , the stimulating indifferent can never be positioned exactly at the level of the stimulating electrode as the precise location of the electrode is unknown. This is exactly what was happening in some of the measurements with patient R, where the measured epidural potential, affected by a nearby stimulating indifferent , were half of the measurements from patient PW using a remoted indifferent.

Second, as all potentials are measured relative to the recording indifferent, the 'absolute' potential at this recording indifferent, in turn, is also critical. When it is either close to the stimulating electrode or to stimulating indifferent where, in both cases, the potential gradients are likely to be steep, a small change of the recording indifferent position will change its absolute potential substantially. This, in turn, will markedly change the recorded fields which will be

difficult to compare with theoretical solutions. On the other hand, when the recording indifferent is close to a recording pole, there will be very little potential difference between them for measurement.

In the early work, the same indifferent was used for the stimulating and recording purposes, and results were highly unsatisfactory : polarisation phenonemon at the indifferent/tissue interface distorted the rectangular shape of the recorded signal. Polarisation cannot be satisfactory modelled in the context of this particular are a of the work, and it was crucial to ensure that the recorded signals followed the same pulse shape as the stimulating current.

Before the availability of multi-site electrodes, epidural measurements had to rely on two or more individual electrode poles with separate percutaneous leads. The major difficulty then involved was the exact position of the recording electrode in relation to the active pole. X-ray pictures had to be taken from patients to locate these electrodes, and vertical misalignment was also common among the poles in the epidural space. A multi-site electrode, with fixed pole separation, eliminates the problem of relative position, and vertical misalignment is also reduced. In fact, the electrode system is so advantageous that it was also used for the in vitro fields measurements inside cadaver spinal column, to be described in Section 5.4.

Early validation work (COBURN, 1981) has tried

different types of electrode combinations for stimulating/recording, mostly because there were only two implanted electrodes. Figure 5.2 shows three ideal arrangements, but in practice, the recordings were found to be very sensitive to the relative positions of the indifferents and electrodes.

An important point concerned with this study is the 'absolute' potential at the recording indifferent. This absolute value is an unknown during clinical measurements as it can never be measured relative to 'earth'. Recall that every measured potential is relative to this reference potential, the absolute potential in the domain of interest, in particular the epidural space, remains unknown. The actual problem arises when the measured potentials due to a monopolar implant are used to compare with the theoretical solutions which are all in absolute form. The way of getting round this problem, similar to the clinical measurements involving differential measurement, is to subtract the theoretical results by a datum potential taken from a remote position on the model surface. This datum potential represents the absolute potential at the recording indifferent. This is also the reason why, in the clinical measurements, the recording indifferent is located on the extremity where the variation of 'absolute' potential is assumed to be negligible.

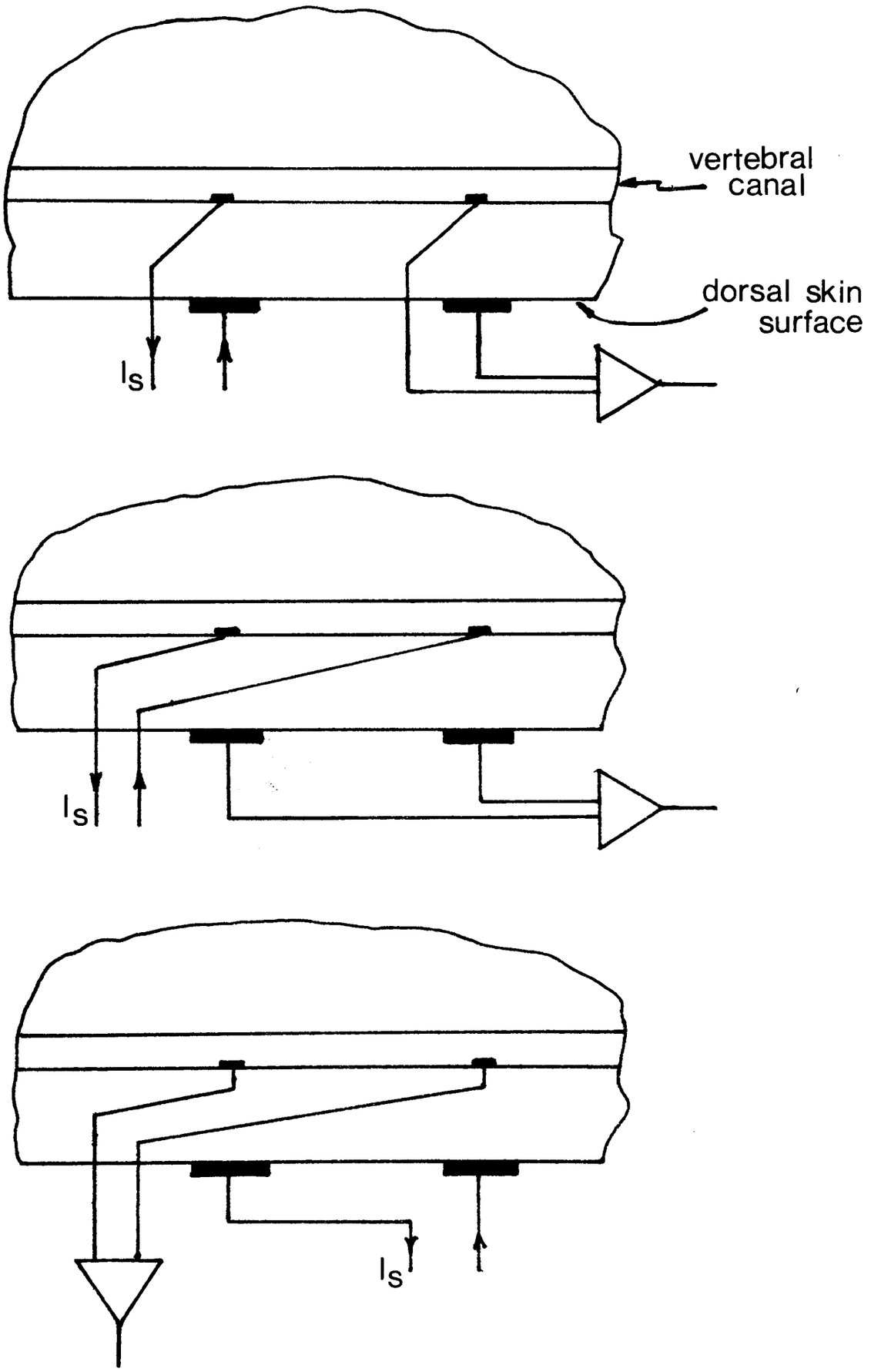

FIGURE 5.2 IDEAL STIMULATING/RECORDING SCHEMES USING SEPARATED IMPLANTED ELECTRODES

5.3 CLINICAL MEASUREMENTS

Three different kinds of stimulating/recording combinations are involved in the clinical scheme :

(a) epidural recording of monopolar epidural stimulation (EDS-M) field

(b) epidural recording of bipolar epidural stimulation (EDS-B) field

(c) dorsal surface recording of EDS-M field

Five adult patients contributed to this validation study, and unless stated, the sessions were conducted by medical staff in Wessex Neurological Centre, Southampton General Hospital.

5.3.1 Epidural Recording of EDS-M Field

Four patients were involved in this scheme , two of them had implanted multi-site electrodes. A schematic diagram for the stimulating/recording combinations is shown in Figure 5.3(a), where each of the four poles was employed as a stimulating pole in turn, and the remaining three recorded the subsequent epidural potentials. The results are plotted as (x) and (+) in Figure 5.4. It should be note that the results of patient R was incomplete, as poles 2 and 3 were found to be shorted internally; and therefore only the measurement taken from pole 1 was useful.

Measurements with the other two patients (CM and E)

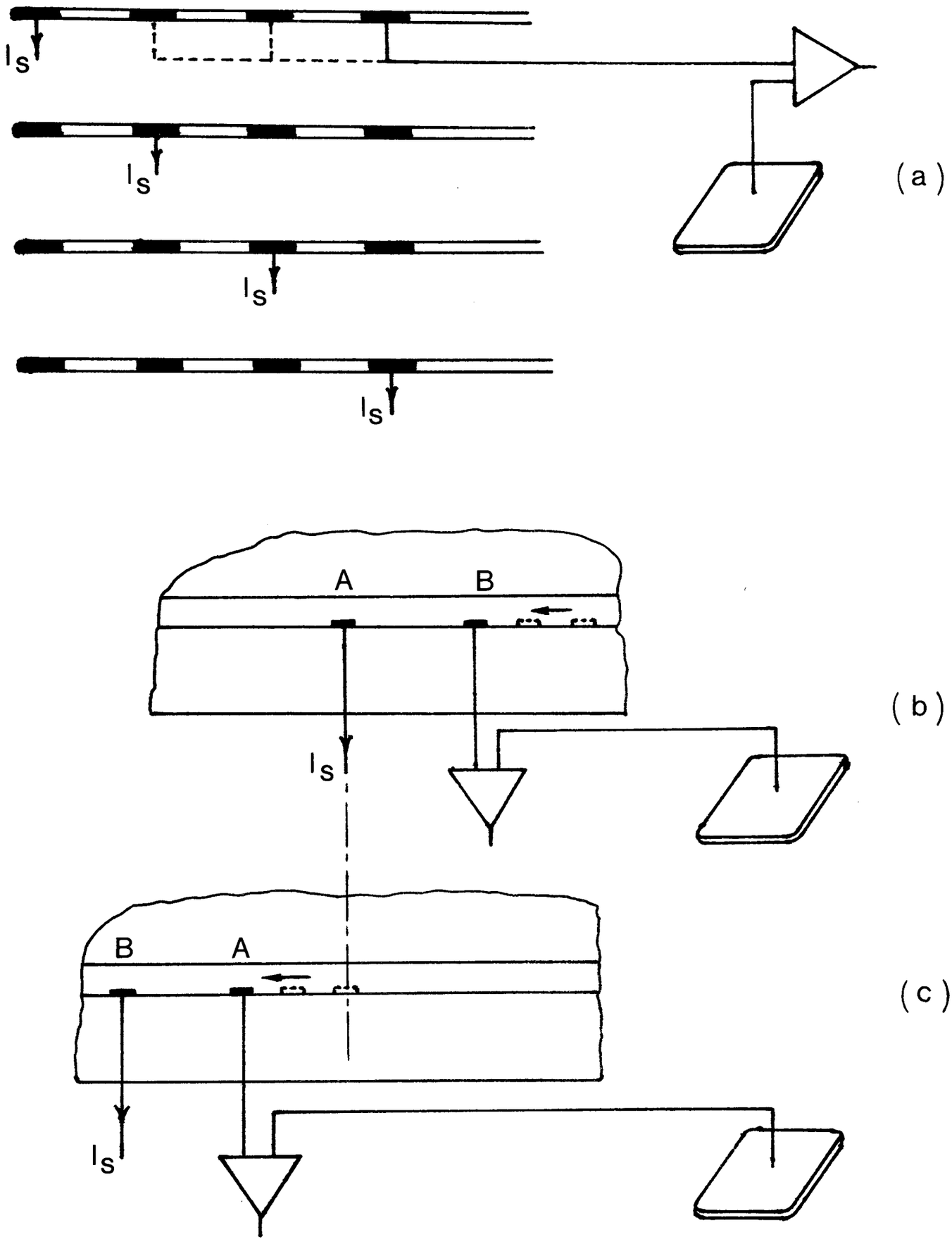

FIGURE 5.3 ACTUAL EXPERIMENTAL STIMULATING/RECORDING SCHEME

For details see text 5.3.1

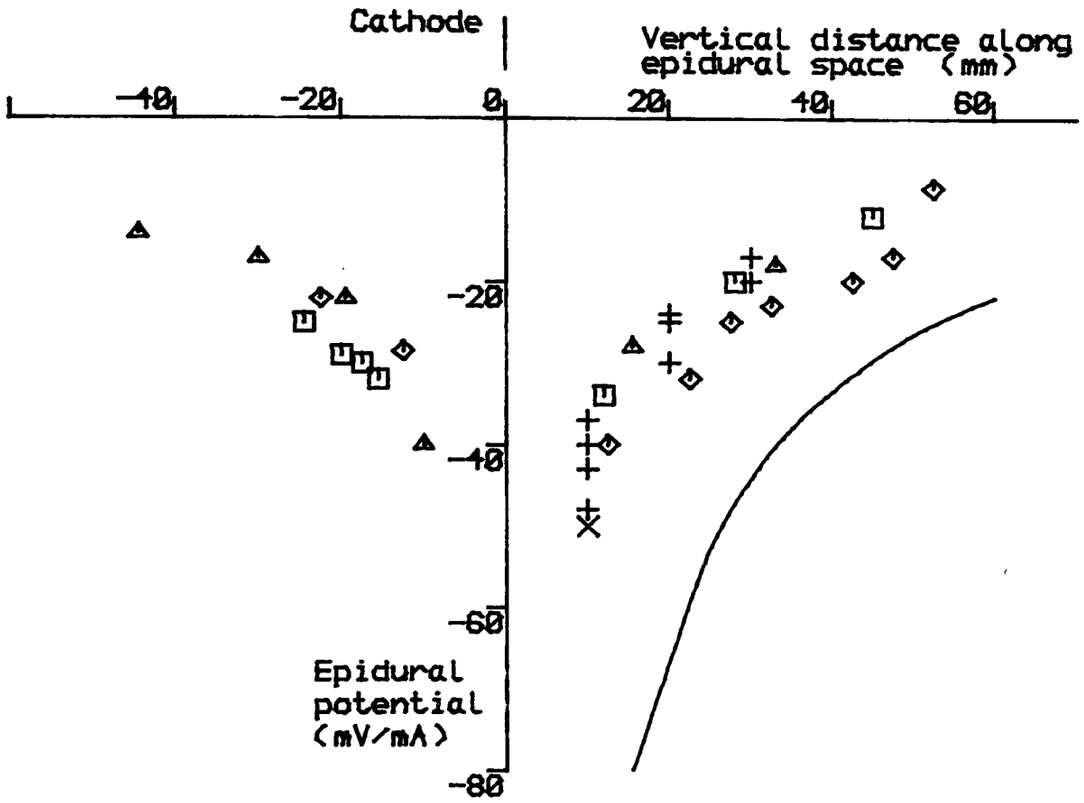

x patient R } recorded with 1980J electrode
+ patient PW } in Southampton

△◇ patient E } recorded with separated pole
□ patient CM } in Houston

FIGURE 5.4 CLINICAL MEASUREMENTS OF EPIDURAL POTENTIAL

Measurements shown as individual points. Solid curve is computer prediction (run no.(1) in Table 5.1) cathode at 0mm level. Other details see text 5.3.1

were conducted during a visit to Texas Institute for Rehabilitation and Research in Houston.

Each of the patients had two separated monopolar electrodes which were about 50mm apart in the epidural space. These electrodes were to be taken out after an assessment period, and field measurements were actually taken during the process of withdrawal.

The session with one of the patient (E) was conducted under continuous X-ray screening and the following procedures were involved :

procedure 1 : the lower electrode (A) was chosen as stimulating pole while the upper one (B) was the recording electrode (Figure 5.3(b)). The recording one was pulled gradually along the epidural space towards the stimulating pole in steps of 0.5-1.0cm , and in each step potential was simultaneously recorded . The procedure continued until the recording electrode was 50 mm past the stimulating one. The results are shown as diamond points in Figure 5.4; where the positive distances represented the positions of the recording electrode before it passed the stimulating one.

procedure 2 : circuit connections to the two electrodes were then interchanged so that the upper electrode (the stimulating pole in procedure 1) became the recording one (Fig. 5.3(c)). Recording procedures was the same as procedure 1 and the results are shown in Figure 5.4 as triangular points.

Measurements with the other patient (CM) followed a

similar pattern, with the exception that X-ray screening was not employed. The distances of electrode movement were therefore estimated by the length of lead being pulled out from the patient. The implanted electrodes were also too close to the 'exit' point to carry out procedure 2 ; and the single set of results is shown in Figure 5.4 as squares.

The solid curve seen above all the measurements is a computer solution from PAFEC using nominal tissue resistivities given in Table 2.1. Note the important point that all values in the curve are relative to a remote position on the model surface.

5.3.2 Epidural Recording of EDS-B Field

The 1980J multi-site electrode also provides opportunities for bipolar epidural stimulation with different pole separations. The general stimulating/recording procedures are similar to those described in Section 5.2, with exception that two of the four poles are needed to act as stimulating electrodes. Electrode combinations and the corresponding results are shown in the schematic diagram of Figure 5.5, where three pole separations and six combinations were used :

a) 1-0 and 2-3 for 10 mm separation,

b) 2-0 and 1-3 for 20 mm separation,

c) 3-0 and 0-3 for 30 mm separation. Usual electrode nomenclature described in Appendix 1 applied.

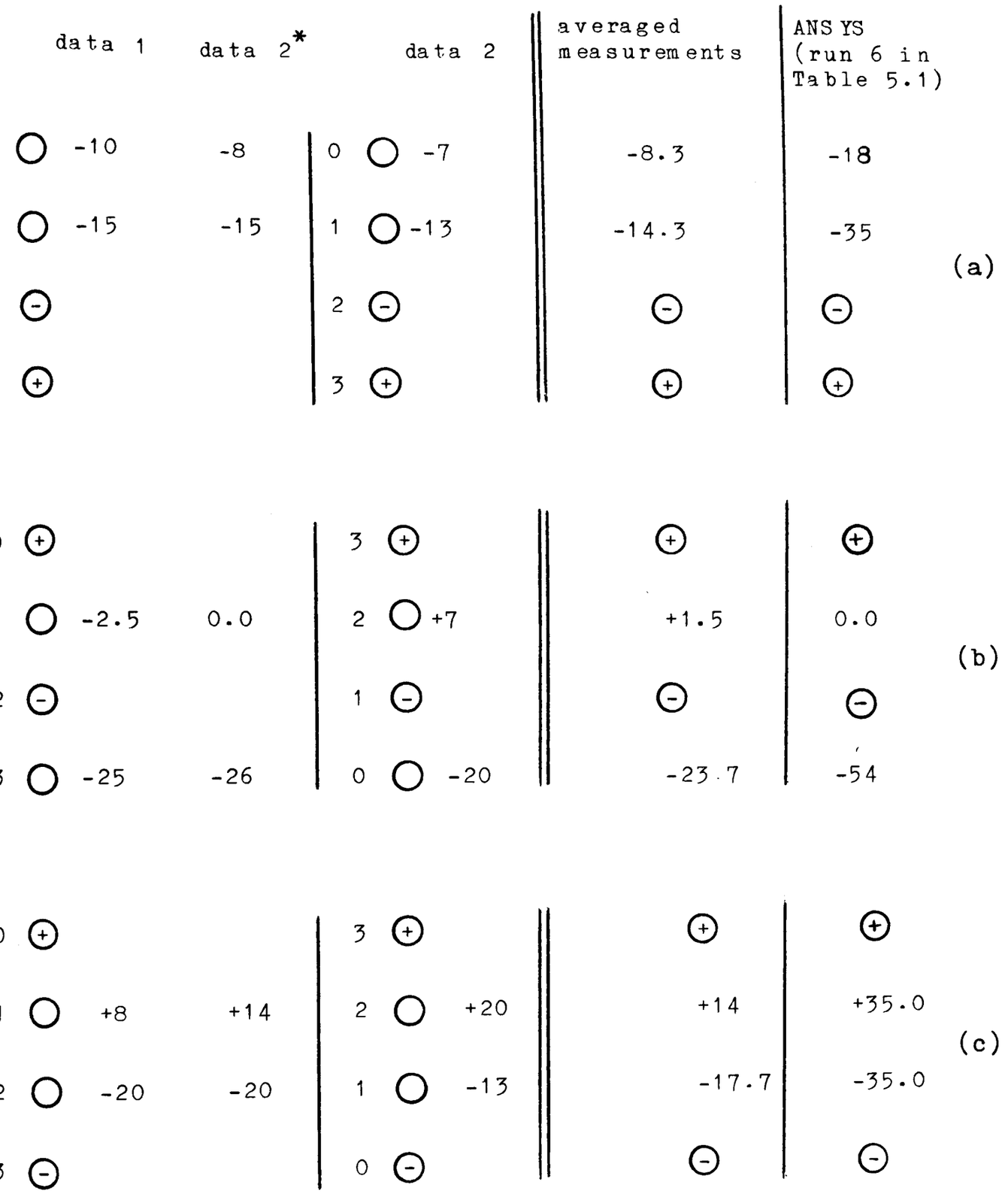

*data 2 was carried out seven days after data 1

FIGURE 5.5 SCHEMATIC DIAGRAM OF BIPOLAR CONFIGURATION OF EPIDURAL FIELD MEASUREMENTS

Details see text

5.3.3 Dorsal Surface Recording of EDS-M Field

This was a measurement session with a patient (AP) with two separated implanted electrodes. First, the position of one of the electrodes, to be used for the stimulating electrode, was estimated from X-ray screening. A recording probe with bare metallic tip recorded the potential on the dorsal surface relative to a remote indifferent on the arm. Figure 5.6(a) shows the results of surface potential along the backbone, while Figure 5.6(b) shows results measured laterally on both sides of the stimulating electrode. A theoretical solution from PAFEC is also included for comparison to be discussed below.

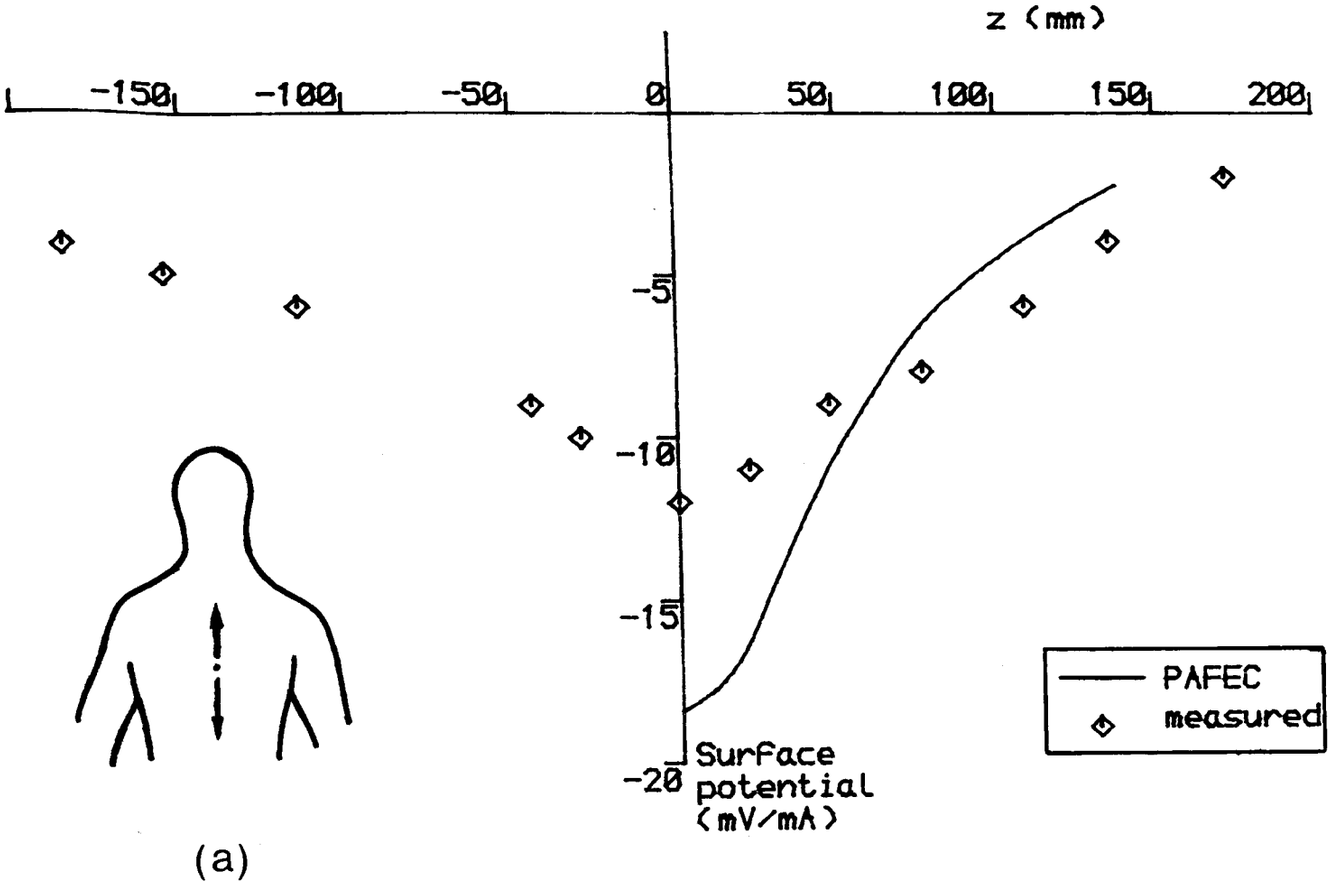

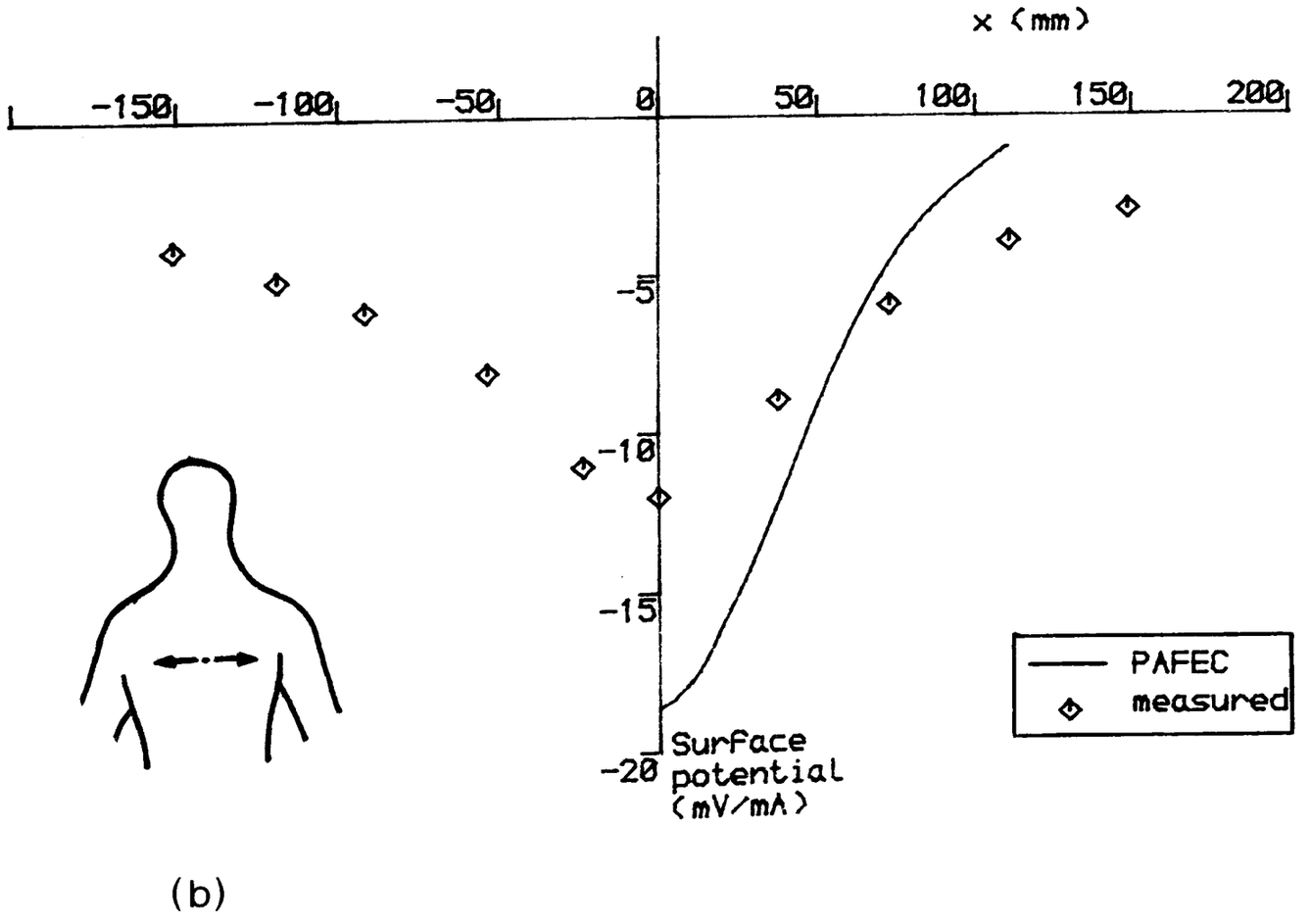

FIGURE 5.6 CLINICAL MEASUREMENTS OF DORSAL SURFACE POTENTIAL

ient. See text 5.3.3 for details

5.4 EFFECTIVE RESISTIVITY OF CADAVER SPINE

The preliminary comparisons in last section showed that theoretical solutions were at least two times higher than those observed clinically. The implication is that certain programmed tissue resistivities might be too high. The one with the most uncertainity value relates, of course, to the bony structures of the vertebral column (spine).

As mentioned in Chapter 3, even if an accurate resistivity value for the bone was available, any model would probably need to be based on an effective overall resistivity for the whole structure. This section therefore describes experimental work with human cadaver spine to estimate such an effective resistivity value.

5.4.1 Basic Scheme

The general experimental scheme can be seen in Figure 5.7 , the intention being to clamp fresh cadaver spines vertically in an anatomically correct position within an electrolytic tank. The surrounding space was filled with normal saline whose resistivity was measured separately.

Stimulating/recording procedures were conducted with a multi-site electrode inside the vertebral foramen.

On the assumption that only one unknown, the spine, is involved, its resistivity could be determined simply by adjusting the programmed resistivity value in a finite element model until the predicted field matched the experiment.

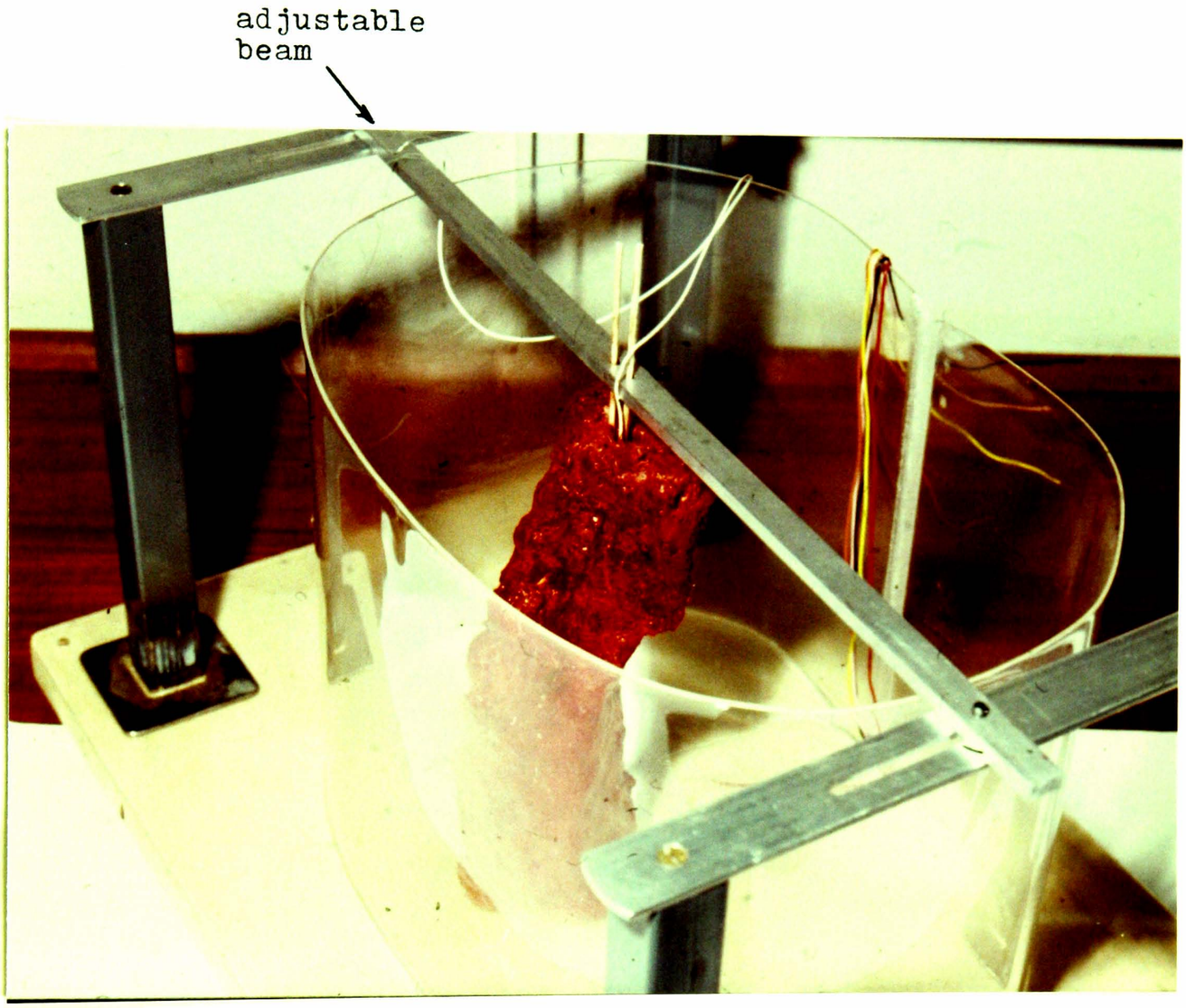

FIGURE 5.7 GENERAL VIEW OF EXPERIMENTAL ASSEMBLY RELATING THE EFFECTIVE RESISTIVITY OF VERTEBRAL COLUMN

See text 5.4 for full description. The coloured wires appeared on the ventral side serve no purposes

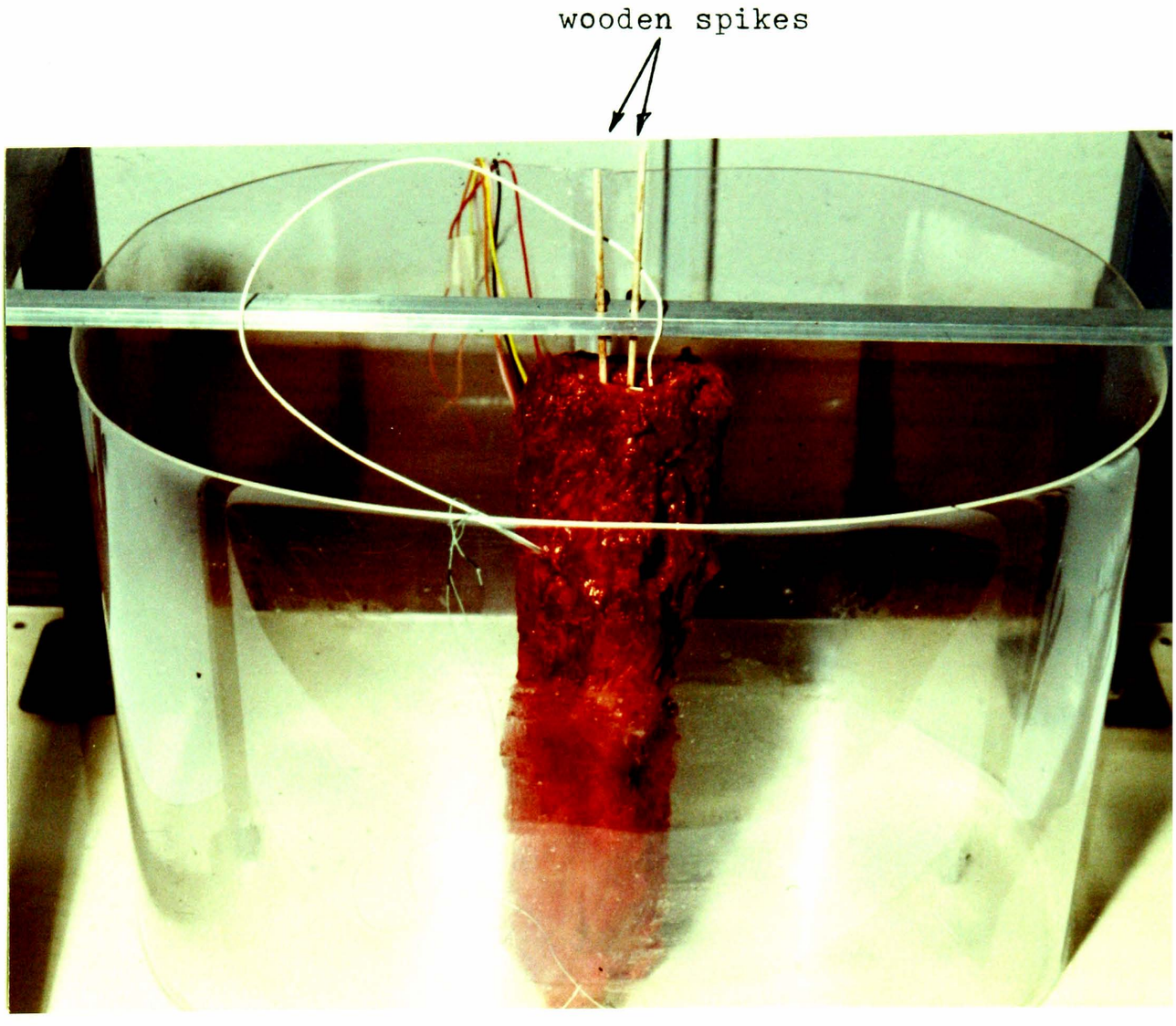

FIGURE 5.8 FRONTAL VIEW OF THE EXPERIMENTAL ASSEMBLY

The two wooden spikes (arrowed) were inserted into the vertebral canal to stabilise the spine

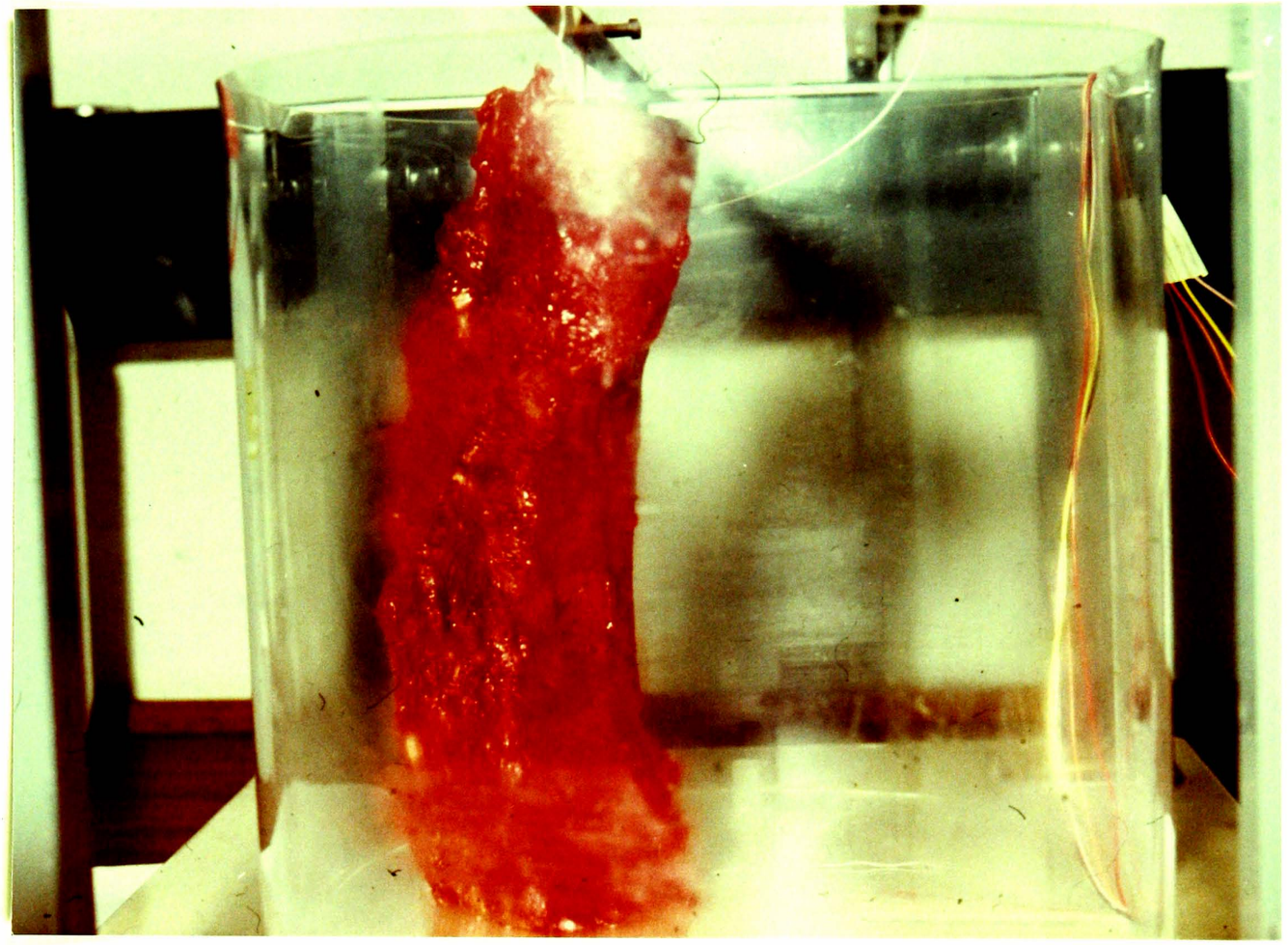

FIGURE 5.9 LATERAL VIEW OF THE EXPERIMENTAL ASSEMBLY

5.4.2 Equipment

The main feature of the equipment was a perspex tank shaped to match the anthropometric average dimensions of adult male mid-thorax. The essential features of the assembly can also be seen in Figures 5.7-5.9.

A thin perspex plate, hardly visible in the figure, was constructed as a 'false bottom'. The idea is to fix the cadaver spine onto the plate before lowering the assembly into the tank. It has an area slightly smaller than the cross-sections of the tank so that the assembly can slip into the tank without any difficulty. Sixteen holes were drilled on the plate in a region where the spine was to be attached. The holes, of diameter 2.9mm each, were on a 4 X 4 grid of spacing 10 mm.

The adjustable beam above the tank included two holes in the central region clamping two short wooden spikes which were used to stabilize the spine by passing into the body of the upper vertebra, as shown in Figure 5.7.

5.4.3 Cadaver Materials

Two spines, 180 mm each long, were used. They were taken from the upper-thoracic region (between C4 and T6) not more than 24 hours after death and kept at 4° C in a damped saline cloth for 12 hours.

The spinal cord and the three meninges were removed, while the spinal roots and tissues were left, filling the intervertebral foramen. The bottom of each specimen was

also trimmed flat for ease of mounting onto the 'false bottom'.

5.4.4 Procedures

The spine was erected onto the 'false bottom' in an anatomically correct position so that the flattened caudal end was above the 16-holes grid. Three small wood screws then fastened the spine onto the plate from the other side.

The multi-site electrode, previously passed down the vertebral canal from the top, was fixed onto the 'false bottom' by a cotton thread so that pole 0 was midway down the canal. The insulating sleeve may be seen as a white wire in Figures 5.7-5.9. The electrode was later clamped at the top onto the adjustable beam.

The whole assembly was placed in the tank and two wooden spikes were inserted into the body of the top vertebra. Note the important point that the specimen contained ligament and collagan, filling the spaces between vertebrae.

The surrounding space and the vertebral canal were then filled with 0.85% normal saline such that the spine was just immersed under the saline surface.

The connected circuit was similar to that shown in Figure 5.1; using the 1-ohm resistor to monitor the "stimulating current". Constant current pulses were delivered through a monopolar electrode (pole 0). The exception is that a silver/silver-chloride (Ag-AgCl) cup

indifferent electrode was employed at the dorsal mid-line of the tank.

Field potentials within the canal were recorded from the other three poles (1,2,3) with respect to another Ag-AgCl indifferent at the ventral mid-line. The measurements were repeated at intervals during the 4-hour session.

Finally a sample of saline solution was taken from the tank for accurate resistivity measurement (Appendix 2).

5.4.5 Computer Model

The finite element model, using the PAFEC package, was based upon the one described in Chapter 2 (Figure 2.1(b)). Two changes were made in order to match the experiments. First, the model contained two materials only : the saline solution and the spine. Second, the physical size of outer thorax was adjusted to that of the tank. The finite sizes of the electrode poles and indifferents were idealised to single points.

5.4.6 Results

Each of the two experiments was carried out at room temperature on different days.

Post-experiment measurements of the saline resistivity showed values of 70 ohm-cm and 100 ohm-cm for the two cases. These differing values were taken into account during subsequent computer modelling.

The measured fields, which remained constant over a period of approximately 4 hours, are shown in Figure 5.10 and 5.11 as diamond points. They have been normalized to an applied current of 1 mA. The theoretical solutions, using different resistivity for the spine, are also shown in the figures. In both cases, the programmed value 1600 ohm-cm for effective spine resistivity give the best match.

A sensitivity test of the saline resistivity on the field was also carried using the computer model. While the spine was held constant at 1600 ohm-cm, saline resistivity was varied ± 30% between the measured values. The results, shown in Figures 5.12 and 5.13, suggest that a ± 30% variation in saline resistivity do not significantly affect the fields.

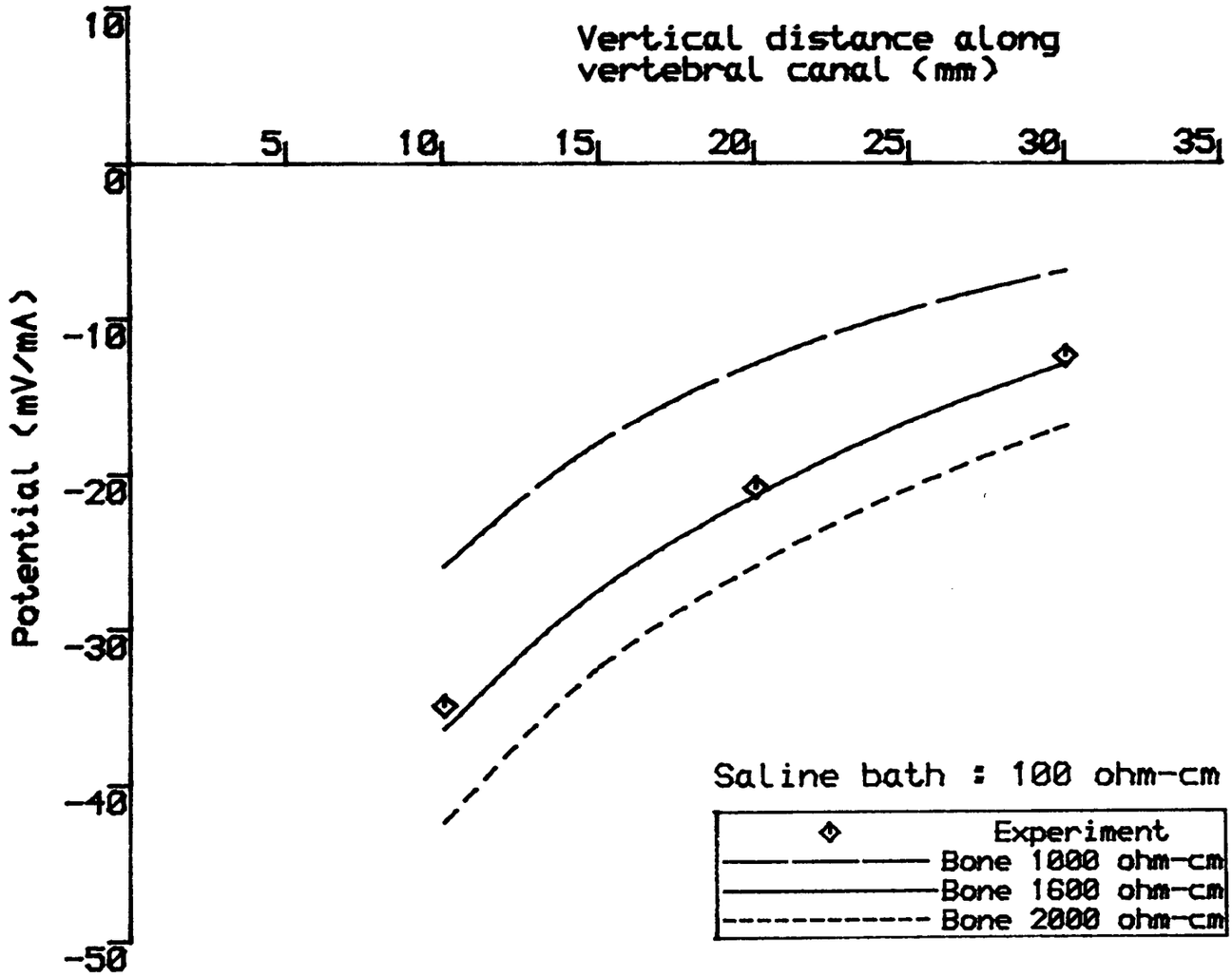

FIGURE 5.10 COMPUTER PREDICTIONS OF POTENTIAL WITHIN THE VERTEBRAL CANAL

Cathode at 0mm level. See text 5.4.6 for details

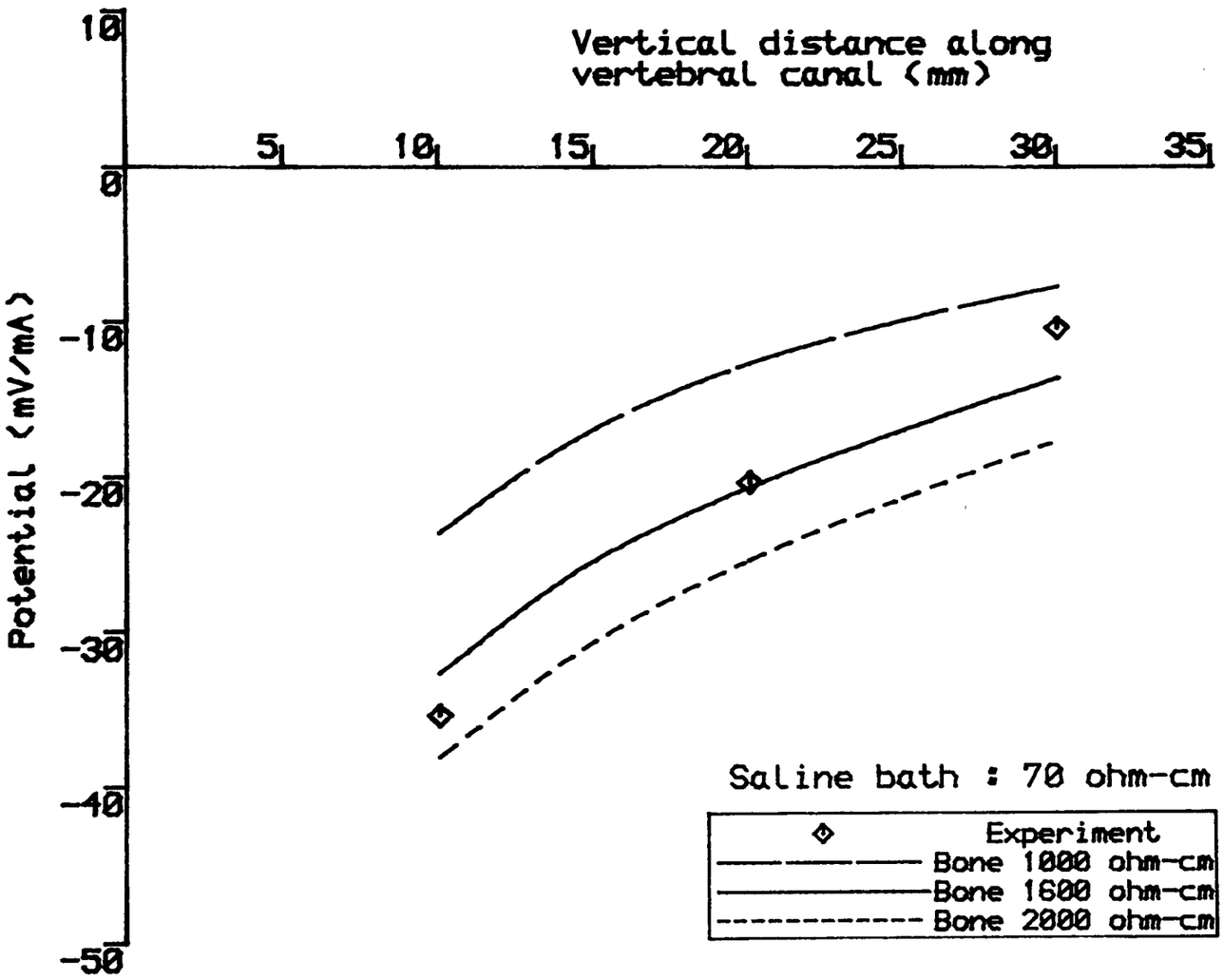

FIGURE 5.11 COMPUTER PREDICTIONS OF POTENTIAL WITHIN THE VERTEBRAL CANAL

Cathode at 0mm level. See text 5.4.6 for details

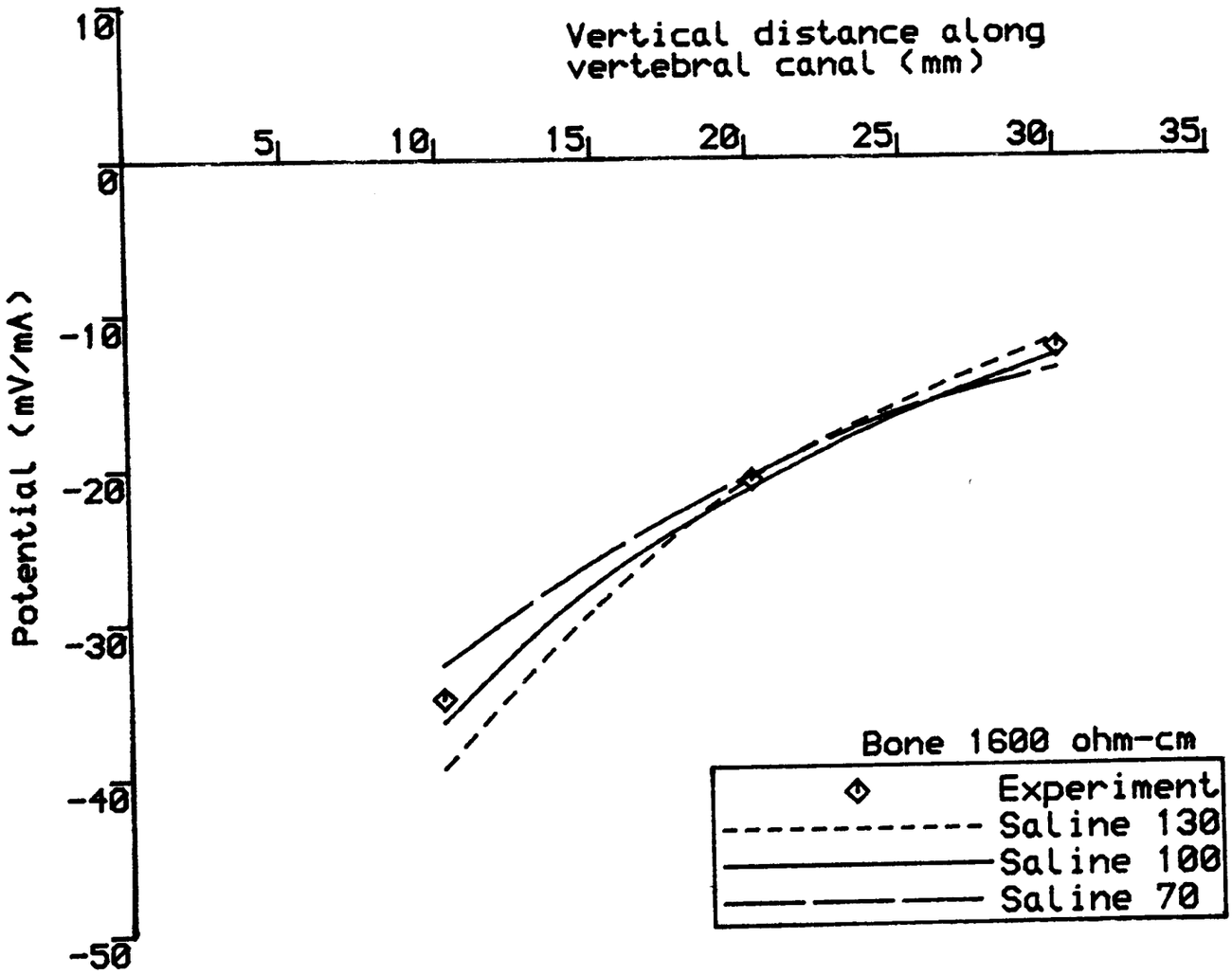

FIGURE 5.12 SENSITIVITY TEST OF SALINE RESISTIVITY

Bone maintained at 1600 chm-cm. Solid curve and diamond points correspond to that in Figure 5.10

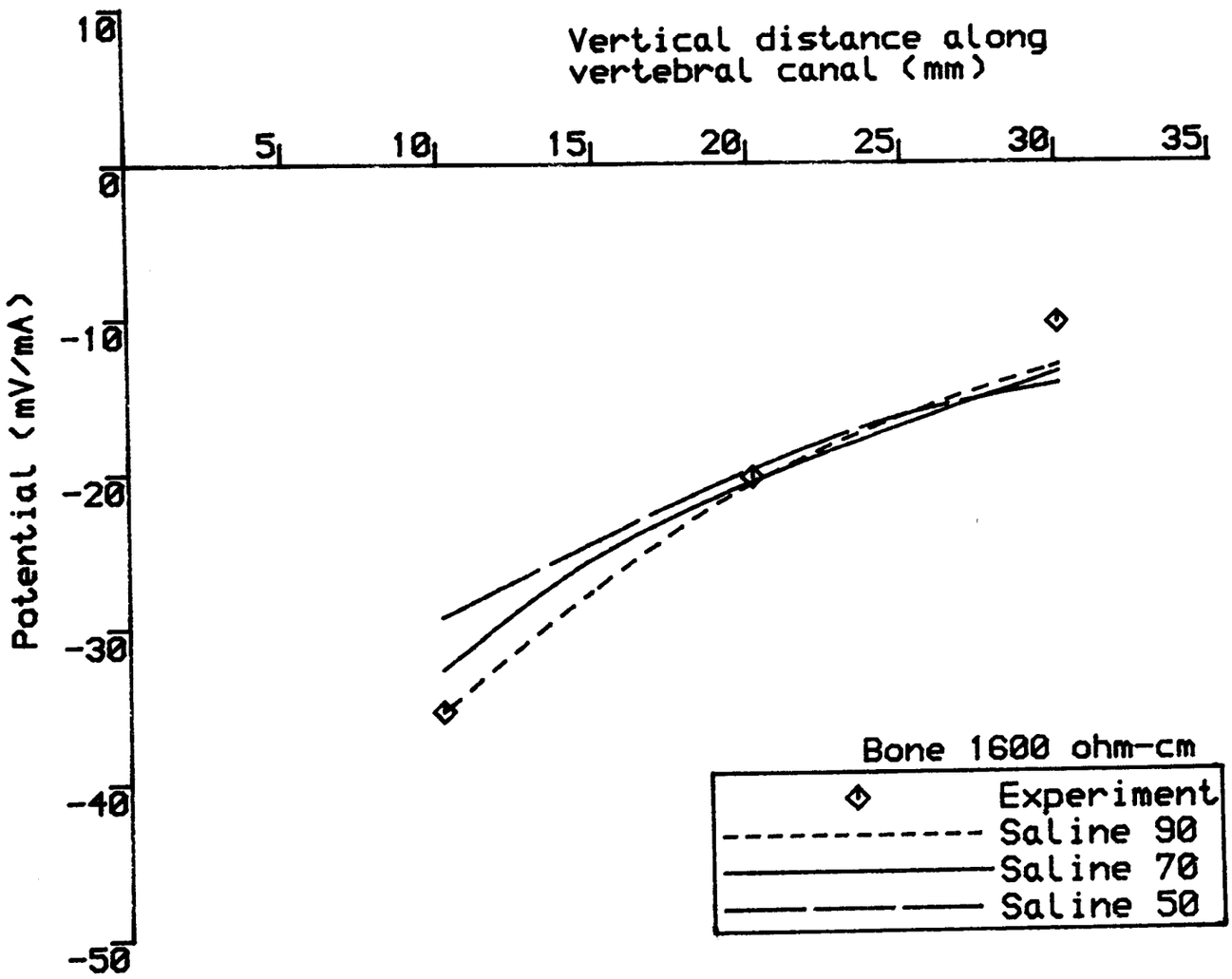

FIGURE 5.13 SENSITIVITY TEST OF SALINE RESISTIVITY

Bone maintained at 1600 ohm-cm. Solid curve and diamond points correspond to that in Figure 5.11

5.5 COMPARISON OF COMPUTER SOLUTIONS WITH CLINICAL MEASUREMENTS

A preliminary comparison between clinical measurements and computer solutions has been presented in Section 5.3. This section shows in detail how the programmed tissue resistivities are adjusted in order to match the solutions with clinical measurements.

5.5.1 Computer Model

With the exception of one single run (bipolar), PAFEC was used for the tests. The 3-D model for monopolar case (run numbers (1)-(5)) used the configuration described in Figure 2.1(c) to represent a single 'remote' indifferent. As the model represents only one-half of the thoracic domain, the total height of the model is increased to 500mm to reduce truncation errors. The stimulating indifferent is at the ventral side of one end , while the 'recording indifferent' is assumed on the other end.

5.5.2 Comparison

A total of eight computer solutions were generated, and Table 5.1 summarises the set of resistivities used in each run.

TABLE 5.1

Tissue resistivities (ohm-cm)

run number	gm	wml	wmt	csf	edf	vb	gt	sm	sr	f
(1)	400	138	1211	60	2000	4000	400	950	675	1066
(2)	"	"	"	"	"	1600	"	"	"	"
(3)	"	"	"	"	"	1600	260	"	"	260
(4)	"	"	800	"	"	1600	260	"	"	260
(5)	"	"	800	"	60	1600	260	"	60	260
(6)	400	138	1211	60	2000	4000	400	950	675	675
(7)	"	"	"	"	"	1600	"	"	"	1066
(8)	"	"	800	"	60	1600	260	"	60	260

(1)-(5) are EDS-M, (6)-(8) are EDS-B with 10mm separation. All runs except (6) used PAFEC 75, (6) used ANSYS package. Refer to Table 2.1 for tissue abbreviation.

Figure 5.14 compares the results for EDS-M, where the computer solutions are plotted as full and dotted curves. The numbers in the brackets correspond to the number shown in Table 5.1. Clinical measurements in Figure 5.4 are also reproduced in Figure 5.14 as individual points, using the ordinate as symmetry line, to amalgamate "left"

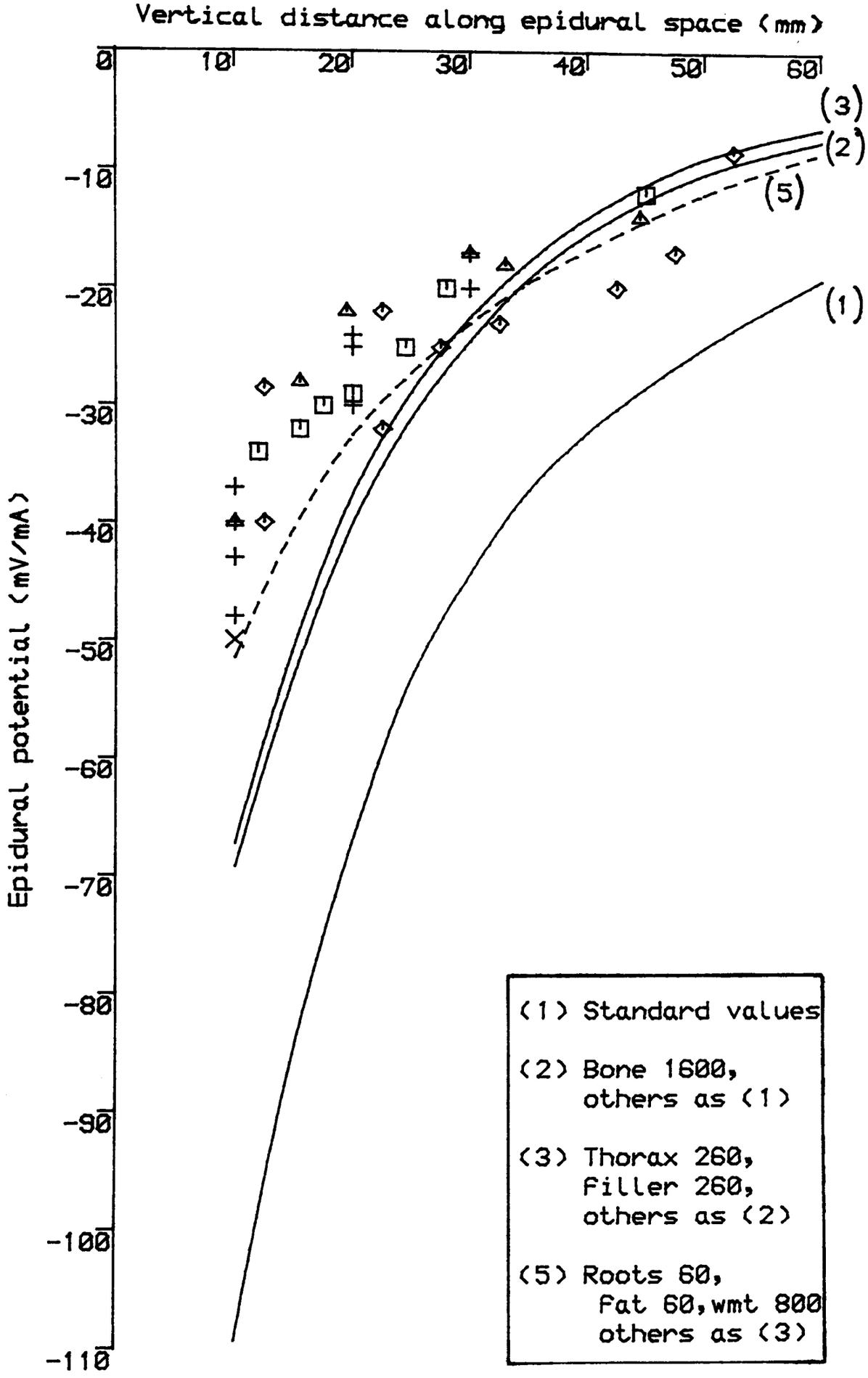

FIGURE 5.14 COMPARISON OF COMPUTER PREDICTIONS OF EPIDURAL POTENTIAL WITH CLINICLAL MEASUREMENTS

Monopolar cathode at 0mm level. See Table 5.1 for details of tissue resistivities used for the curves.
Other details see text 5.5.2

and "right" results by reflection.

Curve (2) was obtained by using 1600 ohm-cm for vertebral column compared with curve (1). The resultant epidural potential is markedly reduced, by at least 35%, although in general it is still higher than the clinical measurements.

The next step was to reduce the resistivity of the general thorax , as it constitutes more than 85% in volume of the model. A value of 400 ohm-cm is normally used, but recently MEIJER et al (1982) determined the lowest value of human thorax to be 290 ohm-cm. As circumferential stimulating/ recording electrode strips were used in their experiments, 290 ohm-cm actually represented an overall value of torso including dorsal skeletal muscle and vertebral column.

If different tissue components in the torso are represented by parallel 'conductor rods' of different resistivities, then the overall impedance (Ro) is given by

$$\frac{1}{Ro} = \frac{1}{Rgt} + \frac{1}{Rsm} + \frac{1}{Rvb} + \left(\frac{1}{Rwm} + \frac{1}{Rgm} + \ldots \right)$$

As the three components (gt , sm and vb) occupy more than 99% of the total cross-sectional area of the finite element model, wm , gm and the like may be neglected. Hence we may write

$$\frac{Ao}{\rho_o{}^L} = \frac{Agt}{\rho_{gt}{}^L} + \frac{Asm}{\rho_{sm}{}^L} + \frac{Avb}{\rho_{vb}{}^L} \qquad (5.1)$$

where An is the cross-sectional area of the tissue identified by symbol n,

ρ_n is the corresponding resistivity,

Ao is the total area, being the sum of individual tissue area An,

L is the length of 'conductor rod'

ρ_{sm} = 950 ohm-cm

ρ_{vb} = 1600 ohm-cm

By counting the areas from a cross-sectional finite element mesh and substituting into expression (5.1), the appropriate resistivity for the general thorax of the model is found to be 260 ohm-cm.

The finite element model is also simplified by assuming filler (1066 ohm-cm in Table 2.1) to be part of the general thorax and having a value of 260 ohm-cm.

The computer solution with these changes is plotted as curve (3) in Figure 5.14. The striking point is that the result is not greatly affected by these two changes.

It is also evident from the curves that their slopes are in general steeper than the measured data. The implication may be that there is some highly conductive path in the vicinity of the epidural stimulating electrode. Accordingly, the resistivity of white matter measured in the transverse plane is reduced to 800 ohm-cm (TAREN and DAVIES,1970), but the solutions, not shown in Figure 5.14, are only 2% lower than that of run (3).

The next targets for scrutiny are the spinal roots

within the subarachnoid space and the epidural fat. As already mentioned in Section 2.2.2, the pairs of spinal roots are modelled by two prismatic-running columns so that the subarachnoid space is divided into three compartments by a relatively high resistivity tissue (675 ohm-cm). Anatomically, these pairs of roots spring out from the sides of the cord only at intervals along the cord's length, and the spaces between successive pairs of roots are still filled with cerebrospinal fluid. That is to say the presence of these roots should not markedly alter the flow of the current within the subarachnoid space. A programmed resistivity of 60 ohm-cm, equivalent to csf, is therefore assigned to the spinal roots.

The epidural space is another region where the effective resistivity is in doubt. The space so far has been represented wholly by fat of 2000 ohm-cm resistivity. In fact, the space contains areolar tissues and plexus of veins in addition to the loose fat, and it could arguably be considered as merely a potential space moistened by serous fluid. For these reasons, the lowest resistivity value (60 ohm-cm) may again be a justificable assumption for the epidural space. The resulting computer solution is shown in Figure 5.14 as the dotted curve (5) and the notably feature is a significant drop of epidural potential at distances close to the stimulating electrode (< 20 mm).

Figure 5.15 compares bipolar results for 10 mm pole separation. Although there are only two measured values,

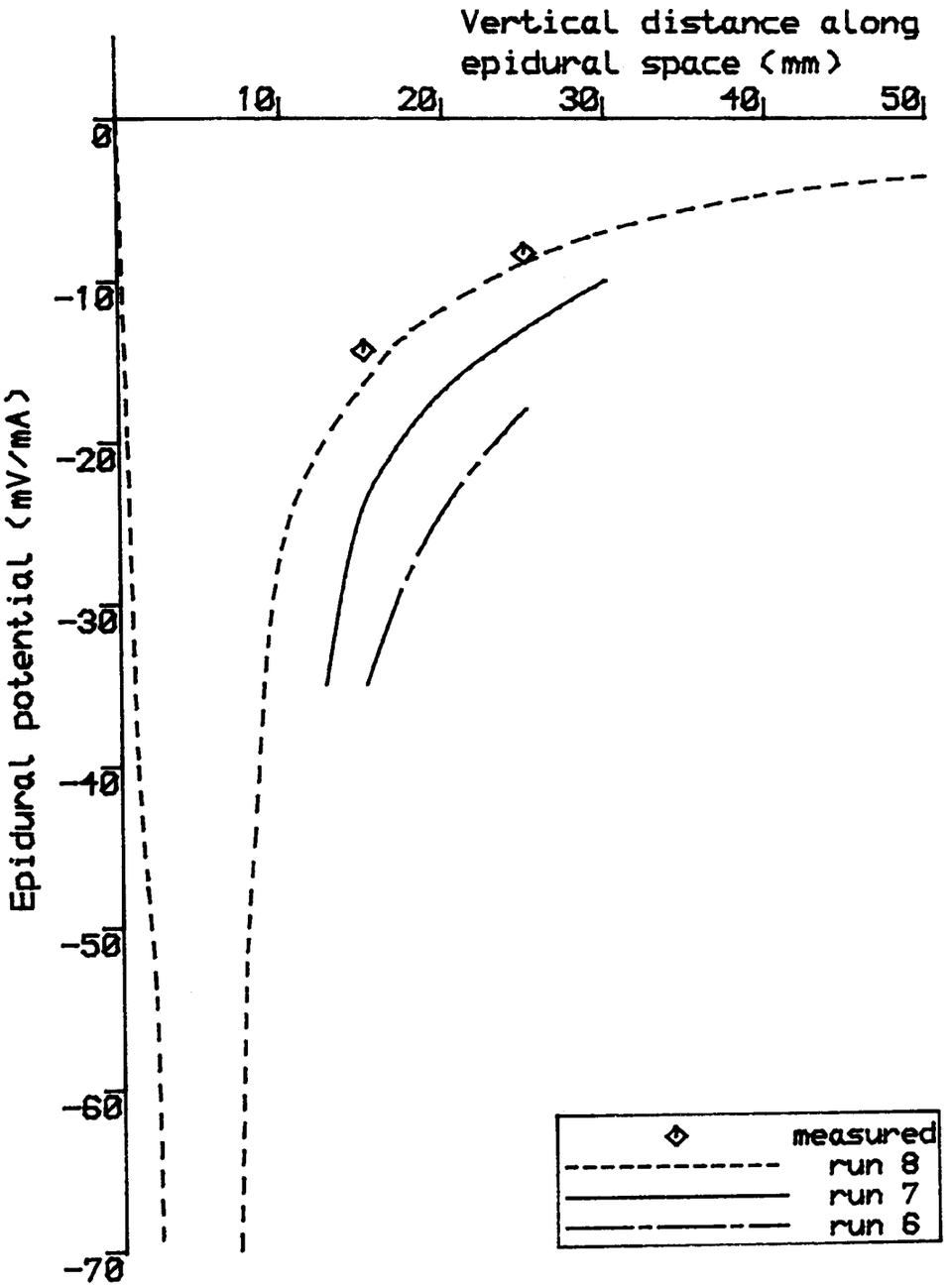

FIGURE 5.15 COMPARISON OF COMPUTER PREDICTIONS OF EPIDURAL POTENTIAL WITH CLINICAL MEASUREMENTS

Bipolar configuration 0-1 with 10mm separation. Cathode at 5mm level. See Table 5.1 for details of tissue resistivities for the curves. See text 5.5.2 for details

the results fit neatly with curve (8) whose set of programmed resistivity is the same as curve (5) in Figure 5.14. Theoretical solutions for 20 mm and 30 mm pole separations, using the same set of resistivity, were not attempted, but the results are expected to show similar trends.

For the comparison of dorsal surface recordings, Figure 5.16 shows the two cases. In both cases, theoretical solutions did not agree with the measured ones (diamond points) : the model predicted that potential should fall faster with distance from the axis of stimulation. They also showed that a drop of bone resistivity from 4000 ohm-cm to 1600 ohm-cm does not affect the dorsal surface potential significantly, as shown by the bottom two curves in each figure.

5.6 VARIATIONS OF POTENTIAL ALONG VERTICAL FIBRES IN THE SPINAL CORD

The potential fields mentioned so far are either in the epidural space or on the dorsal skin surface, but in fact the main region of interest concerned in electrical epidural stimulation is the nerve cells in the spinal cord. An important model of myelinated fibres in relation to remotely-generated electrical field (McNEAL,1976) suggests that the variations of potential along an axon is a significant factor in fibre excitation. Figure 5.17 therefore plots the theoretical 'absolute'

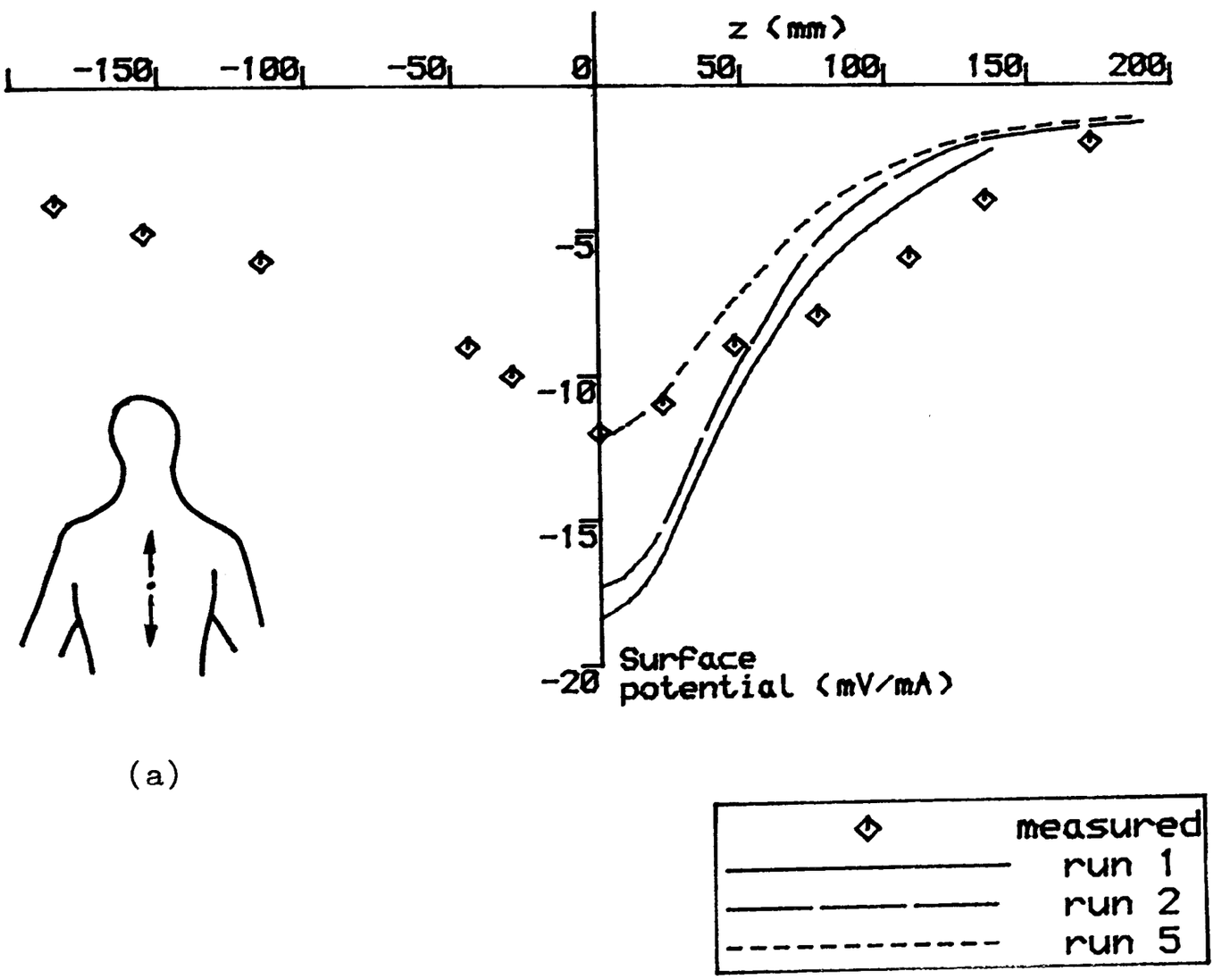

FIGURE 5.16 COMPARISONS OF COMPUTER PREDICTION OF DORSAL SURFACE POTENTIALS WITH CLINCIAL MEASUREMENTS

Epidural monopolar cathode at 0mm level. See Table 5.1 and text 5.5.2 for details
(a) along the backbone
(b) lateral recording

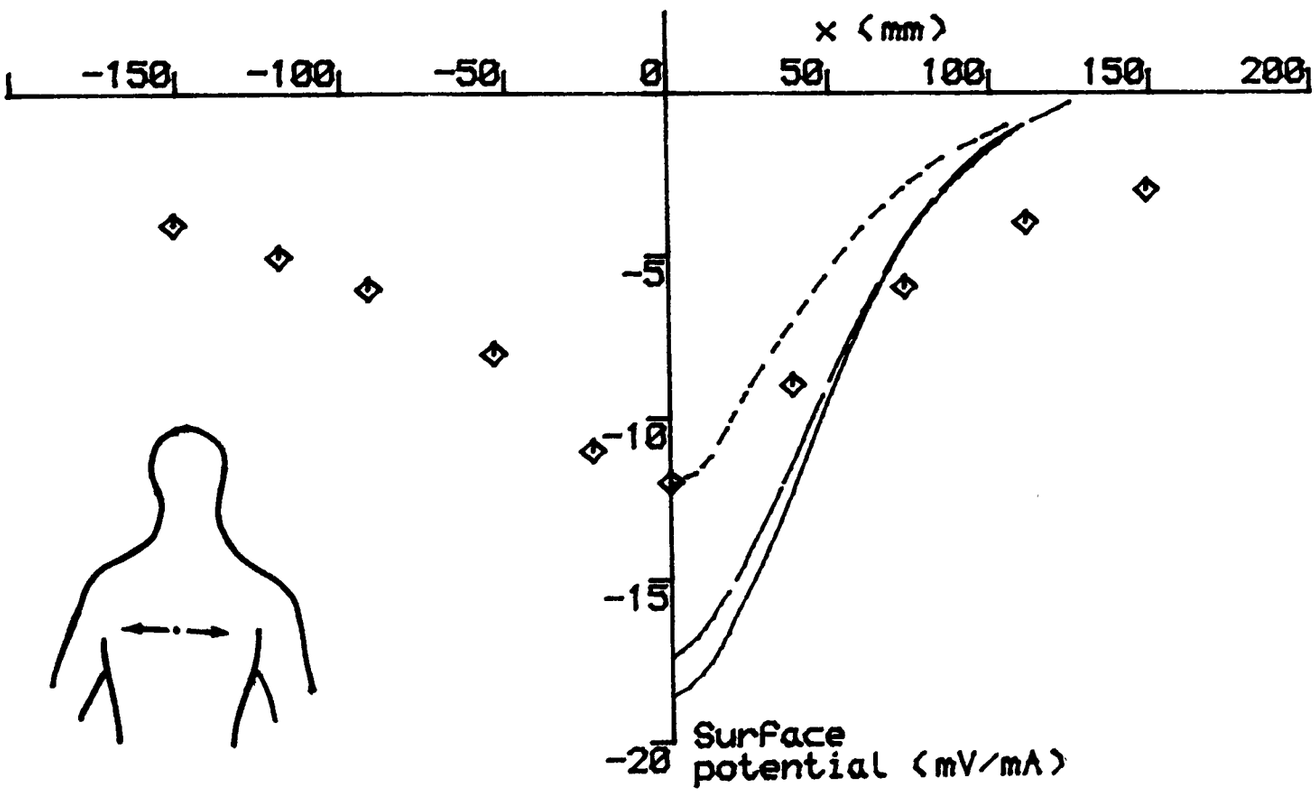
x (mm)
-150
-100
-50
0
50
100
150
200
-5
-10
-15
-20
Surface potential (mV/mA)

(b)

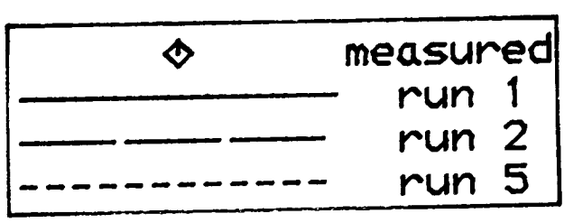
measured
run 1
run 2
run 5

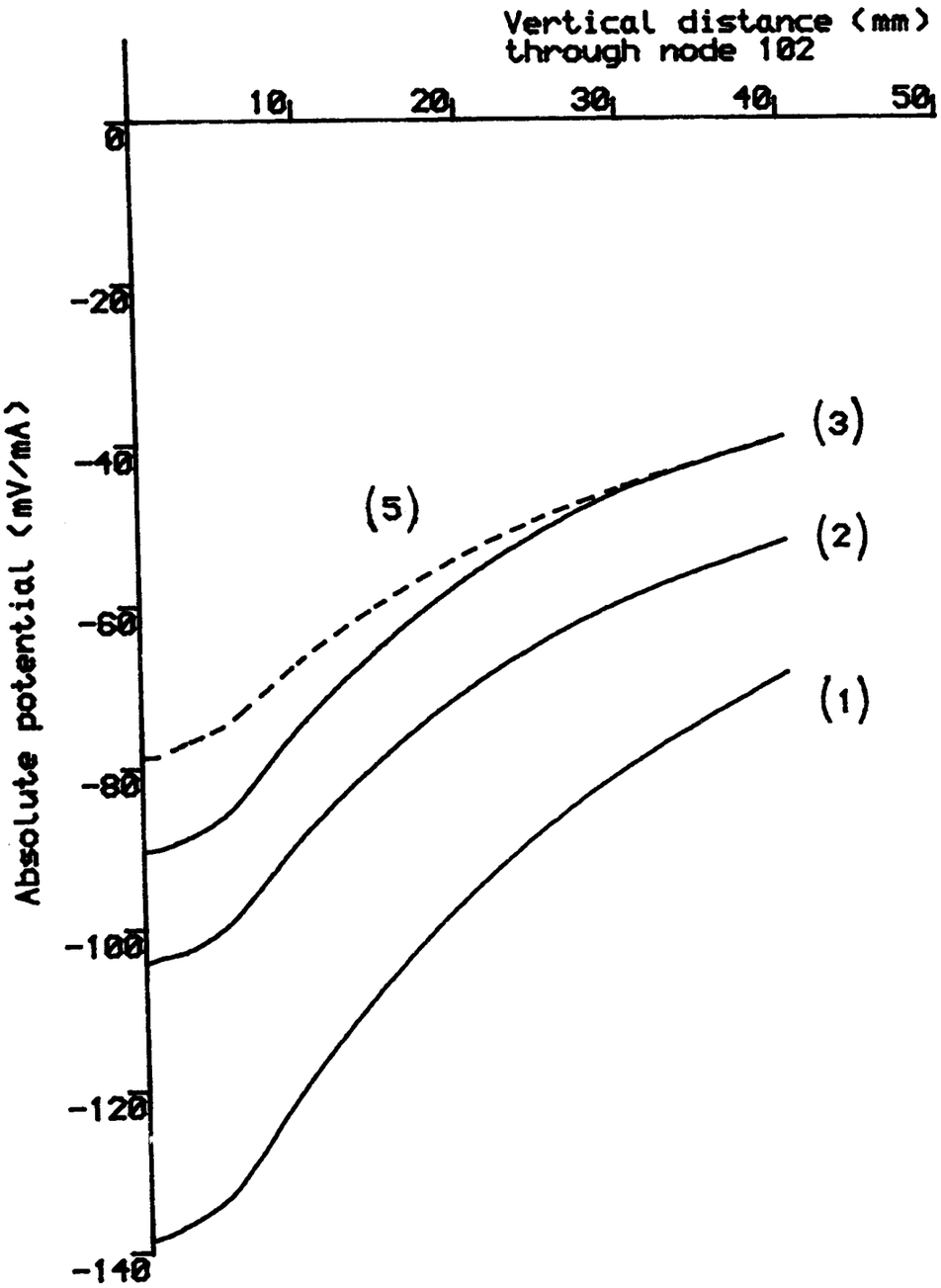

FIGURE 5.17 VARIATION OF POTENTIAL AS A FUNCTION OF VERTICAL POSITION IN THE DORSAL SPINAL CORD FOR EPIDURAL MONOPOLAR ELECTRODE

Distance represent axon track vertically through node 102 in Figure 2.3. Level of cathode at 0mm. See Table 5.1 for details

potentials within the cord along one vertical line in the finite element mesh (node 102 in Figure 2.3). All the curves and the associated numbers in the figure correspond to the potential plots already described in Figures 5.14-5.16. The comparisons are between computer solutions of different programmed tissue resistivities , and the notable feature is that the shapes of the plots are very similar to each other.

CHAPTER 6 FINAL DEVELOPMENT OF THREE-DIMENSIONAL FINITE ELEMENT MESH

6.1 REQUIRMENTS OF A NEW 3-D FINITE ELEMENT MODEL

Although a 3-D finite element model has been used extensively in the last few chapters, a few modifications are still required before the generated field solutions can be used for proper neurological analysis. This model was originally designed and developed from a 2-D model (COBURN,1980) to be run on the CDC7600. For this reason, the numbering system in the model is not systematic and the mesh resolution is also restricted by computer memory size. As the CDC7600 in ULCC has just been replaced by a CRAY-1S/1000, making available at least four times working core-store available for finite element analysis, a 3-D model with better resolution is possible. Moreover, previous work in Chapters 2,4 and 5 accumulate information that should be incorporated in a final 3-D model.

The most desirable feature is a fine mesh within the spinal cord to take account of principal neuro-anatomical divisions. For example, the mesh should model fibre tracts and have sufficient nodes to define fibre pathways. The size of grey matter should also be allowed to vary according to the level of stimulation.

The second point is that theoretical solutions within the spinal cord will be used for further analysis. These

solutions can be used directly with single neuron models, such as (i) the straight long myelinated fibres in the dorsal columns or (ii) afferent fibres in the dorsal roots. On the other hand, when the neuron model is more complex, like a fibre system containing branches with different orientations, the mesh within the cord may still not be fine enough. One way of overcoming the problem is to extract the solutions within the cord and use them as boundary conditions for a second run using a restricted model with a finer mesh. In this second case, the whole domain need be only the spinal cord and relatively fine meshing is feasible. The third point is the need for additional element layers for more precise representation of clinical work. In general, the number of layers in the present 3-D model is restricted to eight on the CDC7600.

6.2 DESCRIPTION OF MODEL MODIFICATIONS

6.2.1 Changes in Model Discretization

Figures 6.1-6.2 show the transverse sections of the modified meshes, while Figure 6.3 shows the types of 'standard' tissues represented in the model. The 3-D model is still prismatically built with gradual increases in element height upwards, away from the region of electrodes. Although the feature of idealised boundaries is retained, the overall resolution is finer; and there are 117 elements in one layer compared with only 76 in the original one used on the CDC7600.

In the vertebral canal, as seen in Figure 6.2, the mesh is especially fine in two areas. The first is in the dorsal area surrounding a semi-circular region which can be an finite size electrode. The second is within the spinal cord where different kinds of idealised fibre tracts can be modelled (Figure 6.4). Variations in the grey matter size , according to the level of the cord, can be represented too (Figure 6.5).

6.2.2 Modifications in Anatomical Structures

In addition to changes in mesh fineness, the anatomical structure of the 3-D model is modified.

The first change is in the outer boundary of the thorax where the shapes and dimensions are modified from two kinds of sources. The first one is computer

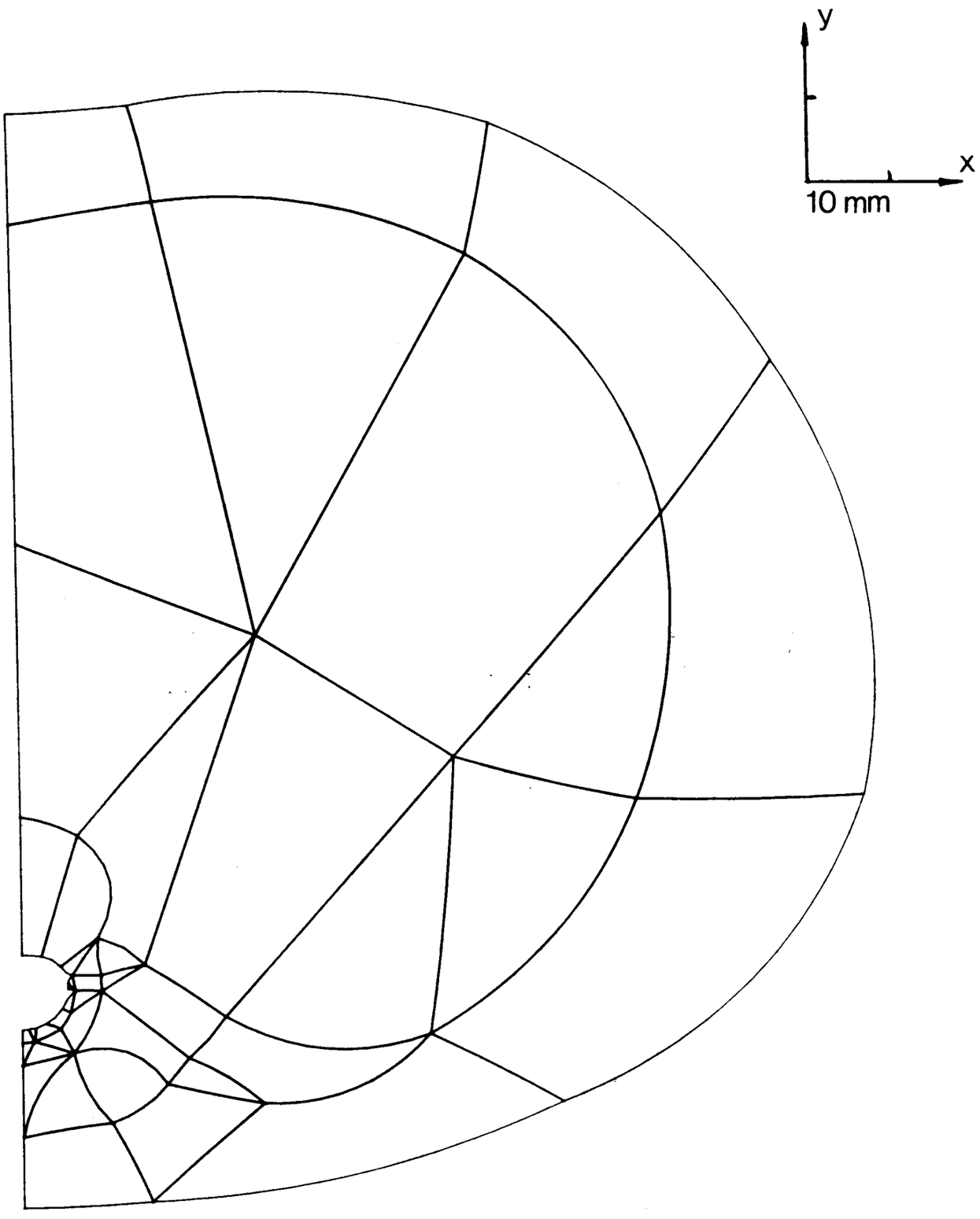

FIGURE 6.1 FINITE ELEMENT MESH OF TRANSVERSE SECTION THROUGH THE HUMAN THORAX AND VERTEBRAL COLUMN

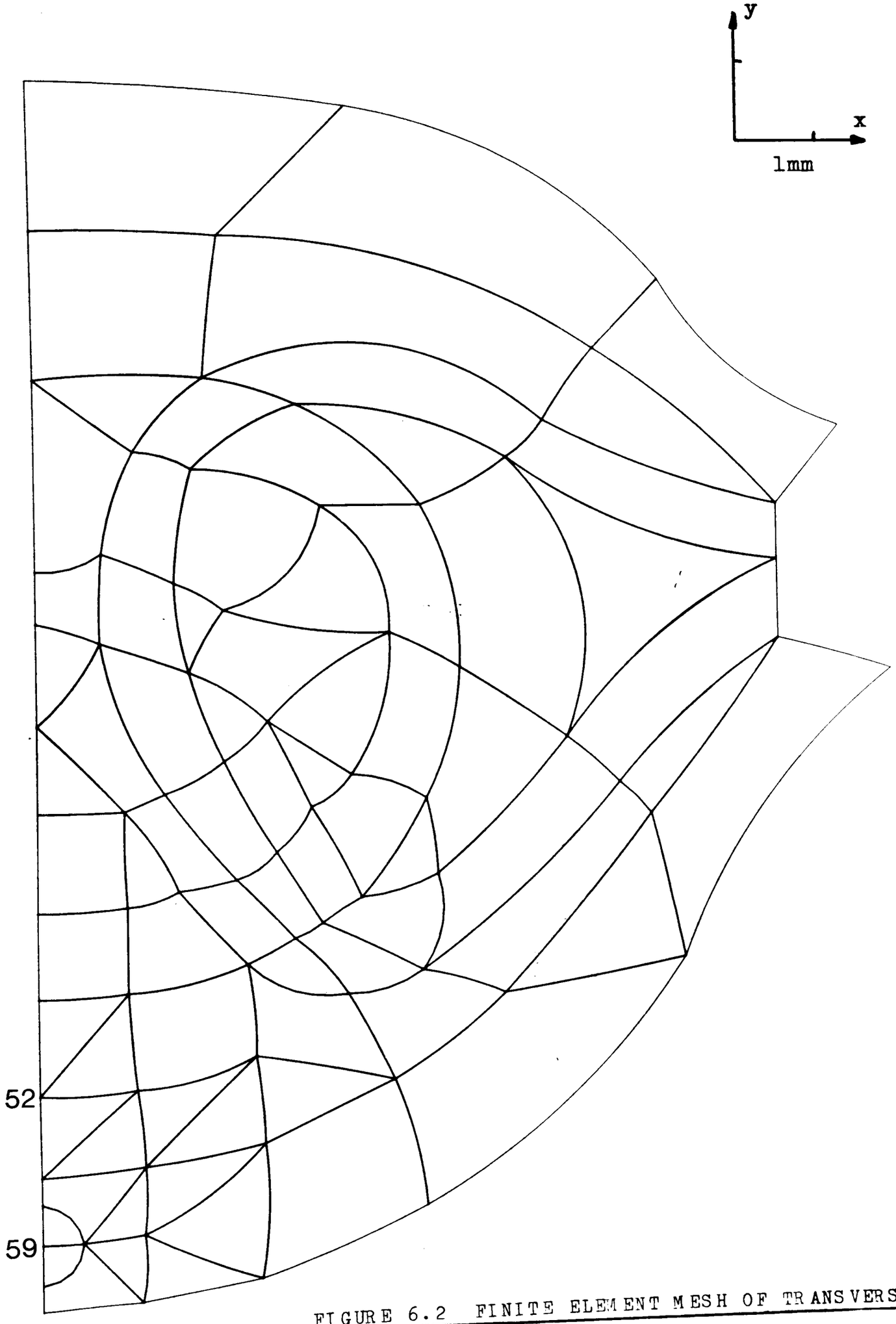

FIGURE 6.2 FINITE ELEMENT MESH OF TRANSVERSE SECTION THROUGH THE VERTEBRAL CANAL

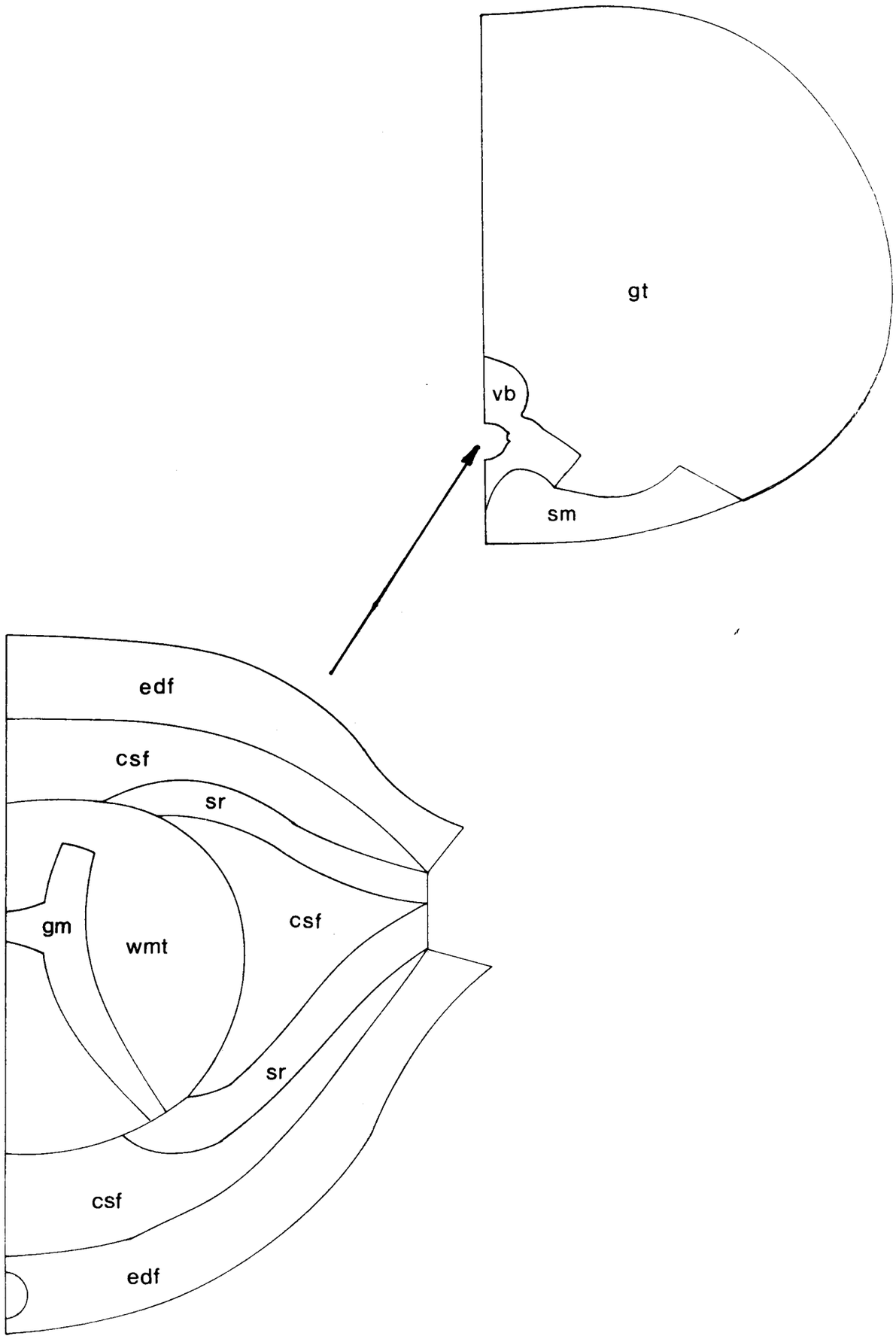

FIGURE 6.3 IDEALISED BOUNDARIES BETWEEN DIFFERENT TISSUES IN THE MODEL

See Table 2.1 for tissue abbreviations

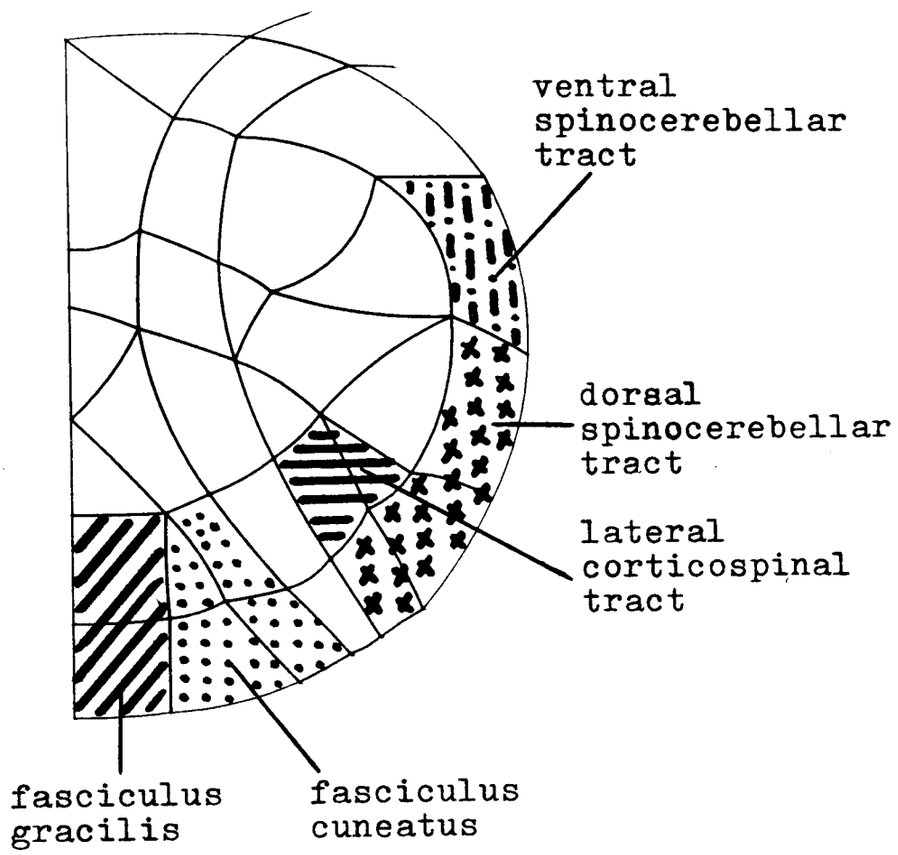

FIGURE 6.4 IDEALISED FIBRE TRACTS IN THE SPINAL CORD

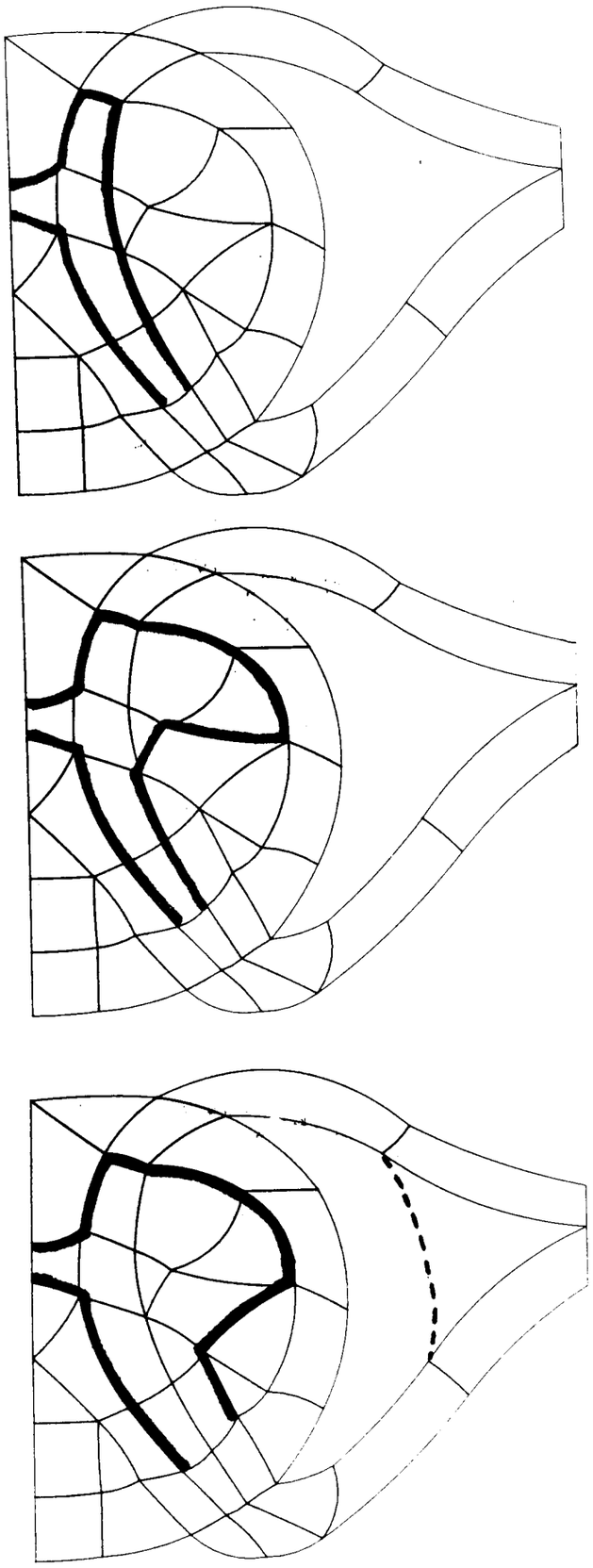

(a) T6

(b) C6

(c) L3

FIGURE 6.5 VARIATIONS OF SIZE OF GREY MATTER AT DIFFERENT LEVEL OF THE SPINAL CORD

tomography (CT) scans. (*) The other sources are anthropometric data (DAMON and STOUDT,1963; HASLEGRAVE,1979,1980; STOUAT,1981; WHITE,1979). CT scans have also been used to determine the shapes , dimensions and relative positions of vertebral column, vertebral canal and the spinal cord.

Note that all dimensions are the average values of male and female. CT scans show that, in general, there is no significant differences concerning the sizes of vertebral column and spinal cord. The differences lie in the dimensions and shape(!) of the outer thorax which can easily be adjusted if required.

The second change is that the orientations of the spinal roots are moved back to a lateral position.

6.2.3 Numbering System in the Mesh

There are 1287 solid elements and eleven element layers in the structure, and the total number of nodes including mid-side and mid-plane nodes are 5172.

As there are eleven layers in the prismatic model, the numbers of transverse (X-Y) planes are 12. A detailed node numbering scheme of the first plane is shown in Figures 6.6-6.11. The scheme is to assign node numbers to all corner nodes within one plane before defining the mid-side nodes. Thus node numbers 1 to 108 refer to corner points, while 109 to 332 represent mid-side nodes. The

---

(*) 8 male and 7 female. Northwick Park Hospital, Watford Road, Harrow, Middlesex, England.

next step is to define the 'mid-plane' nodes which are mid-way between the corner nodes of the present plane and that of the next plane. As the total numbers of these mid-plane nodes are the same as the corner nodes, the node numbers are from 333 to 440. The numbering scheme of the whole model can be found in Table 6.1.

TABLE 6.1

element layer	X-Y plane	corner nodes	mid-size nodes	mid-plane nodes	element numbers
1	1st	1-108	109-332	333-440	1-117
2	2nd	441-548	549-772	773-880	118-234
3	3rd	881-988	989-1212	1213-1320	235-351
4	4th	1321-1428	1429-1652	1653-1760	352-468
5	5th	1761-1868	1869-2092	2093-2200	469-585
6	6th	2201-2308	2309-2532	2533-2640	586-702
7	7th	2641-2748	2749-2972	2973-3080	703-819
8	8th	3081-3188	3189-3412	3413-3520	820-936
9	9th	3521-3628	3629-3852	3853-3960	937-1053
10	10th	3961-4068	4069-4292	4293-4400	1054-1170
11	11th	4401-4508	4509-4732	4733-4840	1171-1287
12	12th	4841-4948	4949-5172		

Note that there is a constant of 440 between adjacent nodes in the same z axis. Similarly, there is a constant, 117, between element number in adjacent layers.

The element numbering scheme of the first layer, as shown in Figures 6.12-6.14, contains element numbers 1 to 117. The figures are slightly mis-leading, as the element numbers actually refer to 3-D solid elements, instead of 2-D planes. Nevertheless, using a similar procedure as for the node numbers, the element number for the second layer are,therefore, from 118 to 234, 235 to 351 for the third layer and so on. This scheme is also listed in Table 6.1. The node numbering scheme is intended for ease of extracting a computer solution from an execution run prior to further analysis; while the element numbering scheme is 'indirectly' related to the requirement of core memory during a run.

PAFEC 75 and ANSYS both ultilize the 'frontal solution' algorithm (IRONS, 1970) in the solution routine for solving large problems. The overall computational efficiency of this algorithm, in particular core store requirement, is related to the element data input sequence presented for the solution routine. Details of how the element order is related to memory size must be left for

standard texts (HINTON and OWEN, 1977; CHEUNG and YEO, 1979). It must also be noted that the software packages have pre-processing programs which can be called to resequence these element order so as to reduce storage requirements at the later processing stage. In general, element ordering generated by these pre-processors has a significant improvement over the original element order.

The modified thoracic model has been tried on PAFEC 75 with automatic re-ordering, but the subsequent element order was surprisingly unsatisfactory. Instead , a minimum storage achieved so far is to arrange the elements to be read 'layer by layer' during the solution algorithm. With the numbering system as shown, only an explicit statement is required in the datafile to 'feed' the elements into the solution programs, regardless of the actual order of the elements appearing in the datafile.

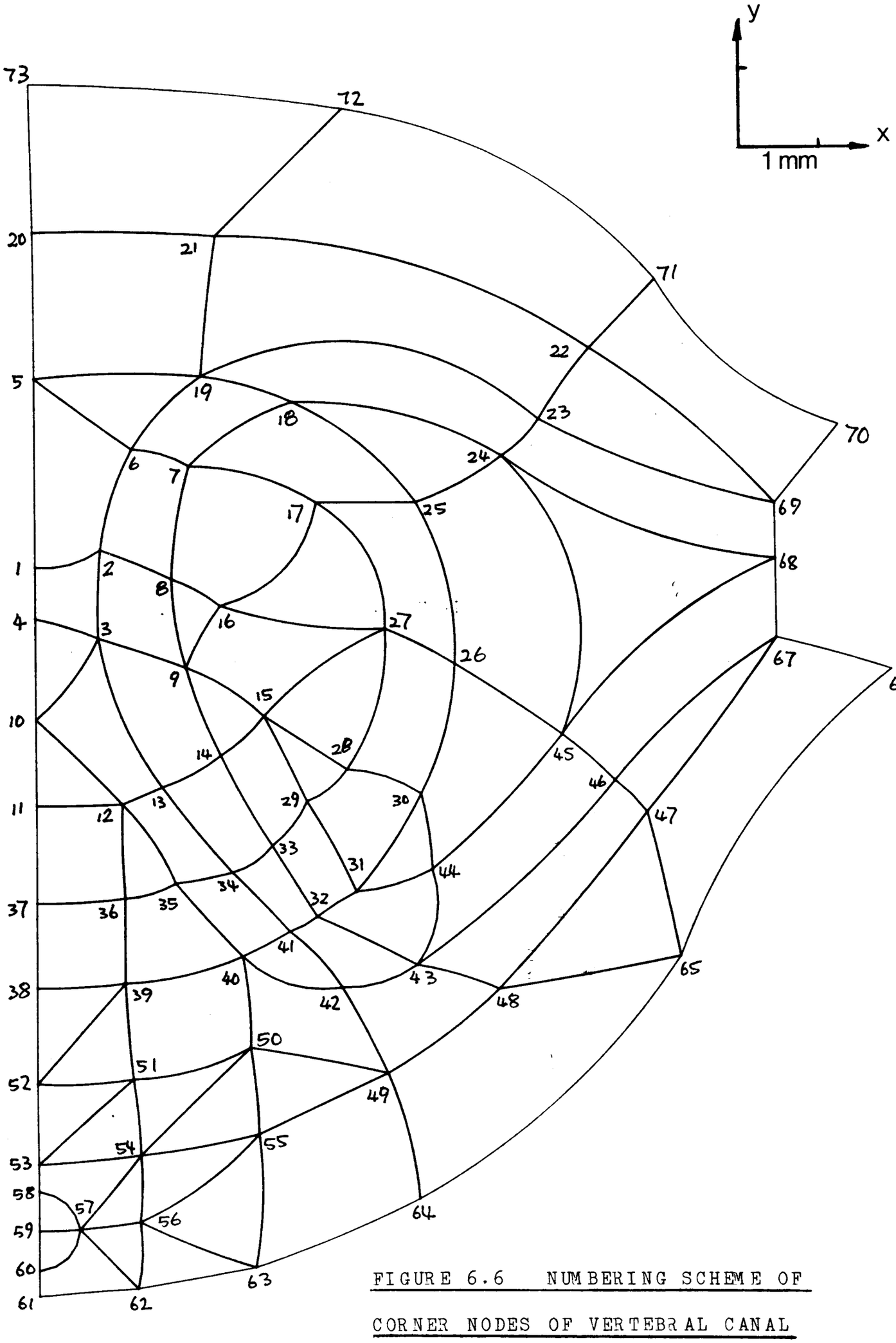

FIGURE 6.6 NUMBERING SCHEME OF CORNER NODES OF VERTEBRAL CANAL

First layer as defined in Table 6.1 sho
See text 6.2.3 for details

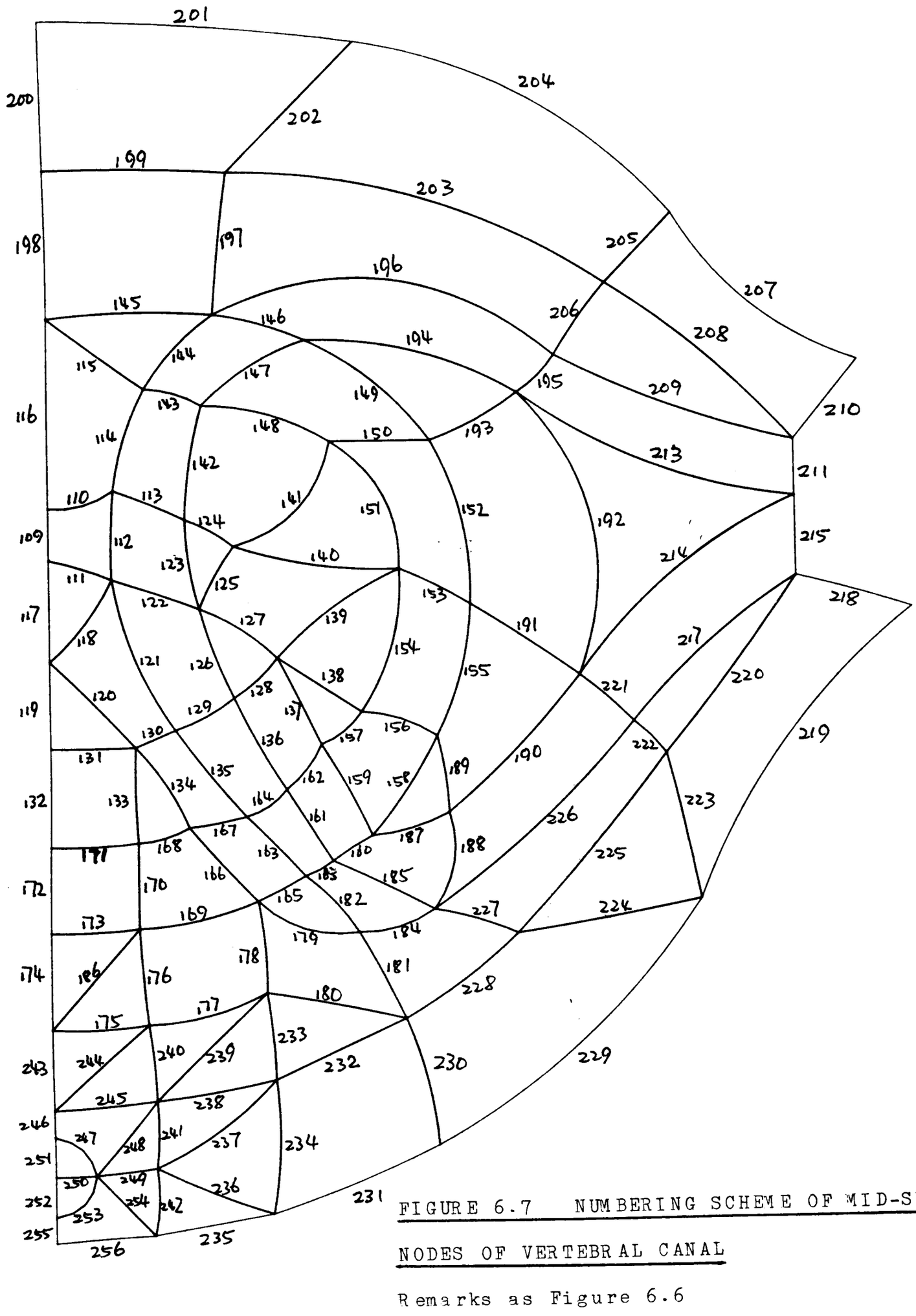

FIGURE 6.7 NUMBERING SCHEME OF MID-SI

NODES OF VERTEBRAL CANAL

Remarks as Figure 6.6

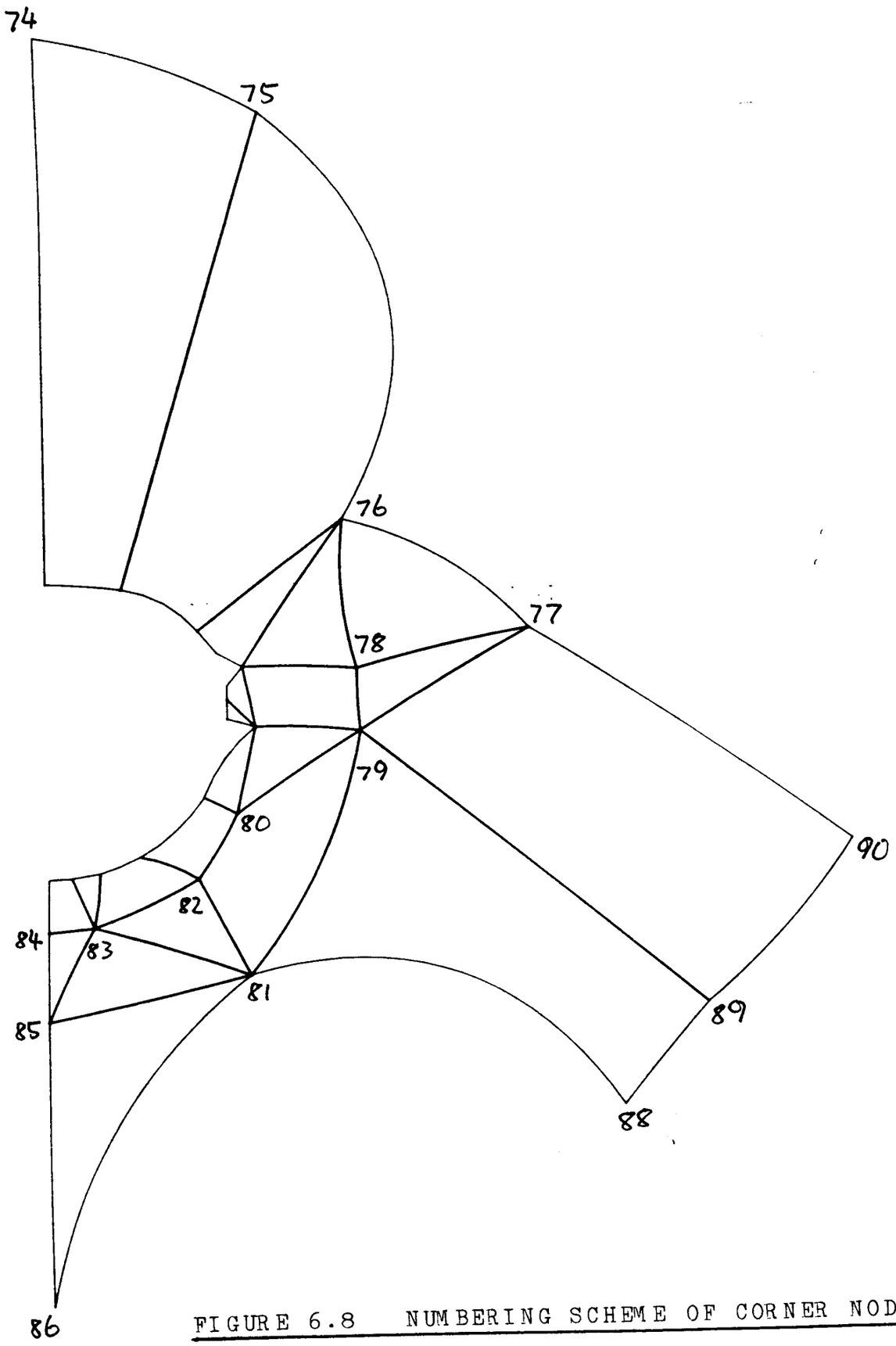

FIGURE 6.8 NUMBERING SCHEME OF CORNER NODES OF VERTEBRAL COLUMN

Remarks as Figure 6.6

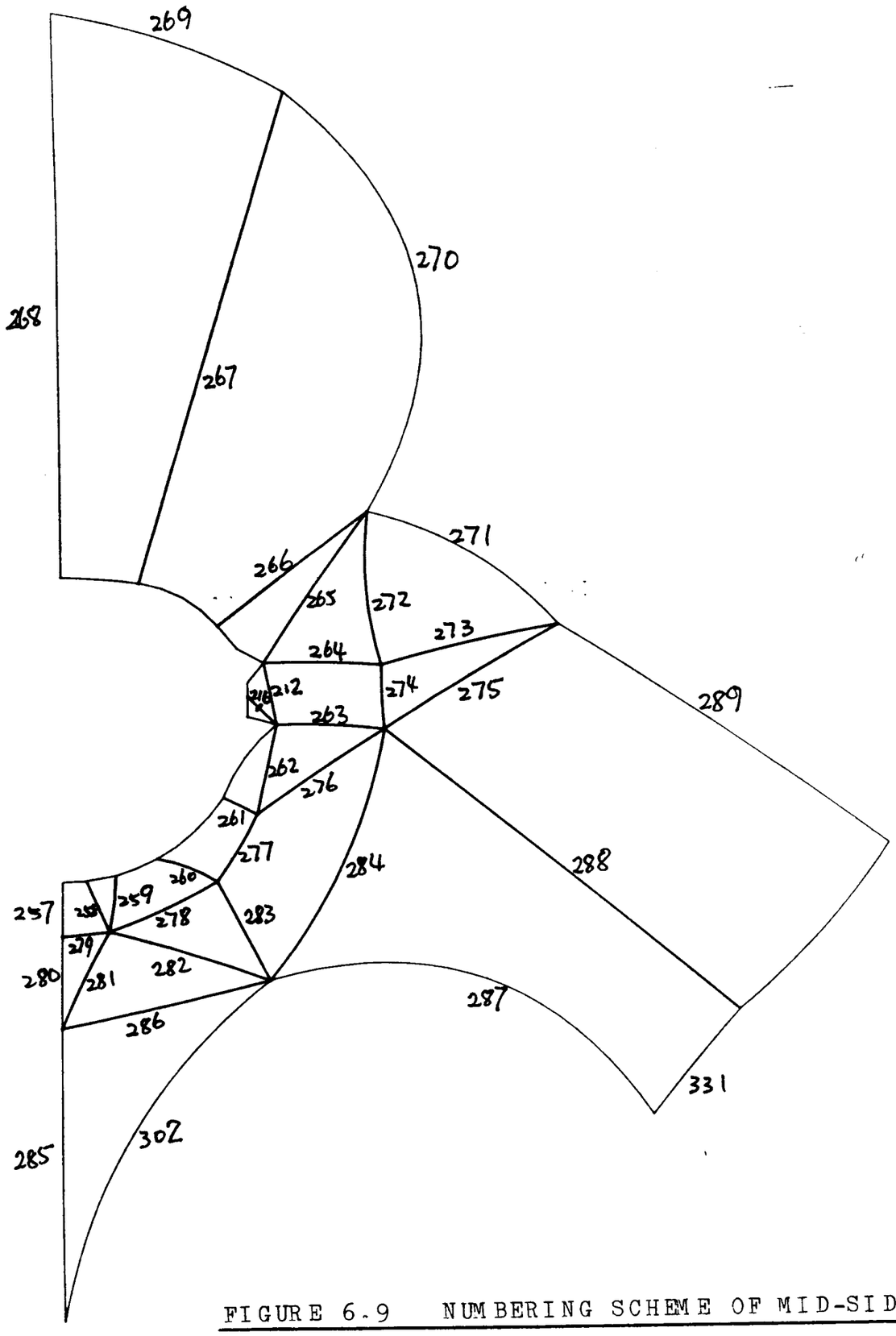

FIGURE 6.9 NUMBERING SCHEME OF MID-SIDE NODES OF VERTEBRAL CANAL

Remarks as Figure 6.6

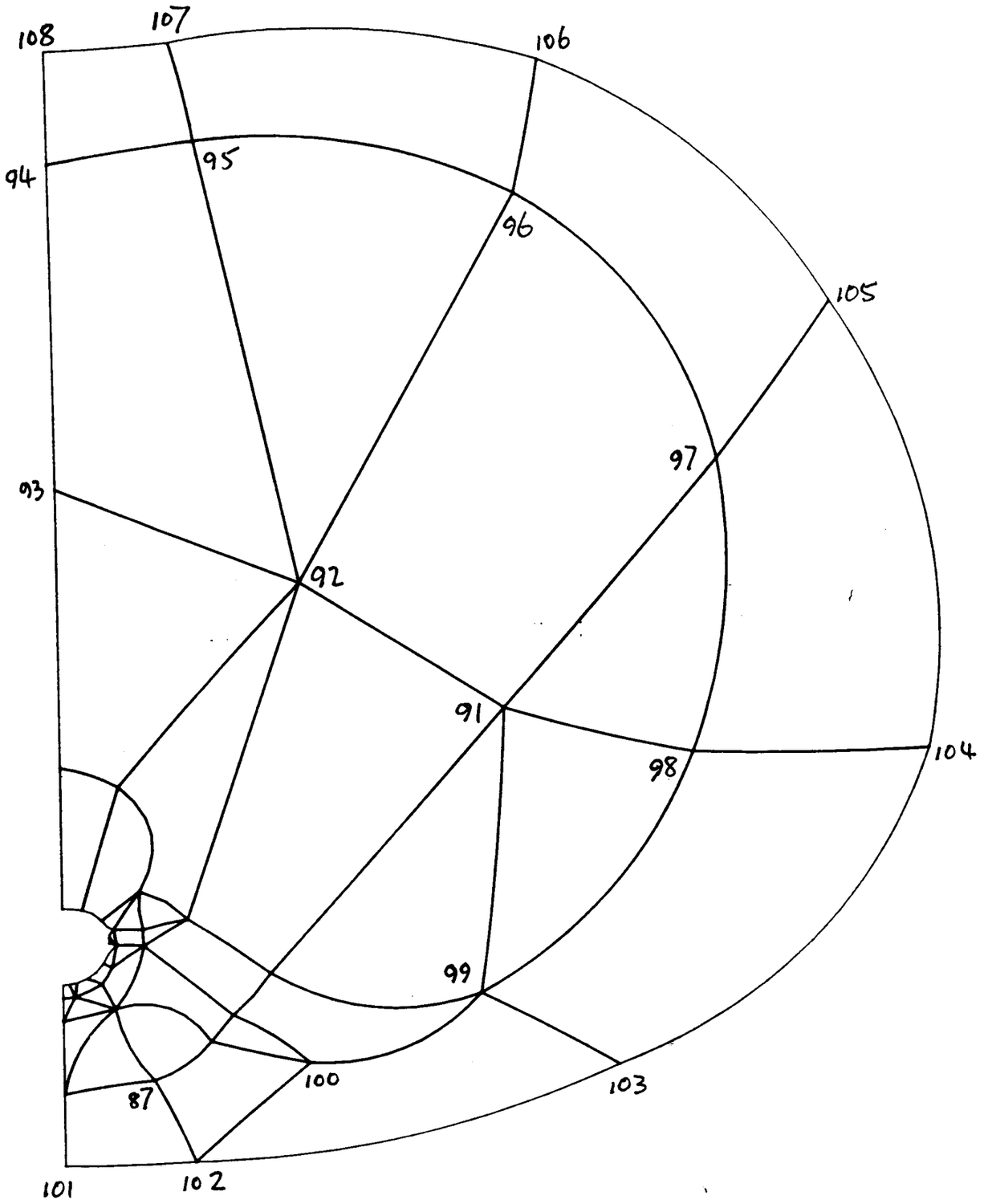

FIGURE 6.10 NUMBERING SCHEME OF CORNER NODES OF THORACIC REGION

Remarks as Figure 6.6

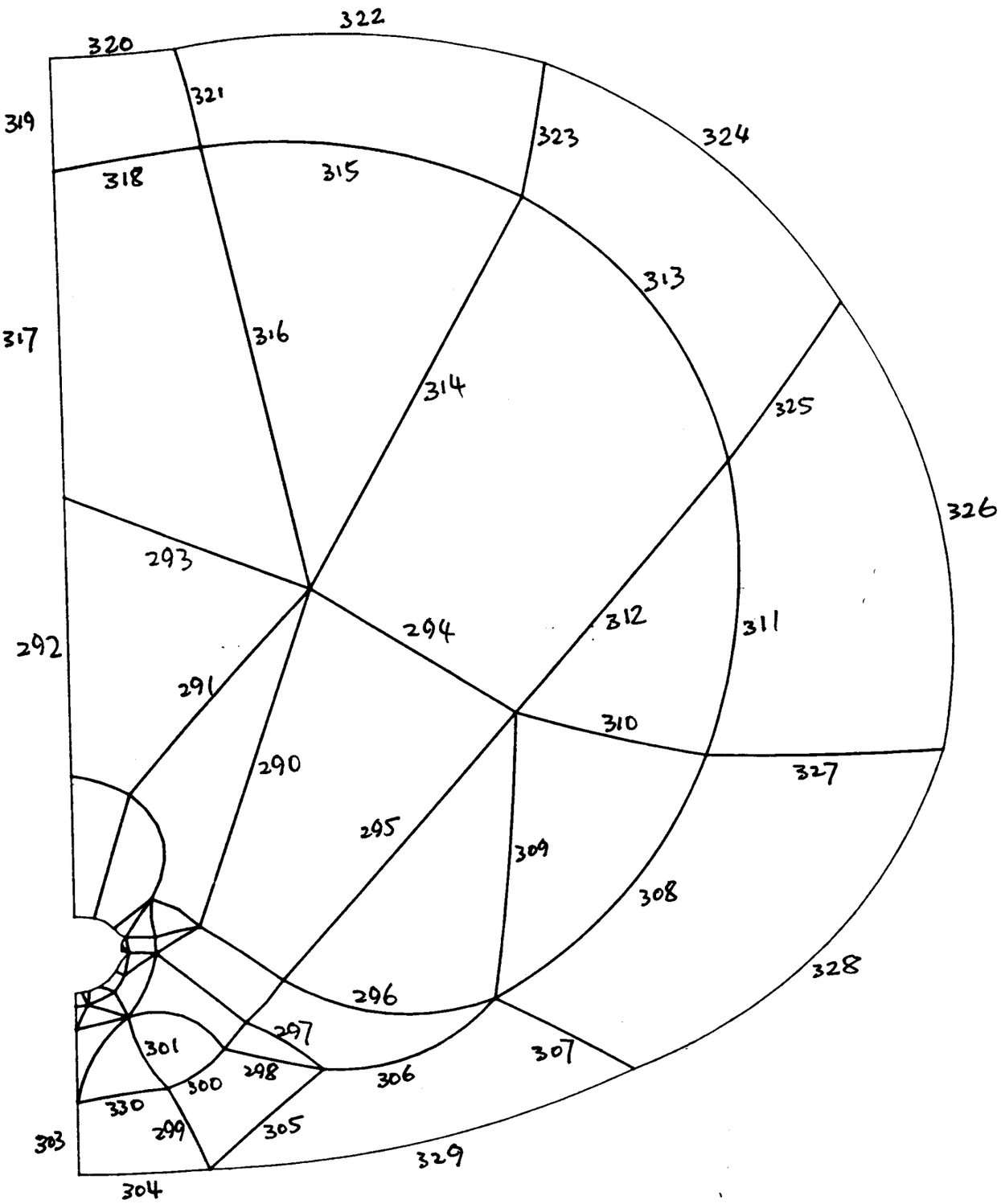

FIGURE 6.11 NUMBERING SCHEME OF MID-SIDE NODES OF THORACIC REGION

Remarks as Figure 6.6

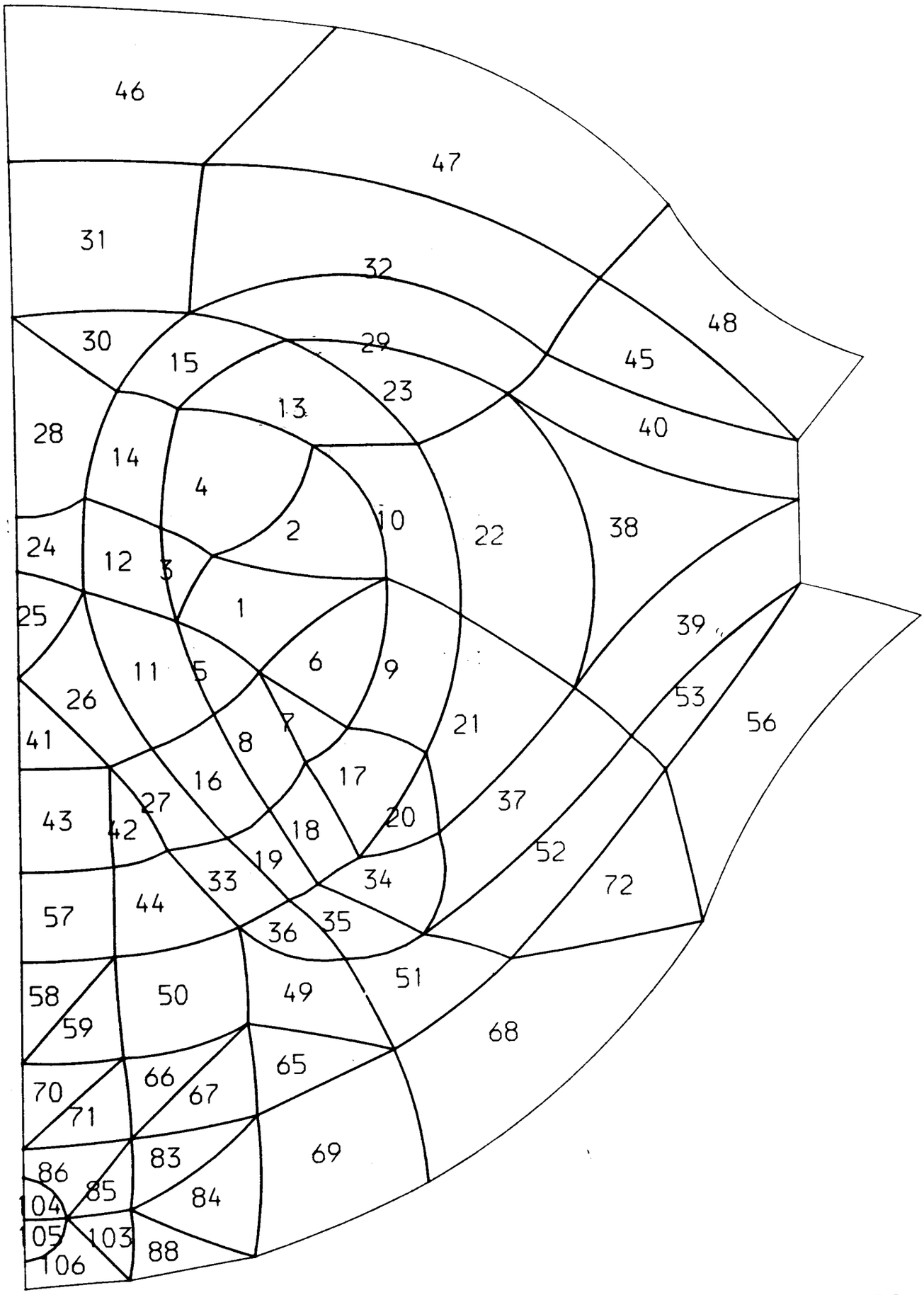

FIGURE 6.12 NUMBERING SCHEME OF ELEMENTS IN VERTEBRAL CANAL

Remarks as Figure 6.6

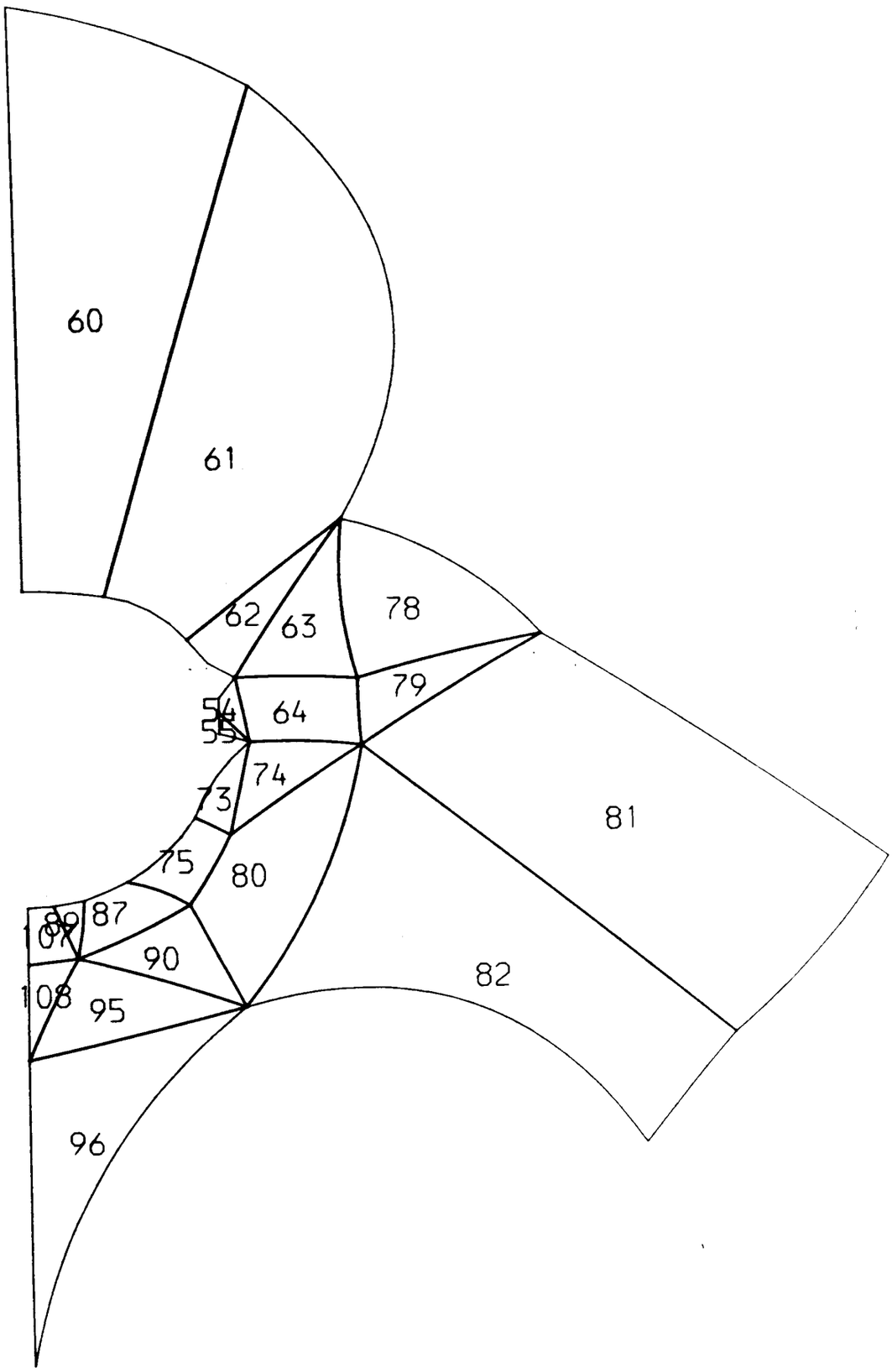

FIGURE 6.13 NUMBERING SCHEME OF ELEMENTS IN VERTEBRAL COLUMN

Remarks as Figure 6.6

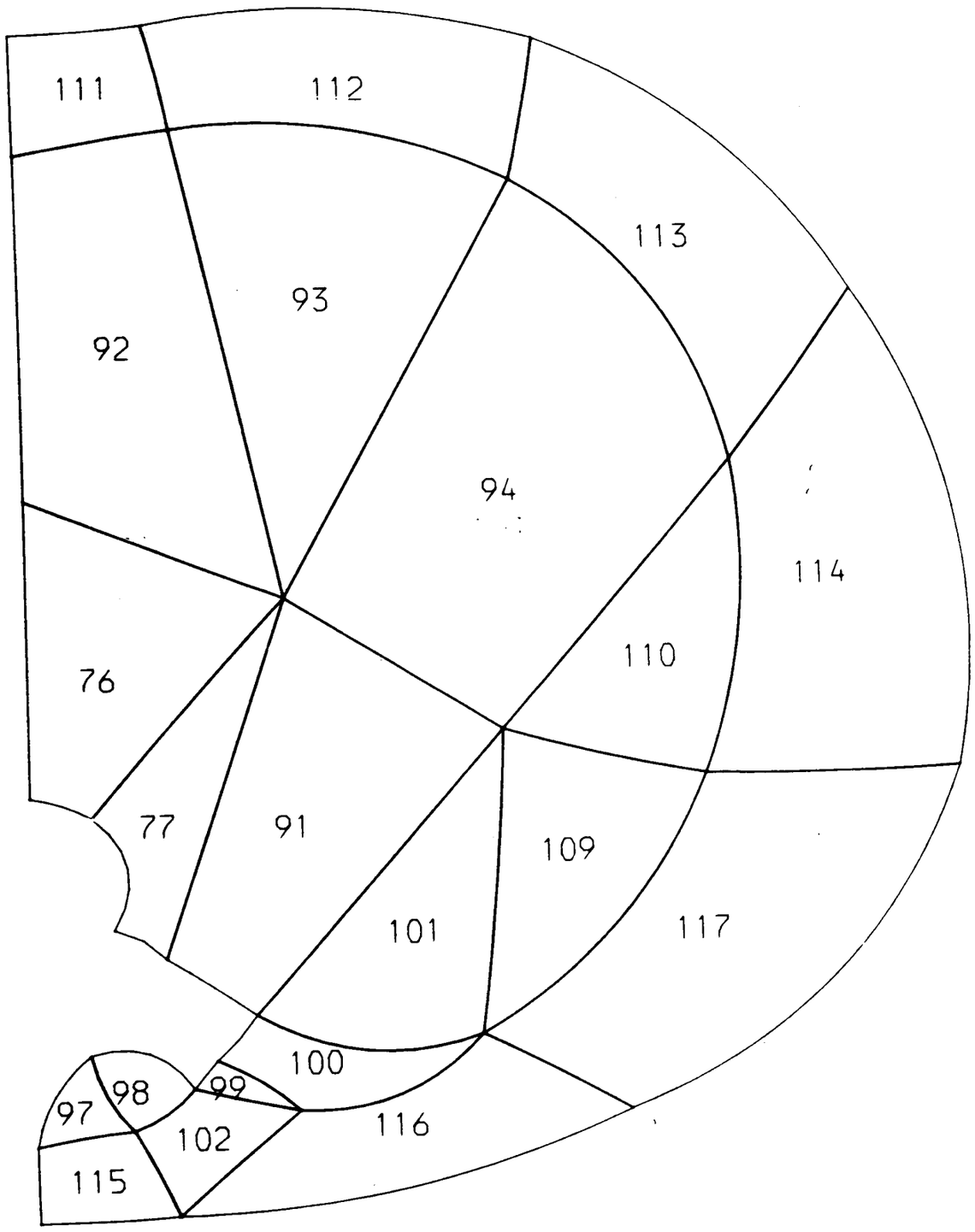

FIGURE 6.14 NUMBERING SCHEME OF ELEMENTS IN THORACIC REGION

Remarks as Figure 6.6

6.3 MODEL TESTING

6.3.1 Homogeneous Volume Conductor Test

The modified model is fully verified against any errors in the datafile. The first full test was a bipolar electrode study (20mm separation) with the entire medium specified as homogeneous. Mirror-image technique as described in Figure 2.1(a) applies, and the height of the model was 110mm. The predicted results are then compared with the theoretical infinite field (exact) solution

$V(r) = \frac{\rho I}{4\pi}\left(\frac{1}{r1} - \frac{1}{r2}\right)$ where r1 and r2 are the distances of point r from electrodes 1 and 2 respectively.

The diamond points in Figure 6.15 are the predicted results plotted along the line on the mid-sagittal plane at the same level of the electrode (in other words, along the y axis at x=0mm and z=10mm). The solid curve is the exact solution. As the source is at y=14.562mm, the theoretical field there tends to infinity. The figure shows that the finite element solution near the electrode is hardly distinguishable from the theoretical solution. It is only within $\pm$ 1mm from the point source that discontinuities are evident.

Another similar check is a plot of potentials vertically (z values) through node 52. The results, as shown in Figure 6.16, are in very good agreement with the exact solution (solid line). Errors due to truncation are also insignificant in the vicinity of the electrode (less

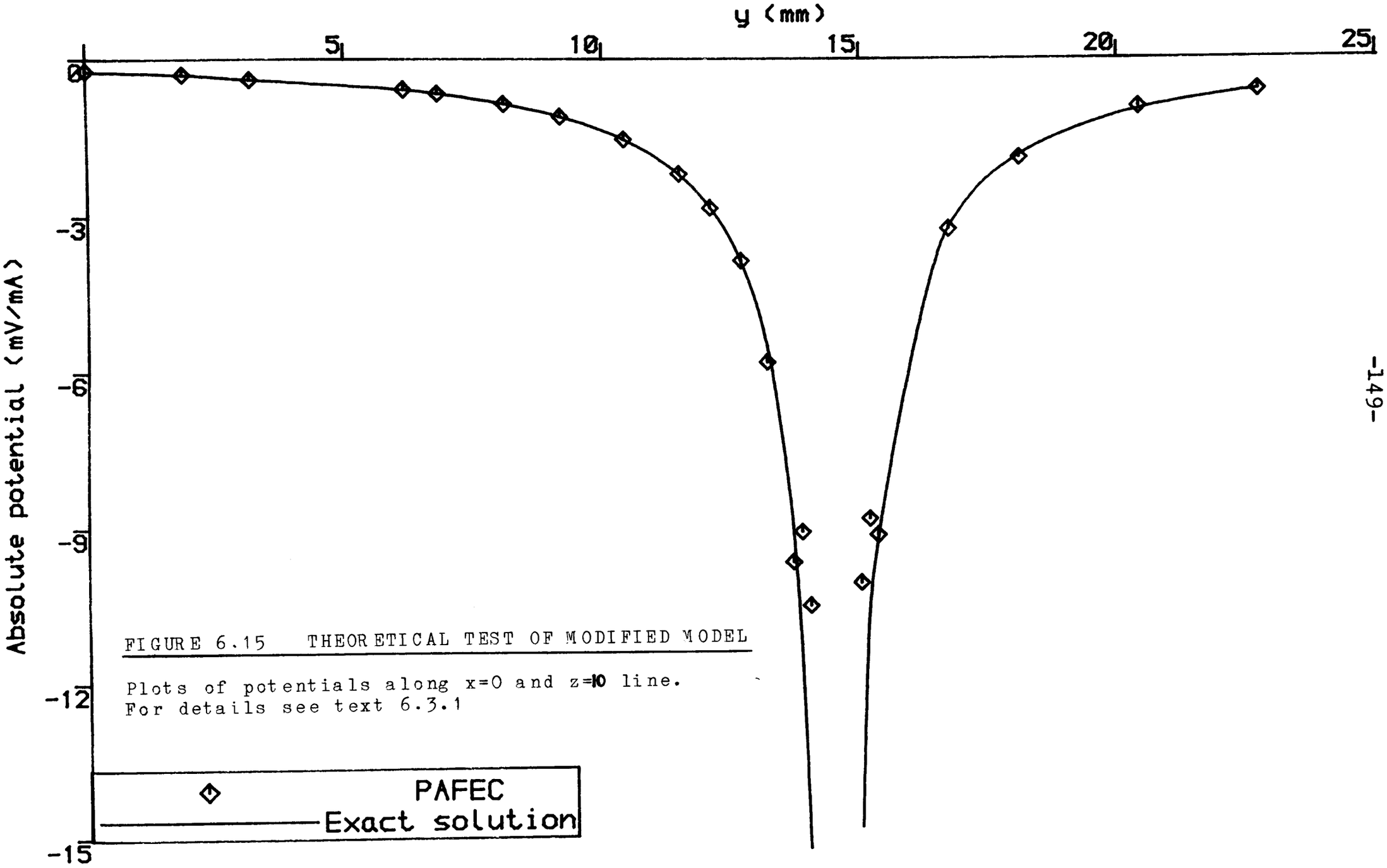

FIGURE 6.15 THEORETICAL TEST OF MODIFIED MODEL

Plots of potentials along x=0 and z=10 line.
For details see text 6.3.1

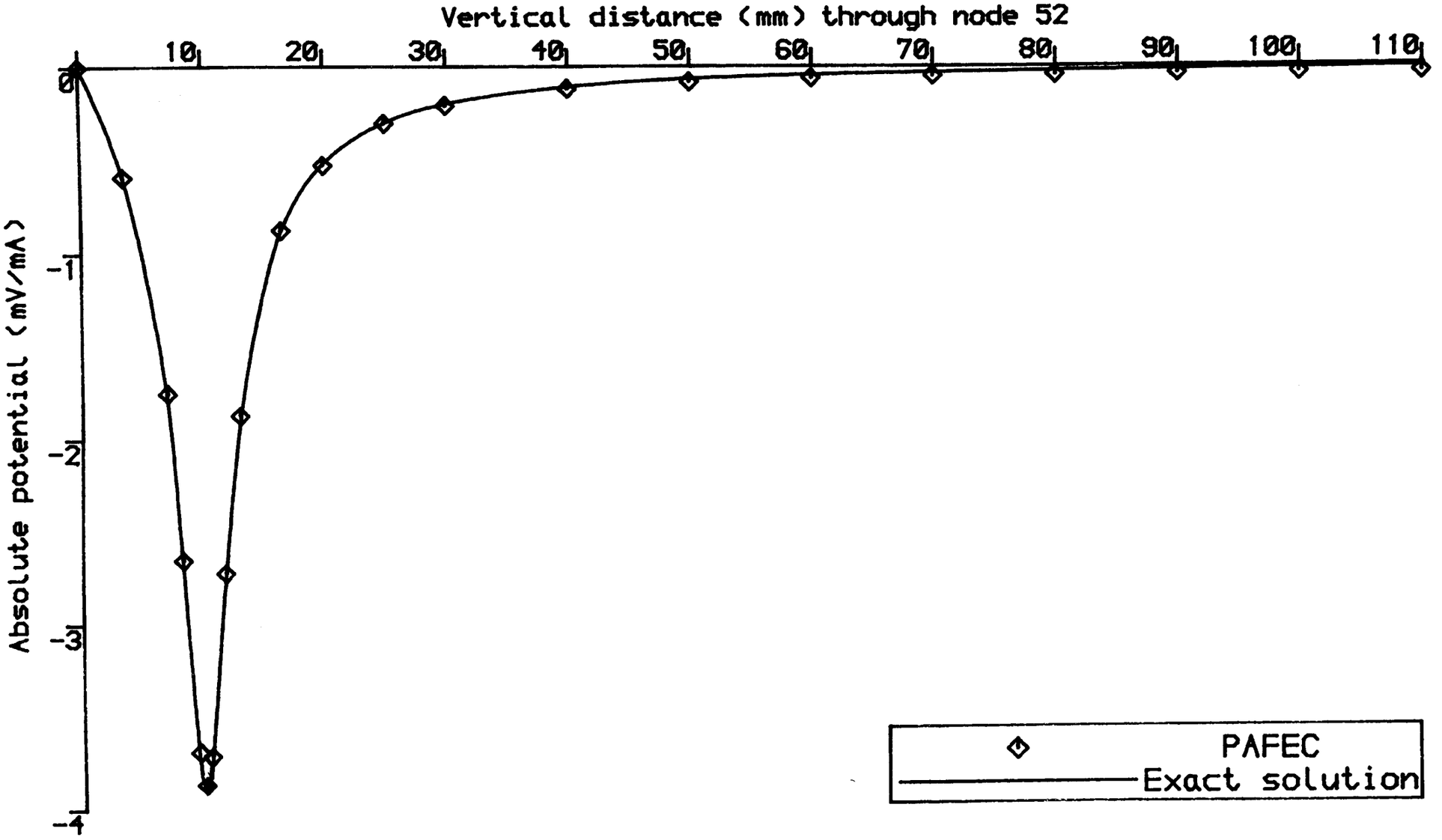

FIGURE 6.16 THEORETICAL TEST OF MODIFIED MODEL

See text 6.3 1 for details

than 40mm on the figure, say), although at the top boundary (100mm), these errors are just visible.

6.3.2 Monopolar Epidural Test

The next check was to model monopolar epidural stimulation using the full set of different tissue resistivities. A total of three jobs were run, and the tissue values corresponded to run numbers (1), (2) and (5) in Table 5.1. The model configuration was the same as the one shown in Figure 2.1(b), representing one-quarter of the whole domain. Cathodic current was applied at a single point in the epidural space (node 59), while the stimulating indifferent was on the ventral surface at the same level as the cathode.

The epidural potentials through node 59 are plotted in Figure 6.17 as solid curves. All potentials are relative to a value at the top boundary, regarding as the recording indifferent. The three curves exhibit smooth characteristics , despite the fact that the feature of PAFBLOCK for localised finer meshing in PAFEC was not used. The three dotted curves are the corresponding computer solutions from the earlier mesh reproduced from Figures 5.16 for comparison.

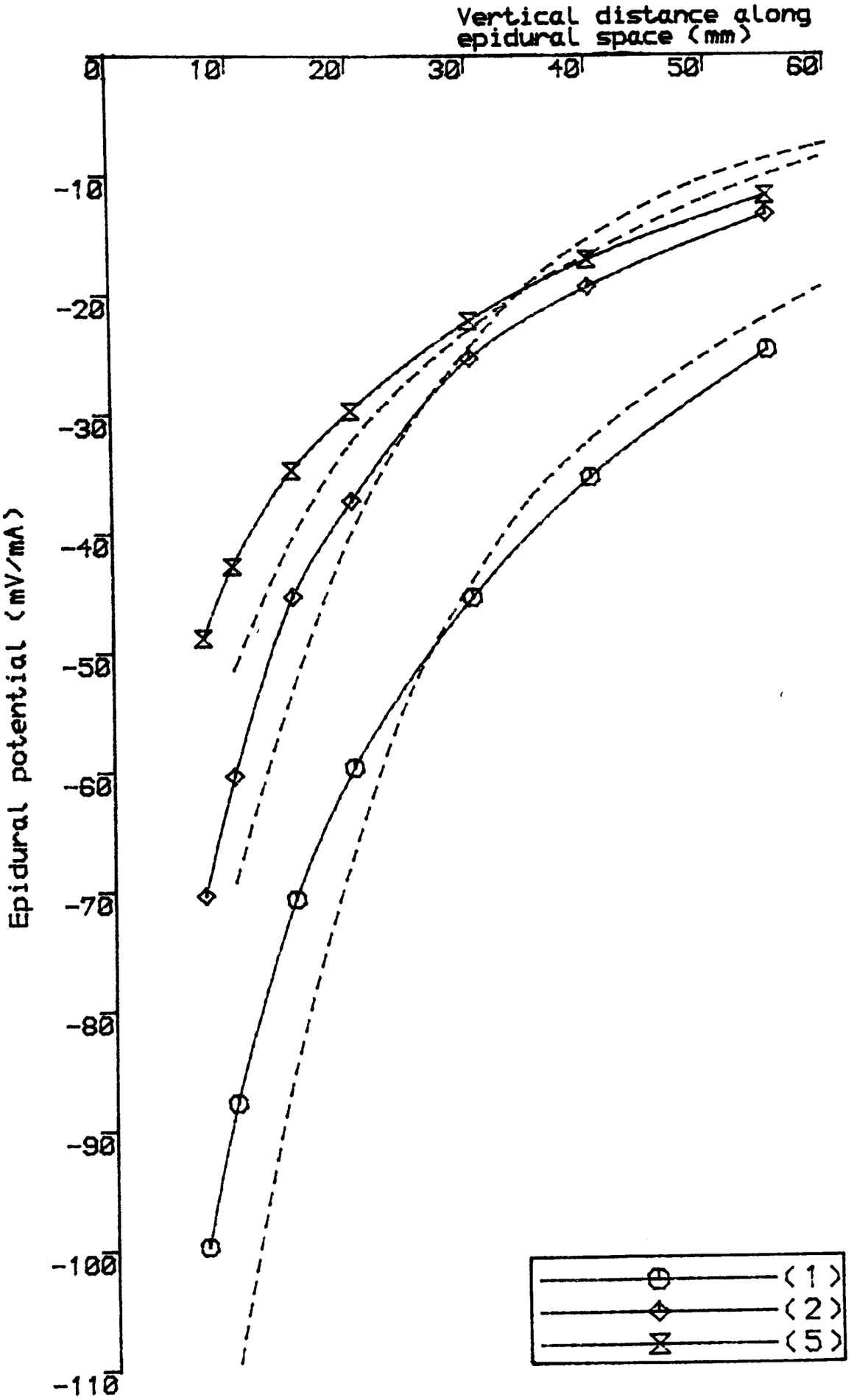

FIGURE 6.17 COMPARISONS OF THEORETICAL SOLUTIONS WITH ORIGINAL 3-D PAFEC MODEL

For details see text 6.3.2

CHAPTER 7

THEORETICAL ANALYSIS OF MYELINATED NERVE FIBRE MODEL

7.1 INTRODUCTION

The finite element analyses described in Chapters 2-6 are only a means of evaluating stimulus fields in the domain of interest. The biophysical interpretation of these fields still depends on the modelling of neuronal elements concerned in the spinal cord. This chapter is the analysis, by modelling, of one such element : the myelinated nerve fibre proposed by McNEAL (1976).

The first part of the chapter describes the formulation of the fibre model and the methods of solution. It is then followed by a theoretical analysis of the model , and the chapter ends with analyses of two possible applications of the model.

The myelinated axon, with its localised nodes of active membrane, lends itself well to lumped circuit models. Figure 7.1 shows a few examples of axon representations The behaviour of the fibre in some cases can be solved analytically (RASHEVSKY,1960; PICKARD,1966; BELL,1981). With the development of digital computer and the need of realistic field modelling. numerical methods now seem to be inevitable.

A straightforward modelling of the fibre is to

(a)

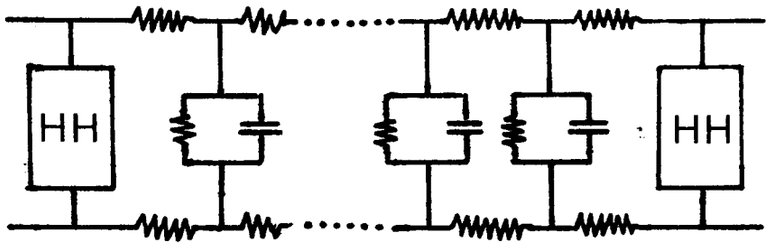

(b)

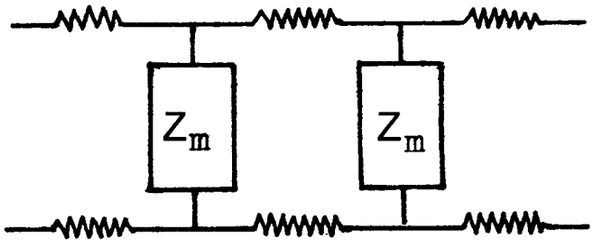

(c)

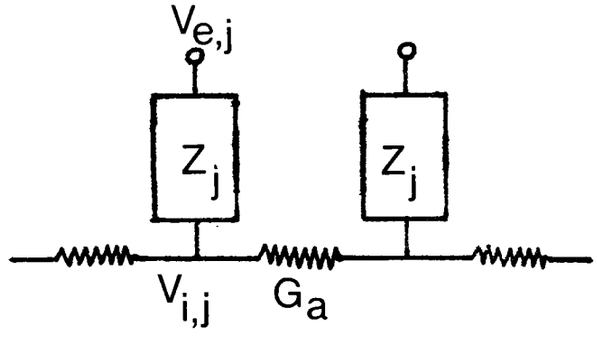

FIGURE 7.1 ELECTRICAL CIRCUIT MODELS OF MYELINATED AXON

(a) HH indicates HODGKIN-HUXLEY membrane model at node of Ranvier (FITZHUGH,1962)
(b) Zm is impedance of node of Ranvier (BeMENT & RANCK,1969b)
(c) Zj is nodal membrane impedance (McNEAL,1976)

consider the myelin sheath as a linear distributed leaky cable. represented by the cable differential equations. The excitable membranes at the nodes of Ranvier can be described by the HODGKIN and HUXLEY (1952) set of ordinary differential equations. This model, shown in Figure 7.1(a), was adopted by FITZHUGH (1962) to study the propagation of action potentials. This approach has proved very popular (GOLDMAN and ALBUS,1968; KOLES and RASMINSKY,1972; BRILL et al,1977) although a further set of equations by FRANKENHAEUSER and HUXLEY (1964) were used by those groups to represent the excitable membranes. A major drawback of the model, however, is that stimulus current has to be applied directly at the nodes to initiate action potential. In regard to the type of electrical stimulation involved by epidural electrodes, a model that can take account of remote stimulation is desirable. Another drawback is that the modelling of leaky sheath involves a high demand on computer time.

BeMENT and RANCK (1969b) and BEAN (in the appendix of ABZUG et al ,1974) simplified the axon by assuming the myelin as perfect insulator (Figure 7.1(b)). The relationship of threshold current-electrode position was derived by the latter author. The solutions, however, were limited to current pulses of infinite duration.

An even more simplified model proposed by McNEAL (1976) can be used for predicting threshold current of a fibre subjected to any known stimulus field and duration time. As shown in Figure 7.1(c), the external network is

omitted: instead the external potentials. Ve, at the nodes of Ranvier are now determined solely by the stimulus field. That is to say, the stimulus field becomes the system input, which may be a function of both the electrode configurations and time. This approach is particular useful as a stimulus field to be applied can be first determined from finite element analysis. The requirement for the model is to define the path taken by the fibre of interest through a field and to note the potentials at intervals along that path corresponding to the internodal spacing.

7.2 QUALITATIVE DESCRIPTION OF FIBRE MODEL

7.2.1 Fundamental Formulation of Model

The network representation has been illustrated in Fig. 7.1(c). Essentially, the myelin is assumed to be a perfect insulator. The diameter of the axon is considered to be so small that the external potential, Ve.j, around any node j is constant. Lumped impedance Zj described the excitable membrane at each node, while a linear conductance, Ga, represents each internodal axoplasm.

Following the general method of COBURN (1981), the system equations governing the rate of change of membrane depolarisation, $\dot{E}$, can be written in conventional matrix state-variable notation :

$$\tau_2 \dot{\underline{E}} = [A]\underline{E} + \frac{1}{Ga}[U]\underline{Ii} + [F]\underline{Ve} \qquad (7.1)$$

where $\underline{E}$= column vector of membrane depolarisation,

$\underline{Ii}$= column vector of membrane current

$\underline{Ve}$= column vector comprising the potentials in the external medium,

$$\tau_2 = \frac{Cm}{Ga}$$

[A], [U] & [F] are square matrices. Their appropriate values and the derivation of equation 7.1 are given in Appendix 3.

7.2.2 Subthreshold Steady-state Analysis

For subthreshold treatment on the whole model, Gm,j at node j is a constant. The membrane current $Ii.j$ at that node can then be described by $Ii,j=Gm,j*Ej$. Assuming Gm is the same for all the nodes, Eqn.(7.1) becomes

$$\tau_2 \dot{\underline{E}} = [A]\underline{E} + \frac{Gm}{Ga}[U]\underline{E} + [F]\underline{Ve}$$

The system can further be simplified into

$$\tau_2 \dot{\underline{E}} = [C]\underline{E} + [F]\underline{Ve} \quad \text{where} \qquad (7.2)$$

$$[C] = [A] + \frac{Gm}{Ga}[U] \text{ , called the system matrix}$$

and $[F]$ is the distribution matrix.

For a step input of Ve, the steady-state solution of E is given by

$$\underline{E}_{t\to\infty} = -[C]^{-1}[F]\underline{Ve} \qquad (7.3)$$

By taking 15mV as the threshold criterion, threshold current for any specified fibre system subjected to an applied field of infinite duration can be predicted.

The simplicity of Eqn.(7.3) is worthwhile as only simple matrix manipulations are involved. The single mathematical expression (7.3) contains all the system information :

a) orientation and type of fibre ,

b) stimulating field from any electrode configuration and

c) fibre terminals

Another advantage of the steady-state analysis is that the sites of excitation on the fibre can be found without a full fibre simulation. These sites are trivial only for straight myelinated fibre subjected to simple stimulating field. When complicated electrode systems are involved or/and the fibre systems have bends or branches in their paths, these sites will be difficult to tell just by inspection.

Equation (7.3) will be used intensively in Sections 7.3 and 7.4. All the subsequent equations were written in BASIC computer language and run on the local interactive Honeywell 68 DPS MULTICS system.

7.2.3 Analysis Involving Active Membrane

For near-threshold analysis, the membrane conductance at the excitation node, j say, must be allowed to vary, and accordingly its behaviour is modelled by the Frankenhaeuser and Huxley's (F-H) set of equations (1964). A full digital simulation is then required, although simple Euler integration has proved adequate. Steady-state analysis, along the lines of eqn.(7.3), is not available since the system is unstable at threshold, by definition. The total ionic current (Ii,j) at node j is described by

$$Ii,j = \pi dl(i_{Na} + i_{K} + i_{L} + i_{p}) \qquad (7.4)$$

where the terms on the right are the individual components of ionic current. A summary of the F-H equations can be found in Appendix 13.

Consider node j , the governing equations (A3.1) in Appendix 3 becomes

$$\tau \dot{E}_j = (E_{j-1} - 2E_j + E_{j+1}) - \frac{\pi dl}{Ga}(i_{Na} + i_{K} + i_{L} + i_{p}) + (Ve_{j-1} - 2Ve_j + Ve_{j+1})$$

Basically, the same format of equation (7.1) is used for digital simulation. The difference here being simply the use of non-linear expressions for the ionic current terms. Note now that the full simulation permits the field, Ve, to be a function of time, typically a pulse.

In fact, the values Ve and their duration are the two essential inputs for the simulation process. Note that during the simulation, certain elements in the current vector Ii can be specified either to be linear or non-linear. This can speed up the simulation process as only a few nodes in the fibre are active and need to be specified by non-linear equations.

7.2.4 Boundary Conditions of the Model

The corner elements in the leading diagonal of [A] and [F] are not covered by expression (7.1). The values

of these elements, in fact, depend on the types of fibre endings . Three types of fibre terminals, shown in Fig. 7.2 , are considered :

a) zero depolarisations at the end node and at all nodes beyond the solution set (Figure 7.2(a)). This was also the approach by McNEAL(1976) in his analysis.

b) zero internal axial current at the end node , shown in Fig. 7.2(b) , and

c) actual fibre terminals (Fig. 7.2(c)).

Types (b) and (c) are proposed by COBURN (1981). The mathematical treatment of these terminals related to the corner elements are given in Appendix 4.

7.3 THEORETICAL ASPECTS OF FIBRE MODEL

7.3.1 Total Length of Model

The artifical fibre endings in Section 7.2.4 in fact have certain implications on the behaviour of the external applied fields (COBURN,1981). The zero depolarisation in case(a) implies that the axon must extend into a region where the axial field $-(\partial Ve/\partial x)$ is constant. The zero axial current in case (b) suggests that there should be a constant external potential beyond the fibre endings. The usual way to satisfy the above conditions is to have sufficient number of nodes in the model so that those terminal effects do not have an influence back along the fibre into the region of interest. A consideration of

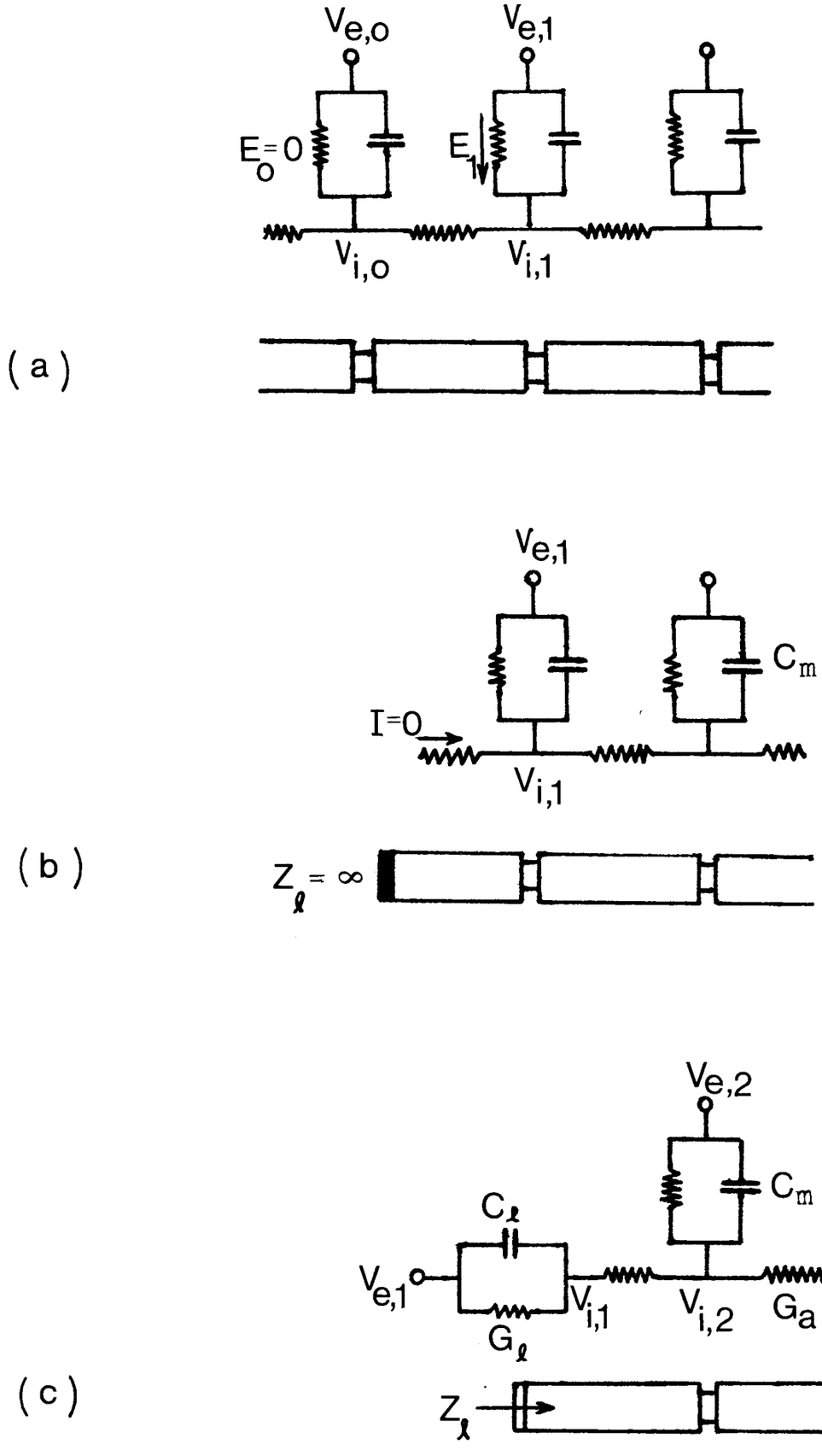

FIGURE 7.2 FIBRE ENDINGS FOR MYELINATED FIBRE MODEL

(a) zero depolarisation, $E_o = 0$
(b) zero internal axial current
(c) actual terminal

cable theory (COBURN,1981) suggested that the boundary effects might gnerally be neglected at distances greater than $3\lambda'$ from the endings, where

λ' = equivalent characteristic length of a myelinated fibre

$$\simeq L\left(\frac{Ga}{Gm}\right)^{\frac{1}{2}}$$

Using the neuron parameters given in Appendix 3 , the number of characteristic lengths in a n-node fibre is $0.69(n+1)$. A model of 19 nodes, say, will have $13.8\lambda'$. Since the results within $3\lambda'$ of either end are neglected , the model is still adequate for monopolar cathodic stimulation, provided that the electrode is close to the central node. On the other hand, there are cases when a longer fibre model is required, for example .

(a) a remote electrode position resulting a very flat potential profile with poor localisation of effect in the central region of a model fibre length, or

(b) anodic stimulation where the region of interest are usually on either side of the node closest to the electrode extending towards the terminals, or

(c) different electrode configurations where many nodes may become active simultaneously.

7.3.2 Omission of External Pathways

The discussion of the fibre endings is in fact only

one limitation of the model, implying a requirement of minimum fibre length. This can usually be overcome by using a long fibre, although the demand on computer time will increase. There is a more fundamental limitation in the model : the lack of external pathways in the extracellular fluid.

With reference to Figure 7.1(c), there is no external network communicating among the nodes of Ranvier. Local circuits (HODGKIN,1965) therefore do not exist and consequently, any action potential that would have been generated cannot propagate. This limitation is justified when the model is used for subthreshold analysis and, to some extent, threshold prediction. However, further theoretical analysis using the present axon model, for example the investigations on action potential propagation and in particular the action of stimulus field on oncoming action potentials will be hindered. Chapter 9 is therefore devoted to the developments of models which incorporate the external conducting path.

7.3.3 Effective Driving Function and Fibre Diameter

Neglecting end conditions, the rate of change of membrane depolarisation, $\dot{\underline{E}}$, in expression (7.1) depends solely on the vector $\underline{Ve}$. In other words, $\dot{\underline{E}}$ depends on the external potential profile seen by the nodes of the fibre. Note that $\underline{Ii,j}$ in expression (7.4) is also a function of $\underline{E}$. $\underline{Ve}$, the system input, will depend on

(a) the track of the axon

(b) the configuration of electrode system and

(c) the electrode current as a function of time

Consider node j in the model , the equation describing the nodal behaviour is recalled from Appendix 3 as

$$\tau_2 \dot{E}_j = (E_{j-1} - 2E_j + E_{j+1}) - \frac{1}{G_a} I_{i,j} + (Ve_{j-1} - 2Ve_j + Ve_{j+1})$$

It can be seen that Ej is "driven" by ($Ve_{j-1} - 2Ve_j + Ve_{j+1}$). The latter, arbitrarily called the "effective driving function", is a discrete approximate to $L^2(\partial^2 V / \partial X^2)$ where x is the distance measured along the axon path. For a straight fibre, it is clear that the sharpness of a voltage maximum or minimum determine the membrane behaviour. It is also important to note that sharp turns in the path of the fibre itself can be equally influential.

With reference to the coefficients associated in eqn.(7.1), τ_2 is only a ratio and the fibre diameter terms are cancelled. The diameter on the Ga term ($\pi d^2 /(4 \rho_i L)$) will be cancelled too when the proper ionic current terms are substituted. Matrices [A]. [U] and [F] do not bear any relation with fibre diameter. It is through the Ve term that the influence of fibre diameter on membrane behaviour finally comes into play. For different fibre diameters, the internodal spacing will be different and the driving function (Ve,j-1 -2Ve.j +Ve.j+1) will be different too.

In order to investigate the significance of driving

function, a simple subthreshold steady-state analysis was carried out. The testing scheme is shown in Fig. 7.3. where a 39-node straight fibre was considered to be immersed in a homogeneous isotropic infinite medium of 300 ohm-cm resistivity. A theoretical point electrode stimulated the fibre at a distance y mm above node 20. The stimuli was a cathodic pulse of infinite duration and 0.1 mA amplitude.

Figure 7.4 shows the variation of depolarisation at node 20 with the driving function for three different electrode distances. The left hand end of each curve corresponds to the lowest fibre diameter of each range, approximate 1μm, the right hand end corresponds to 20μm fibre diameters. Each curve represents fibres of different diameters being stimulated by the same field. The x-axis therefore represents the "driving function" arising from the same field 'seen' by different fibre diameters. The y-axis is the corresponding depolarisation value at node 20 where the driving function is greatest.

A different presentation of the same results is shown in Fig. 7.5. Each curve represents the results from one fibre diameter stimulated by different fields, arising from a range of electrode distances $1mm \leqslant y \leqslant 5mm$. The left hand end of each curve corresponds to the furthest electrode distance, approximate 5mm, while the upper extremes relate to y=1mm.

In general, both figures show that depolarisation is closely related to the driving function, i.e. the product

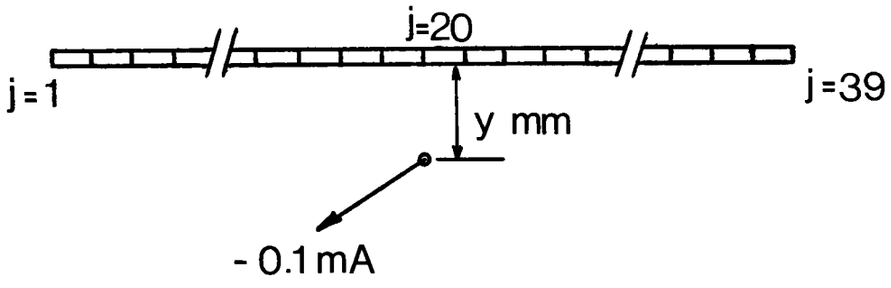

FIGURE 7.3 TESTING SCHEME OF EFFECT OF FIBRE DIAMETER AND ELECTRODE DISTANCE ON DEPOLARISATION AT NODE 20

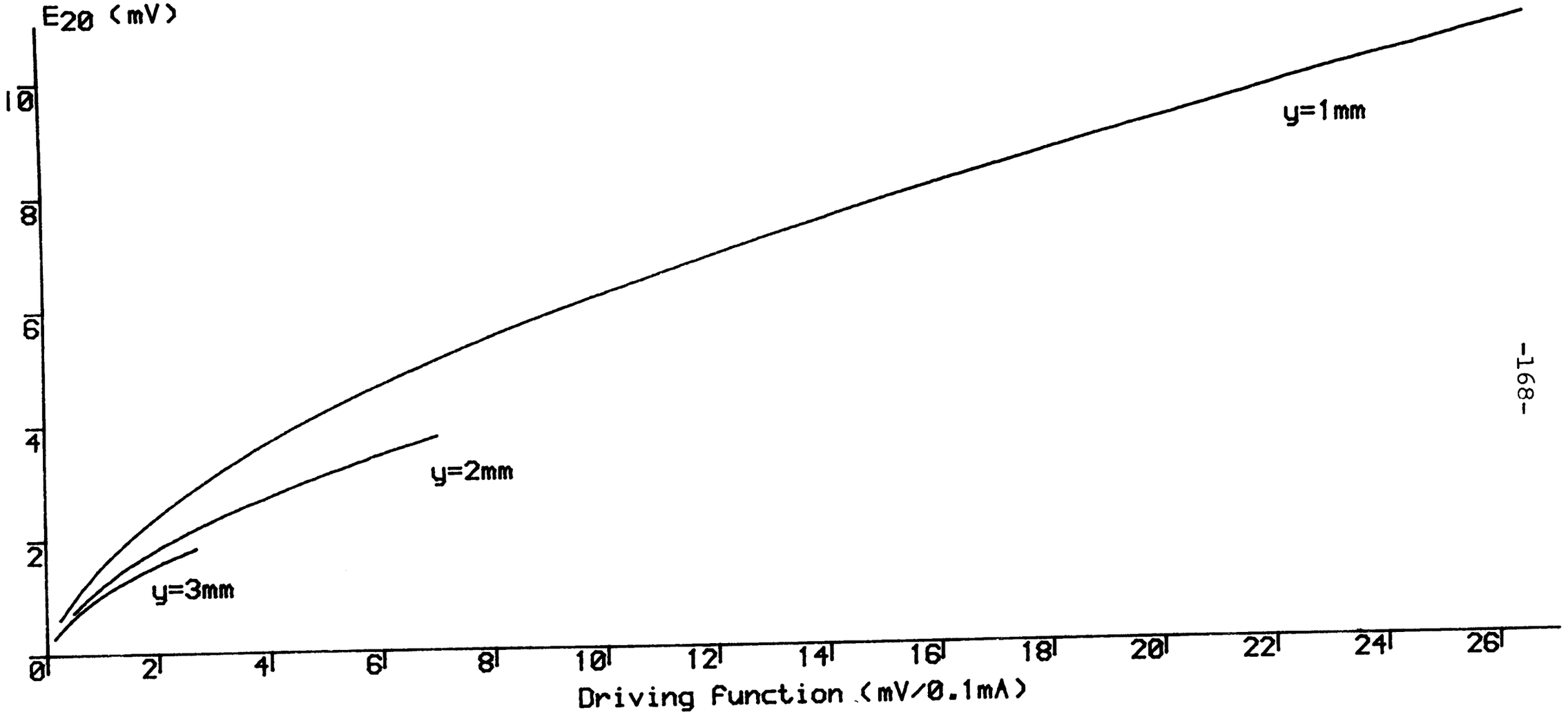

FIGURE 7.4 VARIATION OF DEPOLARISATION AT NODE 20 WITH DRIVING FUNCTION

y is electrode distance. For details see text 7.3.3

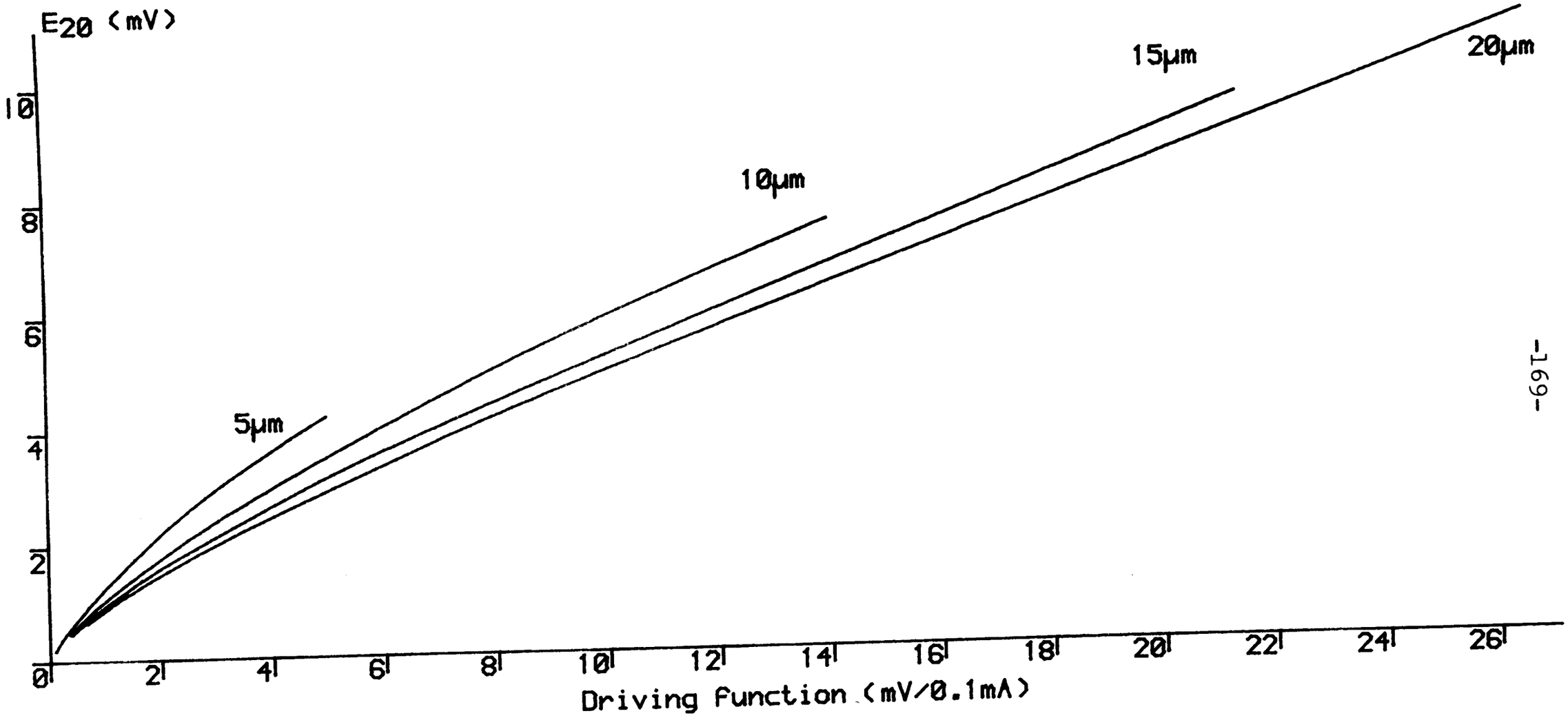

FIGURE 7.5 VARIATION OF DEPOLARISATION AT NODE 20 WITH DRIVING FUNCTION

For details see text 7.3.3

of the square of the internodal space. L^2, and the second derivative of the external potential along the fibre.

7.4 FURTHER APPLICATIONS OF THE MODEL

7.4.1 Fibre Bending

The analyses so far concentrated only on the long straight fibre, and the ascending fibres in the dorsal column of the spinal cord is one obvious area of application. The model, in fact, can be used to represent other types of fibres, and one example is the fibres in the medial bundles of dorsal roots.

After emerging from the root, they move across the funiculus and some of them bend upwards to form the ascending fibres in the dorsal column. A change in the fibre orientation, caused by the bending, will result a change in the external potentials seen by the nodes of Ranvier. This change in Ve, according to the discussion in section 7.3.3, should affect the fibre depolarisation.

The theoretical scheme, seen in Figure 7.6(a), was intented to investigate the effects of bending angle ϕ and electrode distance on depolarisation at node 20. The conditions were the same as the straight fibre in section 7.3.3, with the exception that half of the present fibre was allowed to 'turn'. Three fibre diameters (5μm, 10μm and 20μm) and three electrode positions (1mm, 3mm and 5mm from the fibre) were chosen and the results are shown in Figs. 7.6(b)-(d).

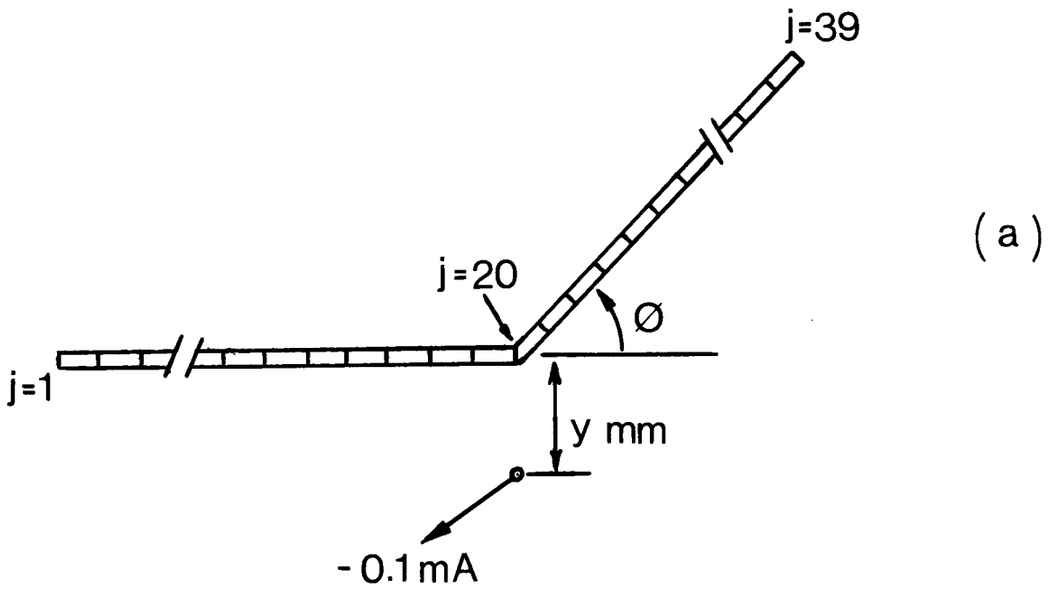

FIGURE 7.6 EFFECT OF FIBRE BENDING ON DEPOLARISATION AT NODE 20

Fibre diameter and electrode distance also vary.
Details see text 7.4.1
(a) testing scheme
(b) 5μm fibre
(c) 10μm fibre
(d) 20μm fibre

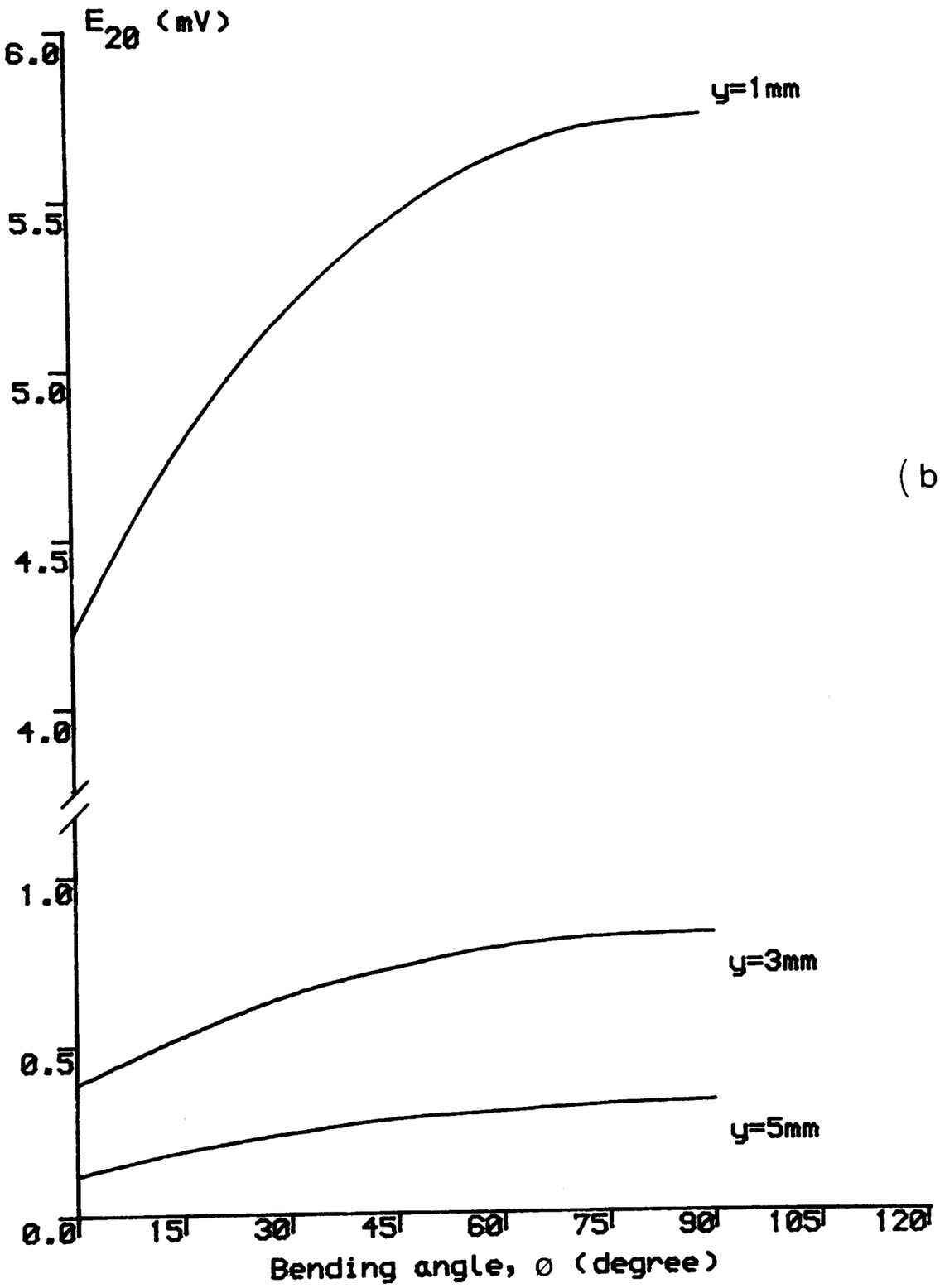
E20 (mV)
6.0
5.5
5.0
4.5
4.0
1.0
0.5
0.0
y=1mm
y=3mm
y=5mm
15
30
45
60
75
90
105
120
Bending angle, ø (degree)

(b) 5μm

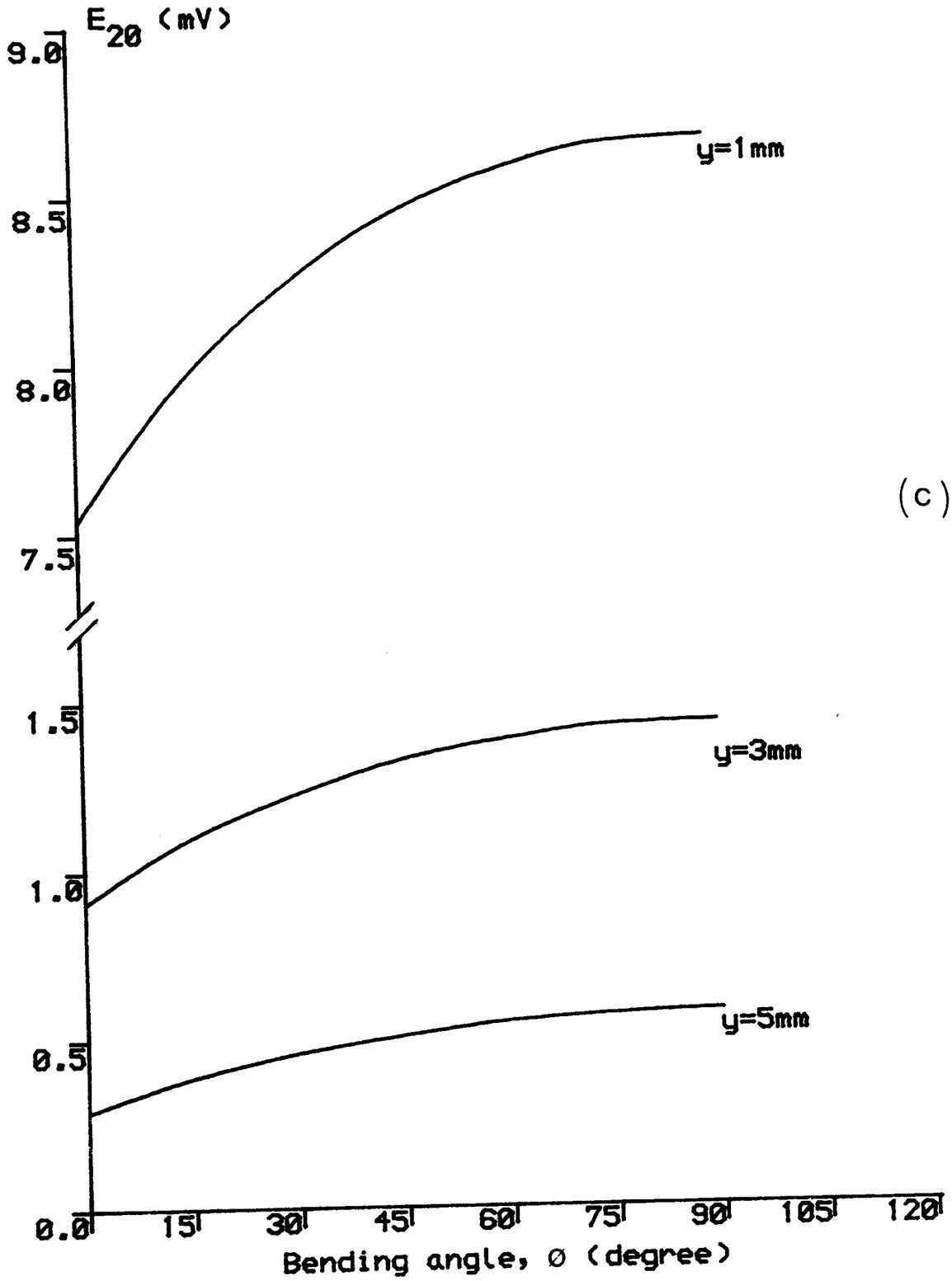
E20 (mV)
9.0
8.5
8.0
7.5
1.5
1.0
0.5
0.0
y=1mm
y=3mm
y=5mm
15
30
45
60
75
90
105
120
Bending angle, ø (degree)

(c) 10μm

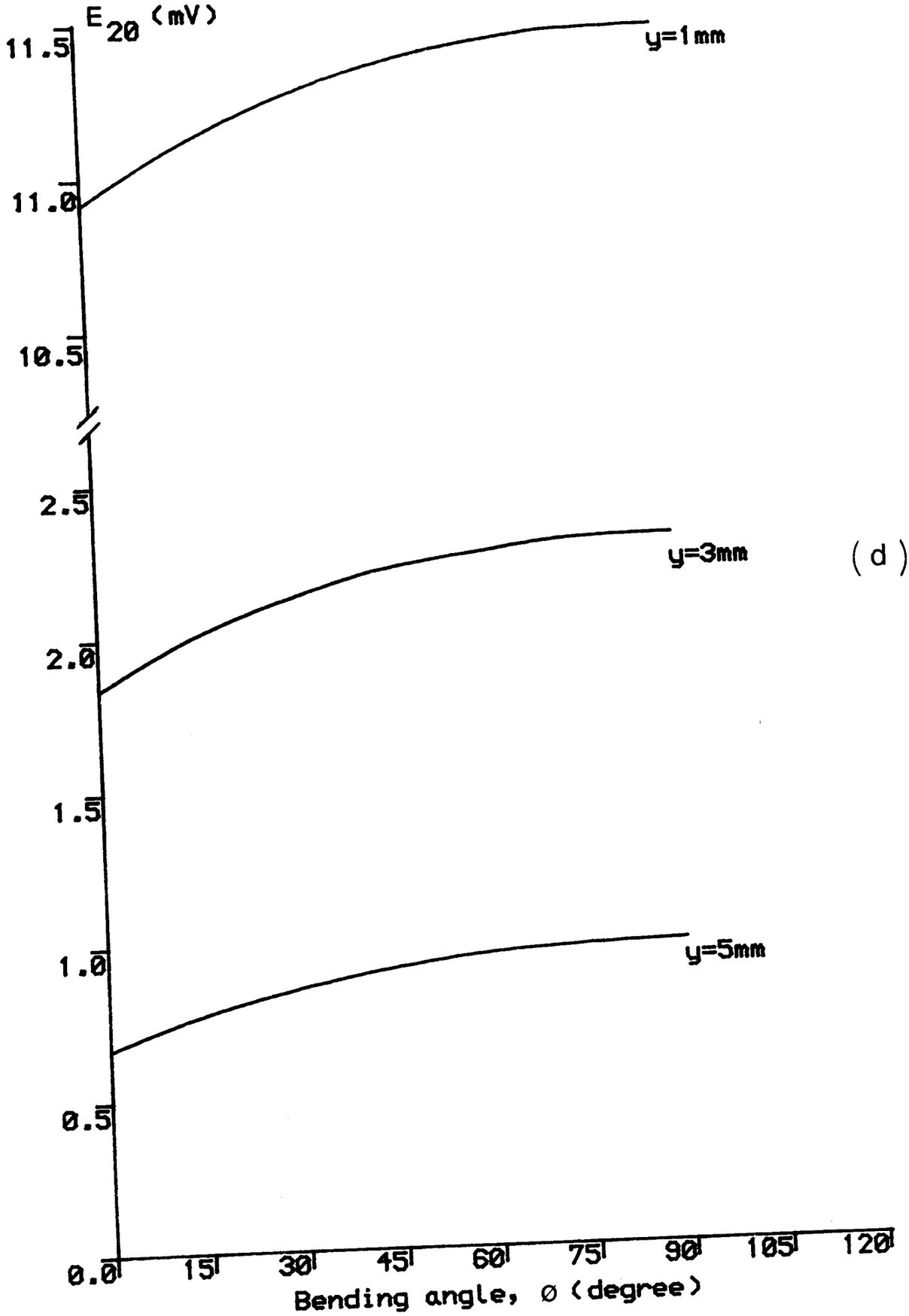
E20 (mV)
11.5
11.0
10.5
2.5
2.0
1.5
1.0
0.5
0.0
y=1mm
y=3mm
y=5mm
15
30
45
60
75
90
105
120
Bending angle, ø (degree)

(d) 20μm

It is evident from the results that an increase of bending angle ϕ will increase the membrane depolarisation. Note also that the highest curve (y=1mm) in each graph also exhibits the greatest sensitivity to bending angle.

On the other hand, for a given fibre diameter and electrode distance, if we define

$$\text{percentage difference} = \frac{E(\phi) - E(0)}{E(0)} \times 100\%$$

where $E(\phi)$ = membrane depolarisation of node 20 with a bending angle of ϕ degrees,

then a plot of percentage difference against ϕ yields the results in Figure 7.7.

The striking point is that, for a given fibre diameter and bending angle, (for example curves (a),(b) and (f) for 5μm fibre) the percentage difference in the depolarisation is larger at large electrode distance than at short distance. The second point is that, for the same electrode distance, (for example curves (a),(c) and (e) for a 5mm distance) bending angle is more effective to small diameter.

The bending angle also affects the region of depolarisation, although the results are not shown here. For the case of straight fibre, the number of nodes depolarised on either side of node 20 are equal. For the fibre shown in Figure 7.6(a). an increase in bending angle will increase the depolarisation values of the nodes on

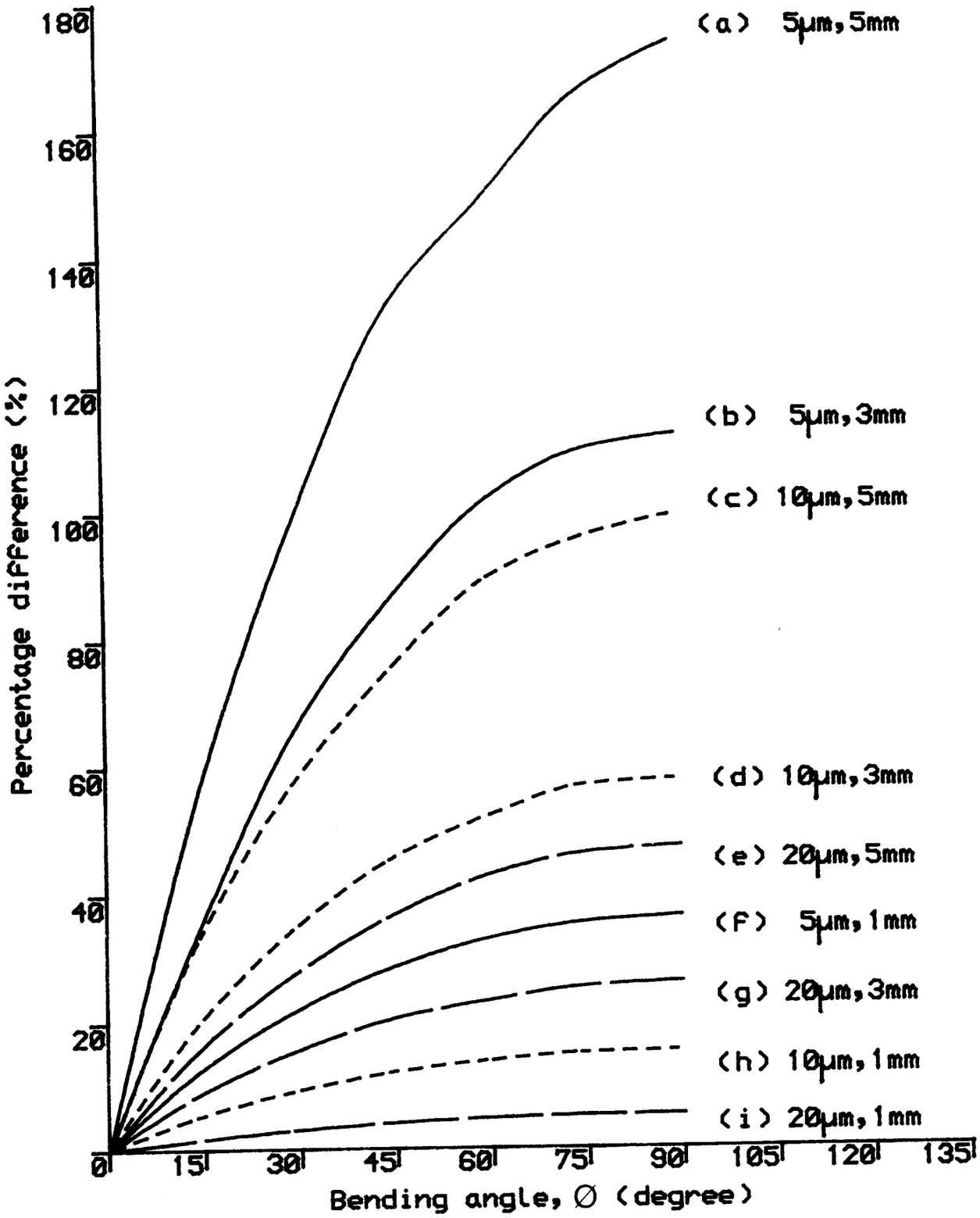

FIGURE 7.7 EFFECT OF FIBRE BENDING ON PERCENTAGE DIFFERENCE OF DEPOLARISATION AT NODE 20

For details see text 7.4.1

the 'stationary' side. But depolarisation on the opposite, 'bending', side decreased; for large angle. (> 75°), some of the nodes which were depolarised for ϕ=0 even become hyperpolarised.

Figures 7.8(a)-(b) are another presentation of the results given in Fig. 7.6. Each picture represents a fixed electrode distance from the fibre. Fig. 7.8(a) is for a 5mm case, where it can be seen clearly that a 5μm fibre with a 90° sharp bend has about the same depolarisation as a 10μm straight fibre (0°). The threshold for a 10μm fibre with 90° bending is also not far from a 20μm straight fibre. Fig. 7.8(b) is for the 3mm case.

A comparison of Fig. 7.8 (a) and (b) demonstrates that bending angle is less effective at short electrode distance. As shown in Fig. 7.8(b), the 5μm fibre with a 90° bending has a lower depolarisation than a 10μm straight fibre, and the 20μm fibre case always remains well above the 10μm fibre.

7.4.2 Fibre Branching

In view of the numerous branches and collaterals present in the course of the nerve fibre in the spinal cord, the single axon model will no doubt be inadequate to model these fibre system in the future. One example is again the dorsal root afferent : upon entering the spinal cord , many of the fibres will divide into ascending and descending branches , and many of these in turn give rise to numerous collateral branches. If the analysis can be

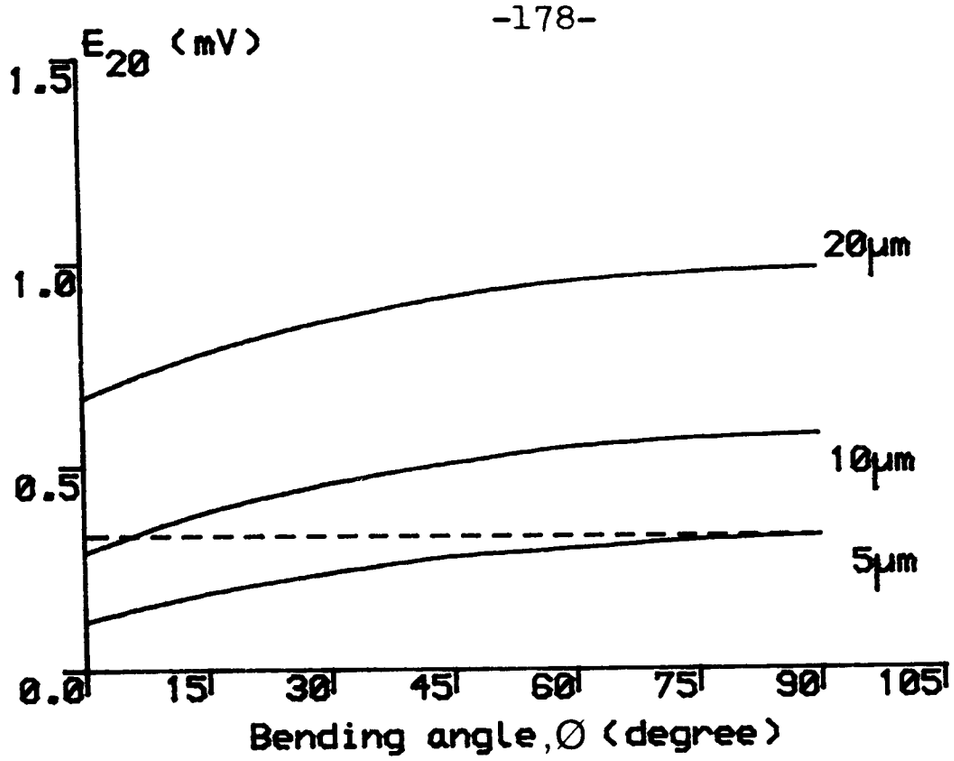

(a)

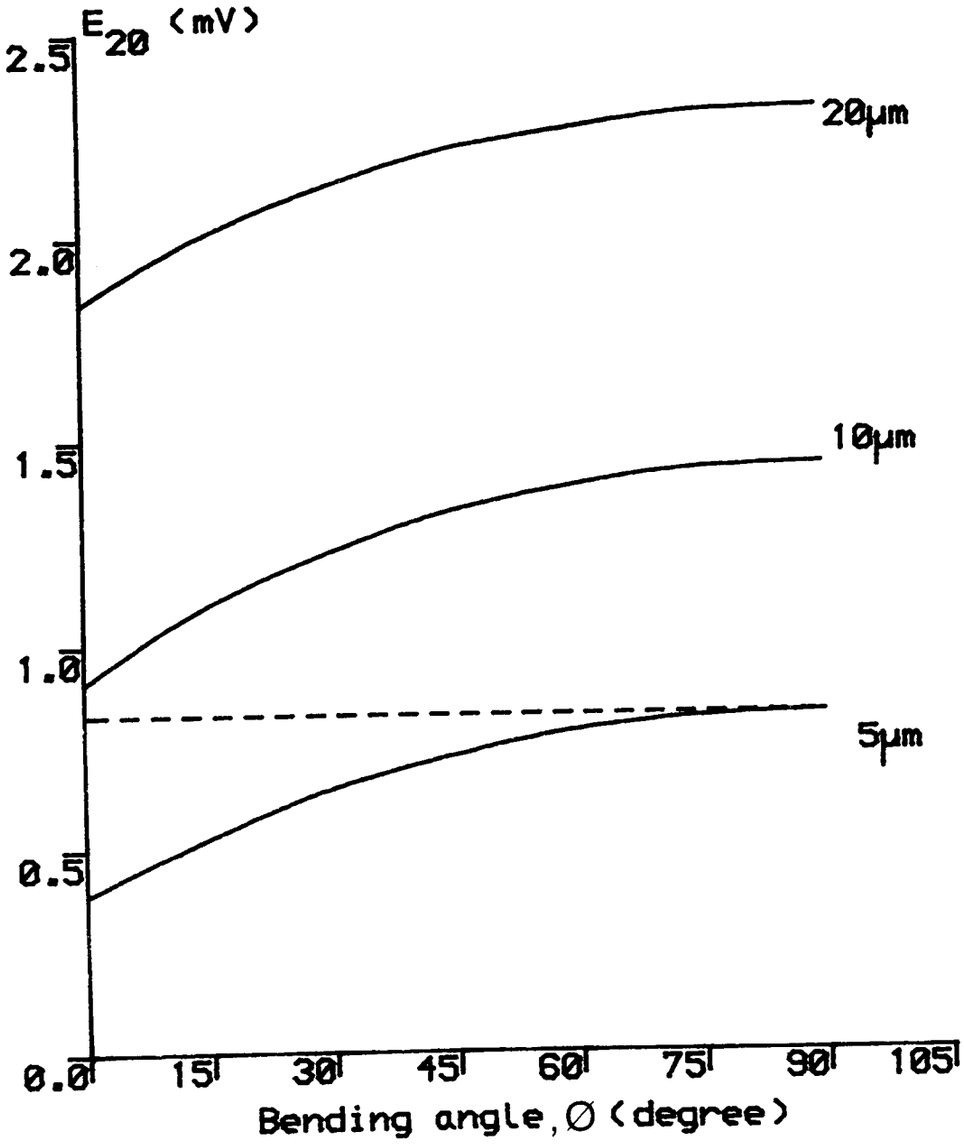

(b)

FIGURE 7.8 EFFECT OF FIBRE BENDING ON DEPOLARISATION AT NODE 20 AT DIFFERENT ELECTRODE DISTANCE

(a) 5mm

concentrated only on the main fibre and the major branches, then the single fibre model can readily be extended to include certain idealised fibre systems.

Figure 7.9 illustrates a simple branch system developed by COBURN (1981) to investigate the effect of branch length on depolarisation. This system is used here to study the influence of fibre diameter and electrode distance on the depolarisation of a 'branching node' (20). The two assumptions involved are

(a) the branch (node 40 to 55) has the same geometrical and physiological properties as the main fibre and

(b) the branch and the main fibre are sharing the same node (number 20) at the junction.

Based upon these assumptions, the system equations (derived in Appendix 3) share many features with the single fibre system. The deviations are the equation governing the 'branching node' (no. 20) and the complication in node numbering system. Note that in the present simplified analysis, the bending angle (ϕ) is always 90° and that the fibre system and electrode are always on the same plane. Stimulus conditions are the same as those in Sections 7.3.3 and 7.4.1, but the results are summarised in Table 7.1 instead.

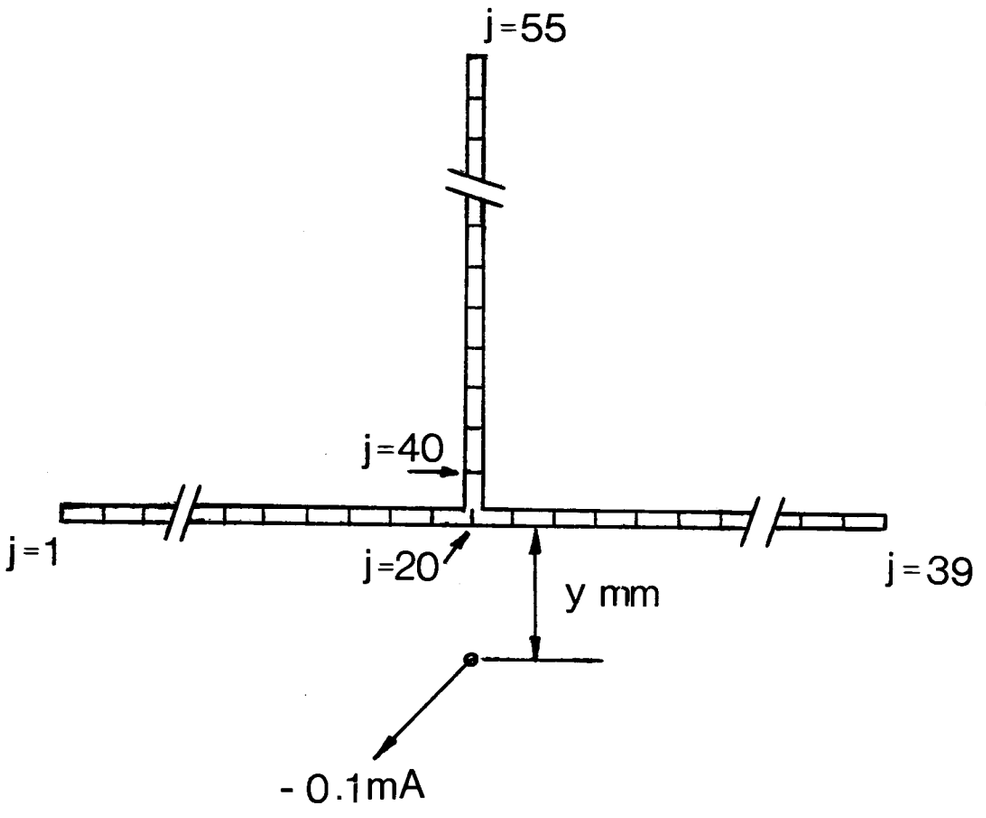

FIGURE 7.9 TESTING SCHEME OF FIBRE BRANCHING ON DEPOLARISATION AT NODE 20

For details see text 7.4.2

TABLE 7.1

electrode distance y (mm)	fibre diameter (μm)	depolarisation at node 20		percentage difference (%)
		straight fibre, E(mV)	fibre with branch, Eb(mV)	
1	20	10 92	13.06	20
	15	9.60	11.80	23
	10	7.54	9.81	30
	5	4.32	6.45	53
3	20	1.84	2.60	41
	15	1.41	2.15	52
	10	0.91	1.61	77
	5	0.39	0.97	148
5	20	0.67	1.10	64
	15	0.48	0.89	85
	10	0.29	0.66	128
	5	0.12	0.42	250

where $\text{percentage difference} = \frac{E - Eb}{E} \times 100\%$

The implications of the results are the same as the last section concerning fibre bending. For the same electrode distance, the influence of the branching on

small fibre is of more significance than on larger one. For the same fibre diameter, the percentage differences due to the branch are directly proportional to the electrode distances from the fibre. For example with reference to electrode distances of 3mm, the 5μm branching system has a higher depolarisation (0.97mV) than a 10μm straight fibre (0.91mV). This is also the case for the 5mm distance (0.42mV to 0.29mV). One more interesting point is that the 5μm branching fibre 5mm away from the electrode has a higher depolarisation (0.42mV) than a 5μm straight fibre 3mm from the electrode (0.39mV).

Finally, it must be kept in mind that the quantitative results in the last sections were obtained under certain stimulus conditions. In particular, the stimulus field and the position of the electrode relative to the fibre were highly idealised.

CHAPTER 8

VALIDATION STUDIES OF MYELINATED FIBRE MODEL

8.1 EXISTING PUBLISHED LITERATURE FOR COMPARISON

The McNEAL (1976) model of myelinated axon, which is a corner-stone of this entire work, required rigorous examination similar to the finite element model in Chapters 4 and 5. An obvious approach is to compare theoretical results, i.e. current-duration and current-distance relationships obtained by digital simulation, with expermental data obtained by independent workers.

In a review article on electrical stimulation of mammalian central nervous system, RANCK (1975) has collected more than 25 sets of relevant experimental data. Unfortunately, suitable data which can be used for direct validation purposes are rare. Firstly, some of these data involved stimulation of neural elements such as cell bodies rather than purely myelinated fibres. Secondly, other relationships like voltage/duration or even current/latency were measured instead of current/duration and current/electrode-distance. Thirdly, even myelinated fibres were stimulated, they were mingled with other neural tissues in such a way that an estimation of the stimulus field required for digital stimulation was difficult.

One possible source is that of BeMENT and RANCK (1969a), who measured current/duration relationships of the dorsal columns of cat, using finite size electrodes in contact with the cord surface. Using these data for comparisons, however, requires another finite element model like the monkey work in Chapter 4 in order to duplicate the stimulus field in the dorsal column.

McNEAL (1976), on the other hand, showed that the theoretical results from his model were consistent with published experimental data (BeMENT & RANCK, 1969a: CRAGO, et al, 1974), although he had not confirmed the fibre model experimentally. Later, TEICHER and McNEAL (1978) calculated the current/distance relationship using long stimulating pulses, and the results were in good agreement with the steady-state predictions by BEAN in an Appendix of ABZUG et al (1974).

COBURN (1981) used a 3-D finite element model to evaluate the stimulus field arising from epidural stimulation in humans. The fields in the dorsal column were interpreted by the McNEAL model to generate dorsal column thresholds. The results, reproduced in Fig. 8.1, compared favourably with the perceived sensory threshold in patients (JOBLING et al , 1980). However, no rigorous proof was provided that long straight myelinated fibres of passage were the primary site of stimulation.

GORMAN and MORTIMER (1983) also used the McNEAL model to represent the nerve fibres supplying the medial gastrocnemius muscle of the cat. The intention was to

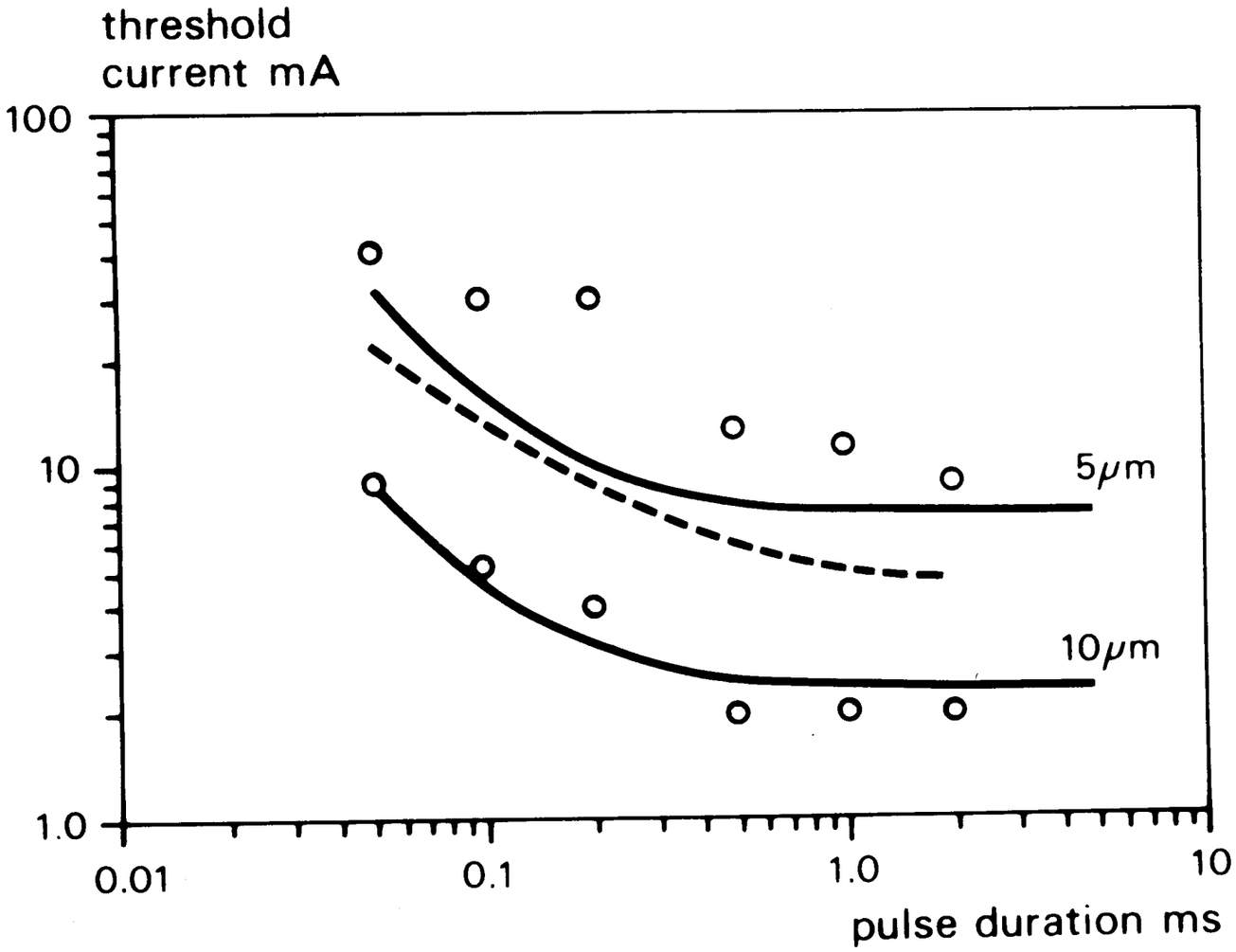

FIGURE 8.1 RELATIONSHIP BETWEEN THRESHOLD CURRENT AND PULSE DURATION FOR DORSAL COLUMN FIBRES

Reproduced from COBURN(1981). Full lines are model predictions for 5μm and 10μm fibres. Circled points are maximum and minimum values of current self-selected by 15 patients in an experiment by JOBLING(1980). Dashed line is experimental mean.

investigate the effects of stimulating parameters on the threshold difference between nerve fibres of different diameters. The investigation was verified by experiments which showed a similar pattern with the predicted results.

Although it has been possible to cite some validation work on the McNeal model in the last three paragraphs. a systematic testing on the model remains highly desirable. This chapter, therefore, describes an extensive validation study on the fibre model. The first part of the study was extracellular electrical stimulation on isolated biventer cervicis nerve-muscle (BVC) preparations from the chick to establish the current/duration and current/electrode-distance relationships. The second part was digital simulation using the fibre model to predict these relationships, which were then compared with the experimental values. The study also involved histology on the biological preparations and careful analysis of electrical field distortions.

8.2 ELECTRICAL STIMULATION OF CHICK BIVENTER CERVICIS NERVE-MUSCLE (BVC) PREPARATION

8.2.1 BVC Preparation

Since the introduction of the preparation by GINSBORG (1960), the preparation has been extensively used in teaching and for fundamental work on the pharmacology of neuromuscular junction.

The BVC system consists of two muscles joined by a

tendon; it contributes to the head-jerking movement of the chick. A remarkable feature is that the nerve enters the first muscle, which some axons innervate, while other nerve fibres pass through the centre of the tendon to supply the second muscle. This feature is a major advantage to the study, as any stimulation of the long fibres passing along the tendon may be detected by the mechanical response of the second muscle. Moreover, the nerve bundle can be considered as a set of parallel-running fibres free from other neural elements.

8.2.2 Basic Experimental Scheme

Figure 8.2 shows the experimental scheme developed in collaboration with the Department of Applied Biology at Brunel University. The BVC preparation was set up vertically, midway down a bath containing Krebs-Henseleit solution. (*) A monopolar electrode, K, close to the tendon in which the motor nerves run, stimulated the preparation. The electrode wire was insulated except at the tip which had a platinum ball of roughly 2.2 mm (Appendix 5) diameter. It was connected to a current-driving stimulator, E, which could deliver a maximum of 40 mA pulse magnitude. Micro-manipulators, C and D, controlled the position of the electrode by vernier adjustment so that the electrode movement could be

---

(*) NaCl 0.69%, KCl 0.035%, $CaCl_2$ 0.028%, $NaHCO_3$ 0.21%, KH_2PO_4 0.016%, $MgSO_4 .7H_2O$ 0.029%, glucose 0.2%

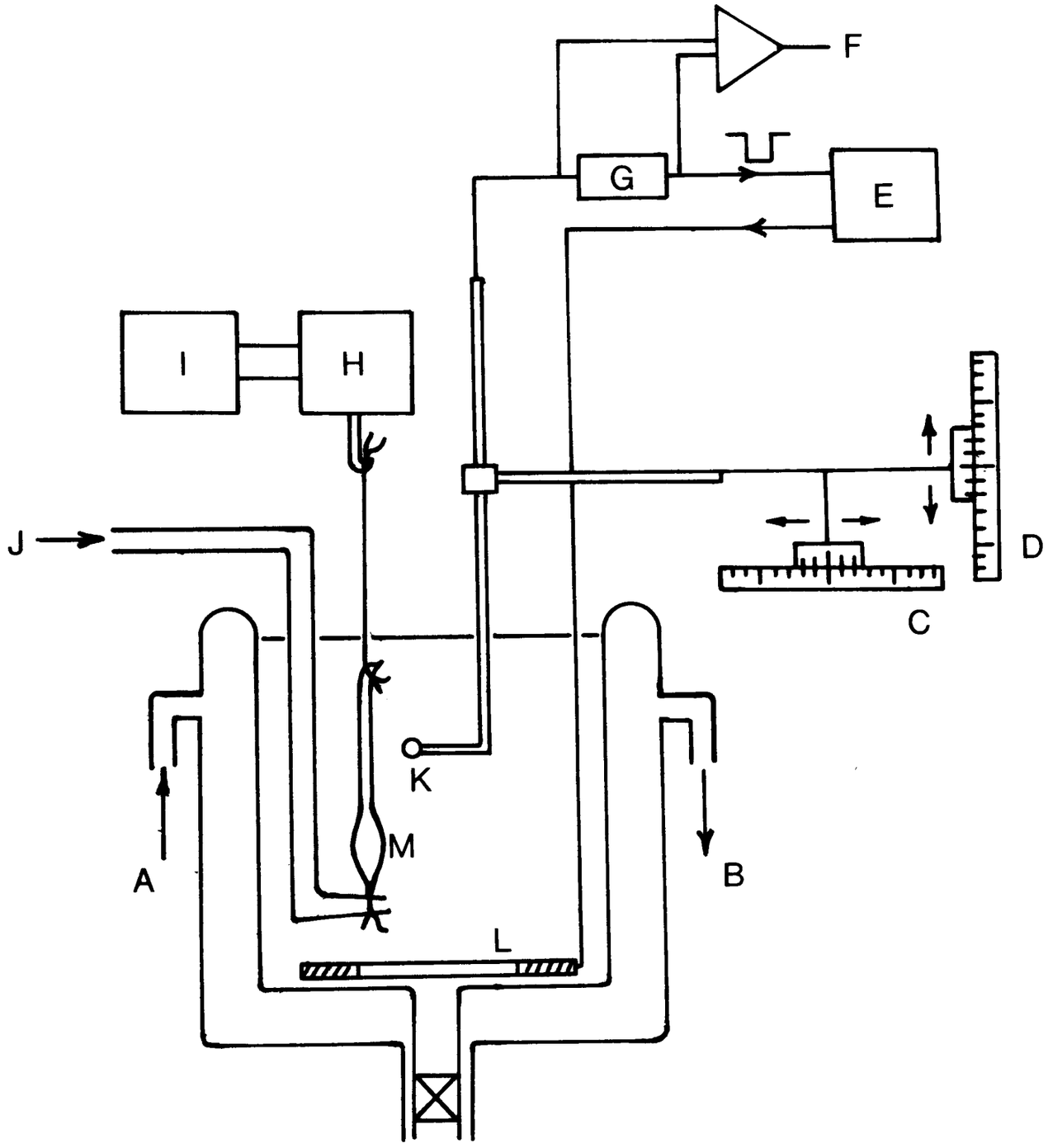

FIGURE 8.2 EXPERIMENTAL SCHEME FOR THRESHOLD STUDIES ON THE CHICK BIVENTER CERVICIS PREPARATION

For details see text 8.2.2

adjusted to an accuracy of 0.1mm. The indifferent electrode, L, was a stainless steel ring on the bottom of the bath. The instantaneous current waveform was displayed on an oscilloscope as the potential difference across a 10-ohm resistor, G. A temperature of 37 °C was automatically maintained in the bath with a circulating water jacket, A to B. and the solution was bubbled through with oxygen containing 5% carbon dioxide, J.

As shown in Fig. 8.2, for the experiment the upper muscle of the preparation was removed and the top end of the tendon was tied to a force transducer H. with a cotton thread. The lower muscle was restrained to the glass tube used for oxygenation. The force transducer was at isometric setting and was coupled to a pen recorder, I. Any muscle twitches therefore resulted in the pen movement whose magnitude depended on the force of contraction.

The basic idea was to obtain threshold current-duration relationships at different electrode positions The current-distance relationship could then also be deduced.

8.2.3 Experimental Procedures

Six preparations, aged 3 to 10 days. were used. Each tendon was between 10 and 15 mm long. The following five steps were involved :

Step 1 : For each preparation. the experiment began with the electrode midway down the bath and 0.5mm clear space from the tendon wall. Details of the spatial

relation between the electrode and the tendon are given in Figure 8.3. Single pulses of cathodic current, in the range from 0.03 to 3.0 ms, were used to stimulate the preparation. At each pulse-width, the amplitude of current was gradually increased, and the minimum response detectable on the pen recorder was considered as threshold current.

Step 2 : The distance of the electrode from the tendon was varied from 0.5 mm to 4.0 mm in increments of 0.5 mm. At each of these horizontal positions, labelled x in Figure 8.3 (a), current-duration relationships were determined.

Sometimes during the experiment air bubbles collected, either around the electrode or on the tendon, which could alter the stimulus current flow pattern. It was necessary to brush any such bubbles away before any reading was taken.

Step 3 : At a particular value of x, described above, the vertical position of the electrode, labelled z in Figure 8.3(a) was varied ± 1.0mm from the original position. In each case steps 1 and 2 were repeated so that a total of three complete sets of cathodic stimulation were performed on each BVC preparation. Note that throughout the experiment the movement of the electrode was restricted in the XZ plane shown in Figure 8.3(a).

Step 4 : Steps 1-3 were repeated for anodic stimulation.

After the stimulating session, the preparation was

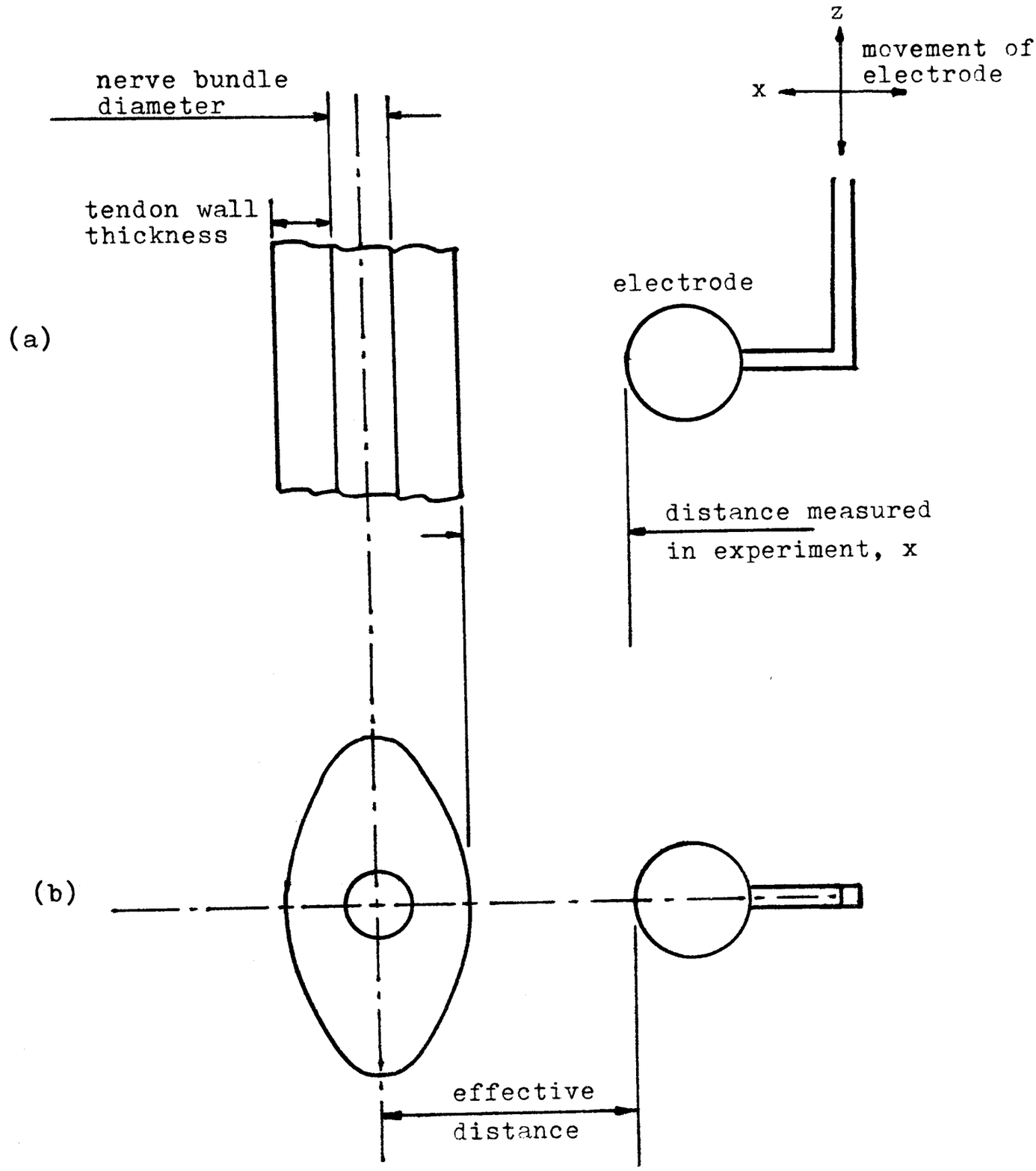

FIGURE 8.3 SPATIAL RELATIONSHIP BETWEEN ELECTRODE AND TENDON

Not to scale. Details see text 8.2.3.

$$\text{effective distance} = \text{measured distance} + \text{tendon wall thickness} + \frac{\text{bundle diamter}}{2}$$

preserved in 0.9% NaCl in 10% Formalin for histological analysis.

Step 5 · The final step of the experiment was to measure the monopolar field distribution in the XZ plane of the bath. A copper wire, having an insulated sheath and a bare tip of 0.5mm diameter, was manipulated up and down to measure the voltage profiles at five different horizontal distances from the electrode. The measured fields were relative to a silver/silver-chloride cup indifferent placed in the bottom centre of the bath. Samples of the Krebs-Henseleit solution were also taken from the bath for resistivity measurements.

8.2.4 Experimental Results

The averaged threshold values, their standard deviations and the number of readings for each value are shown in Table 8.1. It may be seen that the table is not complete in every column; the stimulating current being delivered was limited to a maximum of 40 mA amplitute. and in certain circumstances this was insufficient to stimulate the preparation. Note the important point that the 'measured distance', x, relates to the clear space between the electrode tip and the tendon wall. These data are also presented graphically in Figures 8.9 to 8.11 for comparison with digital simulation results. Nevertheless, a first glance of the results in the table reveals that they have the expected characteristics that an increase in

measured distance (mm)

pulse width (ms)	0.5	1.0	1.5	2.0	2.5	3.0	3.5	4.0
3.0	(12) -2.6 ±0.3 (13) 6.7 ±2.8	(13) -3.6±0.7 (14) 9.6 ±4.2	(13) -5.2 ±0.9 (14) 13.1 ±5.8	(13) -6.8 ±1.5 (12) 16.5 ±6.5	(13)-9.2 ±2.2 (10) 17.5 ±6.2	(13) -11.9 ±2.9 (8) 23.6 ±8.1	(11) -13.2 ±1.9 (7) 23.1 ±5.0	(11) -16.7 ±2.3 (5) 28 ±6.6
1.0	(13) -3.0 ±0.5 (14) 8.3 ±3.2	(13) -4.3 ±0.9 (14) 11.9 ±4.5	(13) -6.1 ±1.5 (14) 15.5 ±6.0	(13) -8.2 ±2.3 (11) 18.8 ±5.1	(13) -11.2 ±3.3 (10) 23.3 ±7.0	(13) -14.5 ±4.2 (6) 23.6 ±5.0	(11) -15.8 ±3.1 (6) 29.3 ±5.8	(11) -20.1 ±3.5 (5) 35.4 ±5.0
0.75	(13) -3.2 ±0.6 (14) 8.7 ±3.2	(13) -4.7 ±1.1 (14) 12.5 ±4.6	(13) -6.7 ±1.8 (14) 16.7 ±6.4	(13) -9.2 ±2.6 (11) 21.1 ± 8.0	(13)-12.3 ±3.6 (10) 22.2 ±6.2	(13) -16.0 ±4.6 (6) 24.4 ±5.7	(11) -17.8 ±3.7 (6) 31.2 ± 6.4	(10) -21.4 ±4.0 (3) 32.7 ±1.2
0.5	(13) -4.0 ±0.7 (13) 10.1 ±3.5	(13) -5.4 ±1.1 (13) 13.8 ±4.7	(13) -7.7 ±2.1 (12) 18.0 ±5.3	(13) -10.7 ±3.1 (9) 22.2 ±5.9	(13) -13.9 ±4.2 (8) 23.8 ±3.8	(12) -17.0 ±4.3 (5) 29.2 ± 5.9	(11) -20.1 ±4.3 (5) 35.9 ±3.2	(7) -22.1 ±3.5 (2) 38.0 ±4.2
0.3	(13) -4.4 ±0.7 (14) 12.4 ±4.1	(13) -6.8 ± 1.5 (14) 17.5 ±5.5	(13) -9.8 ±2.6 (11) 20.6 ±5.9	(13) -13.3 ±3.8 (9) 26.5 ± 8.3	(11) -15.7 ±3.2 (7) 28.3 ±5.7	(11) - 20.7 ±4.2 (4) 31.9 ±4.0	(7) -22.2 ±4.0 (4) 40.0 ± 1.4	(6) -26.7 ±4.0
0.2	(13) -5.6 ±0.9 (14) 15.6 ±5.2	(13) -8.5 ±1.8 (12) 20.1 ±5.9	(13) -12.5 ±3.3 (9) 24.0 ±6.8	(13) -16.3 ±4.2 (7) 28.5 ±5.6	(11) -19.5 ± 3.4 (5) 32.8 ±3.6	(7) -23.5 ±5.1 (4) 40.0 ± 0.8	(5) -27.7 ± 5.7	(2) -27.0 ± 2.1
0.1	(13) -8.9 ±1.5 (10) 23.3 ±8.4	(13) -13.5 ±2.3 (8) 27.3 ±7.8	(11) -17.7 ±2.7 (5) 39.4 ±2.1	(8) -23.7 ±3.2	(5) -29.0 ±3.9	(2) -28.5 ± 0		
0.05	(13) -15.0 ±2.4 (8) 32.1 ±7.1	(11) -21.8 ±2.8	(5) -28.1 ±2.1	(1) -28.5				
0.03	(10) -22.1 ±3.3	(2) -29.0 ± 1.4						
0.02	(4) -25.8 ± 1.6							

TABLE 8.1 EXPERIMENTAL RESULTS

upper value : cathode (mA)
lower value : anode
± one standard deviation
( ) indicates number of readings

electrode distance or a decrease in pulse-width are followed by an increase in threshold current magnitude.

The average field profiles measured in the bath are shown in Figure 8.4. The five curves correspond to five horizontal distances (0.5mm, 1.0mm, 2.0mm, 3.0mm and 4.0mm) measured between the tips of the measuring probe and the electrode. In effect the measuring probe was tracked up and down to determine the voltage profile along a path normally occupied by the centre line of the nerve bundle. These field profiles are the extracellular potentials input, already described in Section 7.2, for digital simulation.

The average resistivity of the Krebs-Henseleit solution, using the method and equipment described in Appendix 2, was 70 ohm-cm. This value was used in conjuction with the above field profiles to estimate the 'effective diameter' of the stimulating electrode (Appendix 5). This diameter, the resistivity of Krebs-Heneleit solution and the anatomical structures of the nerve-tendon are also the parameters required for analysis in Section 8.6 of the likely distortions of the fields of Figure 8.4 caused by the presence of the tendon.

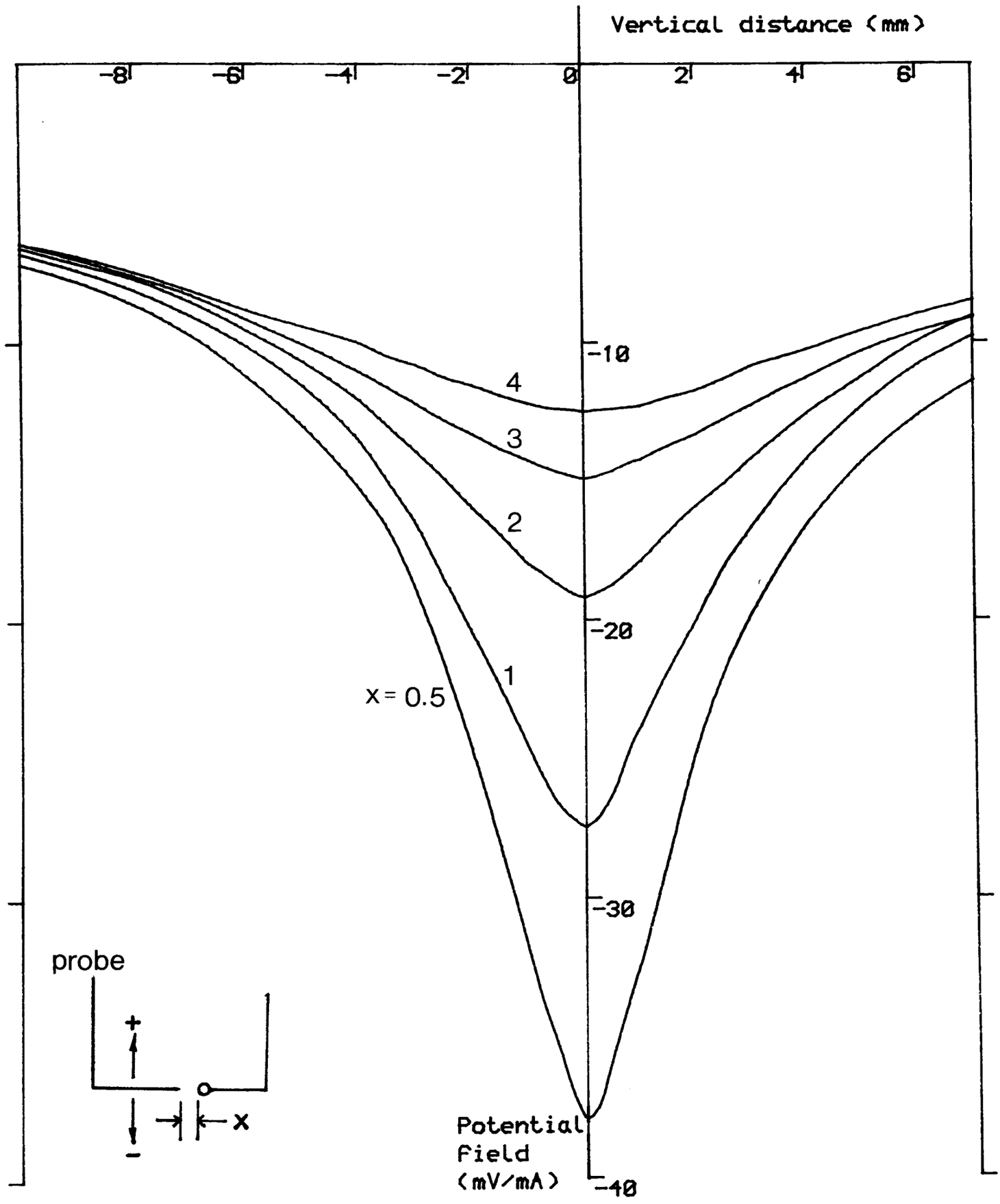

FIGURE 8.4 FIELD PROFILES MEASURED IN KREBS-HENSELEIT BATH

For details see text 8.2.4

8.3 HISTOLOGY OF BVC IN THE NERVE/TENDON SECTION

Histological analysis focussed on the transverse section of the tendon where the fibre diameter spectrum and relevant anatomical factors are of interest. Seven formalin-fixed BVC preparations were examined, six of which had been used in the stimulating experiments. (*) A seventh was included as a control, since the question arose as to whether the repeated twitch loadings during stimulation might generate mechanical damage. The histological sections, of 5μm thickness. were attached on glass slides and photomicrographs were made.

Figure 8.5 shows a typical cross-sectional view of a tendon with the clearly identifiable nerve bundle passing through. Recall that manipulations of the stimulating electrode during the experiments were always in the sagittal plane . The general technique of measuring tissue dimensions from histological sections are well-established (SANDERS, F.K., 1948; YOUNG, J.Z., 1950). The area of interest in the present study are outer diameter of individual fibres, the thickness of tendon wall and nerve bundle diameter. The latter two were measured from the photomicrographs (magnification 340) and the average values were shown in Figure 8.5 too.

A higher magnification (x 810) centred on the nerve

(*) The preparations were processed by the Neuropathology Laboratory of Wessex Neurological Centre, Southampton General Hospital.

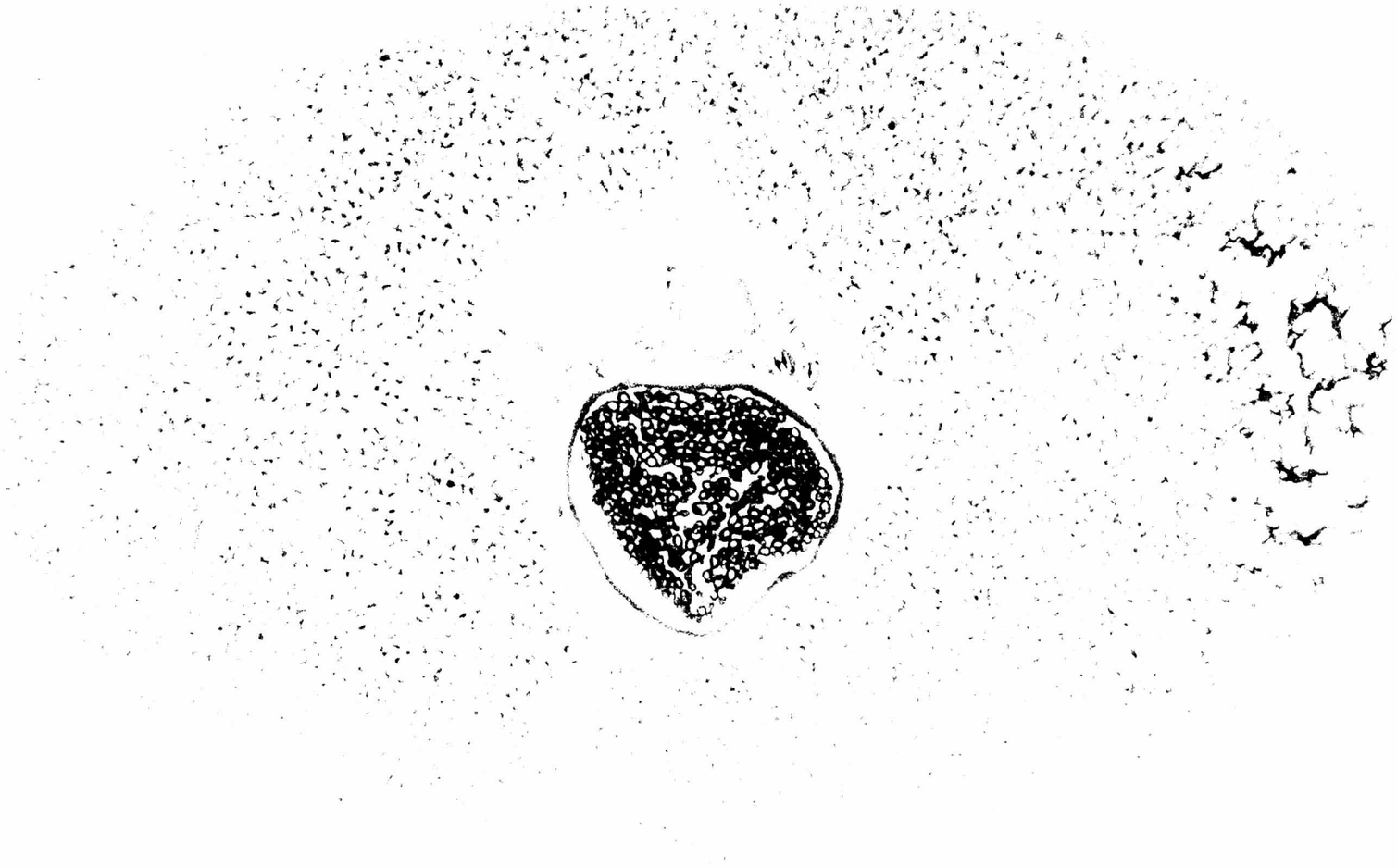

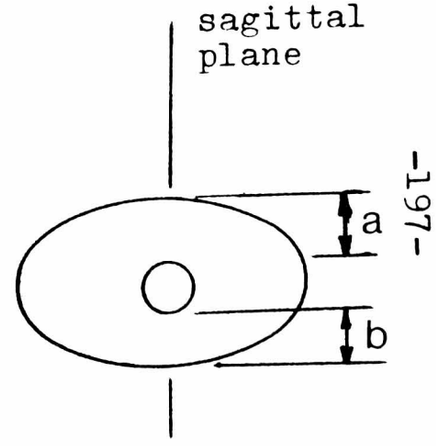

average of a and b
= tendon wall thickness
≃ 0.154mm

average of nerve
bundle diameter
= 0.118mm

FIGURE 8.5 CROSS-SECTIONAL VIEW OF NERVE-TENDON REGION (X340)

For details see text 8.3

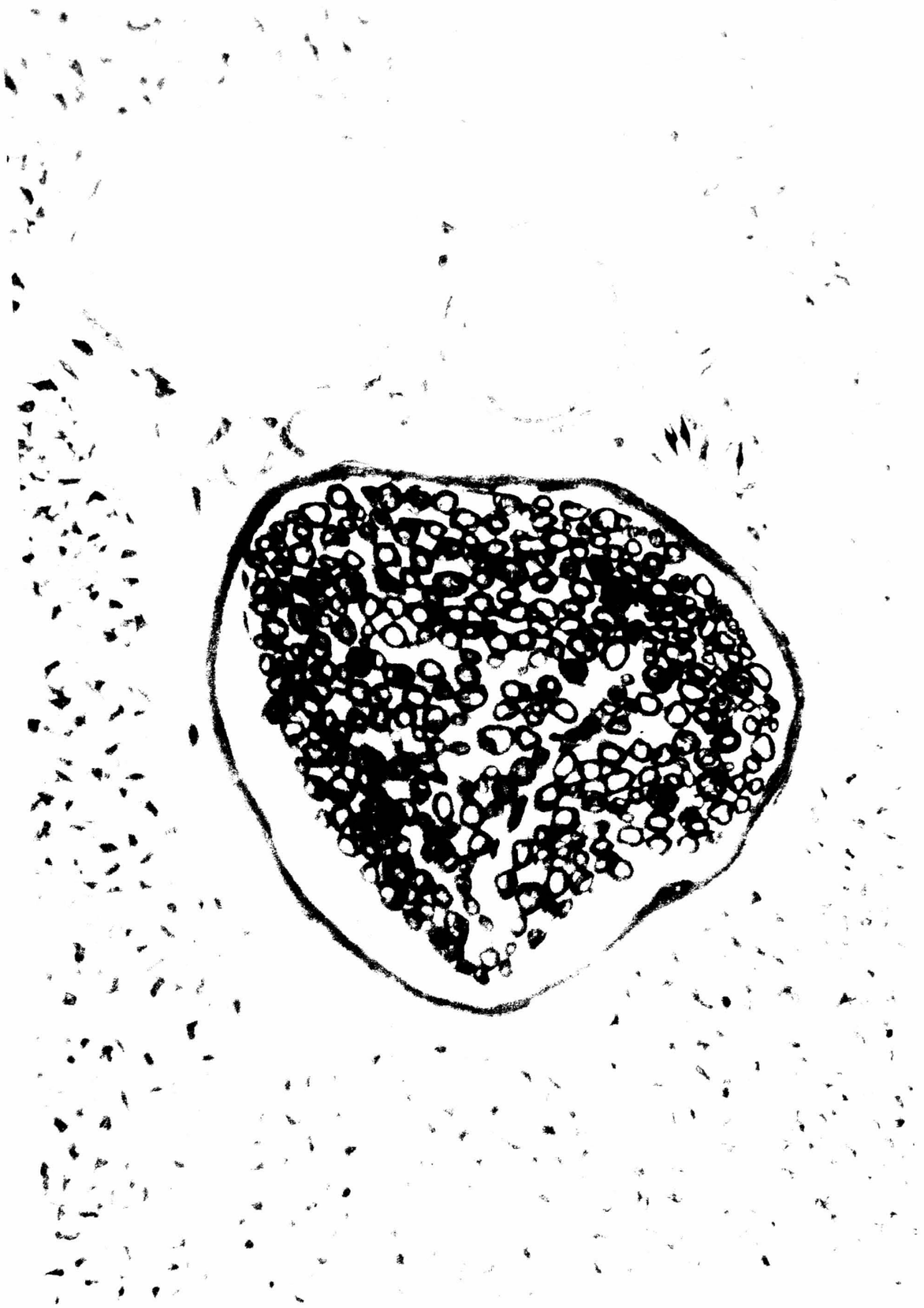

FIGURE 8.6 CROSS-SECTIONAL VIEW OF NERVE BUNDLE (X810)

bundle is shown in Figure 8.6. The myelin sheaths are clearly shown as dark rings. An important point to be noted is that the diameters and the populations of the axon are shown to be distributed evenly within the bundle. A digitising cursor was used to measure the fibre diameters from the photomicrographs, and histograms were generated by graphics software.

A total number of 1940 nerve fibres were seen in the seven preparations, and the fibre diameter histogram is shown in Figure 8.7. The mean value is 4.7μm with a standard deviation of 1.3μm. The histograms of each individual nerve bundle are in Appendix 6. Each bundle has 230 to 350 nerve fibres, and all the bundles have the expected 'bell-shaped' fibre distributions.

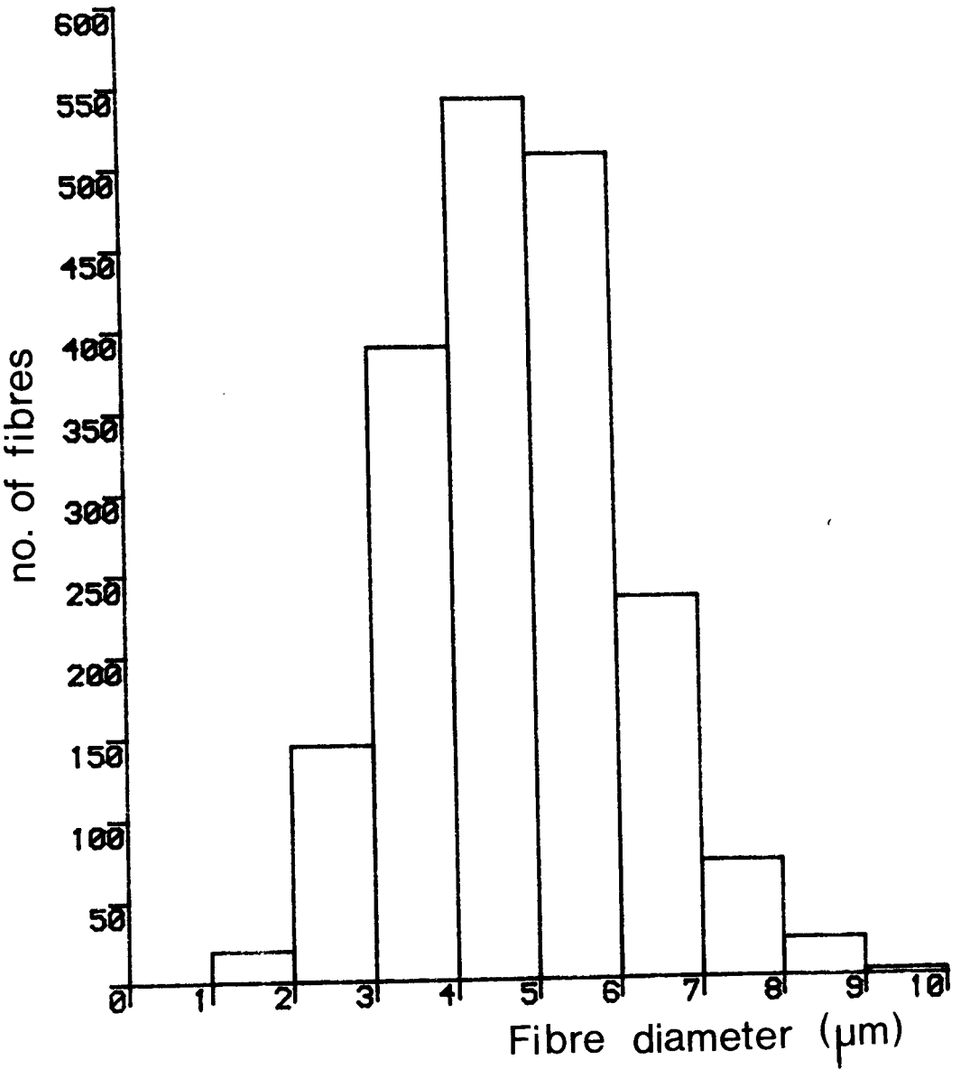

FIGURE 8.7 HISTOGRAM OF NERVE FIBRE DIAMETER OF BVC PREPARATION

Total number of fibres 1940. For details see text 8.3

8.4 DIGITAL SIMULATION OF MYELINATED FIBRE

8.4.1 Description of Fibre Model

The essential features of the myelinated axon model have been described in Chapter 7. The model can predict threshold current of myelinated fibre for any pulse duration and accordingly a computer program was developed which could automatically estimate the threshold current. using repeated runs in an iterative routine.

The criterion is that if the depolarisation value of any one of the nodes exceeds a pre-defined level (15mV) during the simulating period, the latest stimulating field is assumed by the algorithm to be suprathreshold. This field strength is reduced and the simulation process is repeated. Conversely, the field is increased if none of the nodes has its depolarisation value exceeding the pre-defined level. Description of the programming aspects and example output may be found in Appendix 7.

In order to match the fibre model to the experiments. the following points have to be considered :

1) one of the inputs for the program was a set of external potentials along the fibre at each node. These values were deduced from Figure 8.4. Note that these fields were measured after the BVC preparation was taken out from the bath. An analysis of field distortion caused by the presence of the tendon and nerve bundle will be discussed in Section 8.6.

2) one of the boundaries of the fibre computer model was

assumed to be an infinite impedance termination, representing the tendon/nerve bundle end which was cut and tied with cotton thread. The other boundary had the properties of a membrane disc, loosely modelling the neuromusclar junction.

3) the number of nodes in the model was influenced by the finite length of the tendon (which was less than 15 mm long) . The 5μm and 7μm fibre models used 19 nodes, while the 9μm model was restricted to 15 nodes. Table 8.2 summarises the simulating conditions for the model.

4) the absolute temperature appearing in FRANKENHAEUSER and HUXLEY (1964) equations was changed to 310 K, the temperature at which the chick experiments were conducted.

5) axons of different diameters were shown by histology to be distributed evenly over the nerve bundle, and the first axon to become active was assumed arbitrarily to be at the centre. Therefore the 'effective distance' between the stimulating electrode tip and a single active fibre in the BVC preparation is calculated by the expression

effective distance = distance measured in the experiment, x + nerve-tendon correction factor

The correction factor was 0.2 mm, as found in Section 8.3.

The program used standard nerve fibre parameters (except the temperature value) and initial conditions as reported by FRANKENHAEUSER & HUXLEY (1964).

TABLE 8.2

fibre diameter (μm)	total number of nodes, n, in the model	left-end condition	right-end condition	reference no. of the central node (j) nearest to electrode
5	19	↑ infinite impedance termination ↓	↑ membrane disc ↓	10
7	19			9
9	15			7

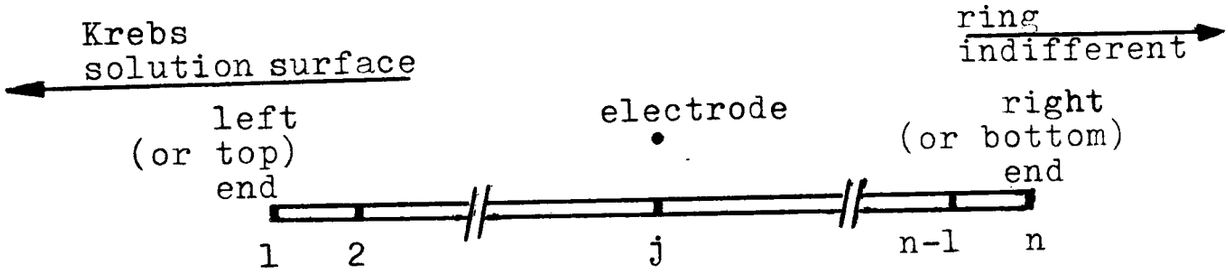

8.4.2 Simulation Results

The results are summarised graphically in Figures 8.8 to 8.10. The curves in Figures 8.8(a) to (i) show the theoretical relationships between threshold current and effective distance for fibres of four different diameters. Pulse duration in each case was constant. A typical running time required for these four cases on a CDC7600 was 160 CPU seconds.

The theoretical current-duration relationships for different fixed distances may be plotted by interpolating the curves in Figures 8.8 (a) to (i). The results are best

shown in logarithmic axes and are given in Figures 8.9(a) to (e). Figure 8.10 is for the anodic case.

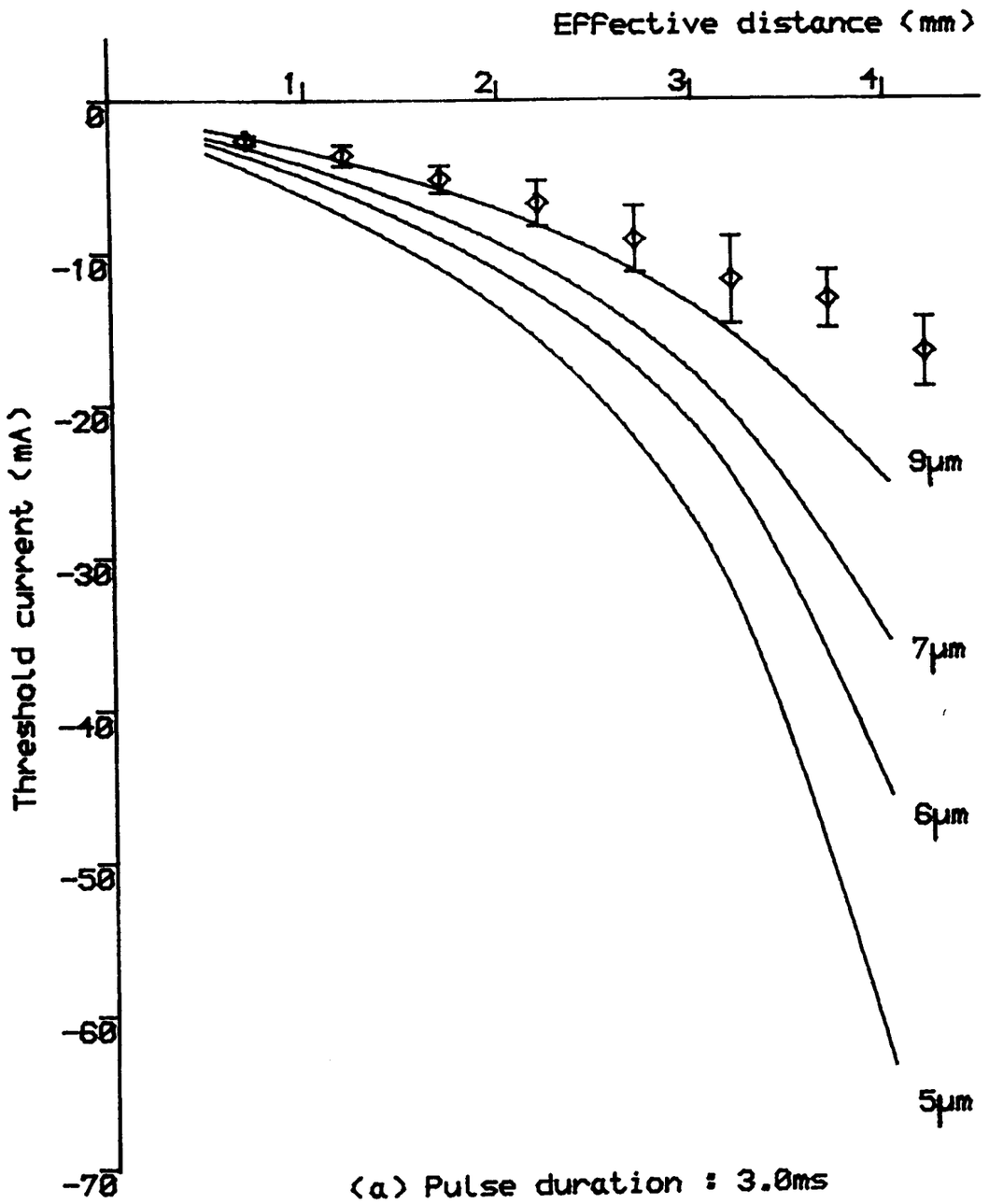

FIGURE 8.8 THRESHOLD-DISTANCE RELATIONSHIPS

Cathodic stimulation
Solid curves are thecretical predictions for different fibre diameters. Diamond points are experimental means. Vertical bars ± 1s.d. Other details see text 8.5

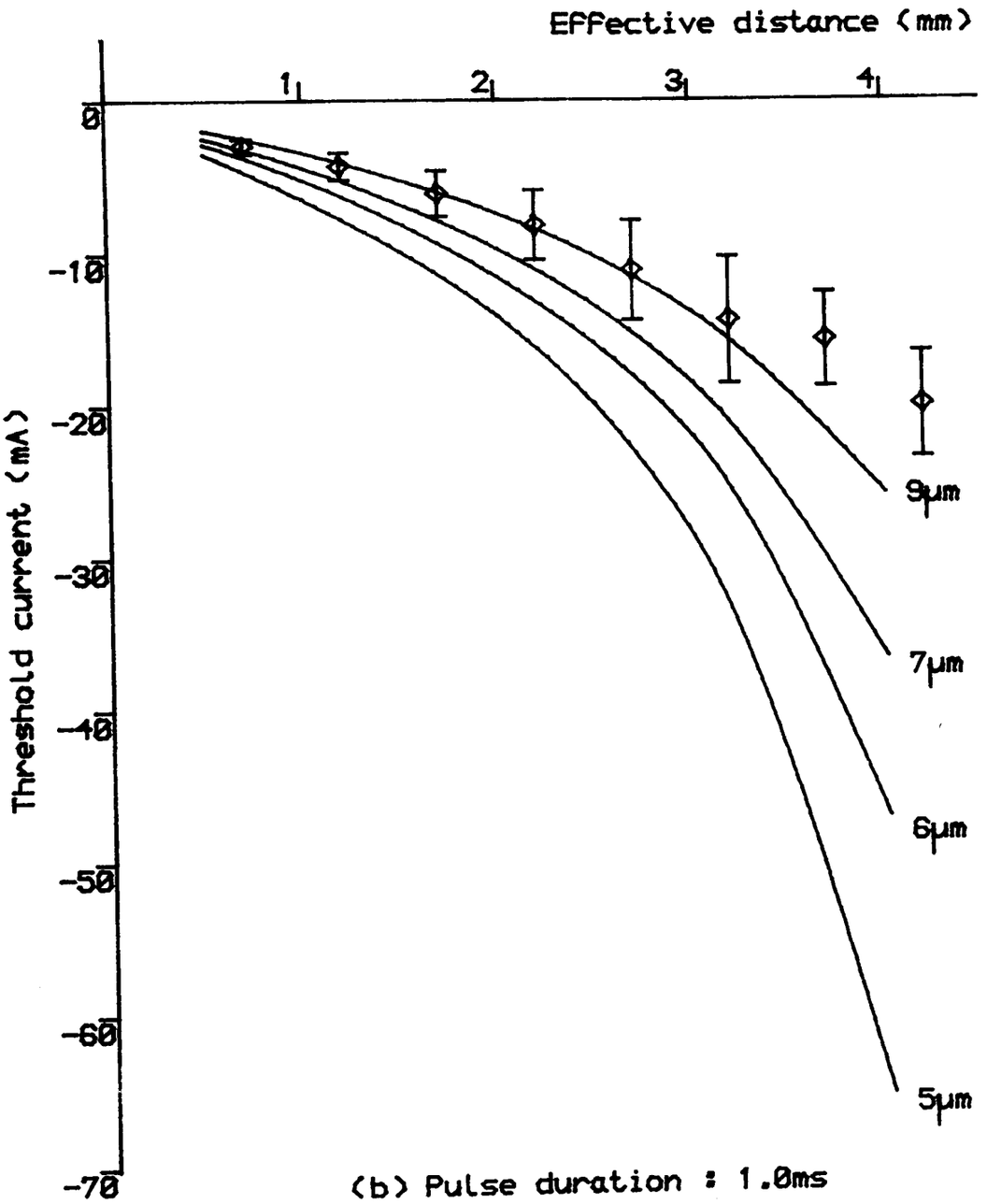

(b) Pulse duration : 1.0ms

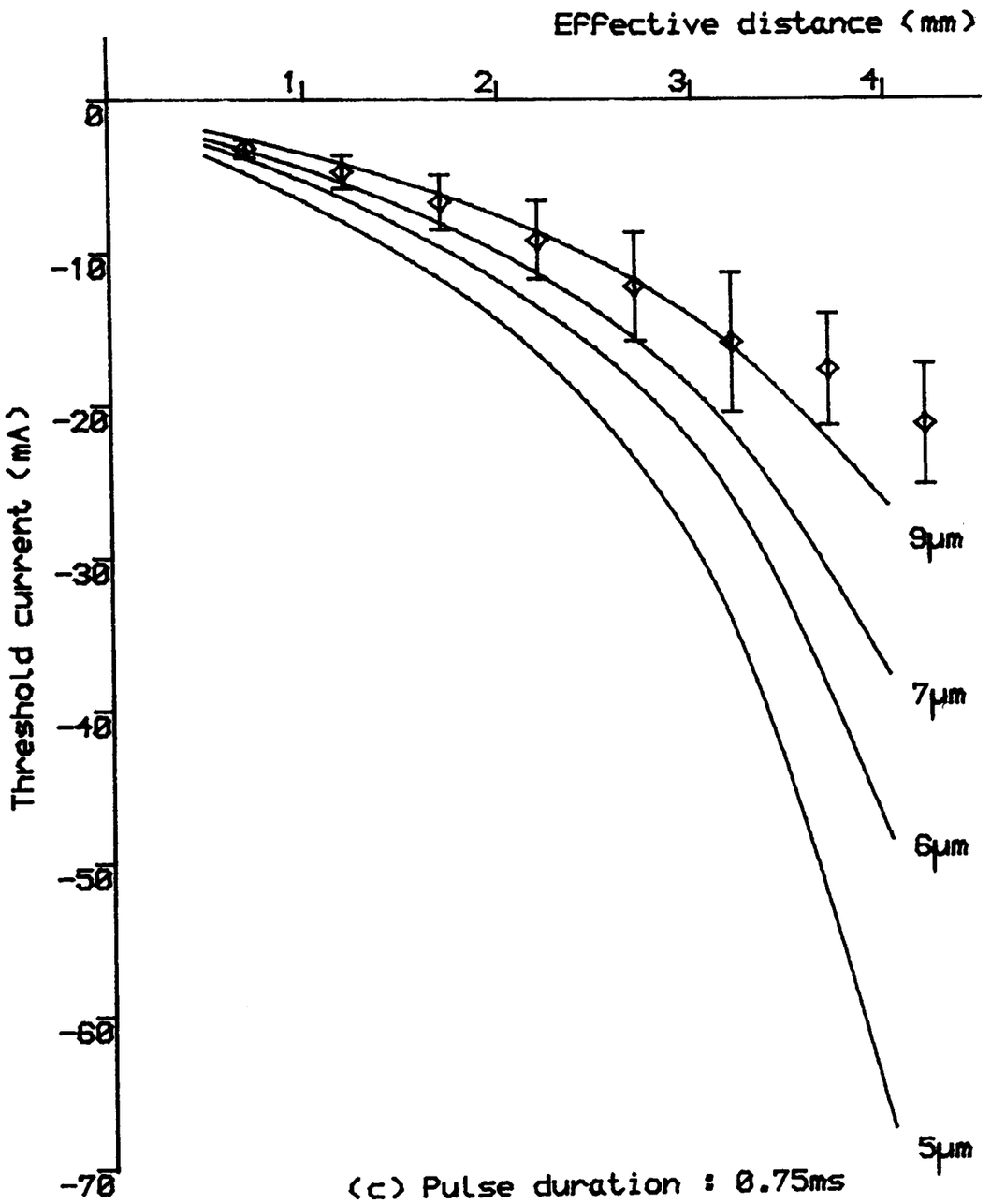
Effective distance (mm)
1
2
3
4
0
-10
-20
-30
-40
-50
-60
-70
Threshold current (mA)
9μm
7μm
6μm
5μm
(c) Pulse duration : 0.75ms

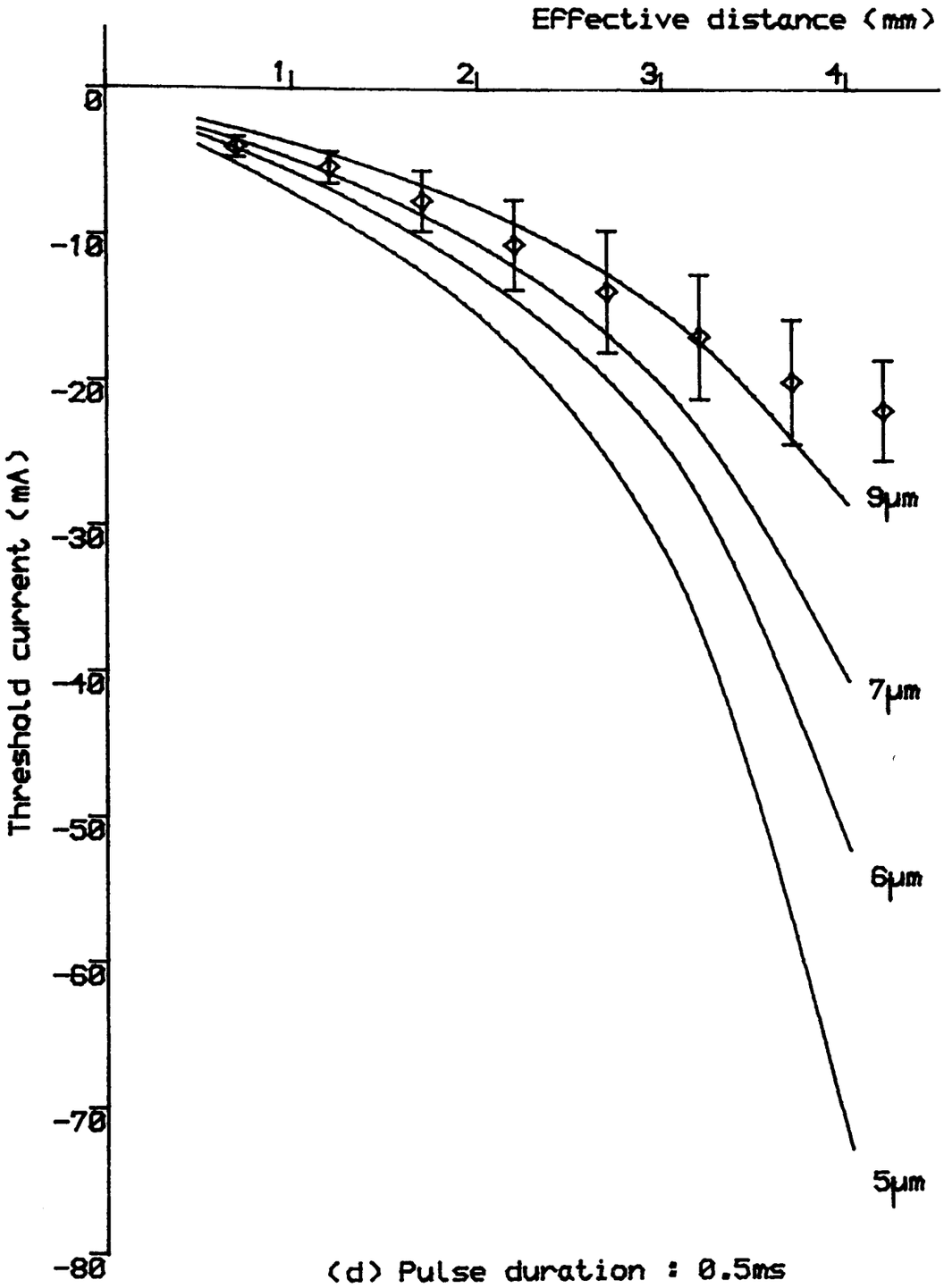

(d) Pulse duration : 0.5ms

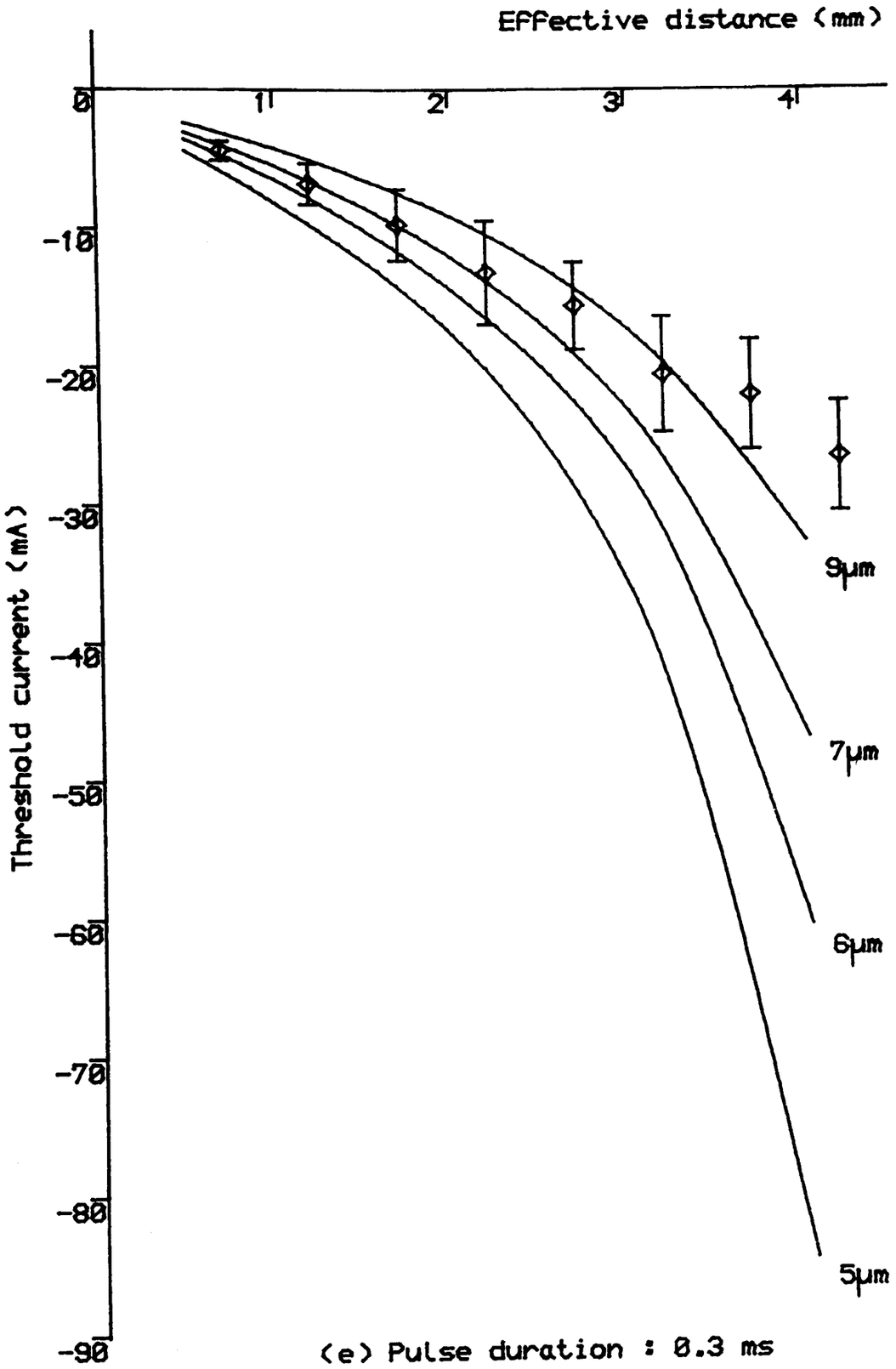

(e) Pulse duration : 0.3 ms

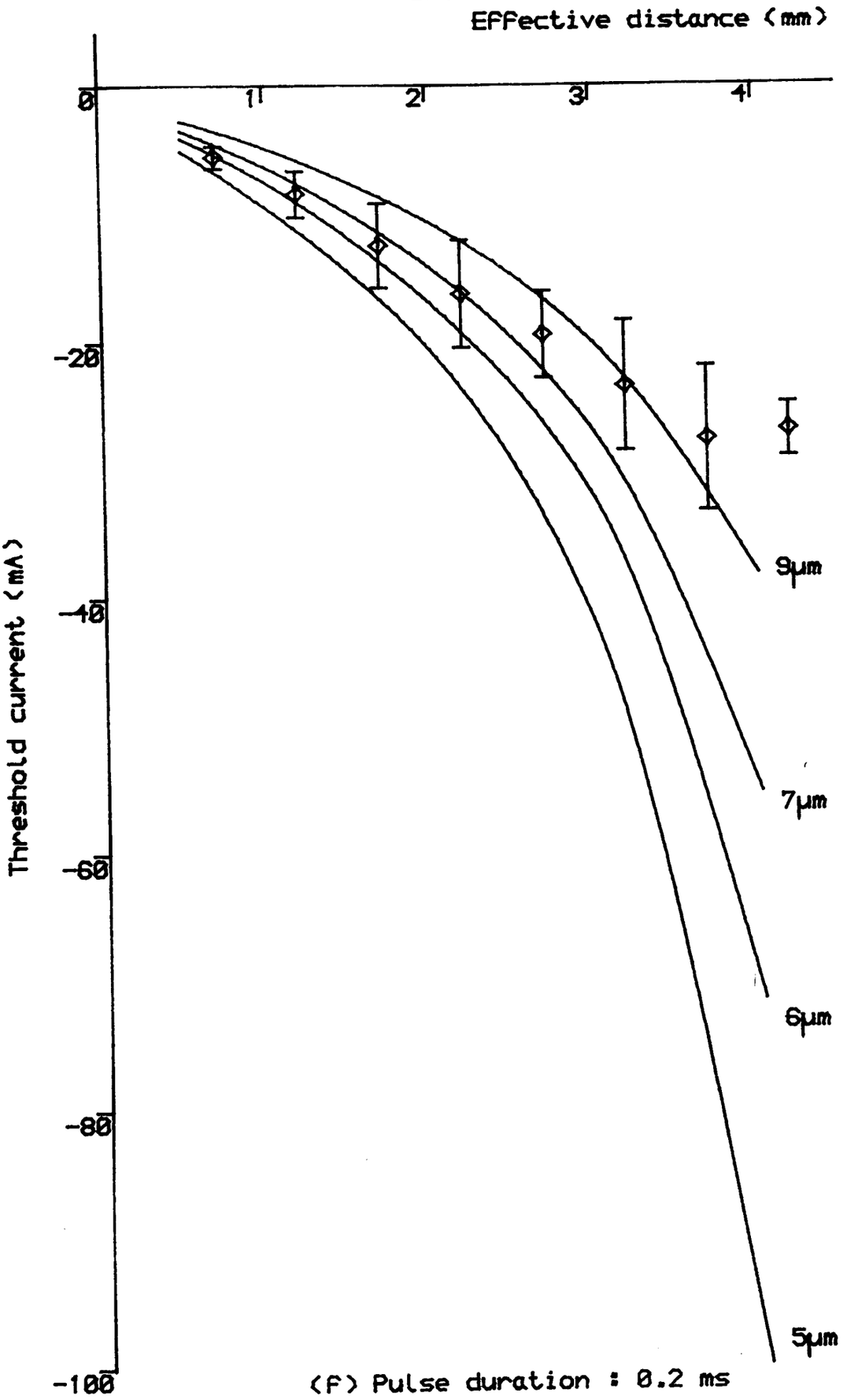
Effective distance (mm)
0
1
2
3
4
-20
-40
-60
-80
-100
Threshold current (mA)
9µm
7µm
6µm
5µm
(F) Pulse duration : 0.2 ms

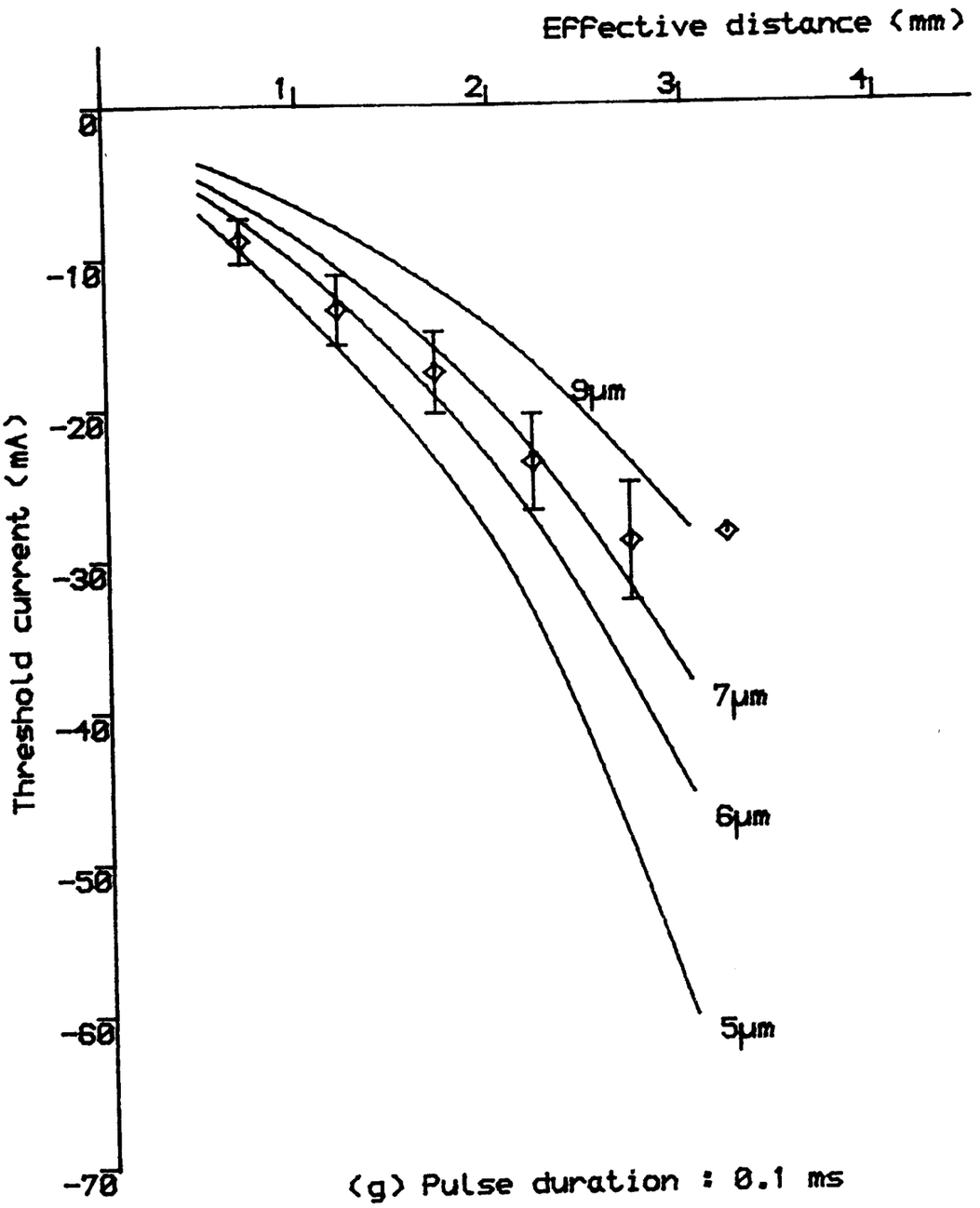

(g) Pulse duration : 0.1 ms

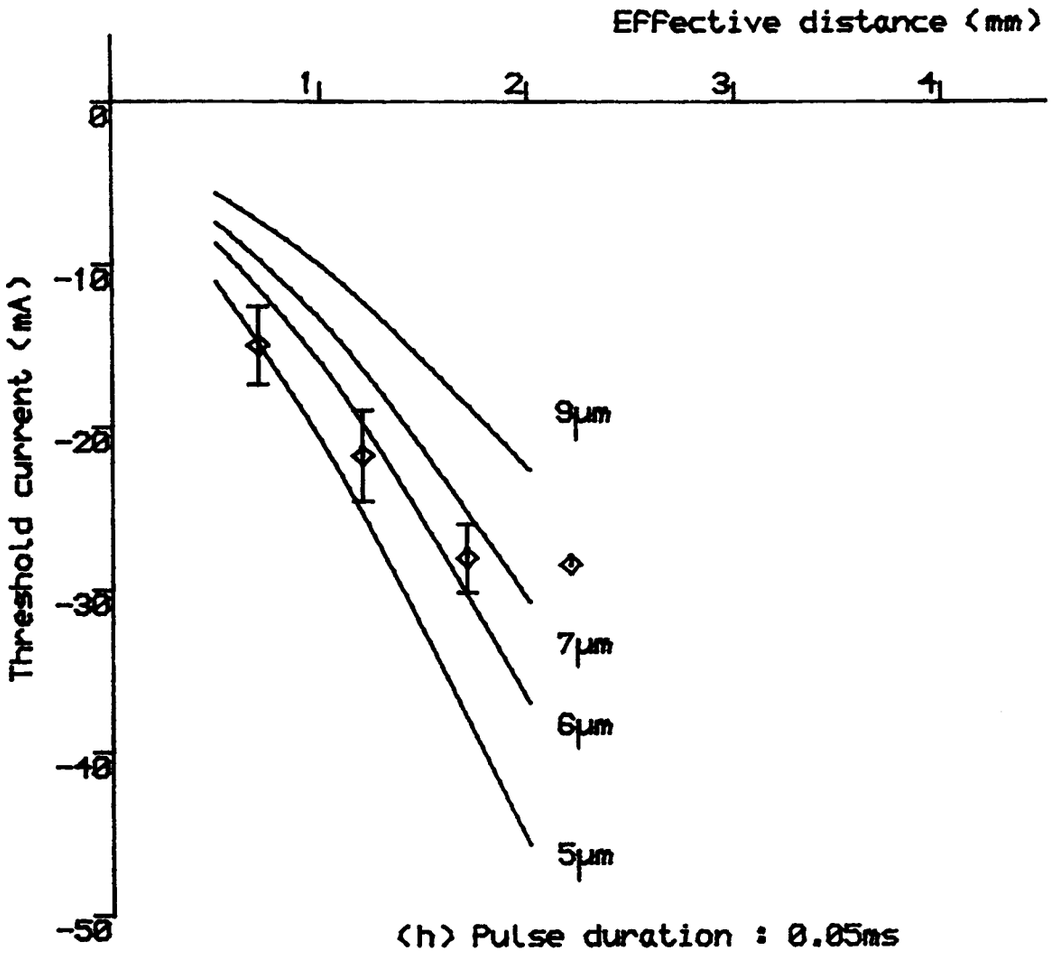

(h) Pulse duration : 0.05ms

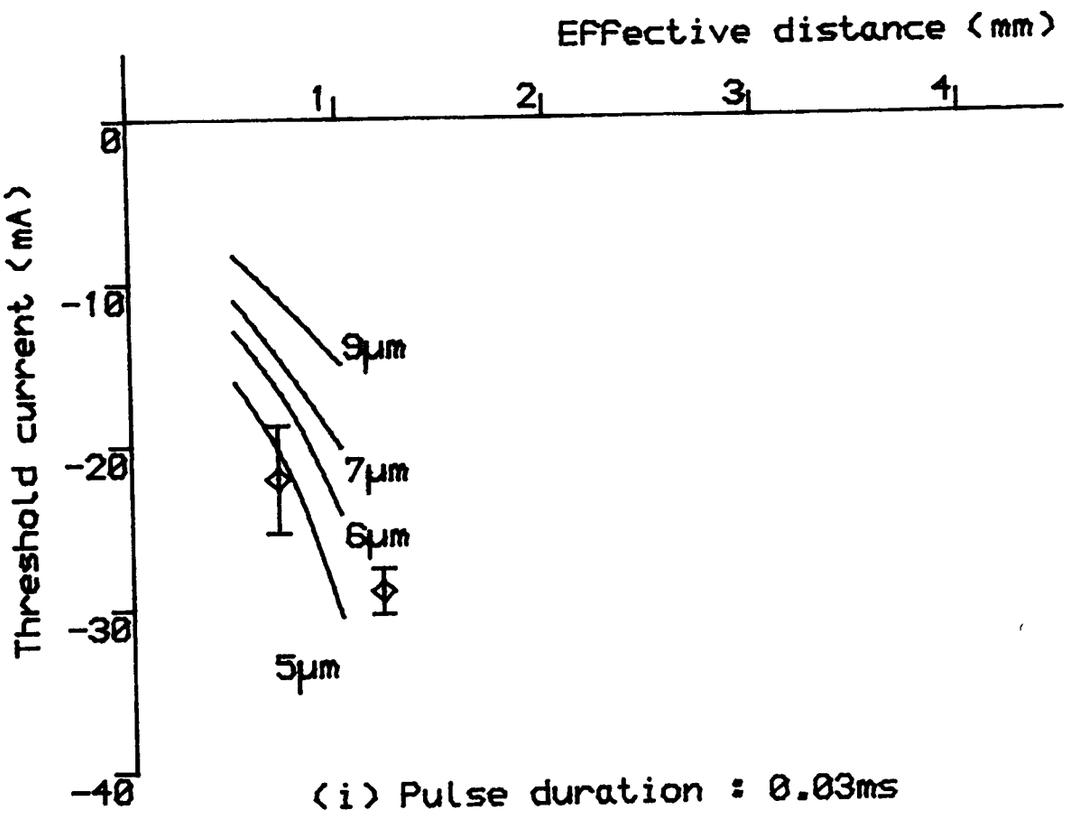

(i) Pulse duration : 0.03ms

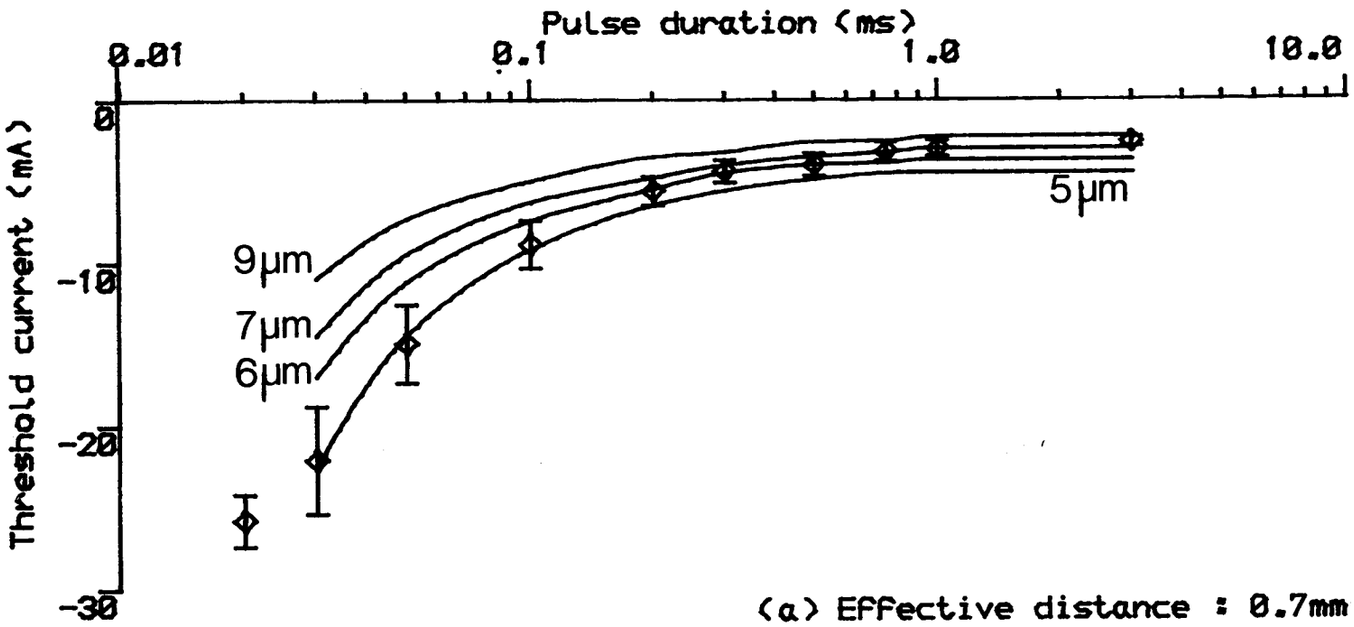

FIGURE 8.9 THRESHOLD CURRENT-DURATION RELATIONSHIP

Cathodic stimulation. For details see text 8.5

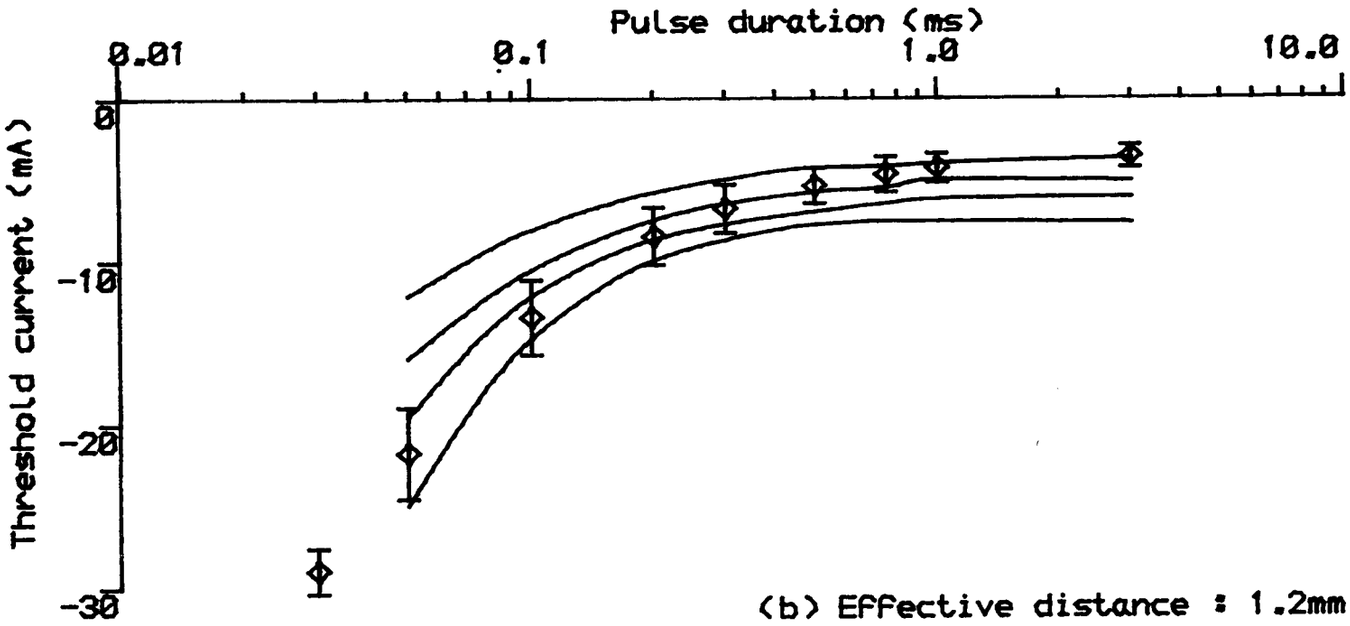
Pulse duration (ms)
0.01
0.1
1.0
10.0
0
-10
-20
-30
Threshold current (mA)
(b) Effective distance : 1.2mm

FIGURE 8.9(b)

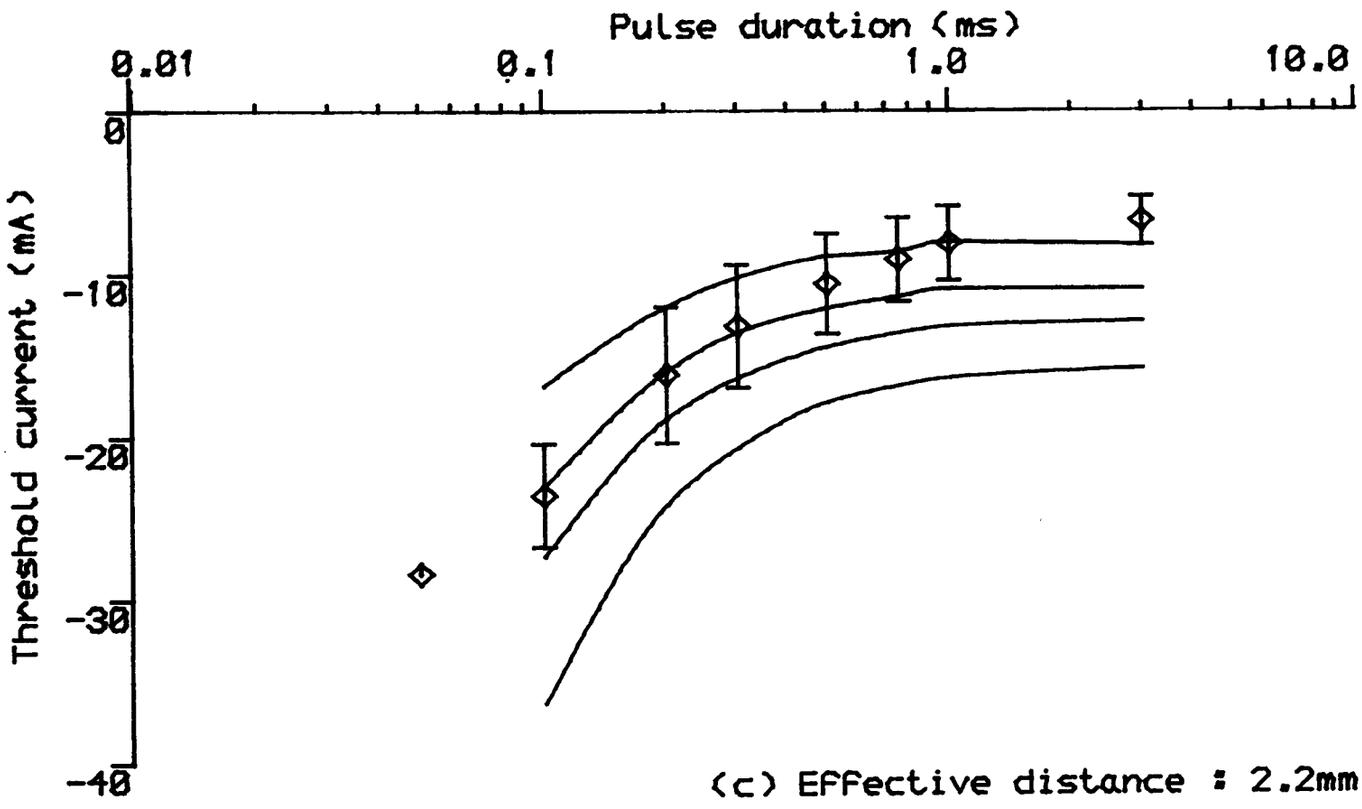
Pulse duration (ms)
0.01
0.1
1.0
10.0
0
-10
-20
-30
-40
Threshold current (mA)
(c) Effective distance = 2.2mm

FIGURE 8.9(c)

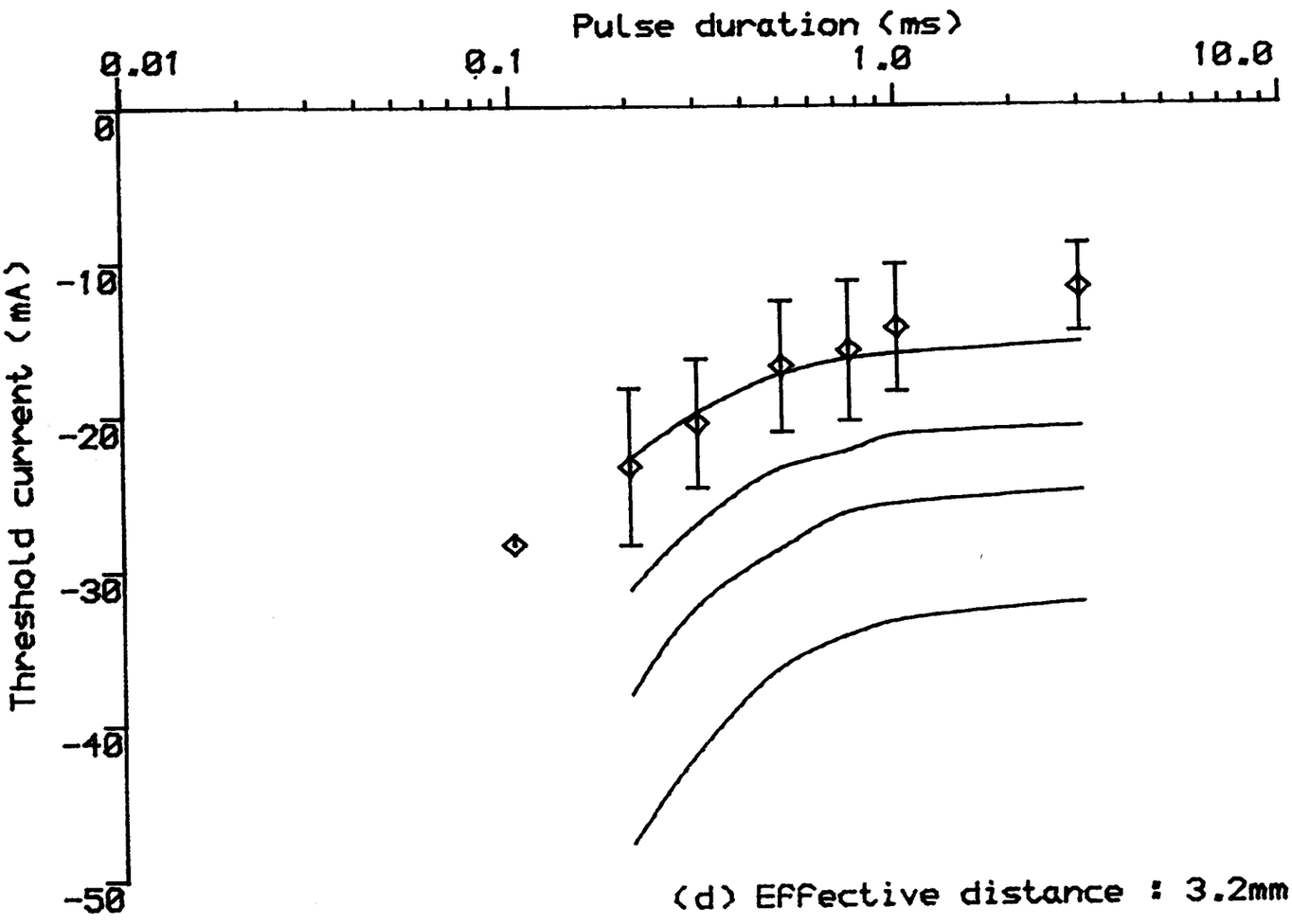
Pulse duration (ms)
0.01
0.1
1.0
10.0
0
-10
-20
-30
-40
-50
Threshold current (mA)
(d) Effective distance : 3.2mm

FIGURE 8.9(d)

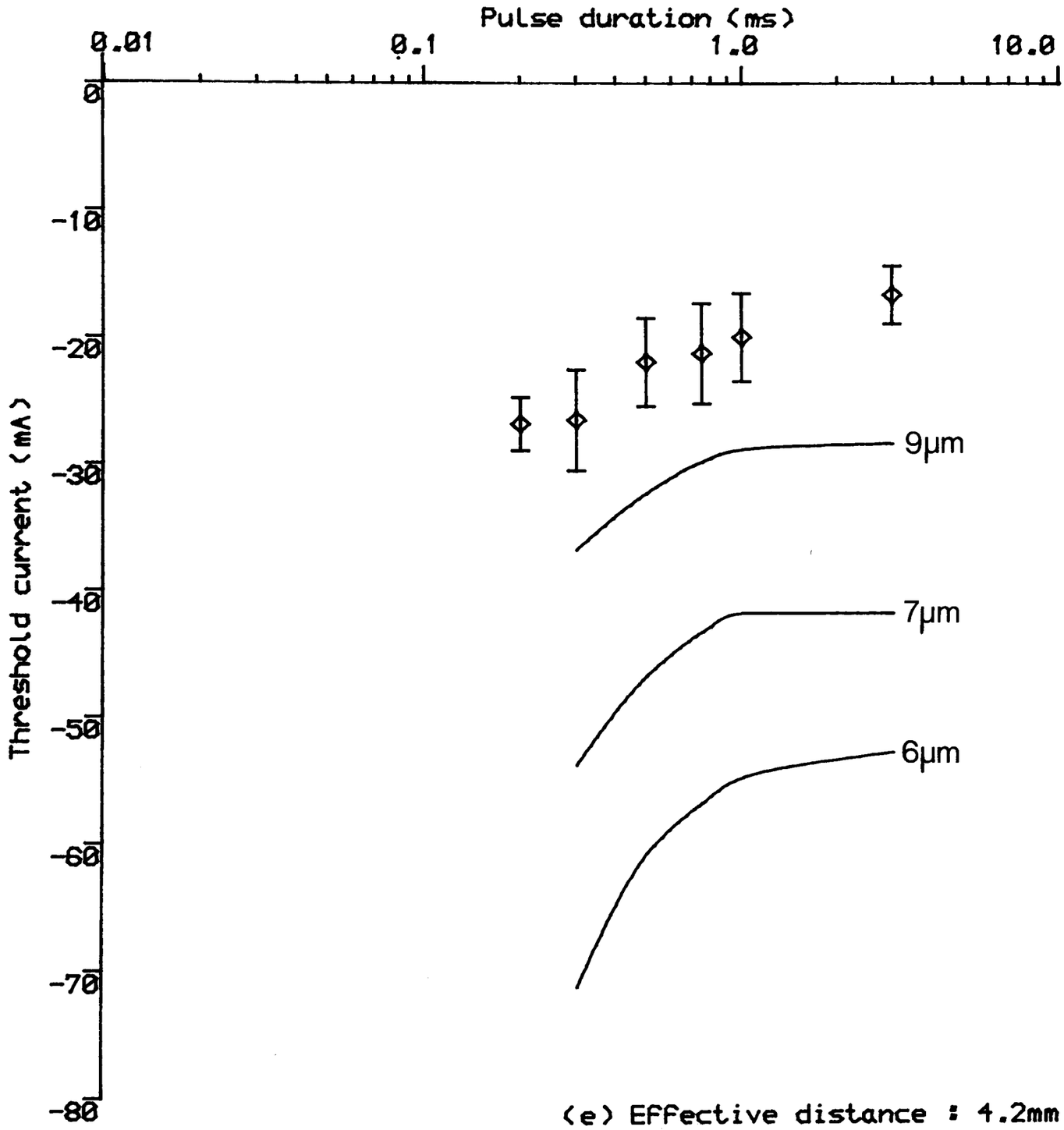
Pulse duration (ms)
0.01
0.1
1.0
10.0
0
-10
-20
-30
-40
-50
-60
-70
-80
Threshold current (mA)
9µm
7µm
6µm
(e) Effective distance : 4.2mm

FIGURE 8.9(e)

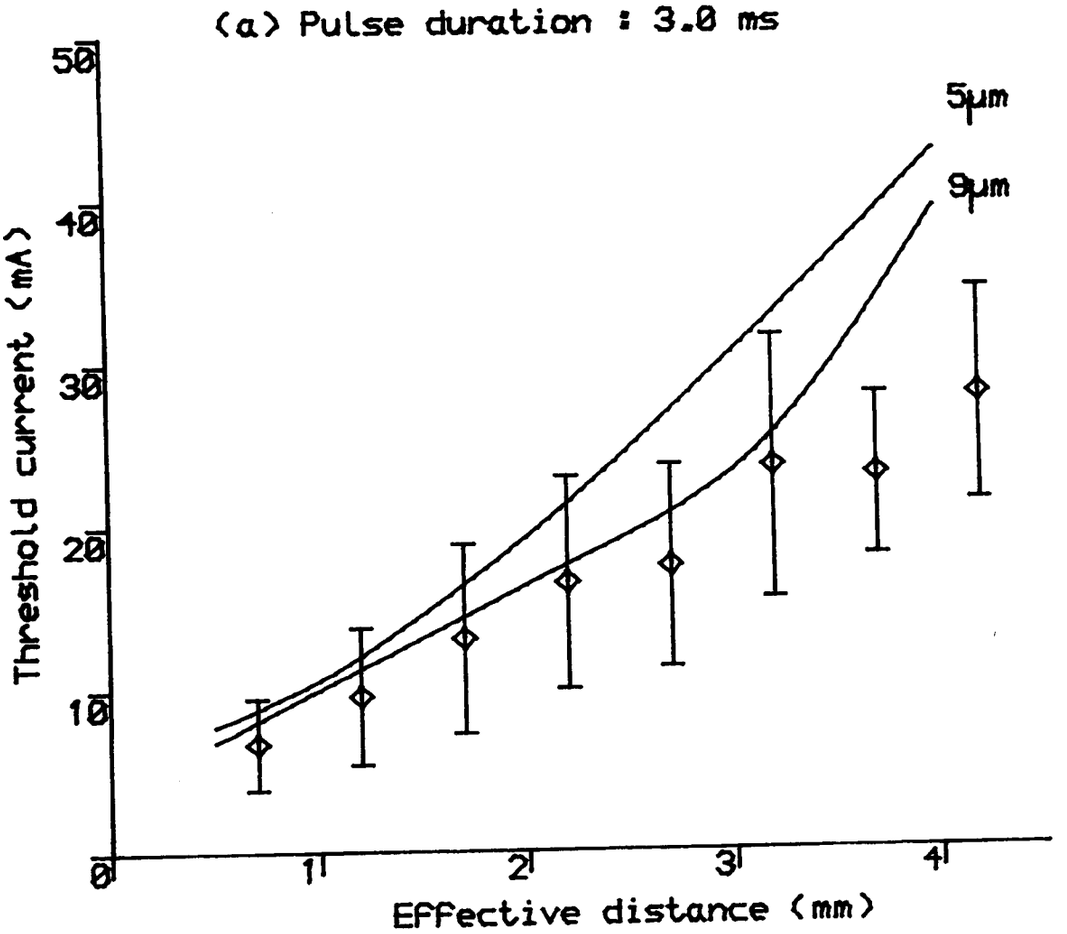

FIGURE 8.10 THRESHOLD CURRENT-DISTANCE RELATIONSHIP

Anodic stimulation. Only 2 theoretical solutions are shown.

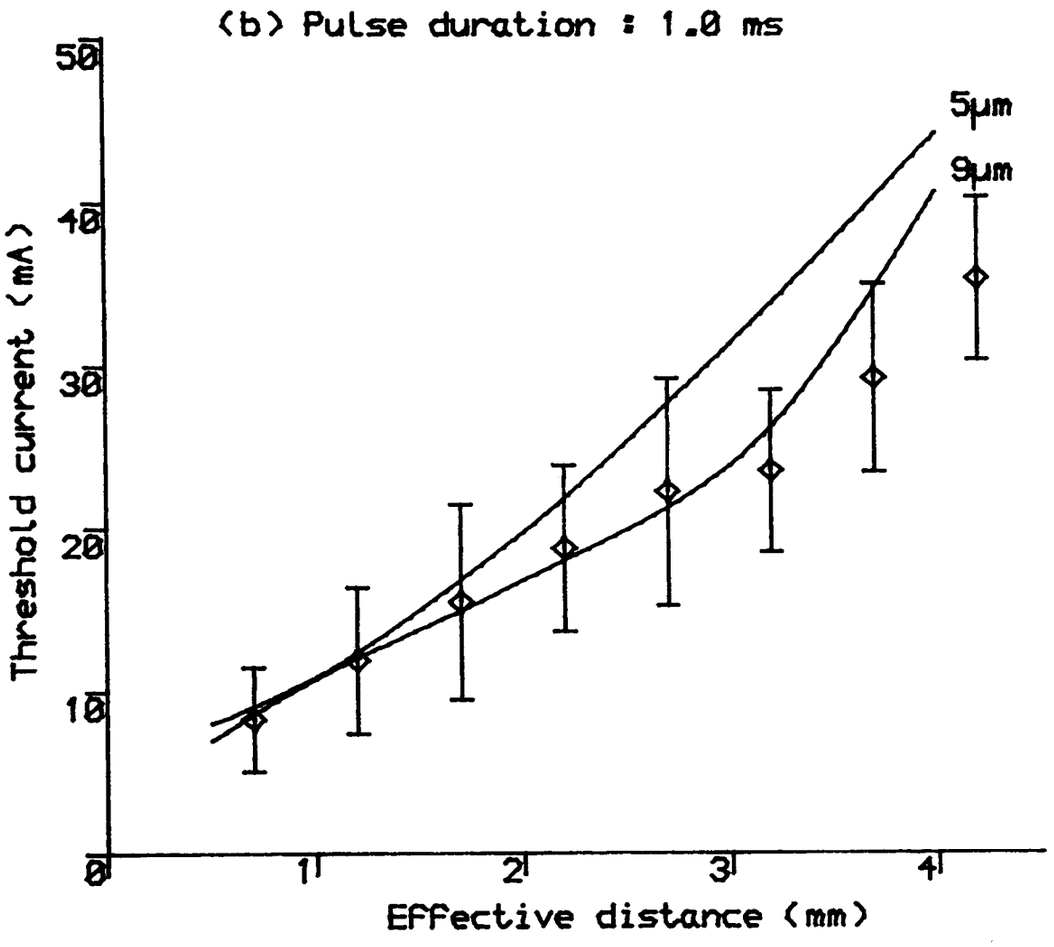
(b) Pulse duration : 1.0 ms
Threshold current (mA)
50
40
30
20
10
0
1
2
3
4
Effective distance (mm)
5μm
9μm

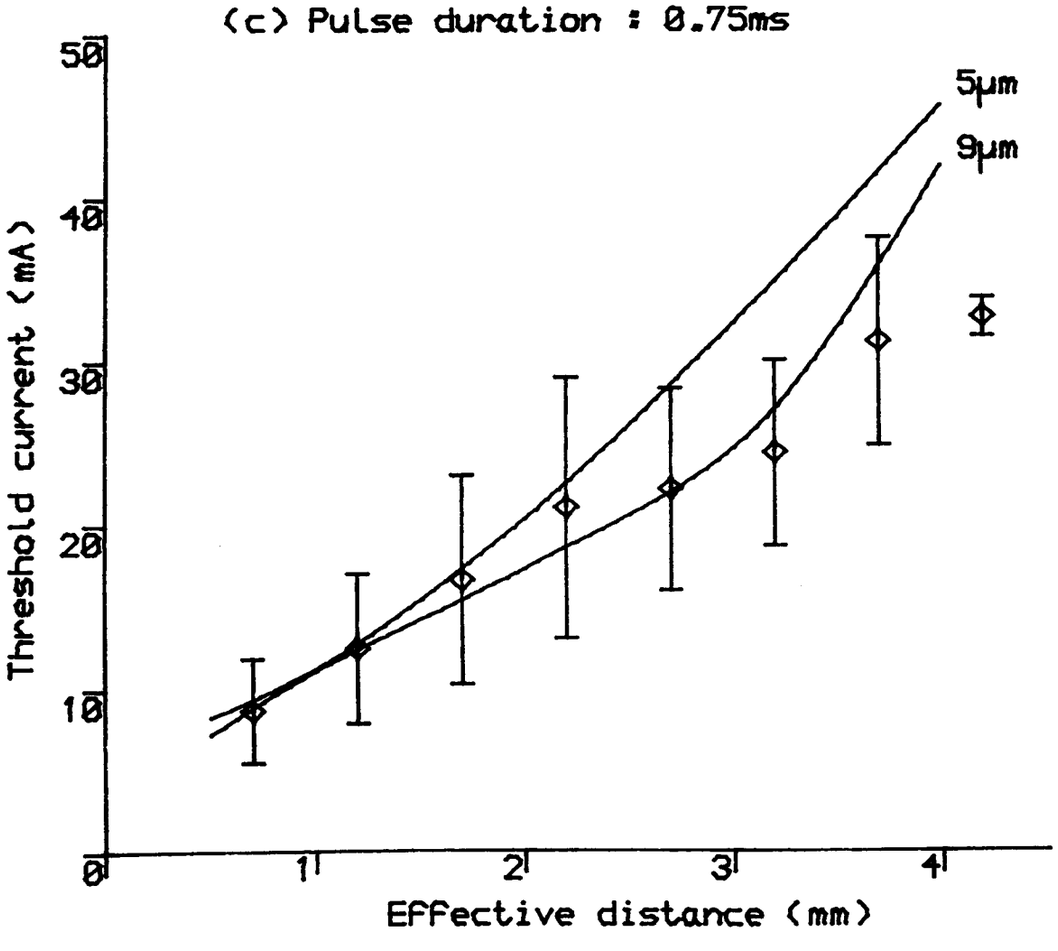
(c) Pulse duration : 0.75ms
Threshold current (mA)
50
40
30
20
10
0
1
2
3
4
Effective distance (mm)
5μm
9μm

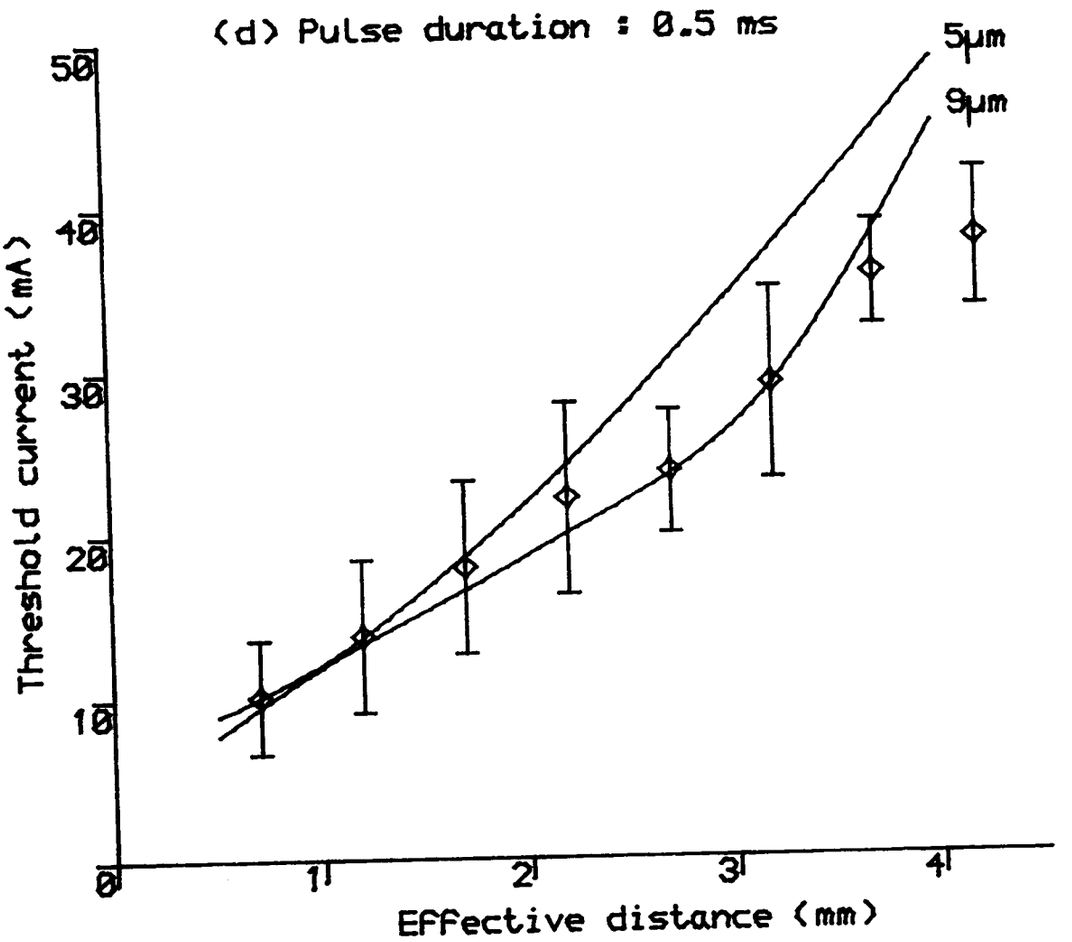
(d) Pulse duration : 0.5 ms
5μm
9μm
Threshold current (mA)
50
40
30
20
10
0
1
2
3
4
Effective distance (mm)

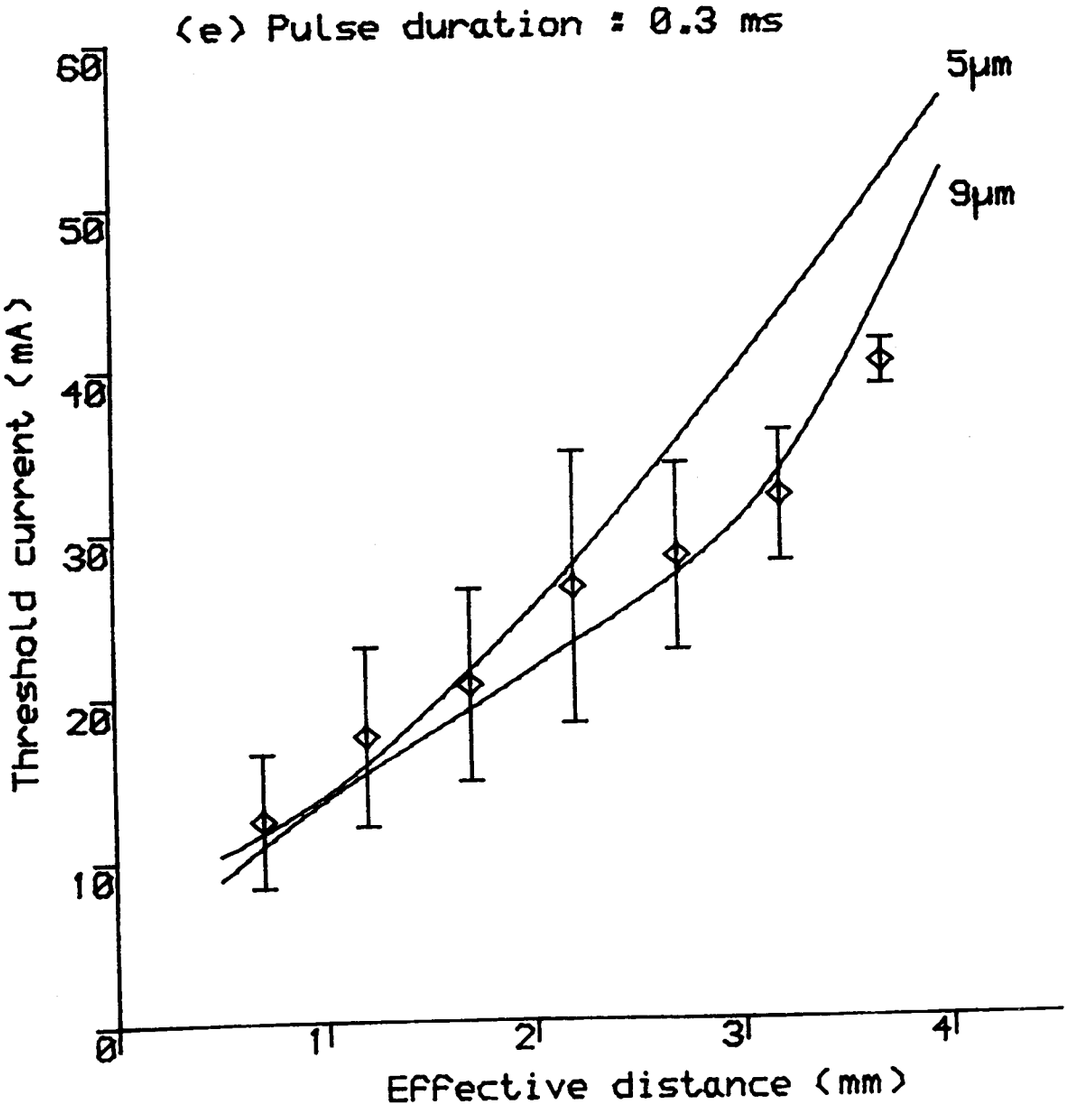
(e) Pulse duration : 0.3 ms
5μm
9μm
Threshold current (mA)
60
50
40
30
20
10
0
1
2
3
4
Effective distance (mm)

(f) Pulse duration : 0.2 ms

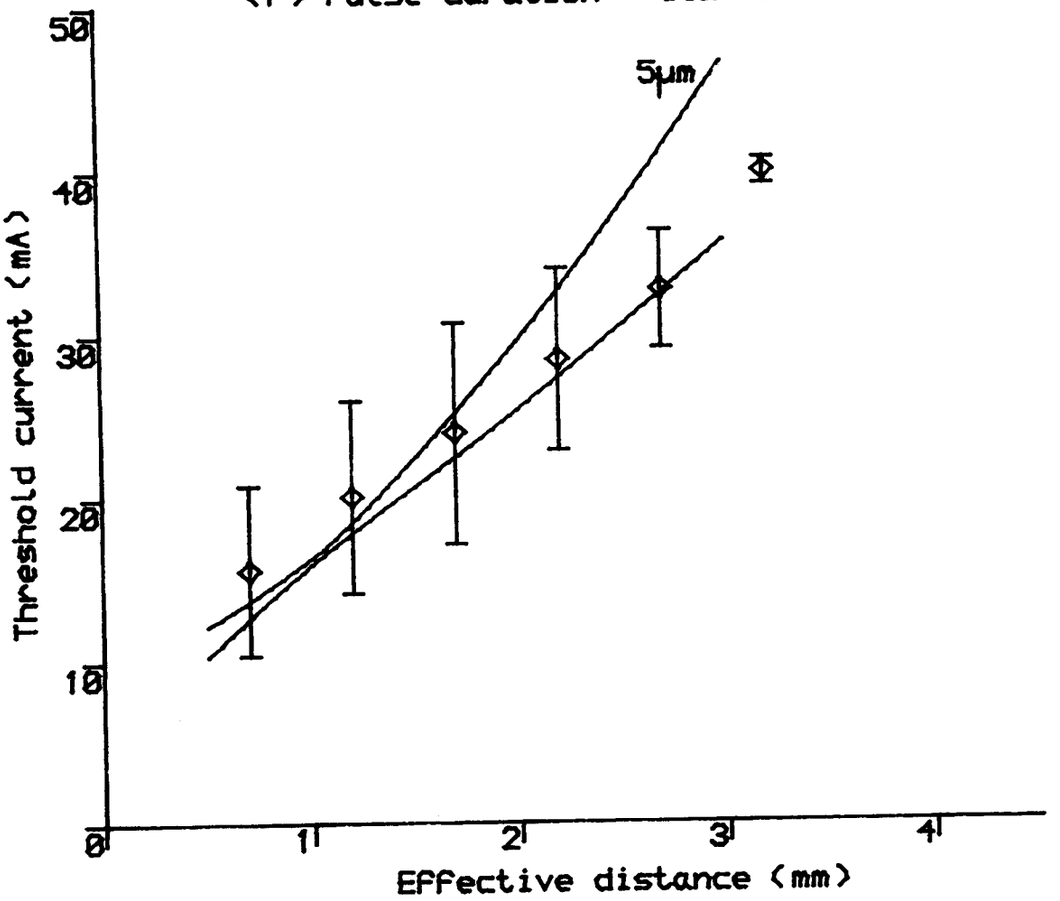

(g) Pulse duration : 0.1 ms

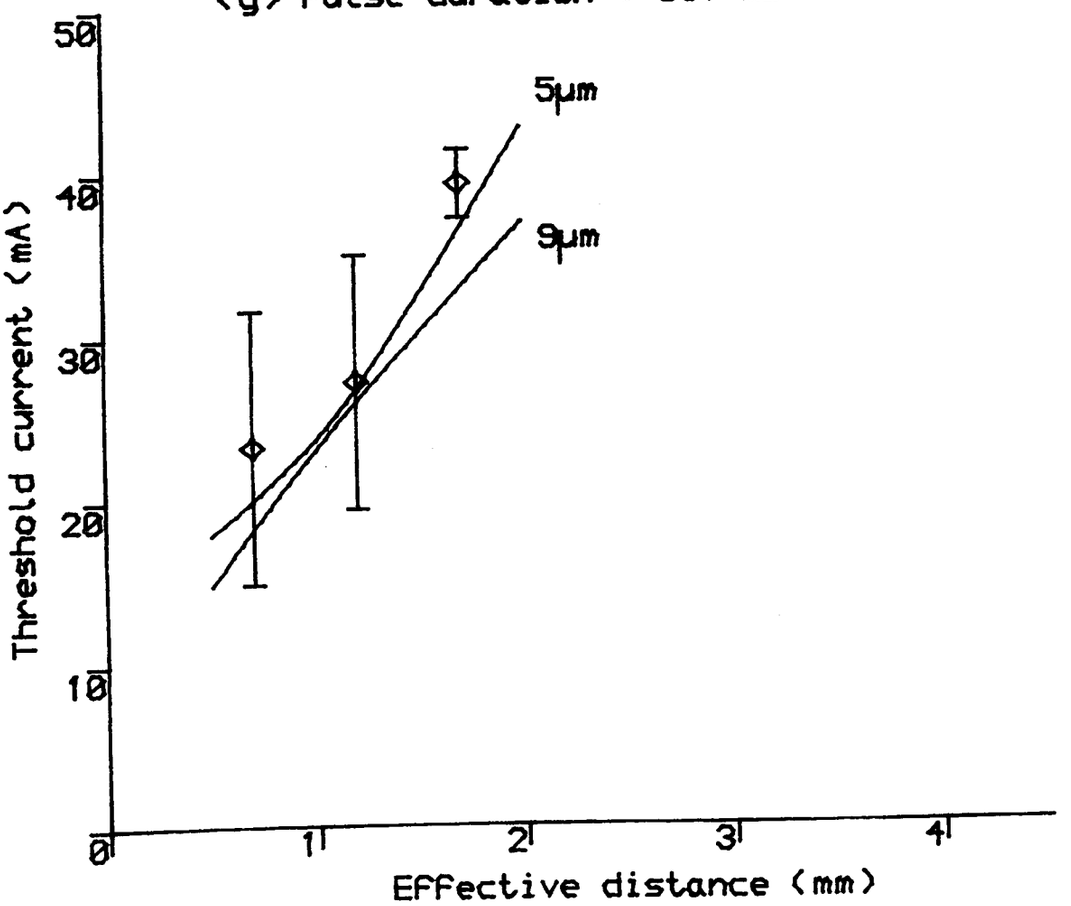

8.5 COMPARISON BETWEEN EXPERIMENTAL RESULTS AND COMPUTER PREDICTIONS

Superimposed on the theoretical curves in Figures 8.8-8.10 are the corresponding experimental data obtained from Table 8.1. The vertical bars indicate ± one standard deviation. Note that the experimental data in Figures 8.8 and 8.10 are shifted to the right by 0.2mm, the correction factor described in Section 8.4.1.

As shown in Figures 8.8 and Figures 8.9, agreements between the predicted and experimental results up to a distance of 3.00mm are good. At distances greater than 3.00mm, the experimental data start to depart from theory and exhibit lower threshold values.

The results for anodic stimulation are shown in Figure 8.10. Although the experimental data may be said to match the theory, there is little difference in the theoretical thresholds predicted for a 5μm and a 9μm fibre. In other words, the experimental data and their standard deviations cover a far greater ranges of threshold values than the model predicts. An examination on the simulation process revealed that the first node to initiate an action potential was the last but one at the end modelling the neuromusclar junction. This junction presented many uncertainties which were neglected in the model, such as orientation and bifurcation of the axon, and the effect of thick muscle on field distribution.

8.6 FIELD DISTORTION ANALYSIS

8.6.1 Testing Scheme

Against the experimental work in Section 8.2, and the theoretical model thereof, is the presence of the tendon wall in the BVC preparation which may distort the field as seen by the nerve fibres. The digital simulation described in last section also assumed that the field was not affected either by the presence of the fibres or the tendon wall. A 3-D finite element model was therefore designed to examine these assumptions.

The finite element model, based upon the experimental assembly, consisted of a tendon suspended midway down a homogeneous bath. The dimensions of the tendon and the nerve bundles were those obtained from histological analysis. A single point source was modelled delivering constant stimulating current close to the tendon wall. The effect of the presence of the wall and the fibres could then be investigated by comparing the theoretical potential profiles along the nerve fibre. Table 8.3 summarises the scheme of the investigation. Little is known about the resistivity of the tendon wall and therefore a range of 70-5000 ohm-cm was examined. Note the conductive anisotropy of myelinated nerve fibres and the dual values for resistivity (transverse and

longitudinal).

TABLE 8.3

case	programmed resistivity values (ohm-cm)			remarks
	nerve bundle	tendon wall	saline bath	
1	70	70	70*	monopolar field in a homogeneous isotropic medium, also considered as 'standard' solution with whom other fields are compared
2	138 long.‡ 1211 tran.	70	70	examine the effect of nerve fibres on fields, i.e. tendon wall effectively not present
3	138 long. 1211 tran.	500	70	(3) & (4) examine the effect of tendon wall on fields. (2) can also be considered of having 70 ohm-cm for the tendon wall
4	138 long. 1211 tran.	5000	70	

* measured value, represent Krebs-Henseleit solution

‡ GEDDES and BAKER (1967)

Table 8.3 does not mention the position of the point source with respect to the tendon. In fact, three positions were examined : 1.75mm, 2.375mm and 3.375mm. These were the separations between the point source and the centre of the nerve bundle, defined as the 'total distance'. Note that if they are corrected with the tendon

wall thickness, nerve bundle radius and the effective radius of the finite size electrode used in the BVC stimulation experiments, they are actually 0.45mm, 1.075mm and 2.075mm: these were the clear distances (x) between the edge of the tendon wall and the electrode tip (Figure 8.3).

Details of the finite element model are given in Appendix 8.

8.6.2 Results of Field Distortion Analysis

Figures 8.11 (a) to (c) shows the theoretical field profiles along the center of the nerve bundle for different electrode positions. The diamond points, cases #1, were the values assuming a homogeneous isotropic medium with no tendon present. The distortion of the field by the nerve fibres with no tendon wall, as shown in cases #2 in the figure, is not significant. Figures 8.11(b) and (c) also show that when the total distance is more than 2.375mm, field distortion is negligible, whatever the resistivity values of the tendon wall are (cases #3 and #4).

On the other hand, when the total distance is less than 2.375mm, the sharpness of the field profile in the nerve bundle is increased by the presence of the tendon wall, increasingly so for higher tendon resistivities.

The analysis can also be interpretated in terms of the 'driving function' described in Chapter 7. The functions of the theoretical field profiles in Figure 8.11

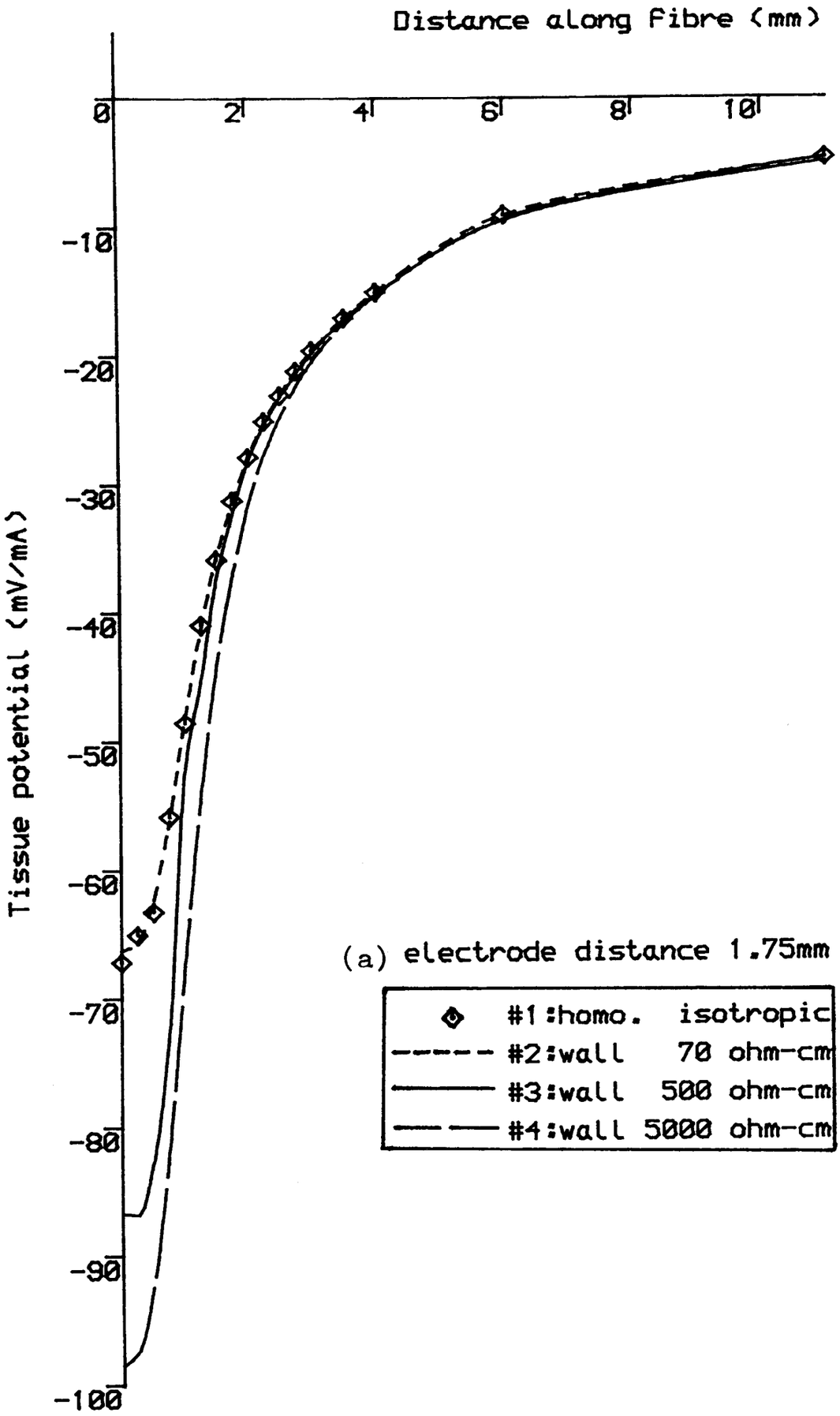

FIGURE 8.11 EFFECT OF TENDON WALL ON FIELD PROFILE VERTICALLY ALONG THE NERVE BUNDLE

For details see text 8.6 2
(a) 1.75mm (b) 2.375mm (c) 3.375mm

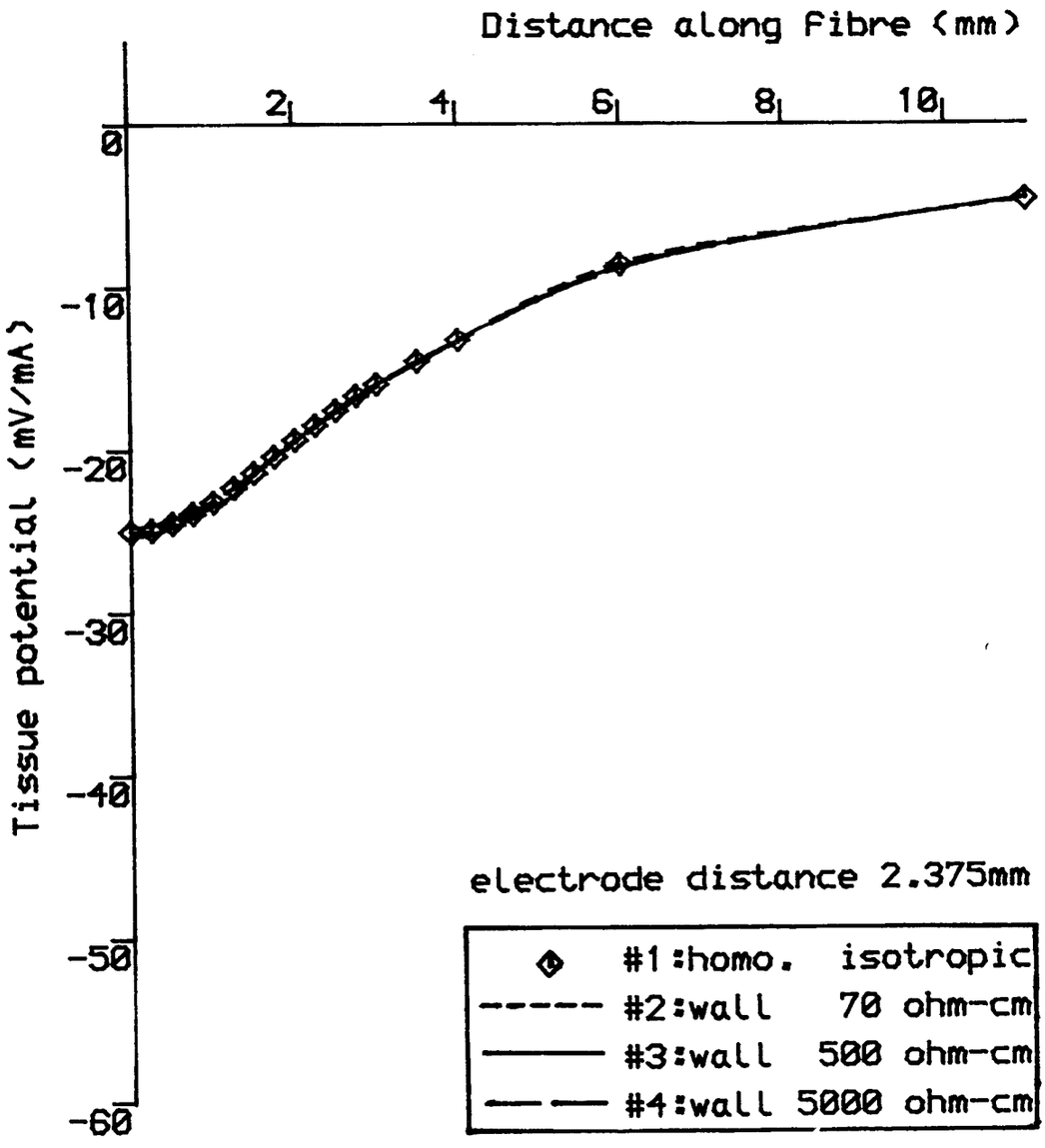
Distance along Fibre (mm)
2
4
6
8
10
0
-10
-20
-30
-40
-50
-60
Tissue potential (mV/mA)
electrode distance 2.375mm
#1:homo. isotropic
#2:wall 70 ohm-cm
#3:wall 500 ohm-cm
#4:wall 5000 ohm-cm

FIGURE 8.11(b)

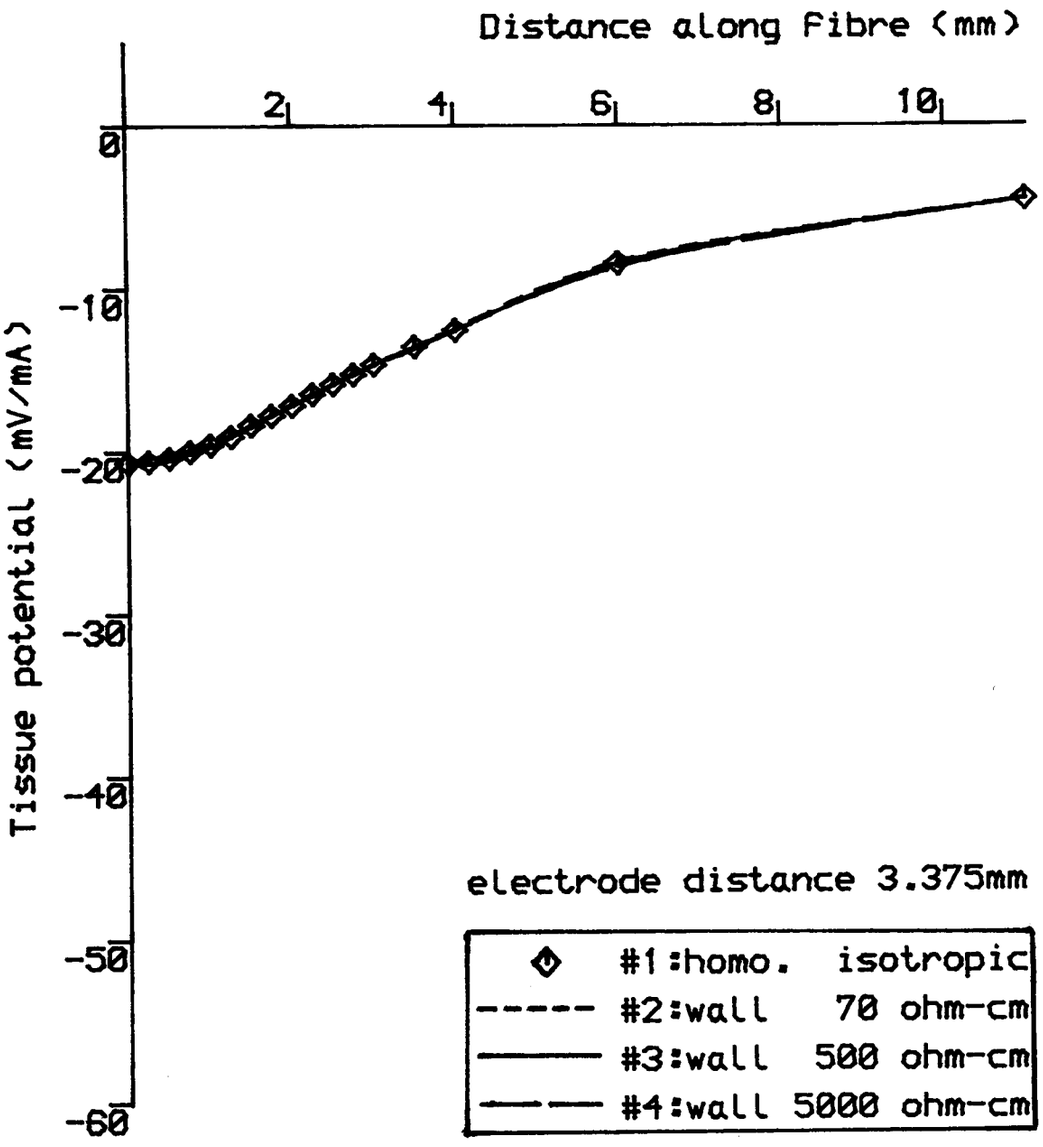
Distance along Fibre (mm)
2
4
6
8
10
0
-10
-20
-30
-40
-50
-60
Tissue potential (mV/mA)
electrode distance 3.375mm
#1:homo. isotropic
#2:wall 70 ohm-cm
#3:wall 500 ohm-cm
#4:wall 5000 ohm-cm

FIGURE 8.11(c)

are now presented in Table 8.4. Each column of the table contains the driving function of the same field, but seen by fibres of different diameters.

TABLE 8.4

(a) total distance 1.75mm
(b) total distance 2.375mm
(c) total distance 3.375mm

fibre diameter (μm)	driving function , Ve.j-1 - 2Ve.j + Ve,j+1. case 1 : homogeneous	case 2 : wall 70	case 3 : wall 500	case 4 wall 5000	
5.0	7.8	8.0	8.6	13.8	
7.5	22.6	20.2	22.4	35.2	(a)
10.0	37.2	36.2	69.2	63.8	
5.0	1.0	1.0	1.2	1.0	
7.5	2.2	2.2	2.4	2.0	(b)
10.0	3.6	3.6	3.8	3.2	
5.0	0.6	0.8	0.6	0.6	
7.5	1.4	1.4	1.4	1.2	(c)
10.0	2.2	2.2	2.2	2.2	

Unit of driving function is mV per mA stimulating current

A comparison of the values in each row reveals that the effective stimulus is distorted only when the total distance is less than 2.375mm.

8.7 RELATIONSHIPS BETWEEN THRESHOLD PREDICTION AND SHARPNESS Of APPLIED FIELD

The threshold of a fibre, as mentioned in Section 7.3.3, depends on the sharpness of the applied field profile 'seen' by the fibre. This section therefore investigates this relationship for cathodic stimulation.

A random check on the simulation process in Section 8.4 confirms that, for cathodic stimulation, the node nearest to the stimulating electrode was the first one to become active.

Figures 8.12(a) and (b) show the current/driving-function relationships for two different pulse durations. The driving functions were calculated from the input files used for the simulation programs in Section 8.4. The corresponding threshold predictions were obtained from Figure 8.8. There are four or five data points for each fibre diameter in the figures, each represents a different electrode distance from the fibre.

The two figures show that for a given pulse duration, the current/driving-function relationship seems to be a simple inverse-proportionality.

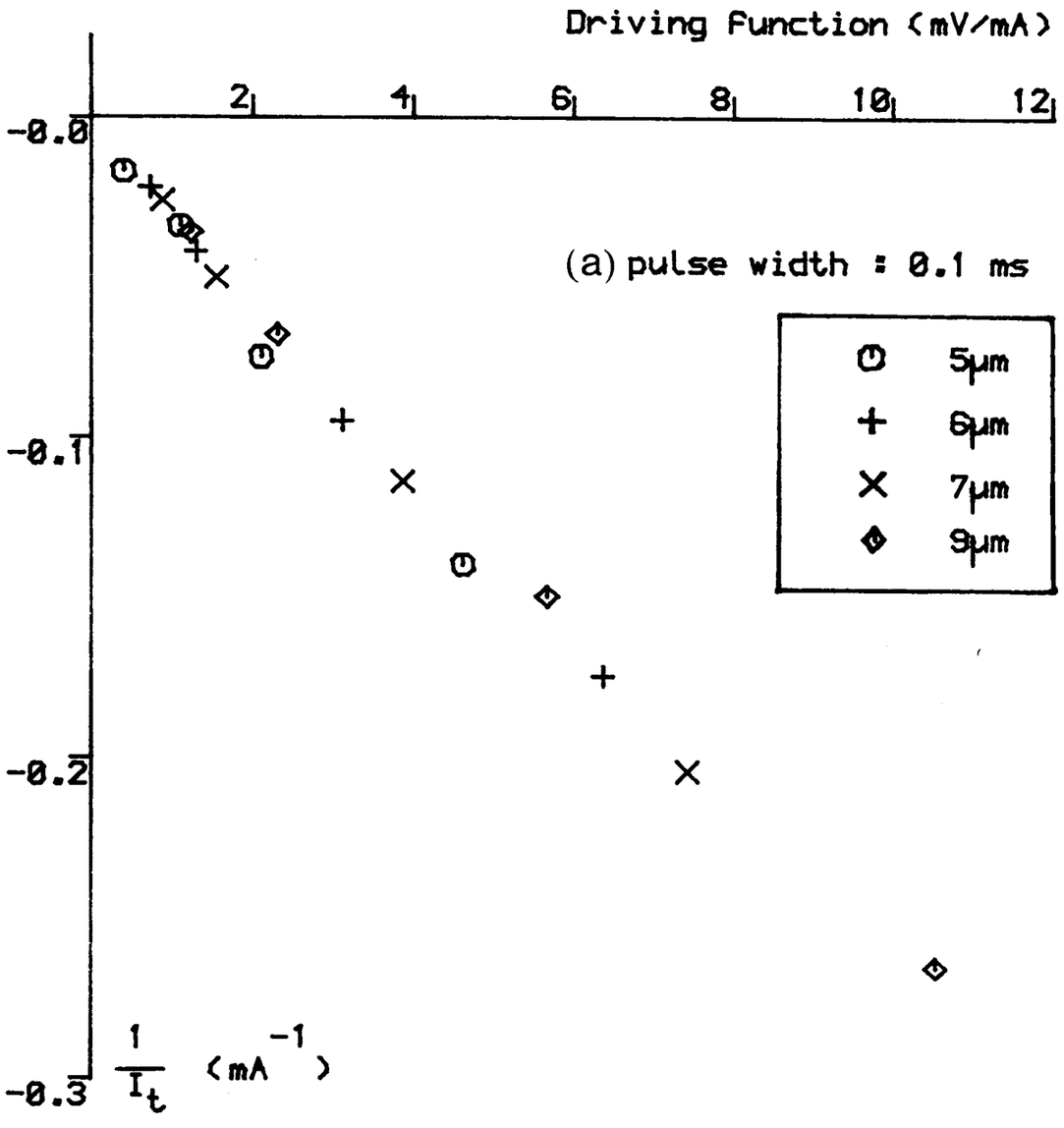

FIGURE 8.12 RELATIONSHIP BETWEEN DRIVING FUNCTION AND THEORETICAL THRESHOLD CURRENT

(a) pulse width 0.1ms
(b) pulse width 3.0ms

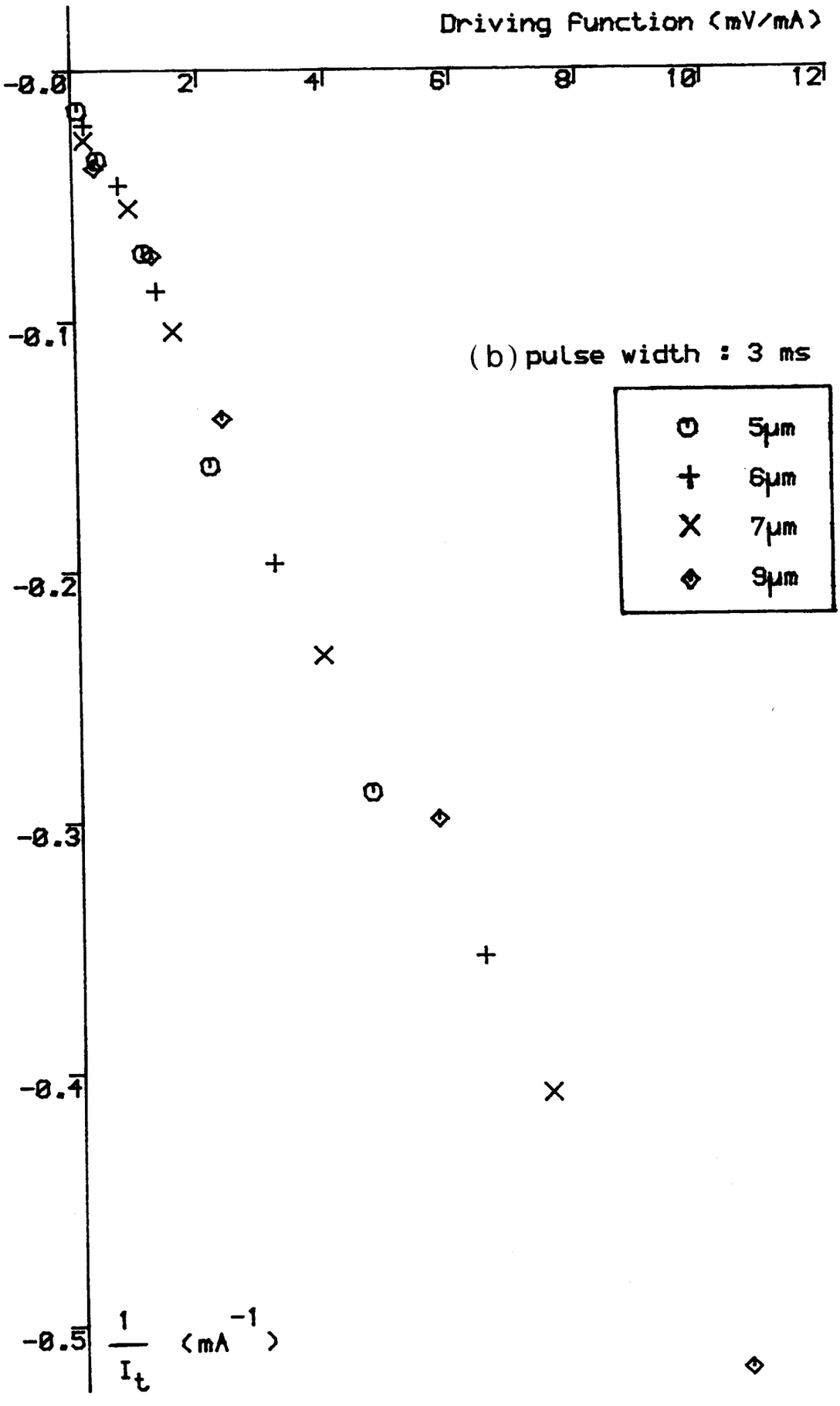
Driving Function (mV/mA)
-0.0
2
4
6
8
10
12
-0.1
-0.2
-0.3
-0.4
-0.5
(b) pulse width : 3 ms
5μm
6μm
7μm
9μm
1/I_t (mA^-1)

CHAPTER 9

FURTHER THEORETICAL ANALYSES OF MYELINATED FIBRE MODEL

9.1 NETWORK MODEL DEVELOPMENT : MODEL A, INCLUDING LONGITUDINAL CONDUCTION IN THE EXTRACELLULAR FLUID

9.1.1 Model Definition

Figure 9.1 shows the new network model developed from the model in Chapter 7. The essential feature is the addition of linear elements, Ge, to represent the external conducting path. Note that the external voltages Ve are no longer under arbitrary control. Instead they will be influenced directly by the membrane activity. The present network, arbitrarily called model A, is in fact an intermediate development. The ultimate aim is a model for the investigation of actions of stimulus fields on propagating action potentials. This model is the subject of the next section. Model A, nevertheless, needs to form the basis for the latter development. Two fundamental fibre properties can be examined in this model : shape of action potential waveform and propagation velocity.

9.1.2 External Conducting Path

Unlike the conductance Ga in the axoplasm, the actual numerical value for Ge is unknown. Provided that the fibre is in a conducting medium, the lower limit of Ge

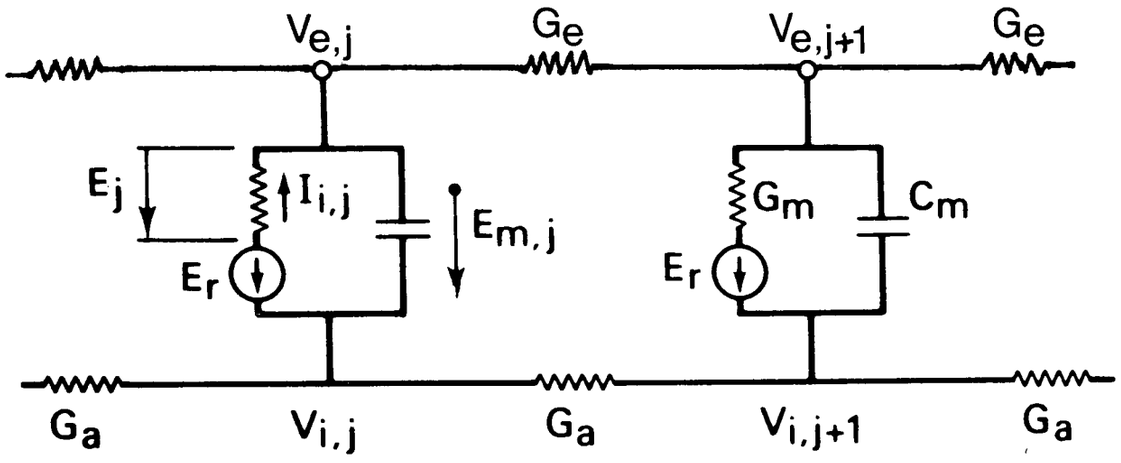

FIGURE 9.1 MODEL A NETWORK

For details see text 9.1.1

should be greater than Ga. The upper limit of Ge. on the other hand, should be lower in vivo than the case when a fibre is immersed in an infinite homogeneous saline solution. Moreover, Ge may also bear a relation with the fibre diameter. Therefore the main idea behind the development of model A is to find an 'optimal' or an 'acceptable' value for Ge. The analysis mainly concentrated on the effects of different Ge values on action potential propagating velocity.

9.1.3 System Equations

The derivations of the equations are included in Appendix 9. In general, the behaviour of the membrane depolarisation at node j is described as

$$C_m \dot{E}_j = \frac{Ga*Ge}{Ga+Ge} (E_{j-1} - 2E_j + E_{j+1}) - I_{i,j} \qquad (9.1)$$

where the ionic current Ii,j is modelled by the F-H set of equations. Equation (9.1) may be "forward-integrated" for each node to yield the time response of the nodal depolarisation. Matrix manipulation may not be necessary; although the benefit of using it is that a fibre system considered can be visualized from the system matrices. Eqn (9.1) shows remarkably similarity with those describing the McNEAL model (Eqn. A3.1 in Appendix 3). The differences between them are the coefficients and the

disappearance of applied external field potential Ve.

9.1.4 Analysis Conditions

The initial and boundary conditions for the analysis of model A are dealt in this section.

Boundary conditions : Owing to the demands on computational time, a 50-nodes model was built which was symmetrical about the left-hand end, i.e. node 1. This condition was equivalent to placing an imaginary node at j=0, and maintaining $E_0 = E_2$. The end condition on the right hand was simply using zero depolarisation ,i.e. E_{50} =0. In other words, the number of 'effective' nodes in the model were 49, and any nodes beyond node 49 were assumed to have zero depolarisation.

Initation of action potential : As the external potential, Ve. no longer appears in the system equations, action potential cannot be initiated by external applied fields. One artifical method was to specify E_1 = 100 mV during the first integration time step. An action potential would develop very soon and propagated along the fibre. Standard initial conditions concerning F-H equations applied.

9.1.5 Computing Method

Euler's method of integration was adequate to solve the system equations, i.e.

$$E(t+\Delta t) = E(t) + \Delta t * \dot{E}(t)$$

Integration time step (Δt) was 0.002 ms and a typical total simulation time was 3.0 ms. The program was written in FORTRAN IV language and run locally on an interactive Honeywell 68 DPS Multics system.

Conduction velocities were calculated from the time taken for the E = 50 mV point on the rising phase of the impulse to travel from node 20 to node 30.

9.1.6 Results

Figure 9.2 shows an action potential curve plotted as a function of time. The location is at node 20 of a 20μm fibre. Initial condition was E_1 = 100 mV at time t = 0 . The figure shows that the curve has an amplitute of 114 mV and a duration of about 1.5 ms. There is a rapid rise to the peak and a slower decay. Although not shown clearly, there is a 0.5 mV undershoot at the tail.

Figure 9.3, from the same data, plots the action potential travelling to the right from the origin (node = 1) at different instants of time separated by 0.5ms. It should be noted that there is also an imaginary impulse travelling from the origin to the left. The constant spacing between each impulse confirms steady propagation. The impulse at t = 2.0 ms, labelled (d) in Figure 9.3, is also reproduced in Fig. 9.4 for detailed examination. The essential features of it are a rapid rise followed by a slower decay, and there is a small amount of undershoot at the tail.

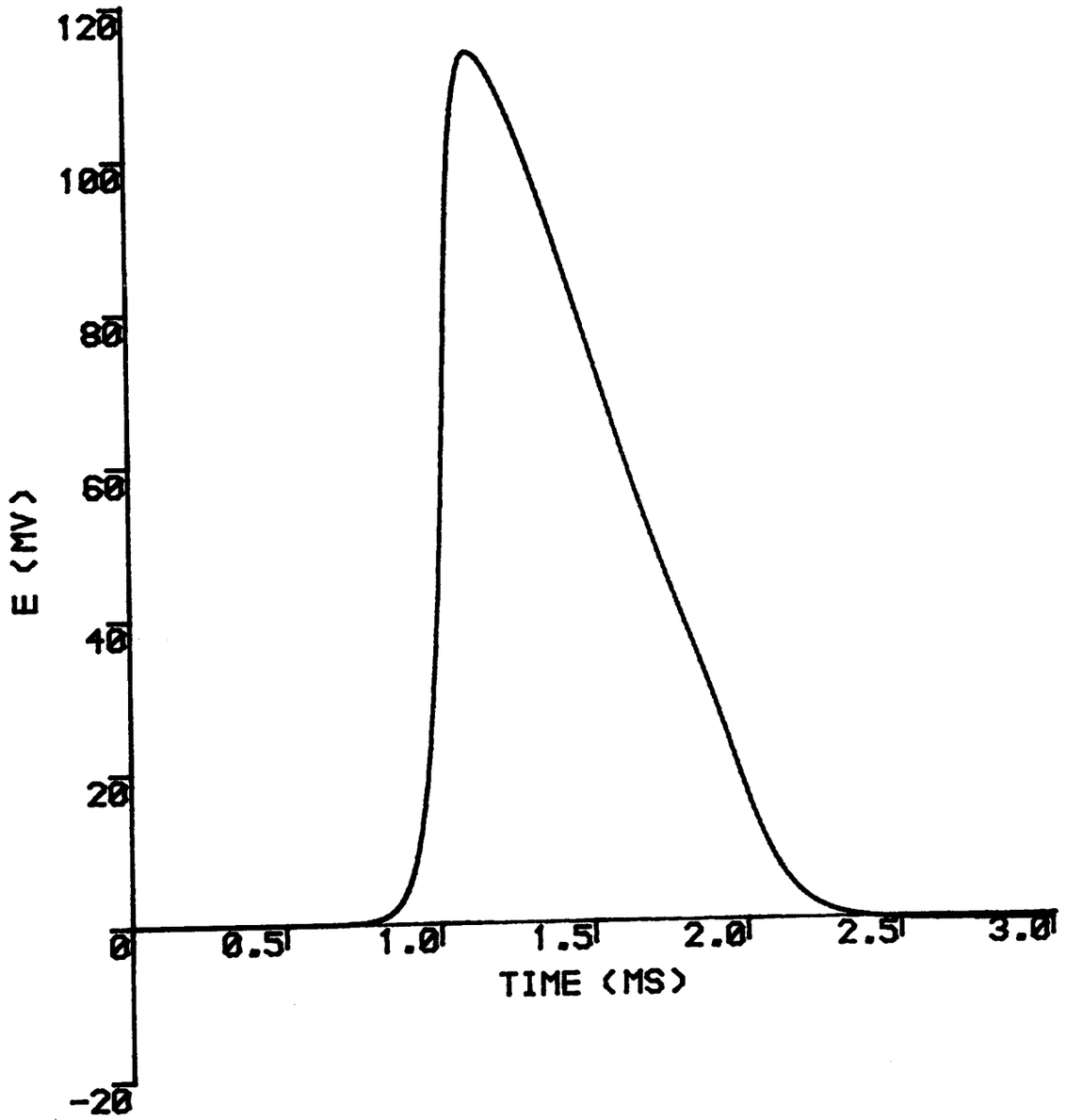

FIGURE 9.2 TEMPORAL ACTION POTENTIAL CURVE

For details see text 9.1.6

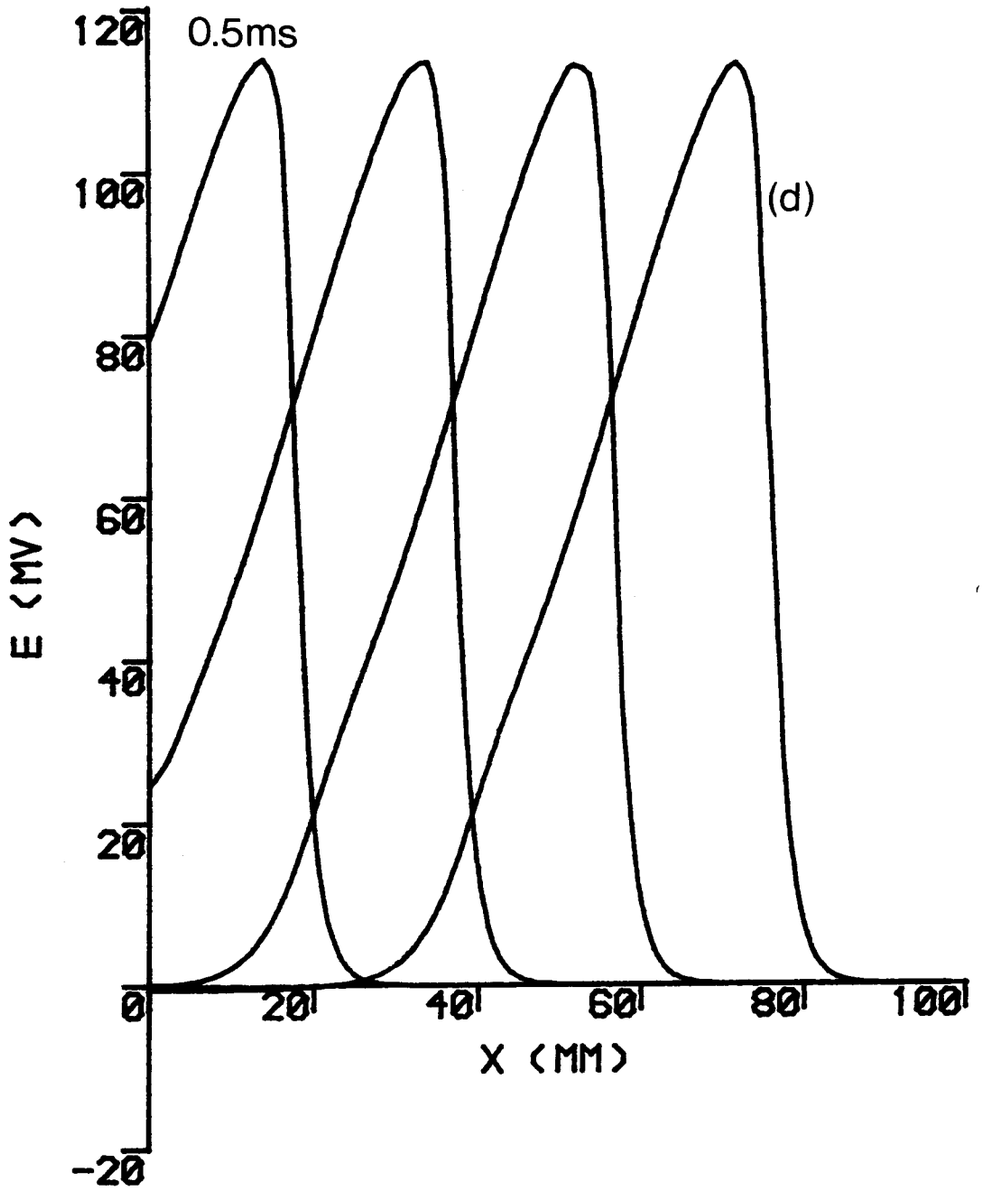

FIGURE 9.3 SPATIAL ACTION POTENTIAL CURVES

For details see text 9.1.6

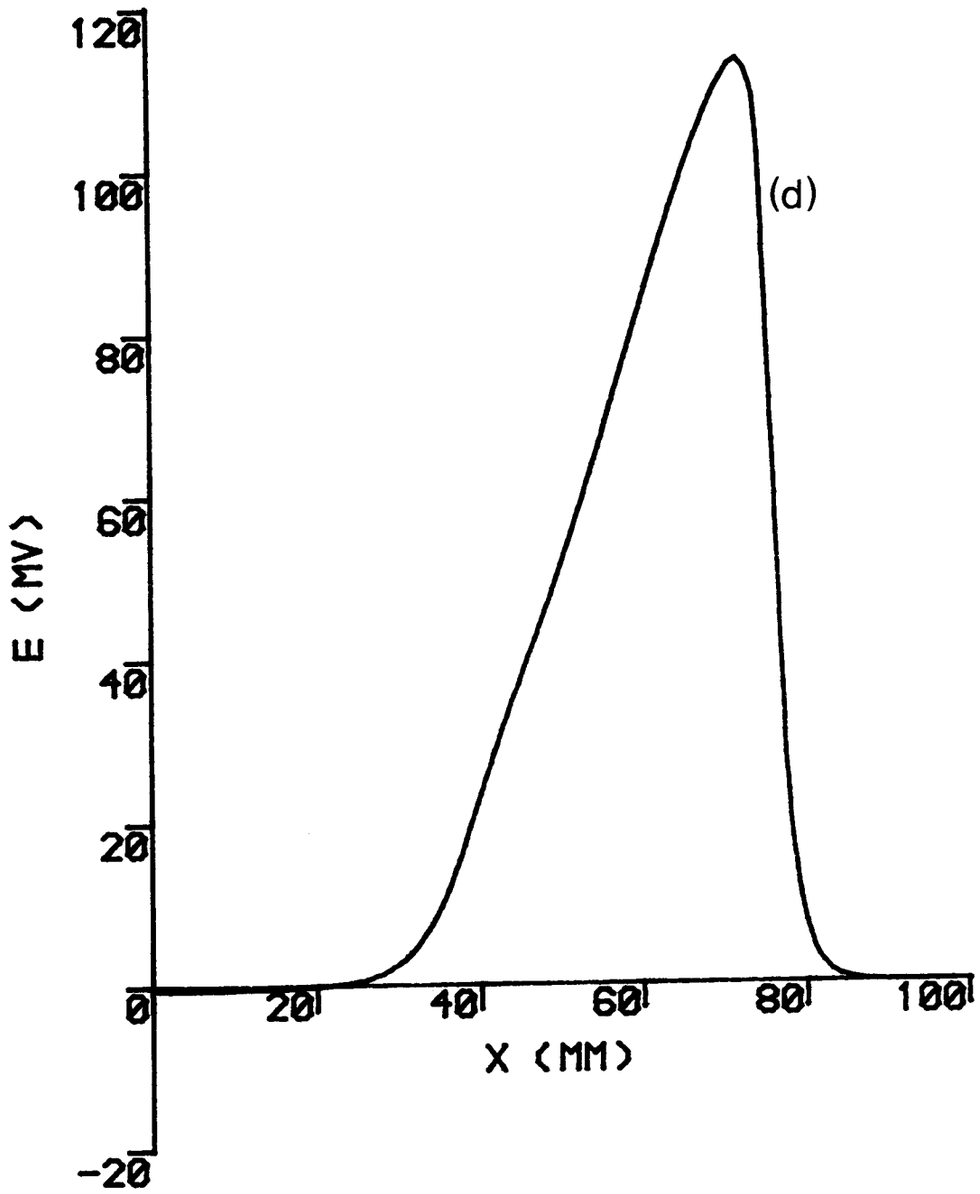

FIGURE 9.4 SPATIAL ACTION POTENTIAL CURVE

For details see text 9.16

The relationship between fibre diameter and conduction velocity for six different values of Ge are shown in Fig. 9.5. All results are based upon a temperature of 20° C. The prediction by GOLDMAN and ALBUS (1968) is also included as dotted line in the figure.

For low values of Ge (below 51.5nS), it is clear that the conduction velocity does not bear a linear relationship with fibre diameter. The velocities depart from the expected straight line and become less sensitive to any increase of diameter. In the case of Ge equal 10.0nS, the velocity even starts to drop when diameter is greater than 20μm (in fact conduction fails at 26μm). The linear relationship begins to appear only when Ge is greater 200 nS . The straight line at the top (Ge=10.0S) is only of academic interest as the Ge value is at least 10^8 times higher than the internal conductance (Ga) of any fibre diameter. On the other hand, the results with Ge equal to 515nS , bear a reasonable linear relationship between diameter and velocity and accordingly , this value is chosen for subsequent analyses. Note that this value is 7 times higher than the internal conductance (Ga) of a 20μm fibre.

The results in Fig. 9.5 (Ge = 51.5nS ,30.0nS . 10.0nS) suggest that Ge may also be proportional to fibre diameter. As the diameter increases. the value of Ge has to be increased in order to restore a linear relationship. Linear electrical properties show that the longitudinal conductance of a single path decreases as the internodal

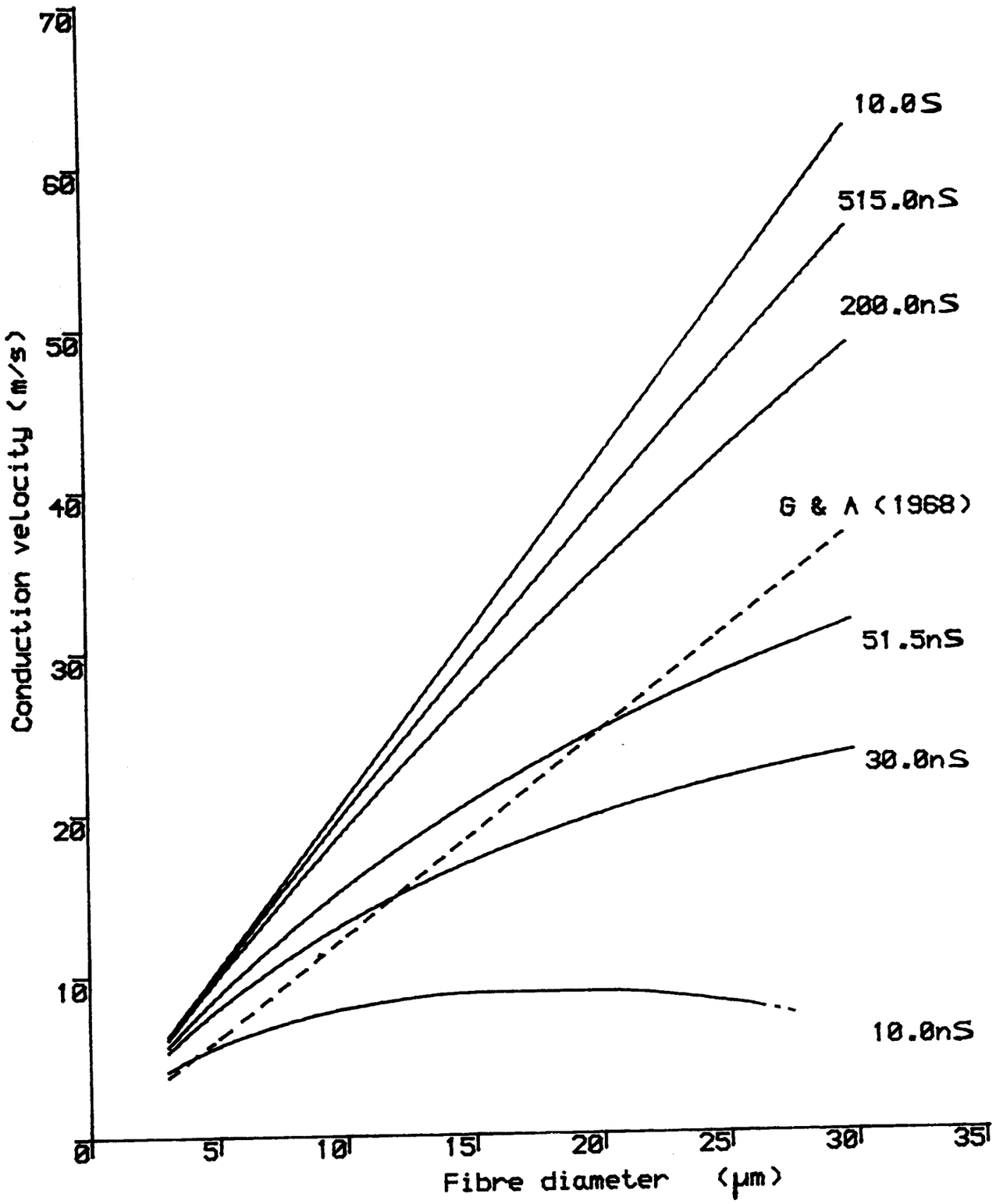

FIGURE 9.5 RELATIONSHIP BETWEEN CONDUCTION VELOCITY AND FIBRE DIAMETER FOR DIFFERENT VALUES OF Ge

For details see text 9.1.6

length increases. In other words, an increase of fibre diameter should result in a decrease of longitudinal conductance. It must be kept in mind that a larger diameter will have a larger circumference at the node of Ranvier, even though the nodal gap is always the same. This circumference will provide a greater path area for the radial outward current from the node of Ranvier, thus creating more parallel longitudinal conducting path area too.

9.1.7 Comparisons with Other Workers

GOLDMAN and ALBUS (1968) predicted the velocity-diameter relationship using a modified model of FITZHUGH (1962). They used an infinite large value of external conductance and employed F-H equations for the membrane. The dotted line in Fig. 9.5 is their result which has a smaller slope than that of model A (Ge=10S). The reason for this lies on the basic construction of their model, which included the myelin leak and capacitance currents. These features caused a reduction of conduction velocity.

On the other hand, HUTCHINSON et al (1970) experimentally determined the relationship between conduction velocity and nerve diameter in single myelinated fibre of Xenopus Laevis. The results, obtained from the fibre immersed in Ringer solution at 23°C, showed a linear relationship between velocity and diameter. The proportionality constant was about 2 (m/s)/μm, which is what model A predicts when Ge is comparatively large (> 515nS).

9.2 NETWORK MODEL DEVELOPMENT : MODEL B INCLUDING THE EFFECT OF EXTERNAL APPLIED FIELD ON ACTION POTENTIALS

9.2.1 Model Description

The model in this section is intended to exhibit both the characteristics of remote stimulation and action potential propagation. Action potential generated by remote stimulation can propagate along the fibre while. the action of external applied field upon oncoming action potential can also be investigated.

Figure 9.6 is the fibre network, arbitrarily called model B. The development here is the inclusion of linear conductances, Gs, which are assumed to be equal for all nodes. Associated with these conductances are currents Is,j. Other terms corresponds to those of model A described in Section 9.1.

It is assumed that at 'some' distance from the axon the stimulus potential field is not affected by either the physical presence of the fibre or by any active currents generated by the axon. This distance is assumed to be small in comparison with the distance from the axon to the stimulating source. Under these conditions. the stimulating potentials. Vs, may be considered to be the free-field potentials corresponding to the positions of the nodes on the axon. On the other hand. the potentials. Ve, immediate outside the nodes are allowed to float according to the currents in the network. These potentials

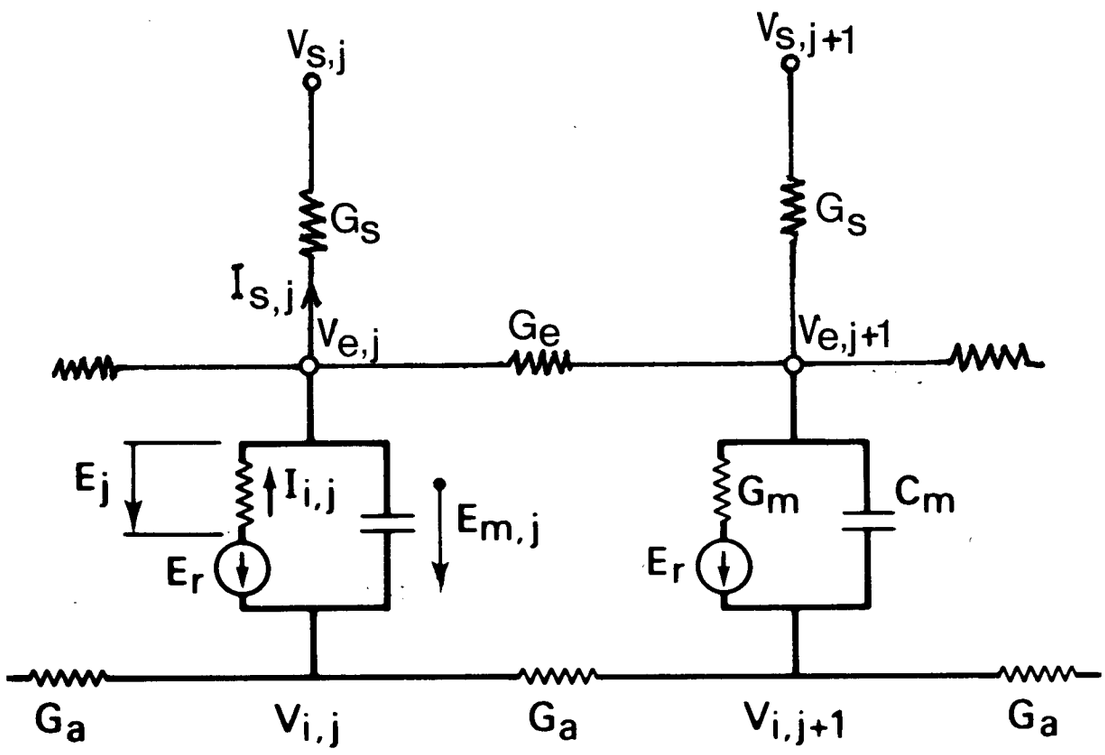

FIGURE 9.6 MODEL B NETWORK

For details see text 9.2.1

can also be influenced indirectly, through the linear element Gs, by the field, Vs. Accordingly, the elements Gs serve as a bridge communicating the 'local' activities with the 'external' events. These events may be due to a remote current source or a nearby active fibre.

9.2.2 System Equations

The detailed derivations of the system equations for model B are given in Appendices 10 & 11. The final form of the solution for a n-node axon is , using standard state vector (matrix) notation :

$$[M]\dot{\underline{E}} = [N]\underline{E} + [P]\underline{Ii} + [L]\underline{Vs} \qquad (9.2)$$

where $\dot{\underline{E}}$, $\underline{E}$, $\underline{Ii}$, and $\underline{Vs}$ are column vectors (nx1),

$[M]$, $[N]$, $[P]$ and $[L]$ are nxn matrices .

Their individual elements of those matrices can be found in Appendix **10** . Note the similarity between eqn.(9.2) and eqn.(7.1) for the McNEAL model in Section 7.2. The vector Vs is now the system input, representing the external applied field. The current term, Ii, is a function of E which in turn, is a function of time. The potentials, Ve. outside the node are implicitly defined in the system equations. Equation (A10.3) in Appendix 10 shows that Ve is a function of both E and Vs.

An examination of the equation derivations in Appendix 10 reveals that the conductance Gs always appears with Ge as ratio (Gs/Ge). As an optimal value of Gs is

unknown, an investigation on the effect of different values of Gs/Ge ratio on steady state subthreshold solution , action potential waveform and conduction velocity are worthwhile.

9.2.3 Steady-state Analysis : Effects of Gs/Ge

The solution method is similar to that of the McNEAL model. The ionic current term Ii is replaced by Gm*Ej as membrane conductance Gm at each node is a constant.

Eqn.(9.2) becomes $\underline{E}_{t->\infty} = -[Q]^{-1}[L]\underline{Vs}$

where $[Q] = [N] + Gm[P]$

Using this model B, a study has been made of a 20μm fibre with 39 nodes stimulated by a cathodic pulse of infinite duration and 0.1 mA amplitude. Electrode distances were 1.0mm, 2.0mm, 3.0mm, 4.0mm and 5.0mm directly above node 20. Other stimulus conditions were the same as Section 7.3.3. Figure 9.7 shows the depolarisation at node 20 as a function of electrode distance. Five Gs/Ge ratios were chosen : 100.0, 10.0, 1.0, 0.1 and 0.01. The diamond symbols are the solution by McNEAL model. In all cases, the solutions predicted by model B are lower than the corresponding McNEAL solutions. The results indicate that the inclusion of elements Gs in the model 'smooth down' the applied field Vs. Table 9.1 shows the percentage reduction of model B solutions from the McNEAL solutions. In general, membrane depolarisations are reduced to

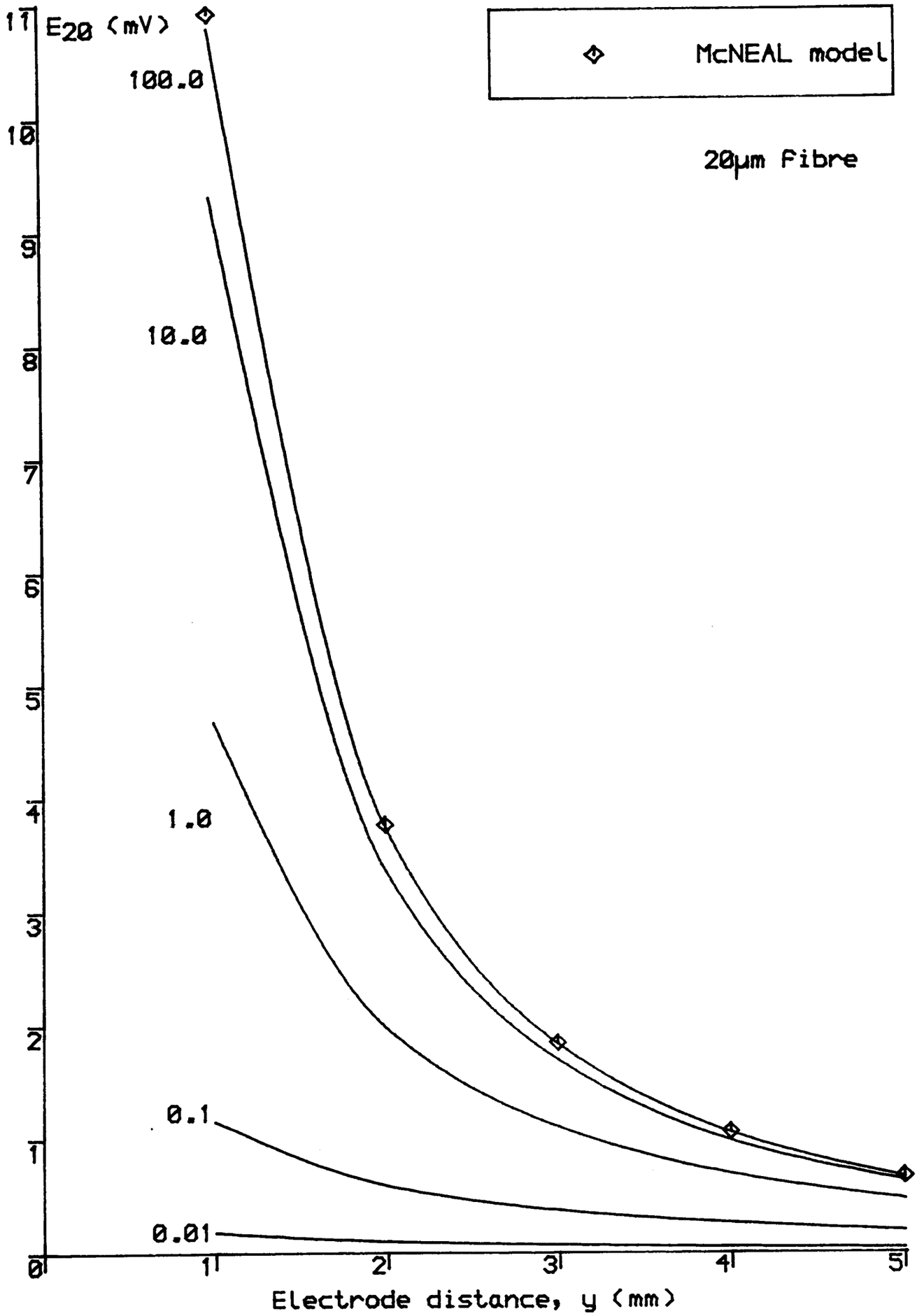

FIGURE 9.7 STEADY-STATE ANALYSIS OF MODEL B FIBRE

Number within the graph are Gs/Ge ratios
For details see text 9.2.3

one-half for Gs/Ge ratios not much less than 1.

TABLE 9.1 Percentage reduction of depolarisation (node 20) from McNEAL predictions

Gs/Ge	electrode distance from the axon (mm)				
	1	2	3	4	5
0.01	98%	97%	96%	95%	94%
0.1	89%	84%	80%	75%	72%
1.0	57%	47%	40%	35%	30%
10.0	15%	11%	8%	8%	6%
100.0	1.2%	0.5%	1.5%	0.9%	1.5%

$$\text{percentage reduction} = \frac{\text{McNEAL solution - model B solution}}{\text{McNEAL solution}} \times 100\%$$

9.2.4 Action Potential Waveform : Effects of Gs/Ge with Zero Applied Field

The system equations (9.2) and the full set of F-H eqns. are used to investigate the waveform of a propagating action potential. Seven values of Gs/Ge ratio are chosen : 1000, 100, 10, 1, 0.1, 0.01 and 0.001. In each case an action potential was initiated by assigning a depolarisation value of 100mV at node 1 and maintaining for a single time step (0.002ms). The action potential

curves were then plotted after 2.0ms when they were about midway down the fibre: they were shown in Figures 9.8 and 9.9.

In Fig.9.8, the solid single curve at the far right is in fact for the ratios of 100 and 1000 as both curves overlap each other. The solid curve just behind it is for the ratio of 10 while the broken line is for a ratio of 1. All four curves have a similar shape and amplitute, although the broken one has a faster decay time and has a small hyperpolarisation in front of the rising phase. Note also that they all show similar shape with the action potential from model A (Figure 9.4).

Figure 9.9 shows pulses for Gs/Ge ratios of 0.1, 0.01 and 0.001. The broken curve is for a ratio of 1, shown here again for comparison purposes. It is clearly shown that, for Gs/Ge < 1, there are uncharacteristic regions of hyperpolarisation ahead of the rising phases. The smaller the Gs/Ge ratio, the larger is the hyperpolarisation. There are also marked oscillations in those hyperpolarised regions.

9.2.5 Propagation Velocity : Effects of Gs/Ge with Zero Applied Field

Figures 9 10(a)-(g) shows the propagating action potentials at different instant of time. Each picture represents one Gs/Ge ratio. Pictures (a)-(f) indicate that , by the time of 0.5 ms. the impulse had settled down and begun to travel steadily along the axon. Picture (g), for

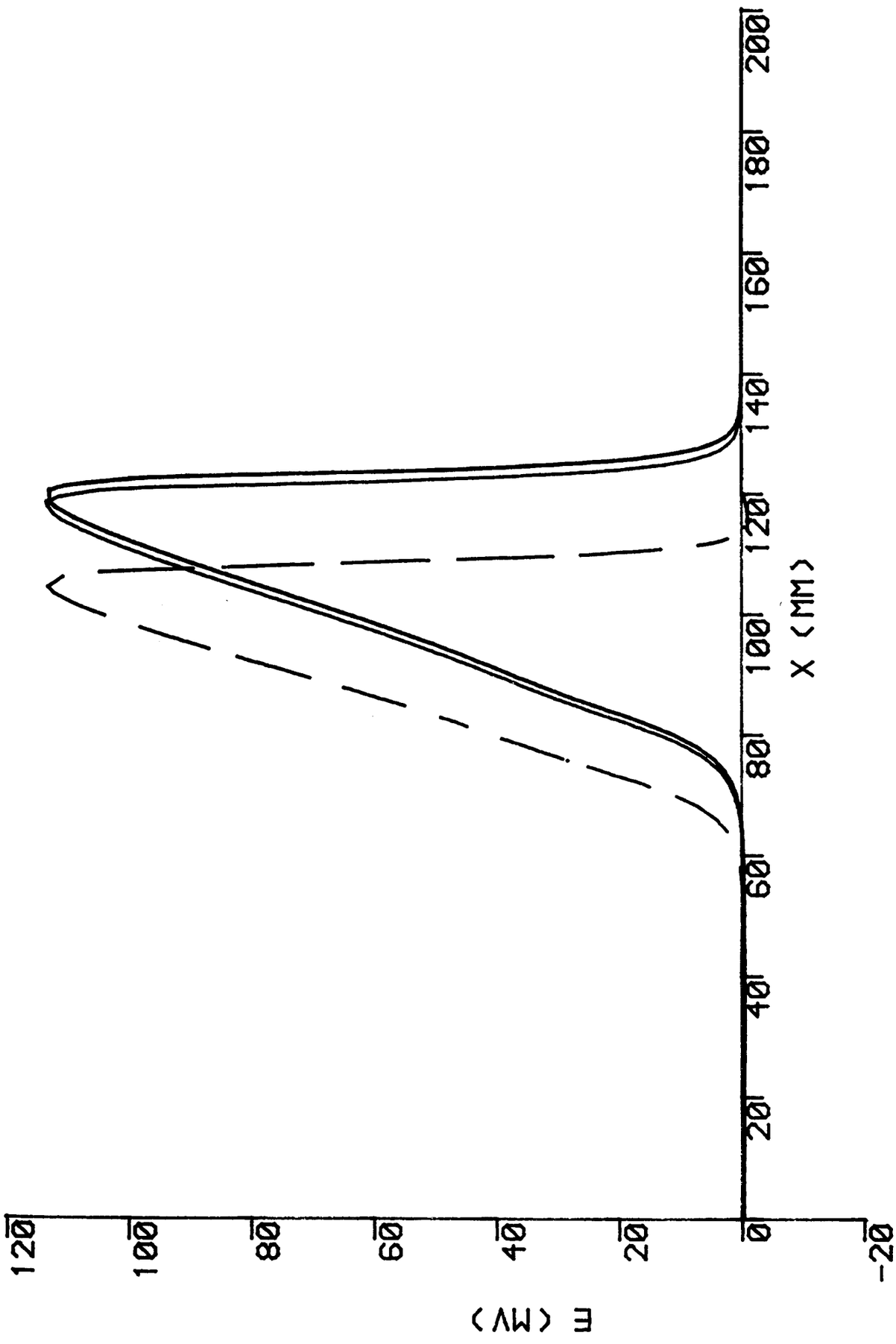

FIGURE 9.8 SPATIAL ACTION POTENTIAL CURVES

See text 9.2.4 for details

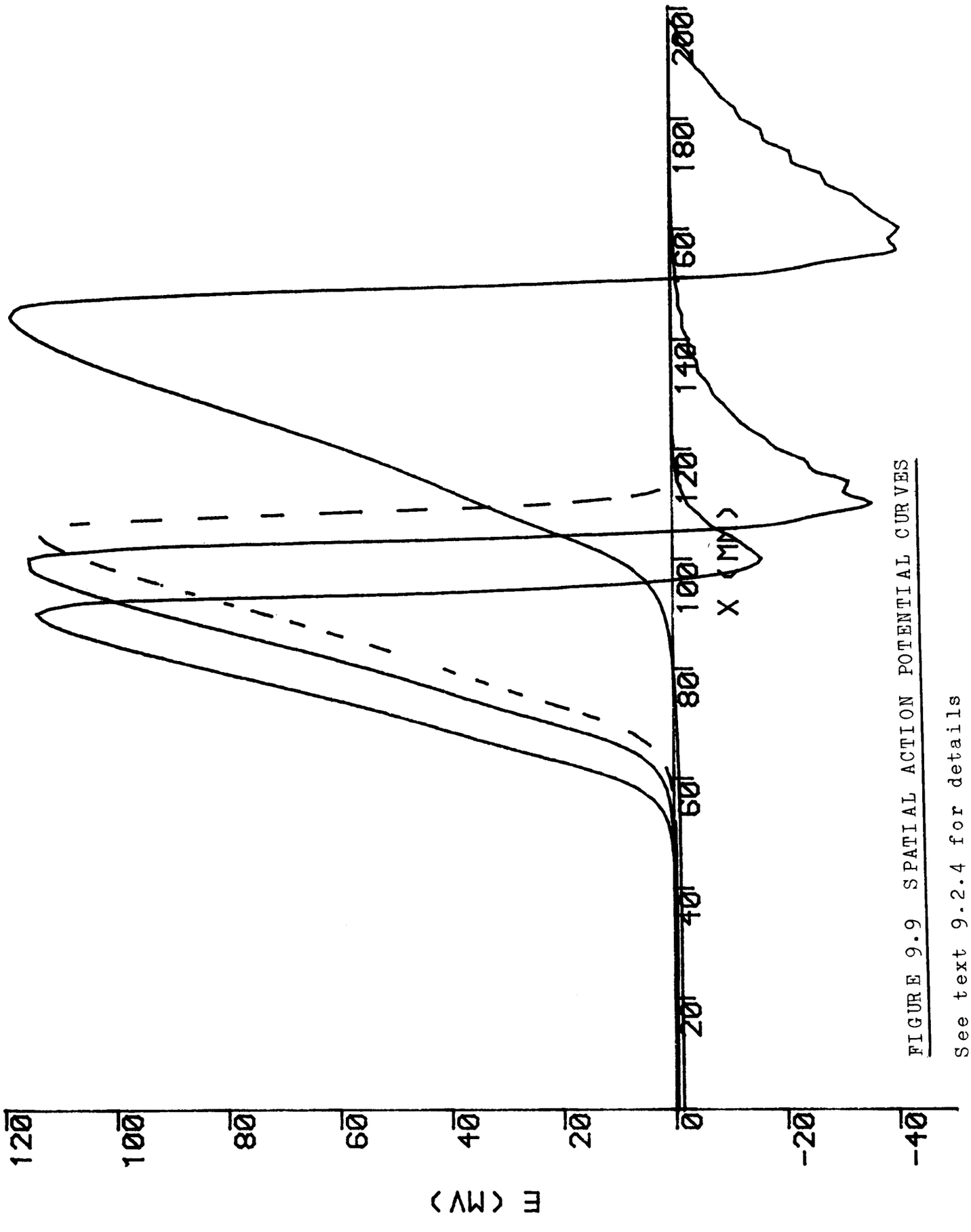

FIGURE 9.9 SPATIAL ACTION POTENTIAL CURVES

See text 9.2.4 for details

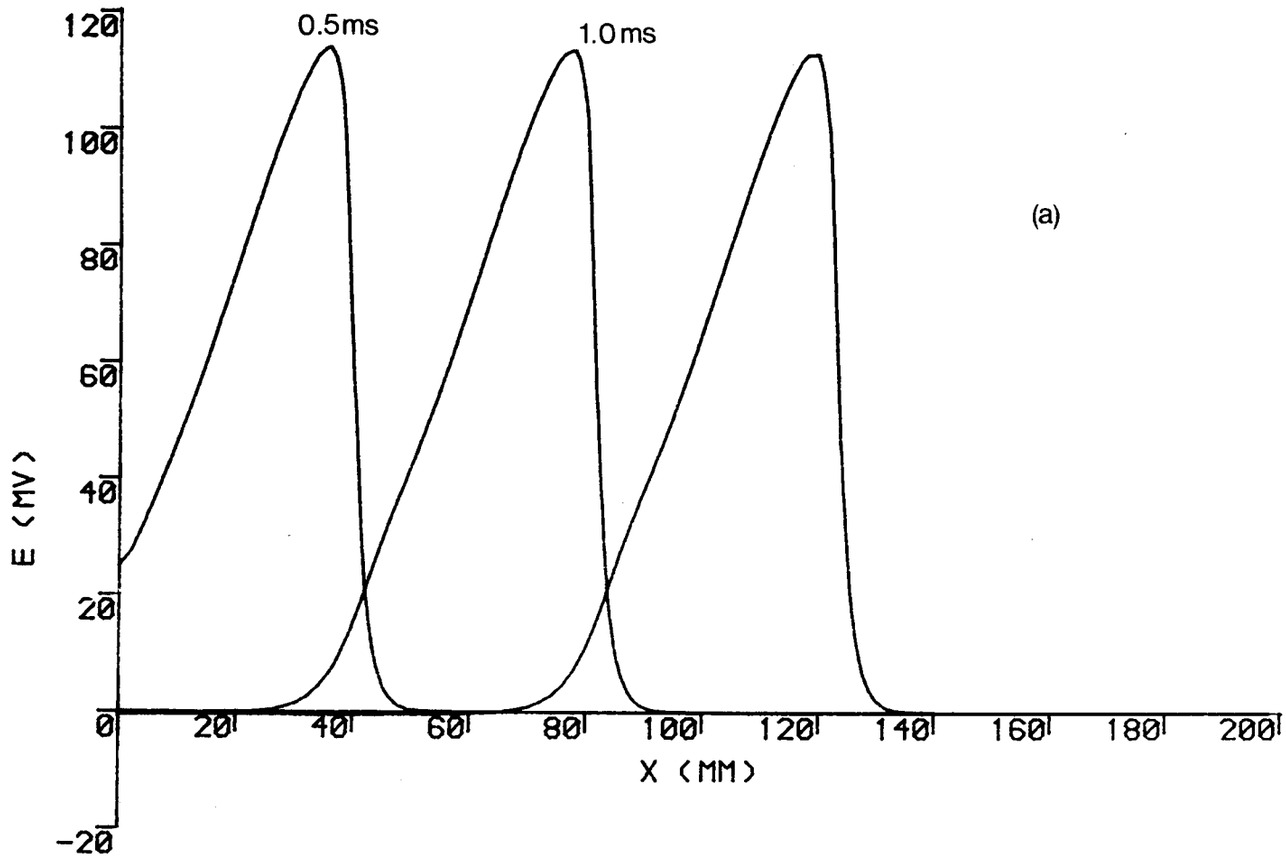

FIGURE 9.10 SPATIAL ACTION POTENTIAL CURVES FOR DIFFERENT Gs/Ge RATIOS

See text 9.2.5 for details. Gs/Ge ratios are
(a) 1000 (b) 100 (c) 10
(d) 1
(e) 0.1 (f) 0.01 (g) 0.001

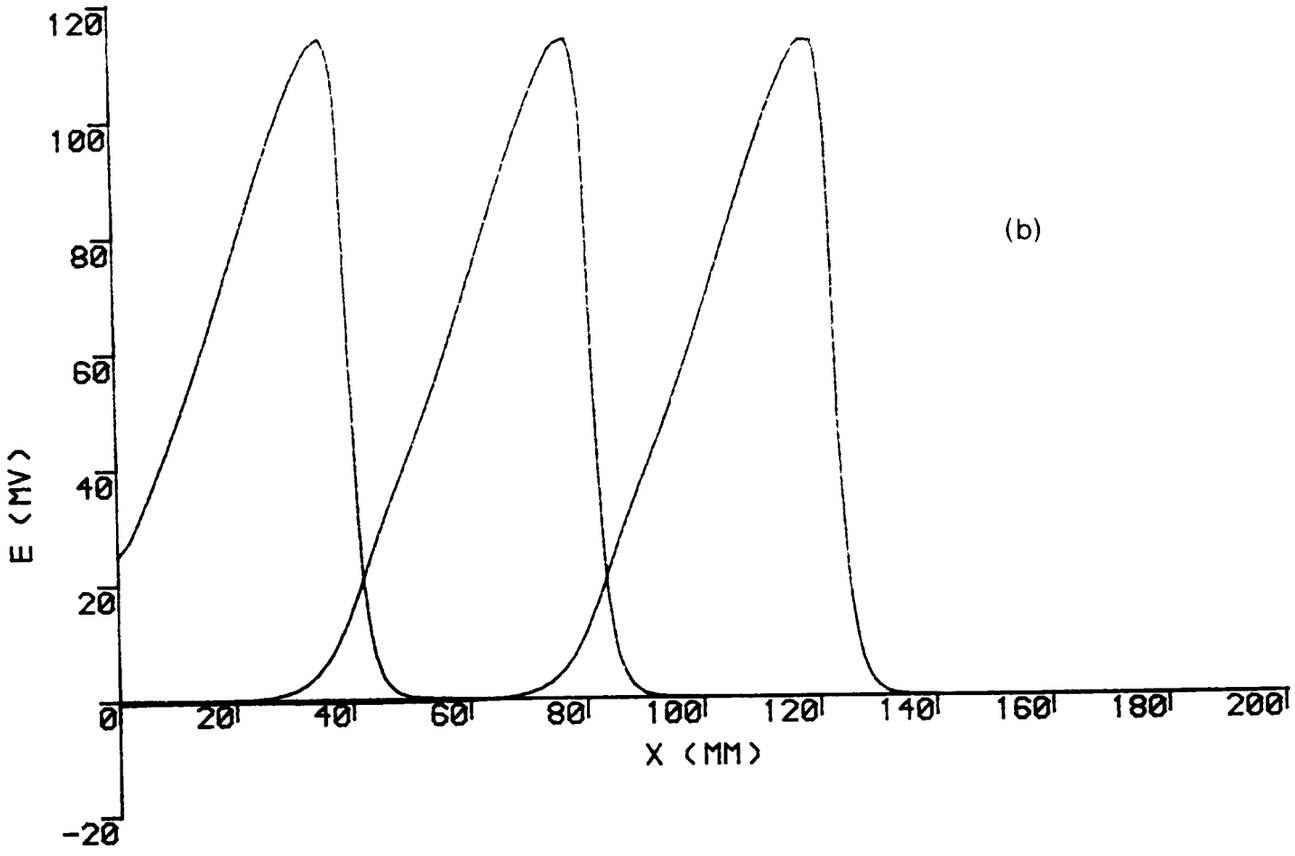

FIGURE 9.10(b)

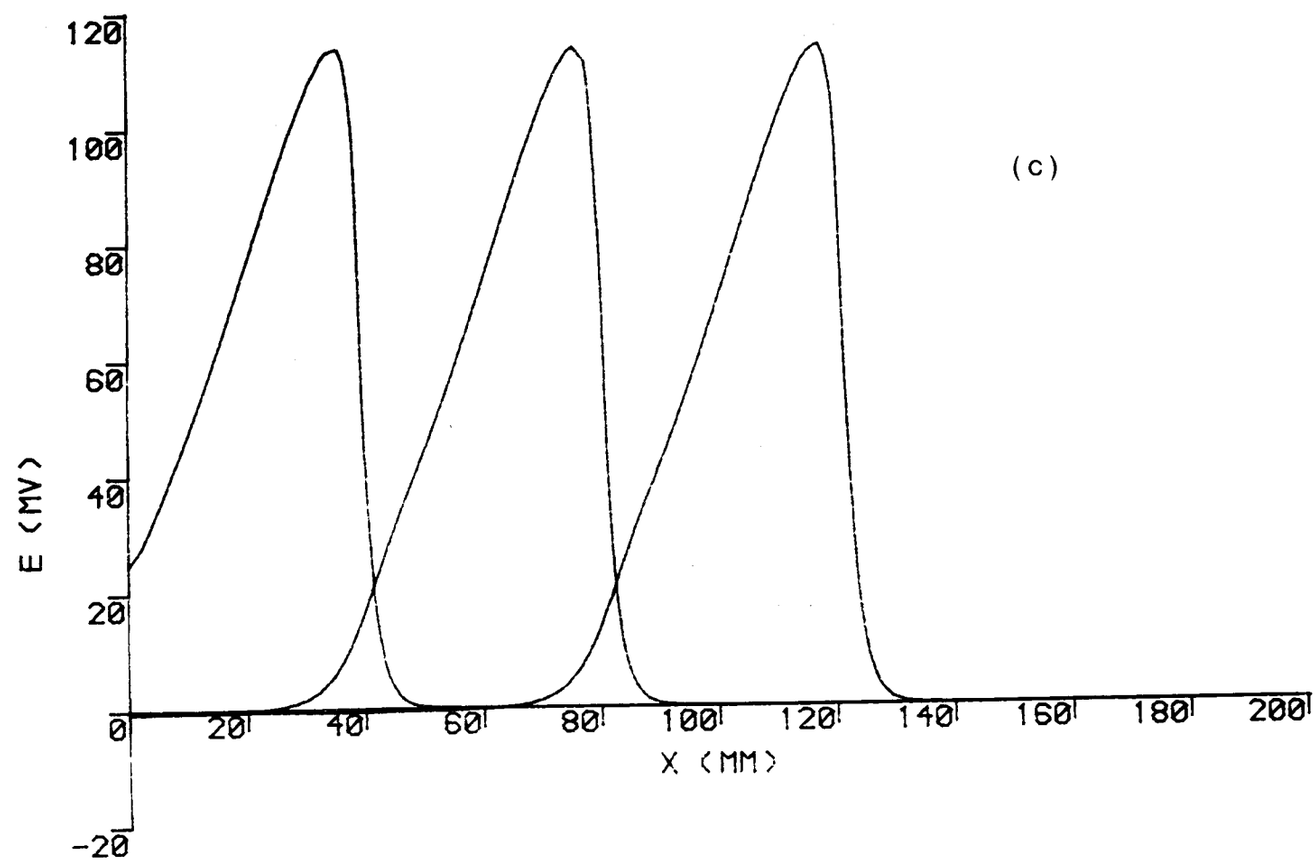

FIGURE 9.10(c)

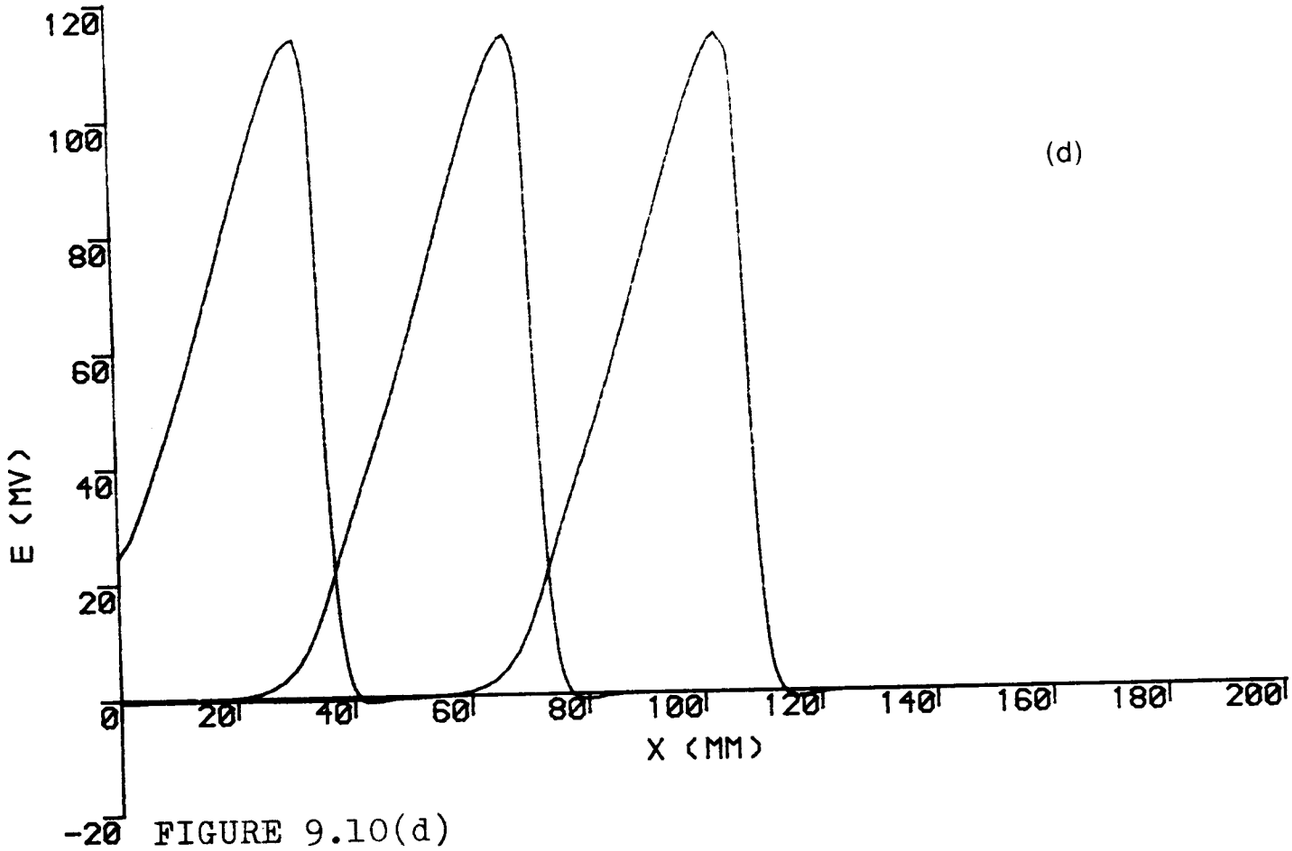

FIGURE 9.10(d)

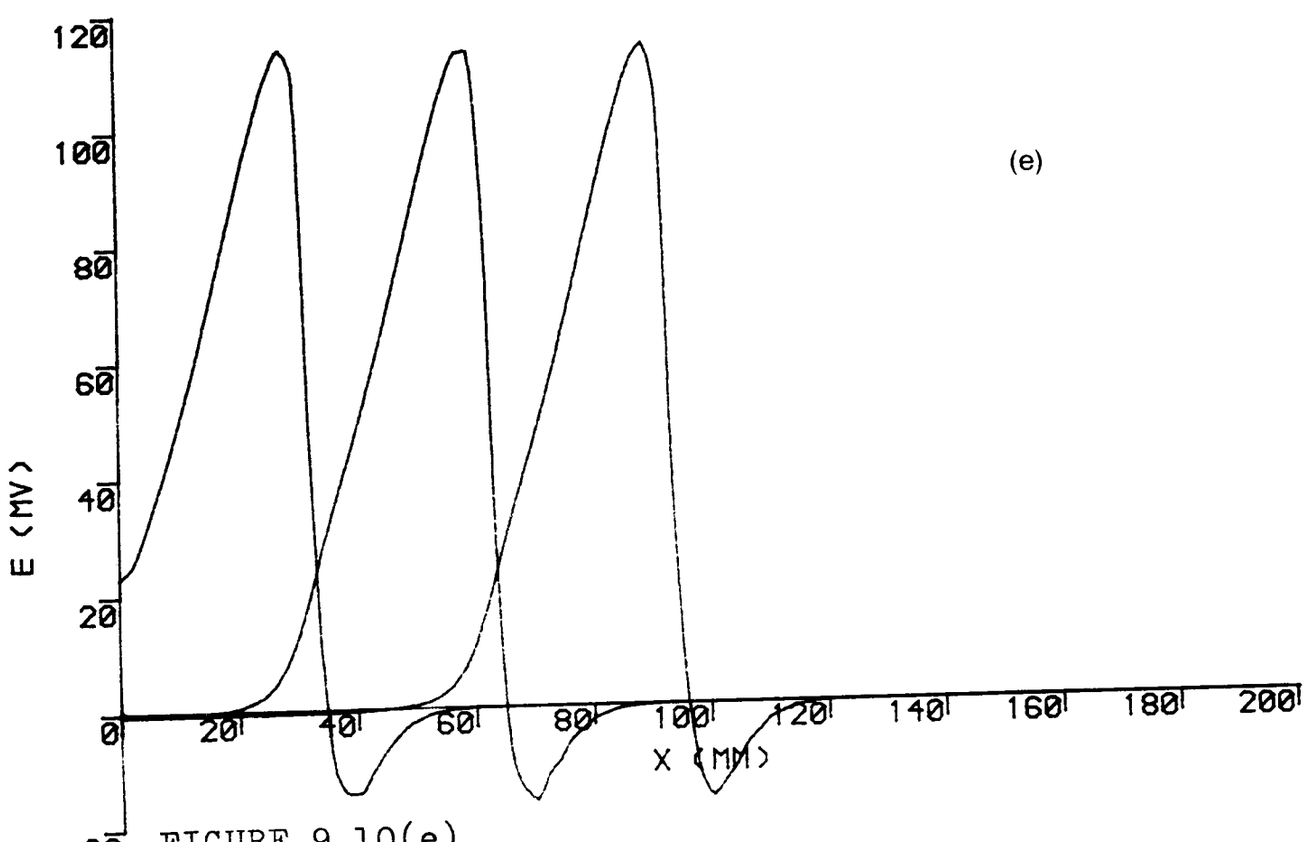

FIGURE 9.10(e)

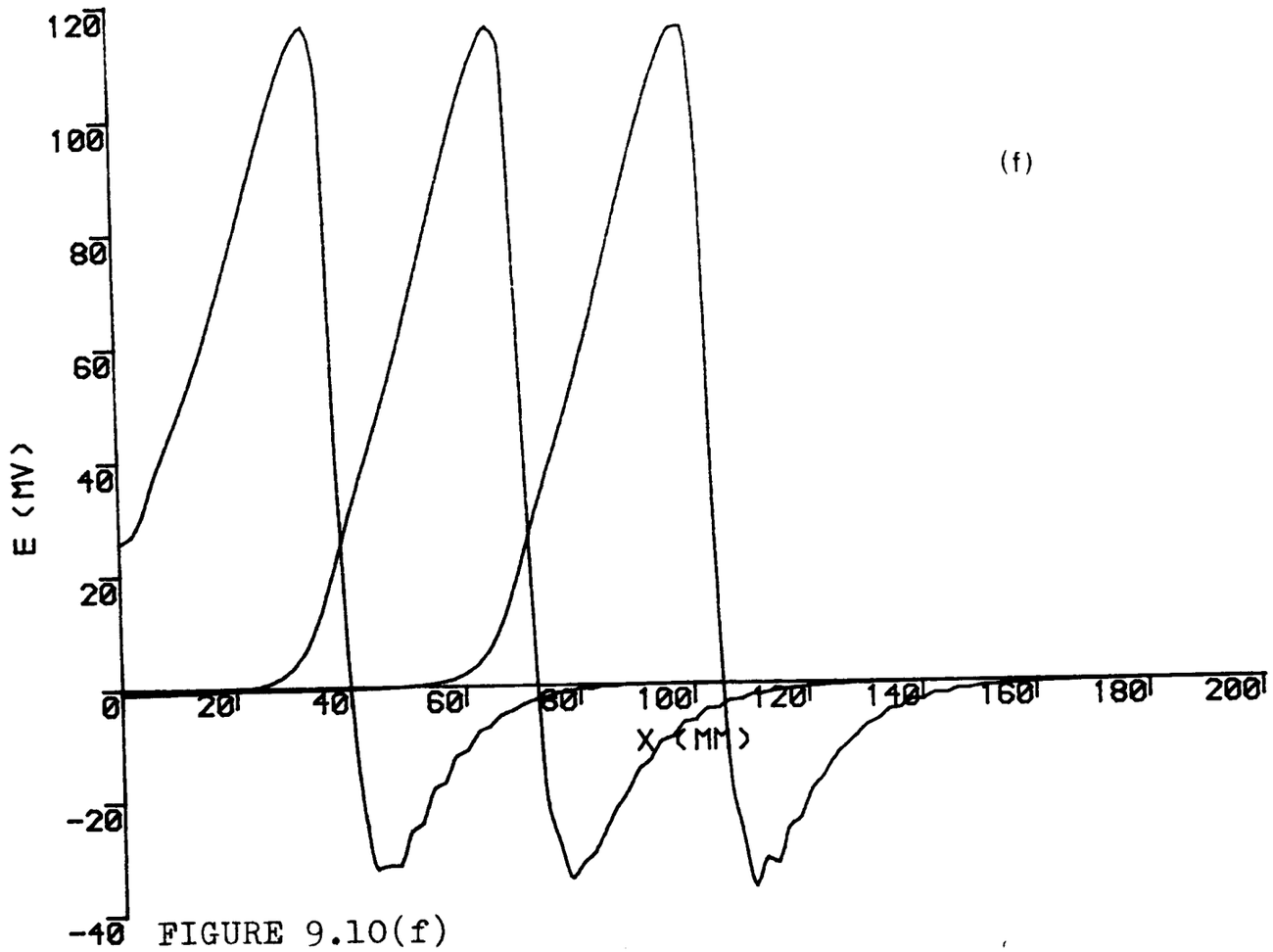

FIGURE 9.10(f)

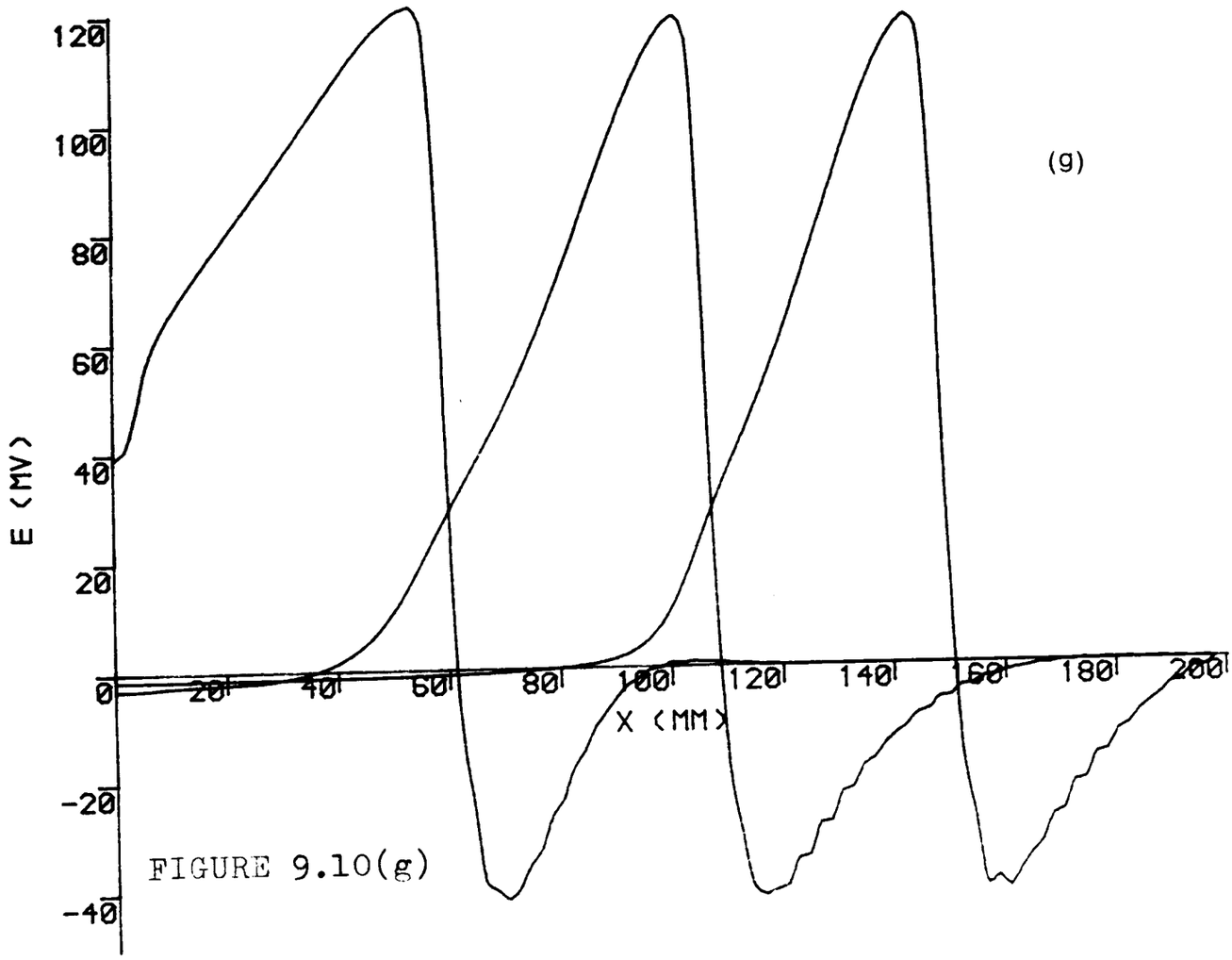

FIGURE 9.10(g)

a Gs/Ge ratio of 0.001, clearly shows that the impulse at t=0.5 ms had still not attained a steady waveform. The propagation velocities for the above ratios are given below.

Gs/Ge	Velocity (m/s)
1000	42
100	42
10	41
1	36
0.1	31
0.01	32
0.001	51

Apart from the case of 0.001, an increase of Gs/Ge ratio tends to increase the conduction velocity.

9.2.6 A Final Comment on Gs/Ge Ratio

Analytically, the variations of Gs should have the following effects :

Gs tending to zero (i.e. Gs/Ge -> 0) should give results equivalent to model A irrespective of the stimulus profile Vs. In other words the fibre is isolated from the stimulus by infinite large resistive sheath. Steady-state analysis in section 9.2.3 did show the depolarisation tending towards zero as expected. Unfortuately, when full propagation work was examined. numerical inaccuracy

causes distortion in action potential shape. Propagating velocities also departed further from the expected linear diameter-velocity relationship.

Gs tending to infinitely large values (i.e. Gs/Ge -> ∞) should convert the model into the McNEAL model. That is to say the stimulus profile Vs is applied directly at the nodes. The external potential profile Ve outside the nodes will always have the same values as Vs, regardless of any membrane activities and the Ge value. This appears to be the graphical trend (Fig. 9.7) shown in the steady-state analysis. Propagation analysis also revealed that the model has the expected characteristics in terms of waveform and conduction velocity.

Numerically, model B is not well-behaved. First, as Gs tends to zero, action potential waveform departed from the expected shape. Second, as Gs is 10 times or more than Ge, overflow conditions arose in the steady-state solutions. In the absence of a proper field solution around the fibre, the difficulty concerning the optimal value of Gs cannot be resolved. Nevertheless, the qualitative analyses in Section 9.2.3-9.2.5 suggested that the optimal value of Gs/Ge was between 1 and 10.

9.2.7 Examples of Effects due to External Applied Fields from Point Sources 2mm Distant from Fibre

A 20μm axon containing 99 nodes of Ranvier was assumed to be immersed in a homogeneous isotropic medium of 300 ohm-cm resistivity. An action potential was first initiated by a monopolar cathodic electrode 2mm above node 1 (the left end). The behaviours of the propagating action potential subjected to different external applied fields were then investigated. The calculation of the external potential Vs,j at node j was simply from the monopolar stimulation

$$Vs,j = \rho_e I/(4\pi Rj)$$ where Rj was the distance of node j from the electrode and I is a cathodic pulse.

The behaviour of the propagating action potential subjected to the external field was then plotted at different instants of time.

Figures 9.11-9.13 show three different cases of external applied fields. In all cases, a nominal value of 1 was chosen for Gs/Ge . The sequences of plots are arranged in alphabetical order and the time interval between each successive picture is 0.5 ms. Moreover picture (a) in each figure is at t=0.5 ms. Each individual picture shows the action potential travelling towards the right and the x-axis of the picture represents the length of the fibre model.

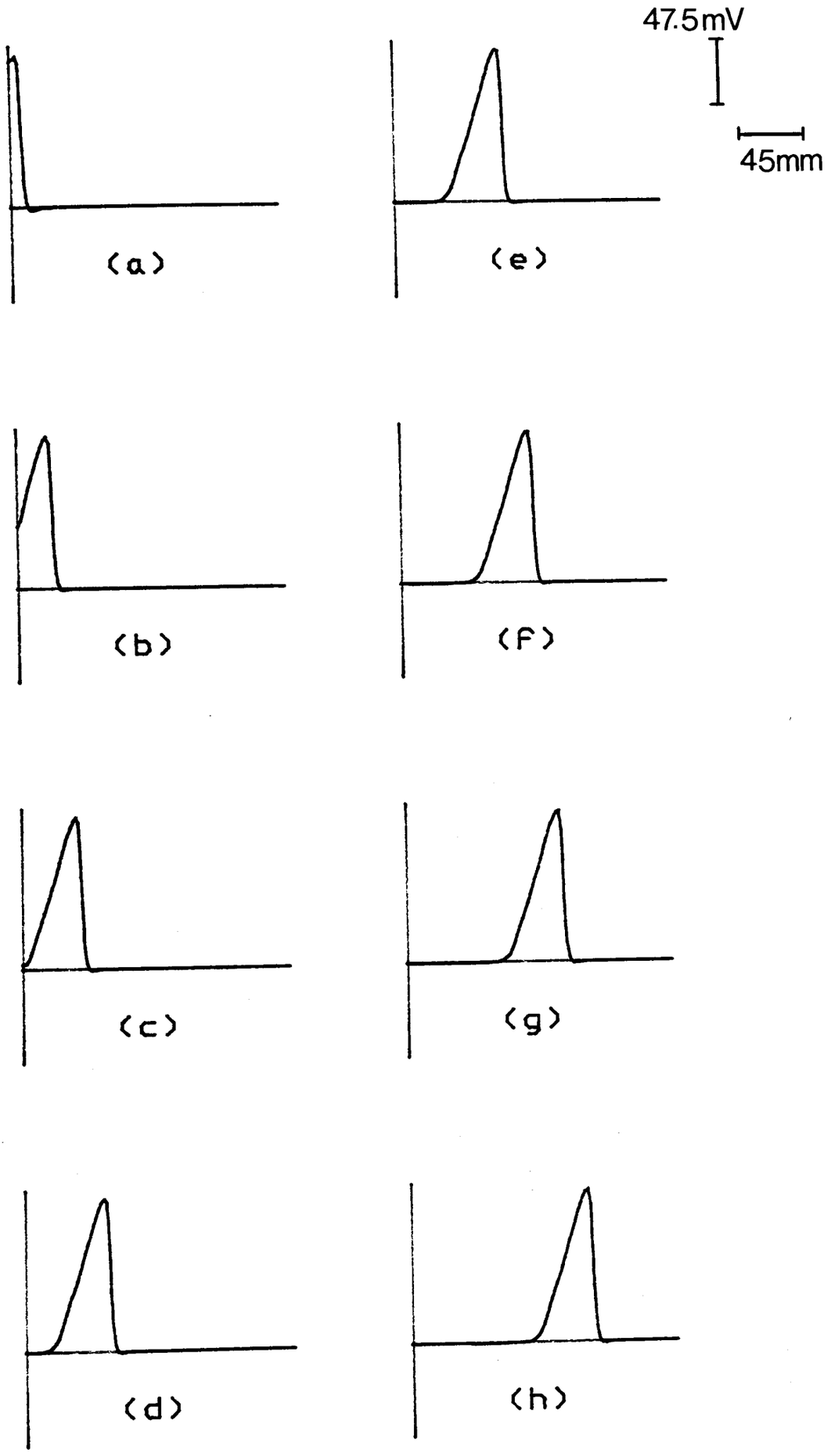

FIGURE 9.11 EFFECT OF EXTERNAL FIELD ON PROPAGATING ACTION POTENTIALS

Applied field : cathodic current of 1mA and 0.5ms duration applied at t=0. Other details see text 9.2.7

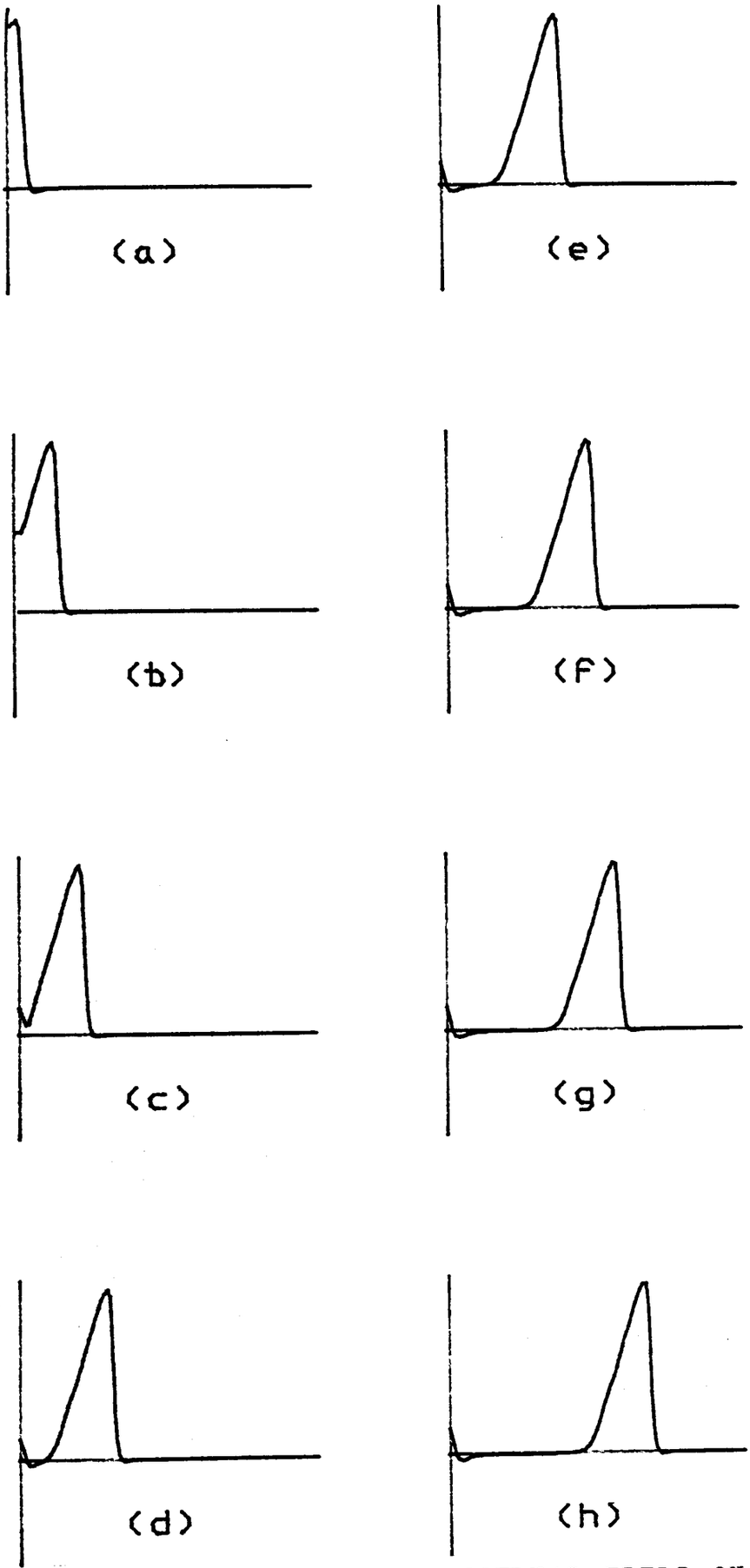

FIGURE 9.12 EFFECT OF EXTERNAL FIELD ON PROPAGATING ACTION POTENTIALS

Applied field : cathodic current of 1mA and infinite duration applied at t=0.
Other details see text 9.2.7

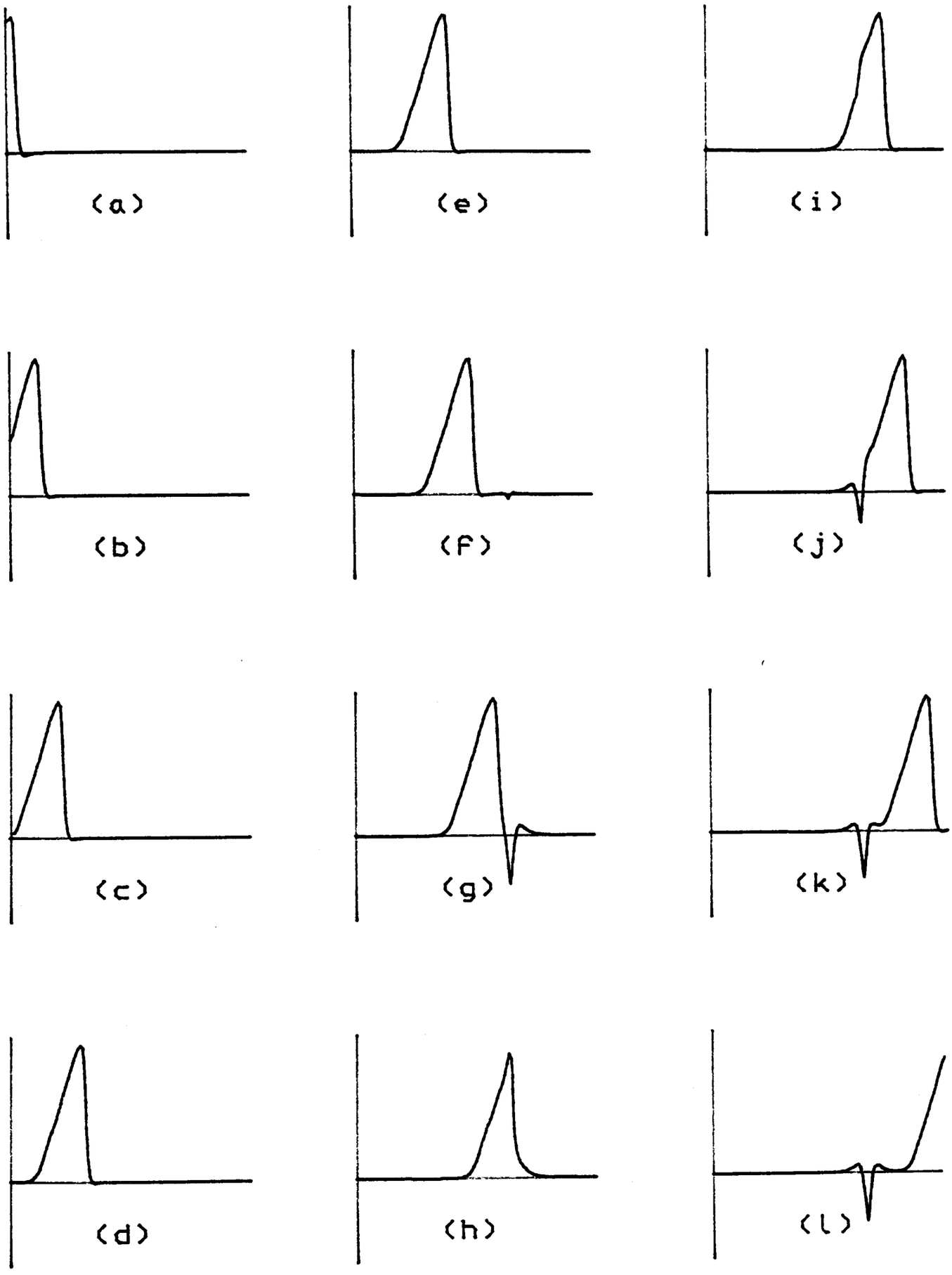

FIGURE 9.13 EFFECT OF EXTERNAL FIELD ON PROPAGATING ACTION POTENTIALS

Applied field : cathodic current of 1mA and 0.5ms duration applied at t=0. Anodic current of 2mA and infinite duration applied at t=3.0ms. Other details see text 9.2.7

In Fig. 9.11, the source to initiate the action potential was a 0.5 ms cathodic pulse of 1.0 mA amplitude above node 1. By the time picture (a) is plotted, the stimulus has just been turned off. The subsequent plots, (b)-(h), therefore show the action potential travelling in a 'free-field' (Vs=0).

On the contrary, an infinite long cathodic pulse (1.0 mA amplitude too) was applied in the case shown in Figure 9.12. Thus the propagating action potential were always subjected to non-zero applied field ($Vs \neq 0$). Note the remaining polarisation induced by the long pulse at the left end of the fibre. Nevertheless, the waveforms and velocity of the action potential are hardly distinguishable from that of Fig. 9.11.

The third case, shown in Fig.9.13, was an attempt to block the oncoming action potential somewhere midway down the fibre by an ANODIC pulse. Initially, the fibre was excited by a cathodic pulse of 0.5 ms and 1mA amplitude, and it can be seen that pictures (a)-(e) of Fig.9.11 and 9.13 are identical. While the action potential was propagating along the fibre, an anodic pulse of magnitude 2.0 mA and infinite duration was applied 2.0mm above node 65 at t=3.0ms. The intention was to set up a hyperpolarised region (reaching -40mV, see plot (l)) in the fibre through which the action potential was going to pass. Picture (f) of Fig.9.13 was the instant when the anodic pulse was applied. The response on the fibre, ahead of the action potential, is just visible. After another

0.5 ms. the propagating action potential began to pass through the developing hyperpolarised region (picture (g)). In picture (h), the shape of action potential was clearly distorted and its amplitude was also reduced. Nevertheless, the impulse 'survived' and continued to travel to the right, as shown in pictures (i)-(l). Note in pictures (l) the characteristic effect of anodic stimulus : a central region of hyperpolarisation accompanied by small depolarisation on each side.

As shown in Fig. 9.13, a hyperpolarisaton of -40 mV was unable to block the oncoming action potential. One may feel that the action potential could have been blocked by increasing the hyperpolarisation, in other words increasing the amplitude of the anodic pulse. But the depolarisations on either side of the hyperpolarised region by that time will be high enough to excite the fibre. Case(1) of Appendix 12 illustrates this phenomenon.

A quantitative analysis of action potential blocking by different pulse amplitudes and electrode configuations are given in Appendix 12. In all those 12 cases, the action potential could not be blocked successfully. Technically, the oncoming impulse can be blocked by exciting the fibre ahead. The newly excited action potential travelling on the opposite direction 'collide' with the oncoming one and 'cancel' out each other. However, the second action potential from the newly excited site will continue to travel in orthodromic direction simply replacing the original.

CHAPTER 10

GENERAL DISCUSSION AND RECOMMENDATIONS

10.1 THEORETICAL ASPECTS OF FIELD SOLUTION USING FINITE ELEMENT METHOD

It is to be emphasised that the following is intended as an overview; detailed discussion of individual elements of the work may be found in the relevant chapters.

10.1.1 Fineness of Finite Element Mesh

The ever existing problem in this work has been the demands of computer storage for 3-D work. A model of eight layers (2500 nodes in 600 elements) requires 100K core store and, less important, 400 CPU seconds on the CDC7600. (*) The meshes, from both the standard of discretization viewpoint and anatomical reality, are very coarse.

Current density estimation from the solution is difficult, although not impossible. For the study of long straight fibres, which has been the main concern in this work, the model is adequate due to the use of 'element-stacking' technique. However, field

---

(*) As the unknowns to be solved in the model are only the potentials at each node, the number of nodes in a model equals the number of unknowns.

interpretation using more complex fibre systems is far more demanding of mesh points. For example, considering an idealised afferent fibre in the dorsal root entering into the cord and dividing into branches. it is clear from the solution shown in Figure 2.9 that the mesh in the transverse (XY) plane needed refinement.

Fortunately, the replacement of the CDC with a CRAY-1S allowed a model with finer meshing. Even a whole human model including the limbs and head may now be possible. The subsequent modified model in Chapter 6 indicates the power of the CRAY machine. The 5000-noded structure required 'only' 600 CPU seconds and 180K memory. these being less than one-quarter of the resources available for finite element work in the CRAY.

A second way of obtaining a finer meshing is the 'double' running technique. In the first instance, a full 3-D model is executed to obtain a general solution. A second model, containing only a restricted numbers of tissues. for example the tissues within the vertebral canal only, is executed with the first set of solution points as boundary conditions. In this second run, finer meshing is possible and solutions are obtained for mesh points between those obtained in the first run.

10.1.2 Modelling of Epidural Electrodes

Turning to a more practical aspects of the physical modelling of the implanted electrode, the first point is the finite size of metal poles. The models used in ANSYS

used an approximated finite-size representation, while the models in PAFEC use a point source.

Direct comparison of field distribution between the models cannot be made as PAFEC 75 does not produce contour plots from 3-D solutions. Nevertheless, Figure 10.1, a 2-D study using the model described in Chapter 3, indicates that there is no difference in regard to the choice of pole modelling as far as the stimulus field generated in the spinal cord is concerned.

The second point is the modelling of insulating sleeve of the electrode. An early 3-D run modelled the connecting sleeves between the electrode poles. Results, however, were numerically unsatisfactory due to the great difference in resistivities between the metal and insulator. For this reason, the sleeves were excluded from any future work.

The third point concerns the presence of passive electrodes in the epidural space, as this situation frequently arises when multi-site electrode systems are connected. The investigation was conducted using a 3-D ANSYS model, where the stimulating condition was bipolar epidural electrodes of configuration 1-2. Although results are not shown, the presence of the passive electrodes (poles 0 and 3) had negligible effect on field distribution, even in the subarachnoid space.

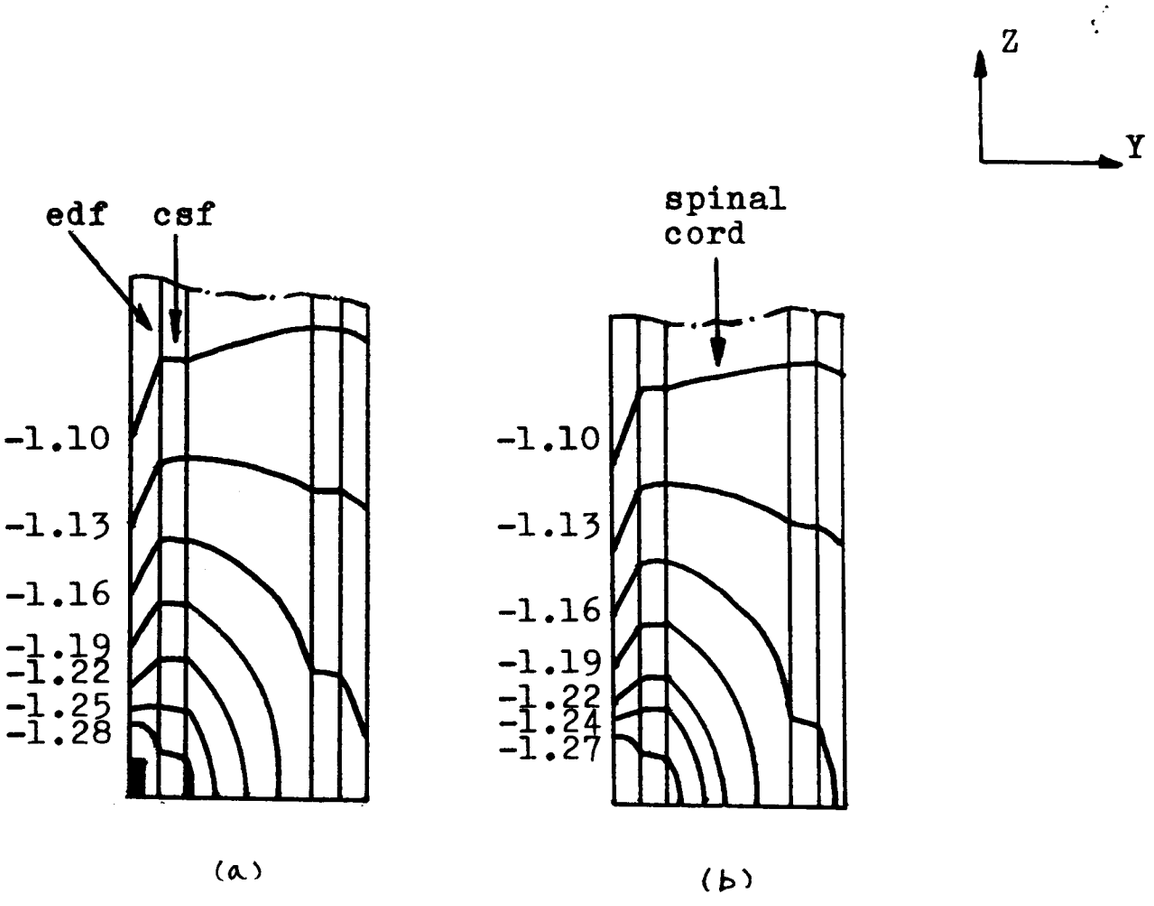

FIGURE 10.1 ISOPOTENTIALS WITHIN THE VERTEBRAL CANAL FOR DIFFERENT ELECTRODE MODELLING

Upper half of fields shown (7 contours) with monopolar cathodic current 1mA. Unit of contour in V. Standard set of tissue resistivity used.
(a) finite size electrode
(b) point source

10.1.3 Usefulness of 2-D Model

The 2-D approach to field solution, restricted as it is, remains as an economical and flexible means for field analysis. It permits an excellent degree of mesh fineness and isopotential contours from 2-D model solution indicate very well qualitative differences among different field distributions. The discrepancy of the approach is that no current flows perpendicular to the 2-D section being considered. Any solution can only be used for comparison and illustration purposes. Current density or field strength cannot be used, say, on McNeal model of a nerve fibre.

Nevertheless, comparison of bipolar cases given in Figure 2.13 and 3.4 shows the similarity of contour plots. The peak current density in full 3-D work is about 6 times smaller. Similarly, a 2-D analysis by COBURN(1980) showed that the peak current density for monopolar epidural electrode was $18\mu A.mm^{-2}$. The 3-D result in Figure 2.10 was $2.8\mu A.mm^{-2}$ which, again, is six times less.

In other words, the qualitative differences shown in a 2-D field analysis give similar results to proper 3-D models.

10.2 VALIDATION STUDY OF FINITE ELEMENT MODEL

10.2.1 General Comments

The main issue in the validity of finite element modelling concerns the electrical property definitions. Major effort has concentrated on finding the optimal combination of electrical properties for the model. Little attention has been given to geometrical sensitivities, although a 2-D study has been conducted in Chapter 3.

The 3-D study of resistivity involved three different approaches, and the results from each approach were compared with theoretical solutions generated by the finite element model. Consistency of experimental results used for comparison was encouraging, reducing the chance of any inherent errors in the methods used.

10.2.2 Experimental Work with Cadaver Materials.

Experiments were conducted to determine the resistivity of the spinal column. Although only two cadaver spines were used, the result, as described in Section 5.4, were consistent. Three points, nevertheless, are worth mentioning.

The first is the difference between the actual spine and the finite element model. The size and more important the curvature of the cadaver spine were different from the model. The second point is the coarse estimation of the position of the electrode inside the vertebral canal. The

third point is the possibility of time-dependence of cadaver tissue resistivity in vitro. However, the measured values (field profile) in each of the two experiments were constant throughout the four-hour sessions.

The results for the spine was 1600 ohm-cm, which is just outside the range of values quoted by GEDDES and BAKER (1967) for pure bone.

The second tissue to be measured was dura mater which was initially considered to be a significant material affecting current flow in the spinal cord. Attempts to measure dura resistivity directly, in vitro, failed and it became clear that highly specialised dedicated equipment is required for the tiny membrane. Fortunately the 2-D studies in Chapter 3 subsequently suggested that peak current density in the cord was only affected by 25%, even when the dura was allowed to vary from 60 ohm-cm to 100000 ohm-cm.

10.2.3 Comparison with Clinical Measurements

The 3-D model was quite well verified with actual measurements on patients, even though the region of measurement was restricted to the epidural space, and some skin surface plotting. The consistency of the clinical results also give confidence in the basic experimental data. This left the problem of searching for a suitable combination of resistivities for the computer model. Three significant changes were made in order to match theoretical and clinical results. A reduction of vertebral

column resistivity brought measured and computer-predicted values to within 50%. Another reduction of resistivity of epidural fat and spinal roots gave a reasonable good match.

These last few statements give a misleading impression of the complications and uncertainties of this area of the work.

With regard to Table 5.1, although the number of computer testing schemes for monopolar and bipolar configurations were five and three respectively. many other schemes were also attempted. The general thrust was to determine the cause of the computer model giving consistently high potentials (in magnitude) in relation to the clinical measurements.

One obvious target was the modelling of leaky paths in the vertebral column. In a finite element study of this. the column was represented by sections of highly resistive tissue (4000 ohm-cm). and between the sections were thin layers of relatively low resistive material, intending to represent intervertebral discs. The resistivity of these thin layers was set to 400 ohm-cm. being the same value as the general thorax.

The second test focussed on the effective resistivity of the general thorax region. It was suspected from Figure 5.14 that the central region of the general thorax might be a relatively conductive medium surrounded at the boundary by layer of muscle. The thorax was therefore modelled by a central region. 200 ohm-cm with a thin layer

, 20mm thick, of 1000 ohm-cm.

The third study was the use of 475 ohm-cm for the sketetal muscle. In other words, a 50% lower resistivity value.

The results for the above schemes were all disappointing. Model potentials for the spinal canal were not significantly brought towards those being measured in patients.

Turning now to the results of dorsal surface recording. Figures 5.16(a) and (b) showed that the shapes of theoretical solutions were different from the measurements; even though the numerical disagreements were less than a factor of two. The implications may be that the resistivity of skeletal muscle (950 ohm-cm) was too high in the model, but this has not been investigated in this issue.

On the other hand, the plots in the dorsal column in Figure 5.17 suggested that, with the final set of tissue properties , the field profiles along the fibre should fall within curves (1) and (5). It is recommended that future effort should shift to the biophysical interpretation of these stimulus fields.

10.2.4 Comparison with SWIONTEK et al (1976) Experiment

Results for this validation study have been discussed in Chapter 4 only. A few more remarks are needed.

The limited scope of this work, as mentioned, was due

to the Swiontek's measurements of current density being in the z-axis direction only. In addition, the whole body could not be fully represented due to the open laminectomy. In particular, no dorsal skeletal muscle was included in the model. Vertebral column, which has been proved to be so crucial for epidural electrode fields, was 'opened'. The situations were worsened by the fact that opposite poles in all three electrode arrays was less than 10mm apart. Current flow was mainly confined within the vertebral canal, and hence the significance of the general thorax could not be fully tested.

Nevertheless, the combined outcome of all the tests, when put together, was encouraging, given the inherent uncertainties of such experimental work. Results were in the right order of magnitude, and in particular those of 3- and 4-electrode arrays compared favourably with the reported results.

The major indication was, as usual, the effects of low-impedance shunt pathways, such as csf, between electrodes in multi-pole arrays.

10.3 ANALYSIS OF STIMULUS FIELD GENERATED BY EPIDURAL ELECTRODE

10.3.1 The Definition of Stimulus Strength

Comparisons of results in this thesis are often made in terms of general field shape, peak current density and in some cases, the variation of potential profiles within the cord. The question of using a standard 'stimulus parameter' on field interpretation has yet to be decided, but the choice depends on the type and level of interpretation.

The parameter 'driving function' is also introduced and from the discussion presented in Section 10.4, the use of 'driving function' in place of current density seems to serve a useful purpose. On the other hand, the full effects of a field on myelinated fibre still needs to be based on the McNeal model, which considers not only the field magnitude but also time response of the applied field and orientation of the fibre.

10.3.2 Field Analysis

A 2-D approach had been used for the analysis of tissue properties and anatomical factors on field distribution. The implication was that the conducting medium in the subarachnoid space is the crucial factor affecting stimulus intensity. It must be pointed out that only a bipolar configuration was used in the study.

The 3-D field solutions were presented in Chapter 2

relating monopolar, bipolar and multi-pole electrodes in the epidural space. Although the set of tissue resistivities were subsequently modified, as described in Chapter 5, those field solutions still provide valuable information due to the lack of data in this area.

A preliminary comparison of mid-sagittal plots in Figures 2.10 (monopolar) and 2.13 (bipolar) shows the similarity of peak current density in terms of orientation and magnitude.

The contour plots of each figure are also similar to the corresponding 2-D analysis (COBURN.1981), even though the current densities of 2-D work were approaching an order of magnitude higher. Figure 2.15 shows a single cathode-double anode (1-20) case while Figure 2.14 gives the fields generated from double cathode-double anode configuration (12-30).

Roughly speaking , spreading the driving current between two poles simply reduces the peak current densities in the dorsal column to about one-half. Sites of excitation in the spinal cord, with reference to myelinated fibre, seem likely to become less localised.

10.4 THEORETICAL ASPECTS OF AXON MODEL

10.4.1 Driving Function as the Stimulus Parameter

'Driving function' was first introduced in Chapter 7 as the parameter that govern the rate of depolarisation towards threshold. The function was related to the sharpness of potential profile along the path of a fibre. Theoretical studies also showed that the function was proportional to membrane depolarisation (Figures 7.4 and 7.5) and inversely proportional to threshold current (Figure 8.12).

Figure 10.2 shows plots of potential profiles from the 3-D ANSYS solutions presented in Chapter 2. The corresponding electrode configurations are monopolar, bipolar 0-3 and multi-poles 1-20 and 12-30. The location is the vertical path through node 133 in the white matter as shown in Figure 2.6. It can be seen that the shapes of the peak region of the three solid curves are very similar in character. The flatter shape of the dotted line was due to the fact that no electrode was at the zero mm level.

Using the definition of the driving function, a value for a 20μm fibre is therefore calculated from the peak region of the three solid curve. The procedure is similar for the configuration 12-30 case, where the three points used for the calculation are indicated as (X) in the curve. The values of the driving functions for four cases (monopolar, 0-3, 1-20, 12-30), are 9mV, 9mV, 8.6mV and 4mV respectively. Note that the total cathodic current in each

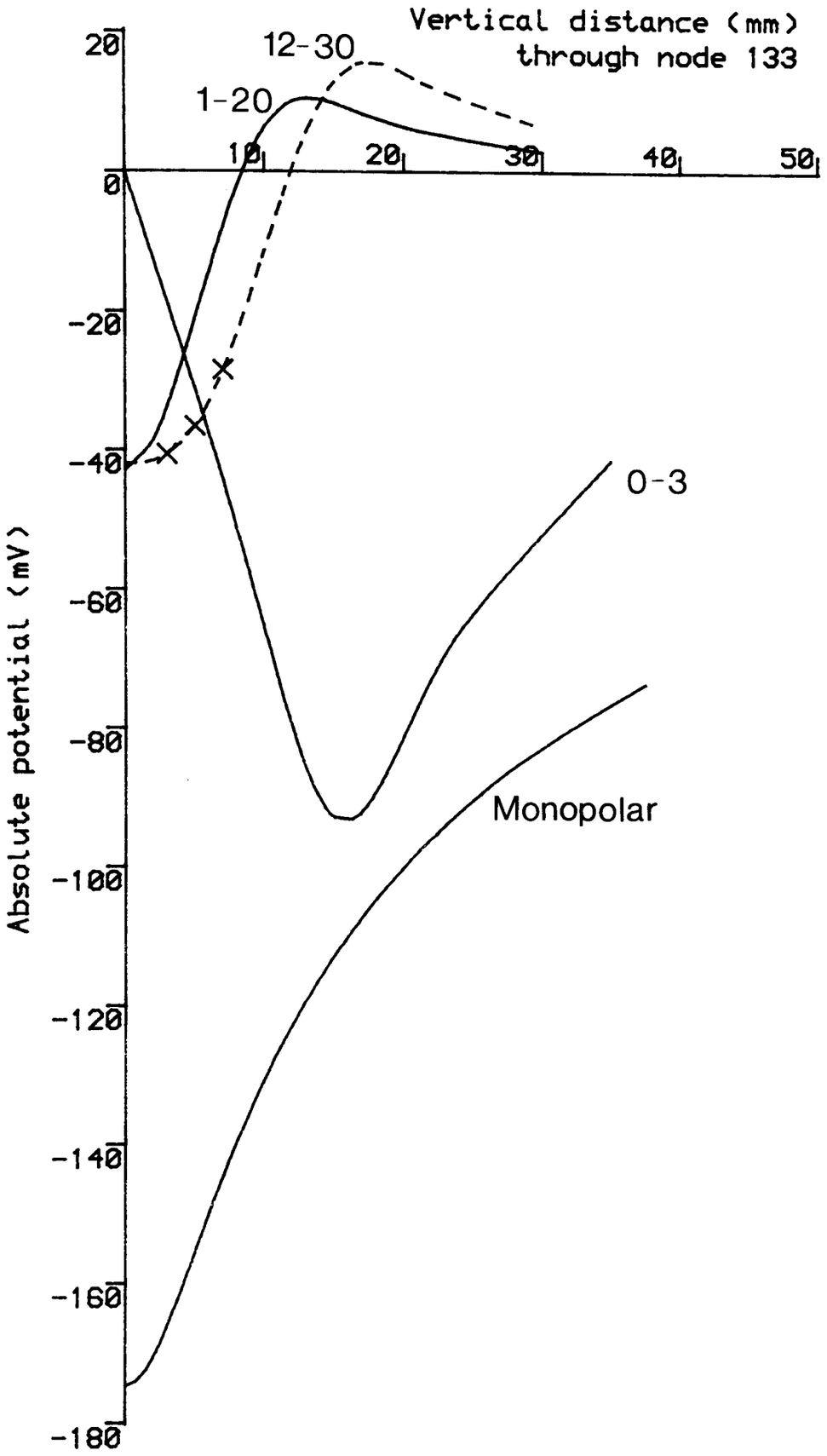

FIGURE 10.2 VARIATIONS OF POTENTIAL AS A FUNCTION OF VERTICAL POSITION IN THE DORSAL SPINAL CORD FOR DIFFERENT ELECTRODE CONFIGURATIONS

node 133 as indicated in Figure 2.6

case was 1mA.

The corresponding current density, as indicated in the figures in Chapter 2, were 2.8$\mu A.mm^{-2}$, 2.5$\mu A.mm^{-2}$, 2.5$\mu A.mm^{-2}$ and 1.3$\mu A.mm^{-2}$. In other words, both the driving function and current density give very similar comparative values. Either driving function or currrent density provide useful, and roughly equivalent, rules of thumb concerning the effect of different fields. However driving function is more convenient in the present context.

10.4.2 Effect of Branching

Theoretical analysis of the effects of a branch on a straight fibre was presented in Chapter 7. The major indication is, of course, that threshold at the 'branching node' was lower, and that the effect of introducing a branch has more effect on smaller fibre further from the electrode.

Note that the corresponding driving function for the branching node, 20, as derived in Appendix 3, was (Ve,19-3Ve,20+Ve,21+Ve,40). This function can also be written as (Ve,19-2Ve,20+Ve,21)+(Ve,40-Ve,20), where the first term is the familiar function for straight fibre. Therefore whether or not the branch will lower the threshold depends on the second term (Ve,40-Ve,20).

For the simplified studies in Section 7.4.2, where node 40 was further away from the electrode than node 20, (Ve,40-Ve,20) became a positive value adding to the first

term. This explains why the fibre threshold was always lower than a straight fibre. That is to say, the orientation of the first node on the branch relative to the branching node is important.

10.4.3 Effect of Temperature on Conduction Velocity

The velocity-diameter ratio predicted by Model A is about 2 (m/s)/μm, as indicated in Figure 9.5. Although this ratio compared favourably with the early experimental work by TASAKI et al (1943), FRANKENHAEUSER and WALTMAN (1959) and HUTCHINSON et al (1970), it is general believed that the velocity-diameter ratio is 5~6 (m/s)/μm in mammalian myelinated fibres (HURSH,1939; RUSTON,1951).

The most obvious factor that causes the difference is the environment, in particular the temperature difference, in which the fibres lie. It should also be noted that the mathematical descriptions of the fibre (FRANKENHAEUSER,1960,1963) were derived at a temperature of 20°C.

The influence of temperature upon nerve activity is a well-known fact. In the mathematical descriptions of nodal membrane (HODGKIN and HUXLEY,1952; FRANKENHAEUSER and HUXLEY,1964), a temperature term appeared in the 'constant field equations' which described the individual ionic current components. In addition, HODGKIN and HUXLEY (1952) used a factor called temperature coefficient, Q_{10}, for the rate constants concerning the activation and inactivation of ionic components. FRANKENHAEUSER and MOORE (1963) also

derived the rate constant-temperature relationships which were, unfortunately, limited to a range of 2.5°C-20°C .

HUTCHINSON et al (1970) determined the relationship of conduction velocity with temperature and fibre diameter in single nerve of Xenopus laevis. The experimental results were summarized in expression

$$\Theta = D(0.06T+0.6) \qquad (10.1)$$

where Θ is conduction velocity in m/s,

D is fibre diameter in μm and

T is the temperature in the range $30°C > T > 10°C$.

Using the above expression, the velocities for 10μm and 20μm fibres at 20°C will be 18m/s and 36m/s respectively, which are also predicted by Model A. Unfortunately, the upper limit of the temperature in expression (10.1) was only 30°C. If a temperature of 37°C had been used in the expression , then the conduction velocity of a 20μm fibre would have been 56.4m/s. The velocity-diameter ratio would then be 3 which is, however, still smaller than that of mammalian fibre.

HUTCHINSON et al (1970) also attempted to derive the theoretical expression (10.1) using a fibre model (GOLDMAN and ALBUS,1968) and the 'shifted' rate constants (FRANKENHAEUSER and MOORE.1963). The mathematical outcome did not agree with the experimental expression and, even worse, the fibre model failed to conduct impulses at 35°C.

On the other hand, the experimental work of HUTCHINSON et al (1970) suggested there was a positive linear relationship between conduction velocity and

temperature in the range 15°C-30°C. If expression (10.1) is used to calculate conduction velocity for 10μm and 20μm fibres at 37°C, then in both fibres, a drop of temperature from 37° C to 20°C will reduce the velocity by 35%. The positive linear relationship of velocity-temperature was found on mammalian myelinated fibres by many investigators (PAINTAL,1965; BUCHTHAL and RASENFALCK,1966: FRANZ,1968). However, their experimental studies indicated that a drop of temperature from 37°C down to 20°C reduced the velocity by about 50%. In other words, the mammalian fibres are more sensitive to temperature variation, too.

The question of velocity-diameter ratio remains to be answered. Nevertheless, MOORE et al (1978) suggested that the correct threshold level was the most important characteristic of a nodal membrane description. Chapter 8 has partially indicated this using only the McNEAL (1976) model.

10.4.4 Development of Fibre Model to Include Extracellular Conduction and External Applied Fields

The development of circuit model of the myelinated fibre has been given in Chapter 9. The main issue was the representation of extracellular medium by means of simple passive networks. In particular, Model B was developed so as to investigate the effect of external applied fields on action potential. In general, the following observations are obtained from the analysis.

(a) conduction velocity was proportional to external

conductance, Ge, as shown in Model A,

(b) conduction velocity agreed with experimental findings (HUTCHINSON et al,1970),

(c) the characteristic of refactory period is adequately modelled, noting that two opposite travel impulses 'cancel' each other when they collided, as shown in model B.

(d) propagating action potentials can never be blocked by external applied fields from a remote electrode not in contact with the fibre, even though the shapes of impulses were clearly distorted during the interaction.

(e) the Model B seems limited in that a second impulse cannot be initated again from the fibre by the same long pulse.

The first three points are supporting models A and B, while the last two differ from the expectations.

The idea of applied field is to set up extracellular field in the medium so as to disturb the 'local circuitry' of the active region. This kind of field interaction is of course depends on the actual representation of the local circuitry field and the applied field. The 1-D representation of the fibre itself is well supported (PLONSEY,1974), but using the same approach to include the external medium, however, is a very coarse assumption. Note that this approach is extremely simplified with respect to the mathematical analyses of extracellular field solutions (LORENTE de NÓ,1947; CLARK and PLONSEY,1968; BARKER,1979). PLONSEY (1974) indicated that

the behaviour of extracellular potential, due to the radial component of current flow, was not easy to characterize.

10.5 VALIDATION STUDY OF McNEAL (1976) NERVE FIBRE MODEL

A full validation study of the model using the chick BVC nerve/muscle has been presented in Chapter 8. The main issue was remote electrical stimulation of the nerve fibre within the tendon, where the firing of nerve fibres was detected through the mechanical response of the muscle. Theoretical solutions were obtained and compared with the experimental results.

The first thing to be discussed is the criterion for threshold determination in the experiment. As mention in Chapter 8, applied current was considered as threshold when there was a minimum twitch response visually detected in the pen recorder. Ideally, response of muscle caused by the firing of only one fibre in the bundle should have been the criterion for threshold. The sensitivity of the pen recorder was 1835mm/N and the minimum movement of the pen detected visually during the experiment was, at most, 0.5mm. In other words, the muscle force detected was 0.5/1835 N, i.e. about 0.27×10^{-3} N. In general, the maximum force obtained from a preparation containing 300 fibres was 29×10^{-3} N. Hence 0.27×10^{-3} N recorded in the experiment corresponded to the excitation of three single fibres, provided that all the 300 fibres were excitable during the experiment, and that

all of the fibres in the bundle were efferent.

The results, in general, deviated from the theoretical prediction at greater electrode distances, and the phenomenon was particular evident for longer pulses.

It was first suspected that this was due to numerical error in the simulation process. Random checks were made using an integration time step ten times smaller and double precision for the real number calculations. Results, however, were about the same as before.

A second suspicion was direct stimulation of the muscle when the electrode was long way from the tendon. The whole assembly was set up again to investigate this possibility. The preparation was first stimulated at two arbitrary pulse settings, each at four electrode distances to ensure that the threshold level of the new preparation was the same as before. Tubocurine was then added to the Krebs-Henseleit bath, to delete the nerve responses pharmacologically, and the preparation was stimulated 30 minutes later. No muscle response was detected at any electrode distances using the two pulse settings. The electrode was finally brought in touch with the muscle and only at this time was the muscle twitch slightly detected. This excluded the possibility of the muscle being stimulated directly.

There were two practical problems with regard to the experiment. The first one was the limited length of tendon section of the BVC preparation. As described in the theoretical aspects of computing in Section 8.4.1, the

short length of fibre limited the number of effective nodes in the fibre model. The maximum numbers of nodes was about 19 for a 5μm fibre, and was only 15 for a 9μm. Therefore a proper clinically-used electrode (3mm long, say) or a multi-pole electrode cannot be used for testing. Other electrode configurations for example bipolar or even an anode, cannot be used either. Another problem was the limited power of the constant-current stimulator which could only deliver up to 40mA amplitude.

10.6 INTERPRETATION OF THEORETICAL FIELDS WITH MYELINATED NERVE MODEL

The 'two-stage' approach of field interpretation has already been presented in Chapter 7 on the analysis of fibre bending and branching. In brief, a simple theoretical field was first obtained, in this circumstance, by formulae. The values of potential corresponding to the positions of nodes (of Ranvier) were then applied to the fibre model either for steady-state analysis or digital simulation. A more realistic situation was also demonstrated in Chapter 8 on the validation study of fibre model.

The above approach is of course equally applicable directly using the long ascending myelinated fibre in the dorsal column of the spinal cord. Stimulus fields can either be the 3-D ANSYS solutions presented in Chapter 2, or solutions using the new modified thoracic model with

the new set of resistivity values.

While the analysis on straight fibres is of highly significant interest, some other spinal nerve systems is also important.

One example is the afferent (group Ia) nerve fibre from the stretch receptors. Figure 10.3 shows the idealised picture of the fibre system in relation to the modified finite element mesh. After entering the spinal cord at an oblique angle, the fibre immediate bifurates, at point (i) as shown, into ascending and descending branches, each extending a few segments along the cord. These two branches, in turn, give rise to branches, at points (ii) as shown, which run across the cord at the same horizontal level into the motoneurone pool.

Such a fibre system, normally 10μm or above in diameter (BROWN,1981), is a good example of a system with both characteristics discussed in Chapter 7: that is bending and branching. Path (iv)-(iii)-(i) in Figure 10.3(b) clearly shows that the fibre bends in the spinal root before entering into the cord. That particular path of the fibre system is also closest to an epidural electrode positioned at the same level. The second point is of course the branching of the system immediately inside the cord. The threshold level of the fibre system may be different from a normal straight fibre of the same diameter due to these two features.

From the theoretical viewpoint, such a fibre system offers the chance of a proper analysis using the finite

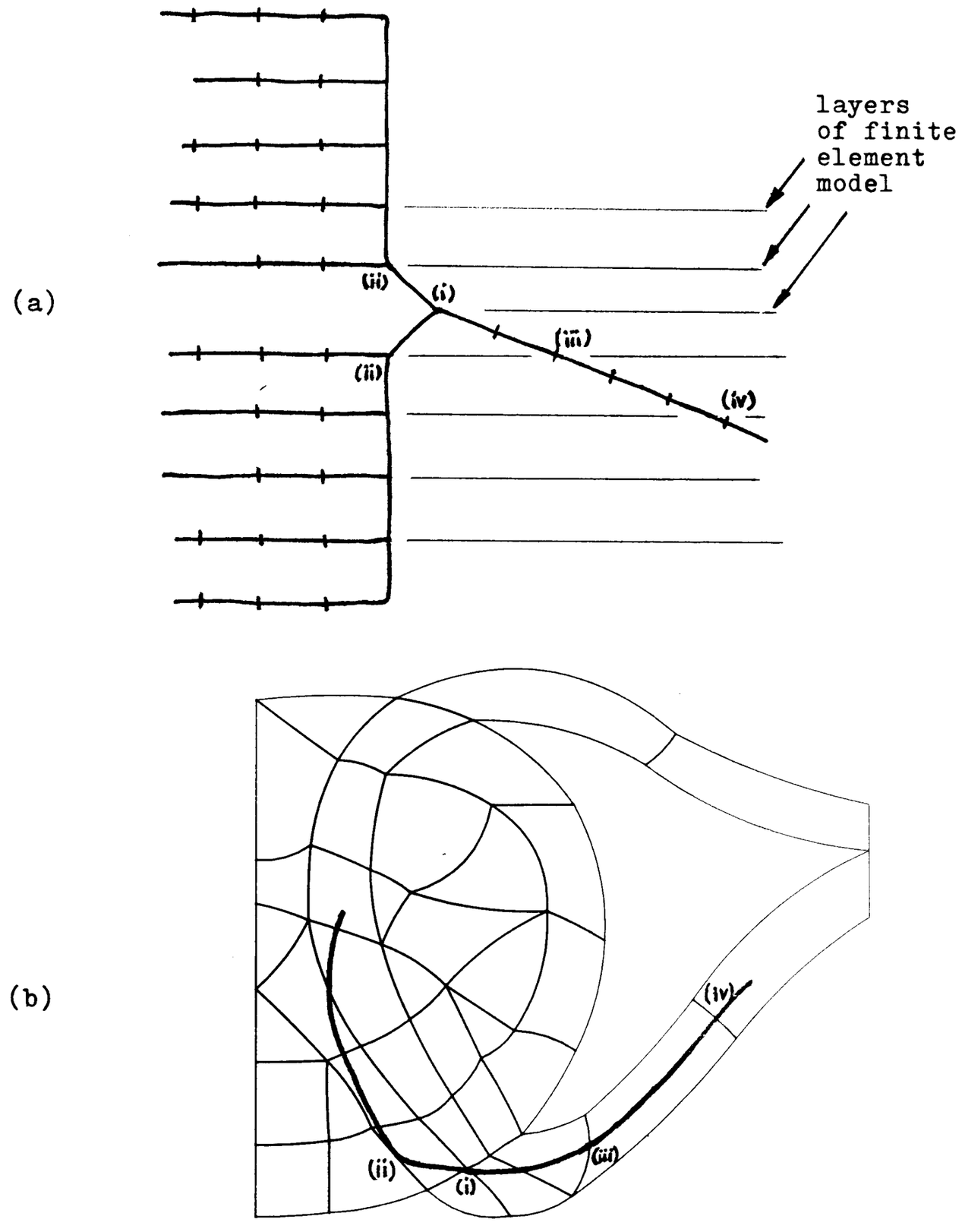

FIGURE 10.3 SCHEMATIC DIAGRAM OF FIBRE SYSTEM WITH RESPECT TO FINITE ELEMENT MESH

Fibre diameter 10μm. Each stroke represent a node of Ranvier

element field solution and McNeal fibre model. Clinically, the system is of significance due to the fact that this fibre system and the ascending myelinated dorsal column fibres are the two that are closest to an epidural electrode. Epidural spinal cord stimulation ideally aims for dorsal column fibres to be stimulated, rather than the root system which goes directly into the motoneurone pool, giving unwanted motor effects. In other words, the threshold difference between the two systems should be as large as possible. One factor affecting the difference is the position of the electrode relative to the fibres, and the other may be the type of electrode configurations. LAW (1983) statistically showed that a maximum threshold difference was obtained by using monophasic stimulation of narrowly separated, longitudinal bipoles with rostral cathodes. This is a good source of clinical data with which theoretical results can be compared.

10.7 RECOMMENDATIONS

Apart from the field interpretation and clinical correlations discussed in the last section, a few more studies are recommended.

The first is a sensitivity study of tissue electrical and geometrical properties of the finite element model. Such a study will help to understand the major parameters that influence the field solutions.

The second concerns the experimental validation of

the McNeal fibre model. The test conducted in Chapter 8 was limited by the short length of the nerve. Delivery current was also confined to below 40mA amplitude. Suitable preparations of longer nerve should be searched for to enable a wider study. More complex electrode configurations should also be investigated.

The third is the theoretical development of Model B for field interaction. The use of simple network is inadequate for accurate representation of external medium and field behaviours. A finite difference approach may be the solution for a proper field analysis by modelling the continuous medium with networks of resistors. The boundary condition imposed on such a model can be first obtained from a finite element model, the development of which now seems virtually complete.

CONCLUDING REMARKS

The final three-dimensional finite element model presented in this work is capable of predicting spinal cord electrical fields generated by epidural electrodes with adequate accuracy for forseeable biophysical and neurological purposes. Extensive validation, involving patients, cadaver studies and published experimental data provides a high degree of confidence in the anatomical structure of the model and the conductive properties of various tissues and biological materials. In particular, an effective resistivity of 1600 ohm-cm for the spinal column has been determined.

Finite element solutions for multi-pole electrode arrays indicate that, for poles separated by more than about 10mm, each current source can be considered as an independent monopole. This statement applies to local current density vectors in the spinal nerve tissue at the level of each electrode pole.

An in-vitro validation study on the main biophysical model of the myelinated axon, used for interpreting neuronal effects of spinal cord fields, gave experimental threshold measurements closely in agreement with those predicted for a wide range of monopolar cathodic electrode distances and stimulus parameters. Predicted thresholds departed from observed values with increasing electrode

distances, in some cases by a factor of three too high.

Theoretical developments of myelinated nerve fibre computer simulations, for use in conjuction with finite element field solutions, have shown that bending and branching of fibre systems may have a profound influence on lowering stimulus thresholds. There are strong indications that a sharp bend in a fibre, or a branch, of particular geometry and orientation in relation to an applied field. may reduce the threshold of a fibre to a value corresponding to straight fibre of twice the diameter.

A theoretical study of nerve action potentials propagating through applied external fields did not confirm the possibility that remote electrodes, for example multipole anodes in the epidural space, may directly block neural activity. It should be noted that the same model was sufficiently well-developed to adequately demonstrate collison blocking.

REFERENCES

ABZUG, C., MAEDO, M., PETERSON, B W. and WILSON, V.J. (with an Appendix by BEAN, C.F.) (1974) Cervical branching of lumbar vestibulospinal axons. J. Physiol. (London), 243, 499-521.

ALLISON, R.D. (editor) (1970) Basic Factors in Bioelectric Impedance Measurements of Cardiac Output, Lung Volumes and the Cerebral Circulations. 3rd Annual Neuro-electric Society conference, Las Vegas, Nevada. Instrument Society of America, Pittsburgh.

BAYLEY, R.H., KALBFLEISCH, J.M. and BERRY, P.M.(1969) Changes in the body QRS surface potentials produced by alternations in certain compartments of non-homogeneous conducting model. Amer. Heart J., 77, 517-528.

BARKER, A.T.; BROWN, B.H. and FREESTON, L.L. (1979) Modelling of an active nerve fibre in a finite volume conductor and its application to the calculation of surface active potentials. IEEE Trans. Biomed. Eng., BME-26, 1, 53-56.

BELL, J. (1981) Some threshold results for models of myelinated nerve. Mathematical Biosciences, 54, 181-190.

BEMENT, S.L. and RANCK, J.B. Jr. (1969a) A quantitative study of electrical stimulation of central myelinated fibres. Expl. Neurol., 24 147-170.

BEMENT, S.L. and RANCK, J.B. Jr. (1969b) A model for electrical stimulation of central myelinated fibres with a monopolar electrode. Expl. Neurol., 24, 171-186

BRIGHTON, C.T.; BLACK, J. and POLLACK, S.R. (1979) Electrical Properties of Bone and Cartilage : Experimental Effects and Clinical Application. Grune and Stratton, Inc., New York.

BRILL, M H., WAXMAN, S.G., MOORE, J.W. and JOYNER, R.W. (1977) Conduction velocity and spike configuration in myelinated fibres: computed dependence on internode distance. J. Neurology, Neurosurgery, and Psychiatry, 40 769-774.

BROWN, A.G. (1981) Organisation in the Spinal Cord : the Anatomy and Physiology of Identified Neurones. Berlin - Springer-Verlag.

BUCHTHAL, F. and ROSENFALCK, A. (1966) Evoked action potentials and conduction velocity in human sensory nerves. Brain Research 3, 1-122.

BURGER, H.C. and VAN MILAAN, J.B. (1943) Measurements of the specific resistance of the human body to direct current. Acta. Med. Scand., 114, 584-607.

CAMPOS, R.J.; DIMITRIJEVIC, M.M.; and SHARKEY, P.C. (1978) Clinical evaluation of the effects of spinal cord stimulation on motor performance in patients with upper motor neurone lesions. Proceedings of the Sixth International Symposium on External Control of Human Extremities. Yugoslav Committee for Electronics and Automation, Belgrave, Yugoslavia. 569-574.

CHAKKALAKAL, D.A.; JOHNSON, M W.; HARPER, R.A. and KATZ J.L. (1980) Dielectric properties of fluid-saturated bone. IEEE Trans. Biomed. Eng., BME-27, 2. 95-100.

CHEUNG, Y.K. and YEO. M.F. (1979) A Practical Introduction to Finite Element Analysis. London : Pitman.

CLARK, J. and PLONSEY, R. (1968) The extracellular potential field of the single active nerve fibre in a volume conductor. Biophysical Journal, 8, 842-864.

COBURN, B. (1980) Electrical stimulation of the spinal cord: two-dimensional finite element analysis with particular reference to epidural electrodes. Med. & Biol. Eng & Comput., 18, 573-584.

COBURN, B (1981) A theoretical analysis of spinal cord stimulation with particular reference to epidural electrodes. Ph.D. Thesis. Brunel University, Uxbridge. Middlesex, UB8 3PH, UK.

CRAGO, P.E., PECKHAM, P.H., MORTIMER, J.T. and Van Der MEULEN, J.P. (1974) The choice of pulse duration for chronic electrical stimulation via surface, nerve and intramuscular electrodes. Annals of Biomedical Engineering, 2, 252-264.

DAMON, A. and STOUDT, H.W. (1963) The functional anthropometry of old man. Human Factors, 5, 485-491.

ERIKSSON, C. (1976) "Electrical properties of bone " in BOURNE, G.H. (ed.) The Biochemistry and Physiology of Bone. Vol. IV, N.Y.: Academic. chapter 8, 330-384.

FITZHUGH, R. (1962) Computation of impulse initiation and saltatory conduction in a myelinated nerve fibre. Biophysical J . 2, 11-21.

FRANKENHAEUSER. B (1960) Quantitative description of sodium currents in myelinated nerve fibres of Xenopus laevis. J. Physiol. (London), 151, 491-501.

FRANKENHAEUSER. B (1963) A quantitative description of potassium currents in myelinated nerve fibres of Xenopus laevis. J. Physiol. (London), 169, 424-430.

FRANKENHAEUSER, B and HUXLEY, A.F (1964) The action potential in the myelinated nerve fibre of Xenopus laevis as computed on the basic of voltage clamp data. J. Physiol. (London) ,171. 302-315.

FRANKENHAEUSER, B and MOORE L.E. (1963) The effect of temperature on the sodium and potiassium permeability changes in myelinated nerve fibres of Xenopus laevis. J. Physiol. (London), 169, 431-437

FRANKENHAEUSER B and WALTMAN, B (1959) Membrane resistance and conduction velocity of large myelinated nerve fibre from Xenopus laevis. J. Physiol. (London). 148. 677-682.

FRANZ, D.N. (1968) Conduction failure in myelinated and non-myelinated axons at low temperatures. J. Physiol. (London), 199. 319-345.

GEDDES, L.A. and BAKER I.E. (1967) The specific resistance of biological material - a compendium of data for the biomedical engineer and physiologist. Med. & Biol. Eng., 5, 271-293.

GILDENBERG, P. (1977) Treatment of spasmodic torticollis with dorsal column stimulation. Acta. Neurochinurgica (Wien). Vol. 24, 65-66.

GINSBORG, B L. (1960) Spontaneous activity in muscle fibres of the chick. J. Physiol. (London), 150. 707-717.

GOLDMAN. L. and ALBUS. J.S. (1968) Computation of impulse conduction in myelinated fibres: Theoretical basis of the velocity-diameter relation. Biophysical J., 8. 596-607.

GORMAN. P.H. and MORTIMER, J.T. (1983) The effect of stimulus parameters on the recruitment characteristics of direct nerve stimulation. IEEE Trans. Biomed. Eng., BME-30. 7. 407-414.

GUHA, S.K., KHAN, M.R. and TANDON. S.N. (1973) Electrical field distributions in the human body. Phys. Med. Biol., 18, 712-720.

GULRANJANI. R.M and MAILLOUX. G.E. (1983) A simulation study of the effects of torso inhomogeneities on electro-cardiographic potentials, using realistic heart and torso models. Circulation Research, 52, 45-56.

HASLEGRAVE, C.M. (1979) An anthropometric survey of British drivers. Ergonomics, 22, 145-153.

HASLEGRAVE, C.M. (1980) Anthropometric profile of British car drivers. Ergonomics, 23, 437-467.

HENSHELL, R.D. (Ed.) (1978) Pafec 75 : data preparation. Pafec Ltd., 40 Broadgate, Beeston, Nottingham, England.

HERINGA, A; STEGMAN, D.F.; UIJEN, G.J.H. and De WEERD, J.P.C. (1982) Solution methods of electrical field problems in physiology. IEEE Trans. Biomed. Eng., BME-29, 1, 34-42.

HINTON, E and OWEN, D.R.J. (1977) Finite Element Programming. London, Academic Press.

HODGKIN, A.L. (1965) The Conduction of Nervous Impulse. 2nd impression, Liverpool University Press.

HODGKIN, A.L. and HUXLEY, A.F. (1952) A quantitative description of membrane current and its application to conduction and excitation in nerve. J. Physiol. (London), 117, 500-544.

HORACEK, B.M. (1974) Numerical model of an inhomogeneous human torso. In RUSH, S. and LEPESCHKIN, E. (Eds.) Advances in cardiology, 10. 51-57.

HURSH, J.B. (1939) Conduction velocity and diameter of nerve fibres. Am. J. Physiol., 127, 131-139.

HUTCHINSON, N.A., KOLES, Z.J. and SMITH, R.S. (1970) Conduction velocity in myelinated nerve fibres of Xenopus laevis. J. Physiol. (London), 208, 279-289.

ILLIS, L.S.; SEDGWICK, E.M.:, OYGAR, A.E. and SABBAHI AWADALLA, M.A. (1976) Dorsal column stimulation in the rehabilitation of patients with multiple sclerosis. Lancet, 1, 1383-1386.

ILLIS, L.S.; SEDGWICK, E.M. and TALLIS, R.C. (1978) Clinical results of spinal cord stimulation. Proc. of the Sixth International Symposium on External Control of Human Extremities. Yugoslav Committee for Electronics and Automation, Belgrave, Yugoslavia, 523-528.

ILLIS, L.S.; SEDGWICK, E.M. and TALLIS, R.C. (1980) Spinal cord stimulation in multiple sclerosis: clinical results. J. Neurology, Neurosurgery and Psychiatry, 43, 1-14.

ILLIS, L.S.; READ, D.J.; SEDGWICK, E.M. and TALLIS, R.C. (1983) Spinal cord stimulation in the United Kingdom. J. Neurology, Neurosurgery and Psychiatry, 46, 299-304.

IRONS, B.M. (1970) A frontal solution program for finite element analysis. International Journal for Numerical Methods in Engineering, 2, 5-32.

JEANS, J.H. (1925) The Mathematical Theory of Electricity and Magnetism. Cambridge University Press.

JOBLING, D.T., TALLIS, R.C., SEDGWICK, E.M. and ILLIS, L.S. (1980) Electronic aspects of spinal cord stimulation in multiple sclerosis. Med. & Biol. Eng. & Computing, 18. 48-56.

KATZ, B. (1966) Nerve, Muscle and Synapse. McGraw-Hill.

KIM, Y; TOMPKINS, W.J. and WEBSTER, J.G. (1981) A three-dimensional modifiable body model for biomedical applications. In COHEN, B.A. (Ed.) Frontiers of Engineering in Health Care, IEEE Conf. Publ., 81CH1621-2, 19th-21st Sept., Houston, Texas. 8-11.

KINNEN, E. (1966) Determining electric current flow patterns in the thorax. IEEE Reg. Six Conf. Rec., 379-381.

KOHNKE, P.C. (1979) ANSYS Engineering Analysis System Introductory Manual (linear statics). Swanson Analysis Systems, Inc. PO Box 65, Houston, PA.15342, USA.

KOLES, Z.J. and RASMINSKY, M (1972) A computer simulation of conduction in demyelinated nerve fibres. J. Physiol. (London). 227, 351-364.

LAW, J. (1983, in press) Spinal stimulation - statistical superiority of monophasic stimulation of narrowly separated, longitudinal bipoles having rostral cathodes. Applied Neurophys.

LORENTE de Nó, R. (1947) A Study of Nerve Physiology. Rockefeller Institute, New York.

McNEAL, D.R. (1976) Analysis of a model for excitation of myelinated nerve. IEEE Trans. Biomed. Eng., BME-23. 4, 329-337.

MARKOVICH, S.E. (editor) (1970) International Conference on Bioelectric Impedance. Ann. NY Acad. Sci., 170. 407-836.

MEIJER, J.H.; REULEN, J.P.H.; SCHNEIDER, H.; OE, P.L.; ALLON, W.; THIJS, L.G. (1982) Differential impedance plethysmography for measuring thoracic impedances. Med. & Bio. Eng. & Comput., 20. 187-191.

MELZACK, R. and WALL P.D. (1965) Pain mechanisms a new theory. Science. 150. 971-979.

MILLER, W.T. and GESELOWITZ, D.B. (1978) Simulation studies of the electrocardiogram. I : the normal heart Circulation Research. 43, 301-315.

MOORE, J.W.; JOYNER, R.W.; BRILL, M.H.; WAXMAN, S.D.; NAJAR-JOA, M (1978) Simulations of conduction in uniform myelinated fibres : relative sensitivity to changes in nodal and internodal parameters. Biophysical J., 21. 147-160.

MORTON, D.J.; TRUEX, R.C.: and KELLNER, C.E. (1941) Manual of Human Cross Section Anatomy. MD Williams and Wilkins Co., Baltimore.

NYOBER, I. (1959) Electric Impedance Plethysmography, Charles C. Thomas, Springfield, I11.

PAINTAL, A.S. (1965) Effects of temperature on conduction in single vagal and saphenous myelinated nerve fibres of the cat. J. Physiol. (London), 180, 20-49.

PICKARD, W.F. (1966) On the propagation of the nervous impulse down medullated and unmedullated fibres. J. Theoret. Biol. vol 11, 30-45.

PLONSEY, R. (1969) Bioelectric Phenomena. New York, McGraw-Hill.

PLONSEY, R. (1974) The active fibre in a volume conductor. IEEE Trans. Biomed. Eng., BME-21, 5, 371-381.

RANCK, J.B. (1975) Which elements are excited in electrical stimulation of mammalian central nervous system: a review. Brain Research, 98, 417-440.

RASHEVSKY, N. (1960) Another interesting case in the theory of nerve conduction IN Mathematical Biophysics. Vol 1, Chapter XXXVI, 431-439, Dover Publication, Inc. NY, 1960.

ROSEN, J.A. and BARSOUM A.H. (1979) Failure of chronic dorsal column stimulation in multiple sclerosis. Ann. Neurol, 6, 66-67.

ROSTERICH, J.D.; FOSTER, K.R. and POLLACK, S.R. (1983) Dielectric permittivity and electrical conductivity of fluid saturated bone. IEEE Trans. Biomed. Eng., BME-30, 2, 81-86.

RUDY, Y. and PLONSEY, R. (1980) A comparison of volume conductor and source geometry effects on body surface and epicardial potentials. Circulation Research, 46, 283-291.

RUDY, Y.; PLONSEY, R. and LIELMAN, J. (1979) The effects of variations in conductivity and geometrical parameters on the electrocardiogram, using an eccentric spheres model. Circulation Research, 44, 104-111.

RUSINKO, J.B.; WALKER. C.F and SEPULVEDA, N.G. (1981) Finite element modelling of potentials within the human thoracic spinal cord due to applied electrical stimulation In COHEN, B A. (Ed.) Frontiers of Engineering in Health Care, IEEE Conf. Publ., 81CH1621-2, 19th-21st Sept., Houston, Texas 76-81.

RUSTON, W.A.H. (1951) A theory of the effects of fibre size in medullated nerve. J. Physiol. (London) 115, 101-122.

SANDERS, F.K. (1948) The thickness of the myelin sheaths of normal and regenerating nerve fibres. Proc. roy. Soc. B, 135, 323-357.

SCHWAN, H.P. and KAY, C.F (1957) The conductivity of living tissues Ann. NY Acad. Sci. 65, 1007-1013.

SHEALY, C.N. MORTIMER J.T. and RESWICK, J.B (1967) Electrical inhibition of pain by stimulation of the dorsal columns : preliminary clinical report. Anesthesia and Analgesia (Cleveland), 46 489-491.

SILVESTER, P. and TYMCHYSHYN, S. (1974) Finite-element modelling of the inhomogeneous human thorax. In RUSH, S. and LEPESCHKIN, E. (Ed.) Advances in cardiology. 10, 46-50.

SMYTHE, W.R. (1968) Static and Dynamic Electricity Third Edition, New York, McGraw-Hill.

STOUAT, H W. (1981) The anthropometry of the elderly. Human Factors, 23, 29-37.

SWIONTEK, T.J. (1975) Distribution of Applied Electrical Current in the Spinal Cord and its Effects on Evoked Potentials. PhD Dissertation, Marquette University. Milwaukee, Wisconsin, USA.

SWIONTEK, T.J., SANCES, Jr. A. LARSON S.J. ACKMANN, J.J. CUSICK, J.F. MEYER, G.A. and MILLAR, E.A. (1976) Spinal cord implant studies. IEEE Trans. Biomed. Eng. BME-23. 4, 307-312

TALBOT, S.A. and GESSNER, U.R.S. (1973) Systems Physiology. Wiley, New York.

TAREN, J.A. and DAVIES, R. (1970) "Human spinal cord impedance : its application in neurosurgical stereotaxic cordotomy." in MARKOVICH, S.E. (ed.) International Conference on bioelectric impedance. Ann. NY Acad. Sci., 170, 783-791.

TASAKI, I.; ISHII, K ITO, H. (1943) On the relation between the conduction rate, the fibre diameter and the internodal distance of the medullated nerve fibre. Japan J. Med. Sci. Biophys . 9 189-199.

TEICHER, D.A. and McNEAL, D.R. (1978) Comparison of a dynamic and steady-state model for determining nerve fiber threshold. IEEE Trans. Biomed. Eng., BME-25, 1, 105-107.

WALTZ, J.M. and PANI, K.C. (1978) Spinal cord stimulation in disorder of the motor system. Proceedings of the Sixth International Symposium on External Control of Human Extremities. Yugoslav Committee for Electronics and Automation, Belgrave, Yugoslavia, 545-555.

WARWICK, R. and WILLIAMS, P.L. (Editors) (1973). Gray's Anatomy 35th Edition, Longman.

WHITE, R.M. (1979) The anthropometry of United States Army men and women : 1946-1977. Human Factors, 21. 473-482.

YOUNG, J.Z (1950) The determination of the specific characteristics of nerve fibres. Genetic Neurology. University Chic. Press, Chicago, 92-104.

ZIENKIEWICZ, O.C. (1977) The Finite Element Method. 3rd Edition, McGraw-Hill.

APPENDICES

APPENDIX 1

NUMBERING CONVENTION OF 1980J MULTI-SITE ELECTRODE

As shown in the diagram, numbers 0 to 3 are assigned to the poles of the multi-site electrode.

There is no confusion concerning with monopolar electrode. A note of the appropriate pole number is all that is required.

For bipolar configuration, pole number for the cathode comes first. It is then followed by a hyphen and the pole number for the anode. Thus a stimulation with cathode at pole 0 and anode at pole 3 will be called 0-3 configuration.

For multi-pole configuration, the above notation also applies together with the use of compound number. For example, if poles 0 and 1 share the same cathodic pulse, and poles 2 and 3 share the anodic pulse. then it will be called 01-23 configuration.

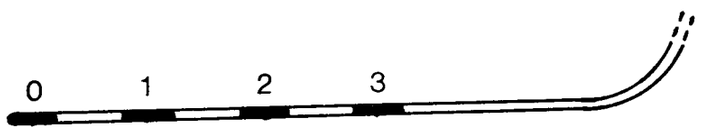

APPENDIX 2

CONDUCTIVITY CELL FOR RESISTIVITY MEASUREMENT

The resistivity of saline solution in Chapter 5 and Krebs-Henseleit solution in Chapter 8 were obtained from the impedance measurements with a conductivity cell and an impedance measuring bridge.

Essentially, the conductivity cell consists of a glass tube (inner diameter 0.78cm) and two detachable circular stainless-steel electrodes. With the electrodes in place, the length (l) between the two electrode surfaces is about 28.0cm. The diameter of each electrode is very slightly less than the bore of the tube. A rubber sleeve is also attached to each of the electrode as a fluid-tight seal.

For impedance measurement, the cell is completely filled with solution and connected to an impedance bridge (WAYNE KERR Universal Bridge B221).

The impedance (Z) between the two electrode can then be measured by balancing the bridge through a null indicator.

Resistivity (ρ) of the solution can then be calculated from

$$\rho = Z \times \frac{\text{cross-sectional area of the tube}}{\text{effective length (l)}} \quad \text{ohm-cm}$$

All measurements were taken at room temperature, and the capacitance components in each case were negligible.

APPENDIX 3

DERIVATIONS OF McNEAL MODEL FOR STRAIGHT AND BRANCHING FIBRE

3.1 Straight fibre

Figure A3.1 is the representation of McNeal model of myelinated axon. The lumped electrical elements, representing internodal axoplasmic conductance, Ga, nodal membrane conductance, Gm, and nodal capacitance Cm are given by

$$G_a = \frac{\pi d^2}{4\rho_i L} \quad , \quad G_m = g_m \pi d l \quad , \quad C_m = c_m \pi d l$$

A consideration of current at node j gives

$$C_m \frac{d}{dt} E_{m,j} + I_{i,j} = G_a (V_{i,j-1} - 2V_{i,j} + V_{i,j+1})$$

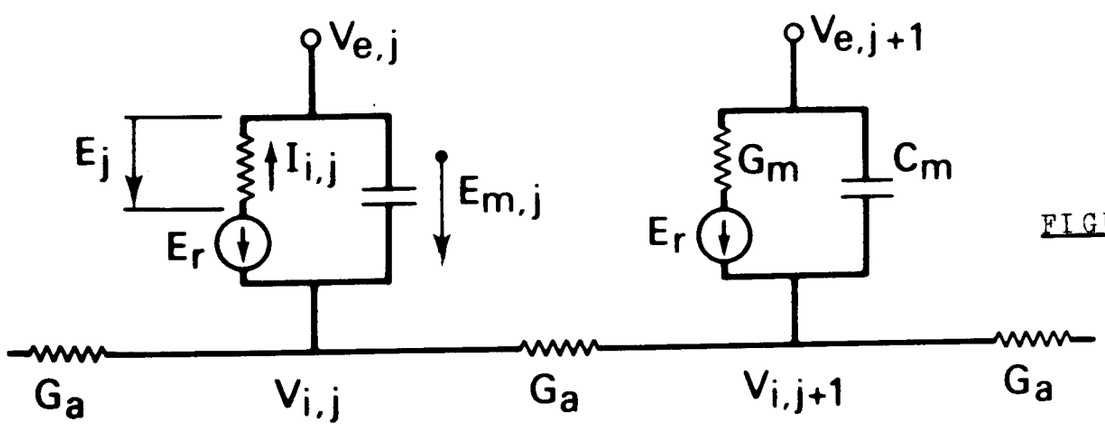

FIGURE A3.1

Substitute Em=Vi-Ve=E+Er gives

$$\frac{d}{dt} E_{m,j} = \frac{G_a}{C_m} (E_{j-1} - 2E_j + E_{j+1}) - \frac{1}{C_m} I_{i,j} + \frac{G_a}{C_m} (Ve_{,j-1} - 2Ve_{,j} + Ve_{,j+1})$$

$$\text{ie. } \tau_2 \dot{E}_j = (E_{j-1} - 2E_j + E_{j+1}) - \frac{1}{G_a} I_{i,j} + (Ve_{,j-1} - 2Ve_{,j} + Ve_{,j+1})$$

$$\text{where } \tau_2 = \frac{C_m}{G_a} \qquad (A\,3.1)$$

Equation (A3.1) does not describe the fibre ending behaviours. These will be treated in Appendix 4.

For a model of n nodes, the set of equations can be expressed neatly in matrix state-variable format (COBURN, 1981):

$$\tau_2 \begin{bmatrix} \dot{E}_1 \\ \dot{E}_2 \\ \vdots \\ \dot{E}_n \end{bmatrix} = \begin{bmatrix} a_{11} & 1 & 0 & & \\ 1 & -2 & 1 & & \\ & 1 & -2 & 1 & \\ & & \ddots & \ddots & \ddots \\ & & & 1 & a_{nn} \end{bmatrix} \begin{bmatrix} E_1 \\ E_2 \\ \vdots \\ E_n \end{bmatrix} +$$

$$\frac{1}{G_a} \begin{bmatrix} -1 & 0 & 0 & & \\ 0 & -1 & 0 & & \\ & \ddots & \ddots & \ddots & 0 \\ & & & 0 & -1 \end{bmatrix} \begin{bmatrix} I_{i,1} \\ I_{i,2} \\ \vdots \\ I_{i,n} \end{bmatrix} +$$

$$\begin{bmatrix} f_{11} & 1 & & & \\ 1 & -2 & 1 & & \\ & 1 & -2 & 1 & \\ & & \ddots & \ddots & \\ & & & 1 & f_{nn} \end{bmatrix} \begin{bmatrix} Ve,1 \\ Ve,2 \\ \vdots \\ Ve,n \end{bmatrix}$$

or $\frac{1}{2}\dot{\underline{E}} = [A]\underline{E} + \frac{1}{G_a}[U]\underline{I} + [F]\underline{V}e$ (A3.2)

3.2 Fibre with branch

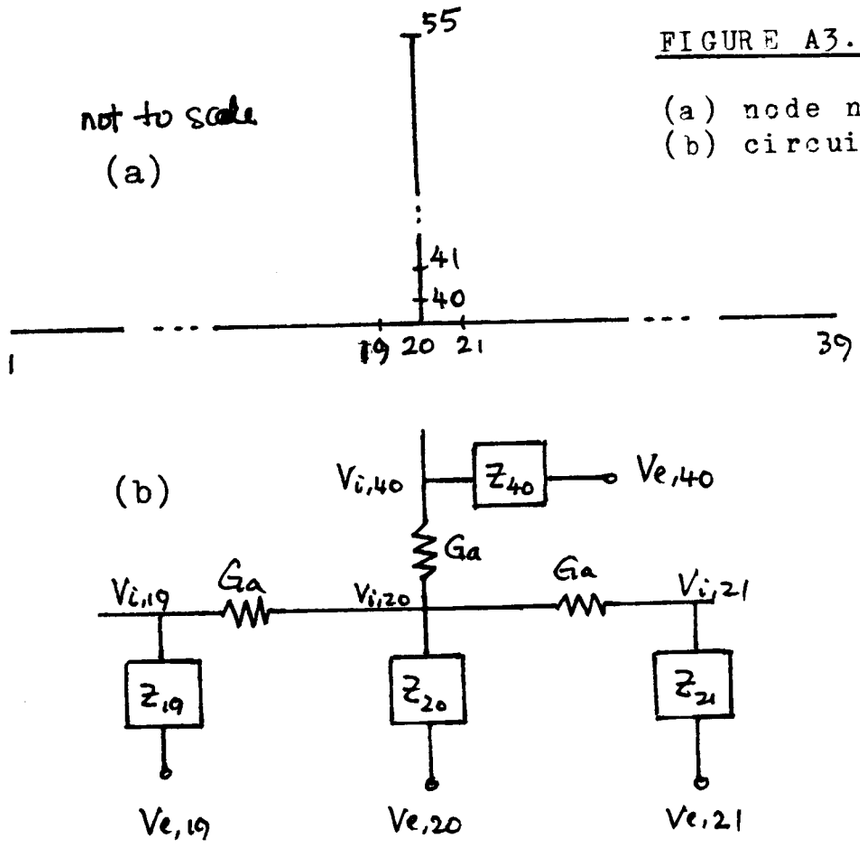

FIGURE A3.2

(a) node numbering scheme
(b) circuit model

For a branched myelinated fibre, as shown in Figure A3.2, the equation (A3.1) developed for a single straight fibre can be applied directly at all of the nodes with the exception of nodes 20, 40 and the terminal nodes 1, 39 and 55. Equations for the terminal nodes will be treated in Appendix 4.

Eqn. (A3.1), in fact, can be applied to node 40 only

with a change in the node number, i.e.

$$\tau_2 \dot{E}_{40} = (E_{20} - 2E_{40} + E_{41}) - \frac{1}{G_a} I_{i,40} + (V_{e,20} - 2V_{e,40} + V_{e,41}) \quad (A3.3)$$

Finally, the branch junction at node 20 needs special treatment due to the additional network. Figure A3.2(b) shows the lumped-circuit model at this point. Equating outward membrane current to incoming axoplasmic currents at this junction, we have

$$\begin{aligned} C_m \dot{E}_{20} + I_{i,20} &= G_a(V_{i,19} - V_{i,20}) + G_a(V_{i,40} - V_{i,20}) + G_a(V_{i,21} - V_{i,20}) \\ &= G_a(V_{i,19} + V_{i,40} + V_{i,21} - 3V_{i,20}) \end{aligned} \quad (A3.4)$$

By using $V_{i,j} = E_j + E_r + V_{e,j}$, (A3.4) becomes

$$\tau_2 \dot{E}_{20} = (E_{19} - 3E_{20} + E_{21} + E_{40}) - \frac{1}{G_a} I_{i,20} + (V_{e,19} - 3V_{e,20} + V_{e,21} + V_{e,40}) \quad (A3.5)$$

In fact, eqn.(A3.5) can be written directly by inspecting the given fibre system. First, note that the number of terms and their coefficients in the E's term and Ve's term are equal. Second, the E's and Ve's terms contain those nodes which are directly connected to node 20. In other words, node 20 connects to nodes 19, 21 and 40; and the E's terms are E_{19}, E_{21} and E_{40}. Third, the total number of these nodes determines the absolute value of the coefficient of E_{20}.

3.3 Fibre parameters for fibre model (from McNEAL, 1976)

c_m	$2\mu F.cm^{-2}$	membrane capacitance
Er	-70mV	resting membrane potential
gm	$30.4mmho.cm^{-2}$	subthreshold membrane conductance
l	$2.5\mu m$	width of active membrane at node of Ranvier
ρ_i	110 ohm-cm	axoplasm resistivity
L/D	100	ratio of internodal distance to fibre diameter
d/D	0.7	ratio of internal myelin diameter to external myelin diameter

APPENDIX 4 TYPES OF TERMINALS FOR FIBRE MODEL

4.1 Zero depolarisation

Consider node 1 in Figure A4.1(a) to be the first node having non-zero depolarisation. Eqn. (A3.1) gives

$$\tau_2 \dot{\epsilon}_1 = -2\epsilon_1 + \epsilon_2 - \frac{1}{G_a} I_{i,1} + V_{e,0} - 2V_{e,1} + V_{e,2} \qquad (A4.1)$$

Similarly, for node n

$$\tau_2 \dot{\epsilon}_n = \epsilon_{n-1} - 2\epsilon_n - \frac{1}{G_a} I_{i,n} + V_{e,n-1} - 2V_{e,n} + V_{e,n+1} \qquad (A4.2)$$

Equation (A3.2) becomes

$$\tau_2 \dot{\underline{\epsilon}} = [A]\underline{\epsilon} + \frac{1}{G_a}[U]\underline{I} + [F]\underline{V_e} + \underline{V_b}$$

where $\underline{V_b} = \begin{bmatrix} V_{e,0} \\ 0 \\ \vdots \\ 0 \\ V_{e,n+1} \end{bmatrix}$, an extra column vector of

dimension n that has to be included in order to fit into

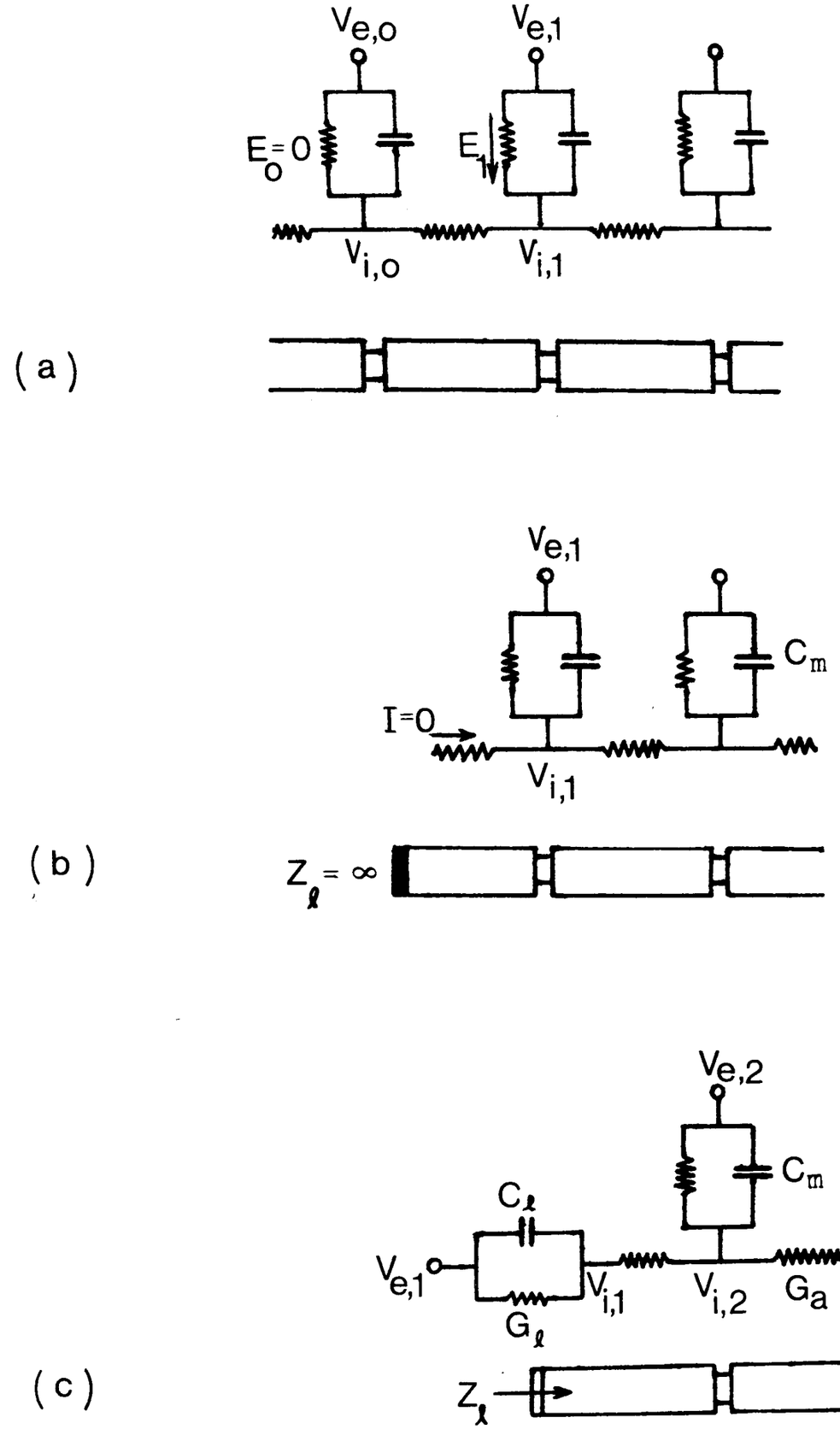

FIGURE A4.1 FIBRE ENDINGS FOR MYELINATED FIBRE MODEL

(a) zero depolarisation. $E_o = 0$
(b) zero internal axial current
(c) actual terminal

the expressions (A4.1) and (A4.2).

The corner elements of [A] and [F] are therefore

$$a_{11} = -2 = a_{nn}$$

$$f_{11} = -2 = f_{nn}$$

4.2 Zero internal axial current

With reference to Figure A4.1(b), if node 1 is the last node to be included in the left-hand end of an axon, and no current enters axially from the left then

$$Ga(Vi,0-Vi,1) = 0$$

Following the derivation corresponding to that for equation (A3.1) gives

$$\tau_2 \dot{E}_1 = -E_1 + E_2 - \frac{1}{G_a} I_{i,1} - Ve,1 + Ve,2$$

Similarly, take node n as the last node on the right end,

$$\tau_2 \dot{E}_n = E_{n-1} - E_n - \frac{1}{G_a} I_{i,n} + Ve,n-1 - Ve,n$$

Accordingly, the corner elements of [A] and [F] in eqn. (A3.2) are

$$a_{11} = -1 = a_{nn}$$

$$f_{11} = -1 = f_{nn}$$

4.3 Actual fibre terminals

Take the example of Figure A4.1(c) a synatic end is represented by lumped conductance and capacitance of G_ℓ and C_ℓ respectively. If the ending replaces node 1 of the previous cases, the equation will be

$$C_\ell \frac{d}{dt} E_{m,1} + I_{i,1} = G_a(-V_{i,1} + V_{i,2})$$

Following the same derivation as for equation (A3.1), we have

$$\tau_\ell \dot{E}_1 = -E_1 + E_2 - \frac{1}{G_a} I_{i,1} - V_{e,1} + V_{e,2}$$

where now $\tau_\ell = \frac{C_\ell}{G_a}$

Multiply both sides by $\frac{\tau_2}{\tau_\ell}$,

$$\tau_2 \dot{E}_1 = -\frac{\tau_2}{\tau_\ell} E_1 + \frac{\tau_2}{\tau_\ell} E_2 - \frac{\tau_2}{\tau_\ell} \frac{1}{G_a} I_{i,1} - \frac{\tau_2}{\tau_\ell} V_{e,1} + \frac{\tau_2}{\tau_\ell} V_{e,2}$$

The non-zero elements of the first row of [A], [F] and [U] in (A3.2) become

$$a_{11} = -\frac{\tau_2}{\tau_\ell}, \quad a_{12} = \frac{\tau_2}{\tau_\ell}, \quad f_{11} = -\frac{\tau_2}{\tau_\ell}, \quad f_{12} = \frac{\tau_2}{\tau_\ell}, \quad u_{11} = -\frac{\tau_2}{\tau_\ell}$$

Note that the area concerned in the lumped conductance G_ℓ and capacitance C_ℓ is the surface area of a disc.

APPENDIX 5

EFFECTIVE DIAMETER OF STIMULATING ELECTRODE USED IN THE BVC EXPERIMENT

finite isotropic medium of resistivity ρ Ωcm

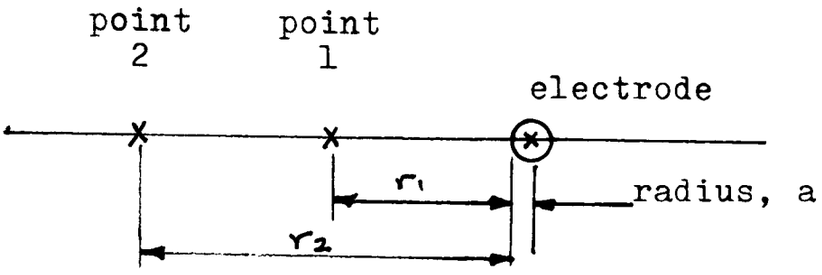

With reference to the above figure, the theoretical potential at point 1 will be

$$V1 = \frac{\rho I}{4\pi} \frac{1}{r_1 + a} + C1 \qquad (1)$$

where C1 is a constant of integral. Similarly, at point 2, the potential will be

$$V2 = \frac{\rho I}{4\pi} \frac{1}{r_2 + a} + C2 \qquad (2)$$

Assume C1=C2, (1)-(2) gives

$$V_1 - V2 = \frac{\rho I}{4\pi} \left(\frac{1}{r_1 + a} - \frac{1}{r_2 + a} \right)$$

Rearrange, the effective radius, a, can then be expressed as

$$a = \frac{-(r_1 + r_2) + \sqrt{(r_1 + r_2)^2 - 4K}}{2}$$

where $$K = r_1 r_2 - \frac{\rho I}{4\pi} \frac{r_2 - r_1}{V_1 - V_2}$$

By taking any two measurements, V1 and V2, from Figure 8.4 in the main text, the effective radius of the electrode can be found. A mean value, by taking sets of two different V1 and V2 at a time, was about 1.1mm.

APPENDIX 6

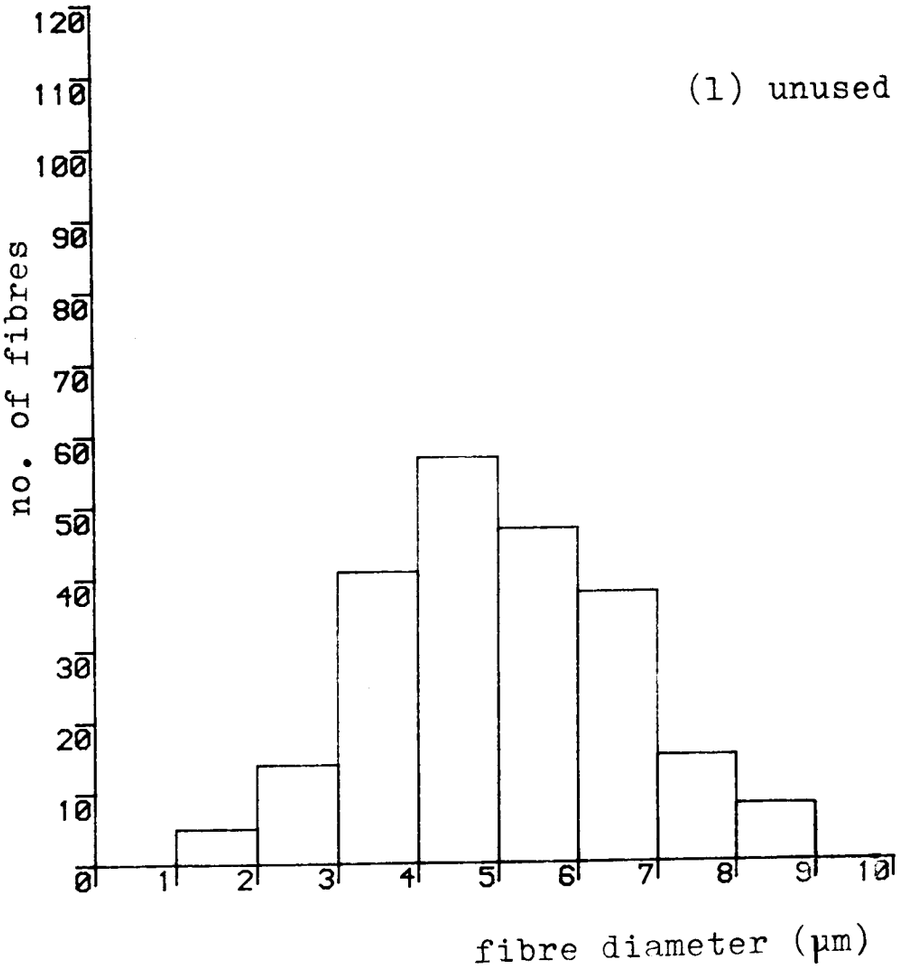

FIGURE A6 HISTOGRAMS OF BVC PREPARATION

Seven preparations were processed. (1) was un-used

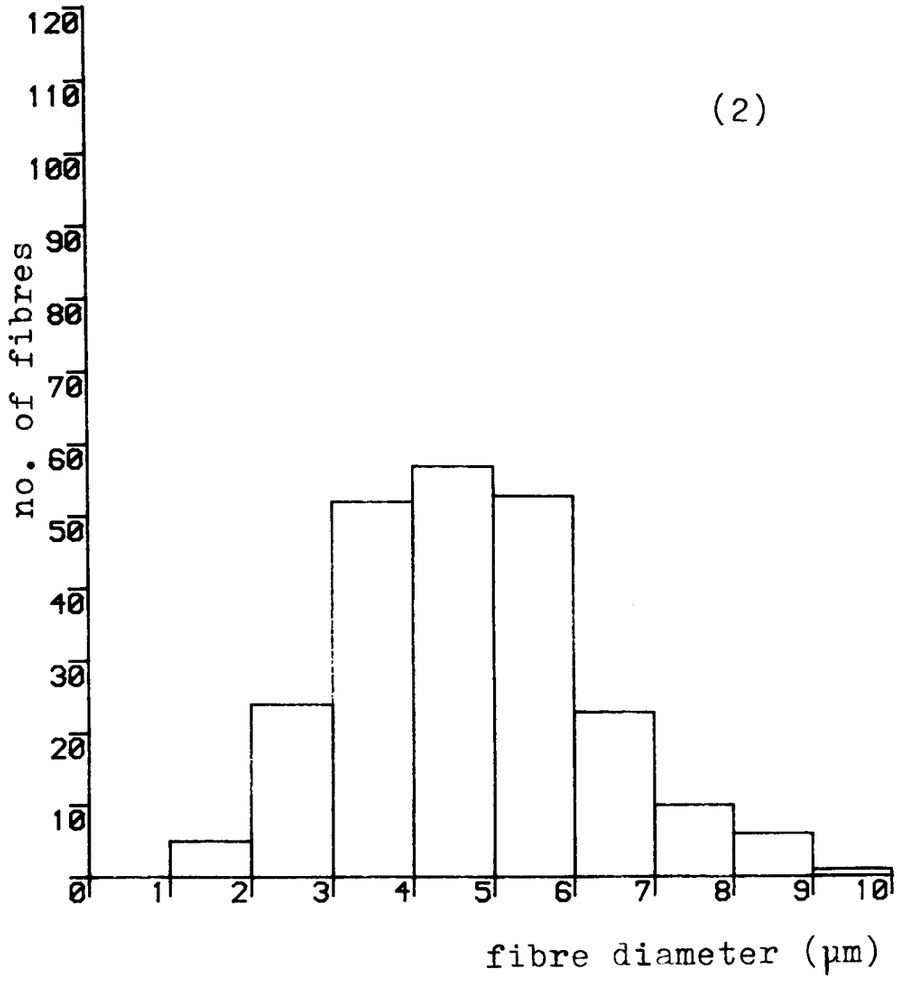
(2)
no. of fibres
120
110
100
90
80
70
60
50
40
30
20
10
0
1
2
3
4
5
6
7
8
9
10
fibre diameter (μm)

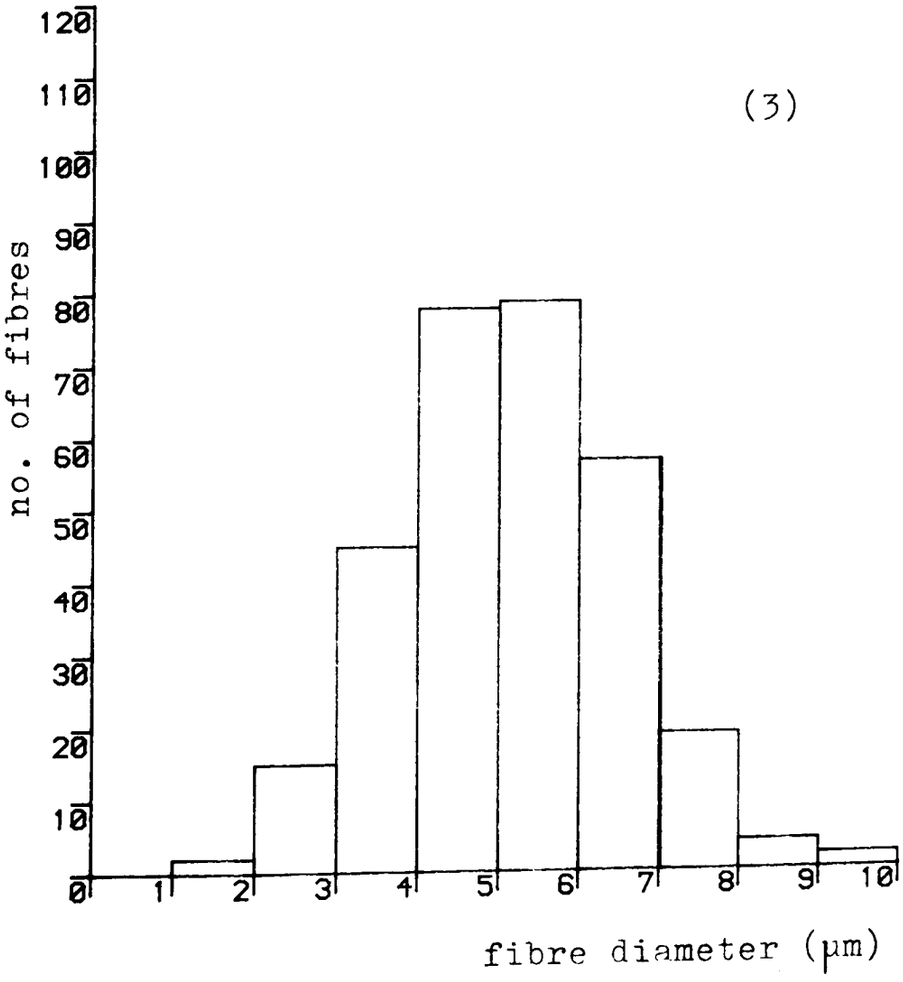
(3)
no. of fibres
120
110
100
90
80
70
60
50
40
30
20
10
0
1
2
3
4
5
6
7
8
9
10
fibre diameter (μm)

(4)

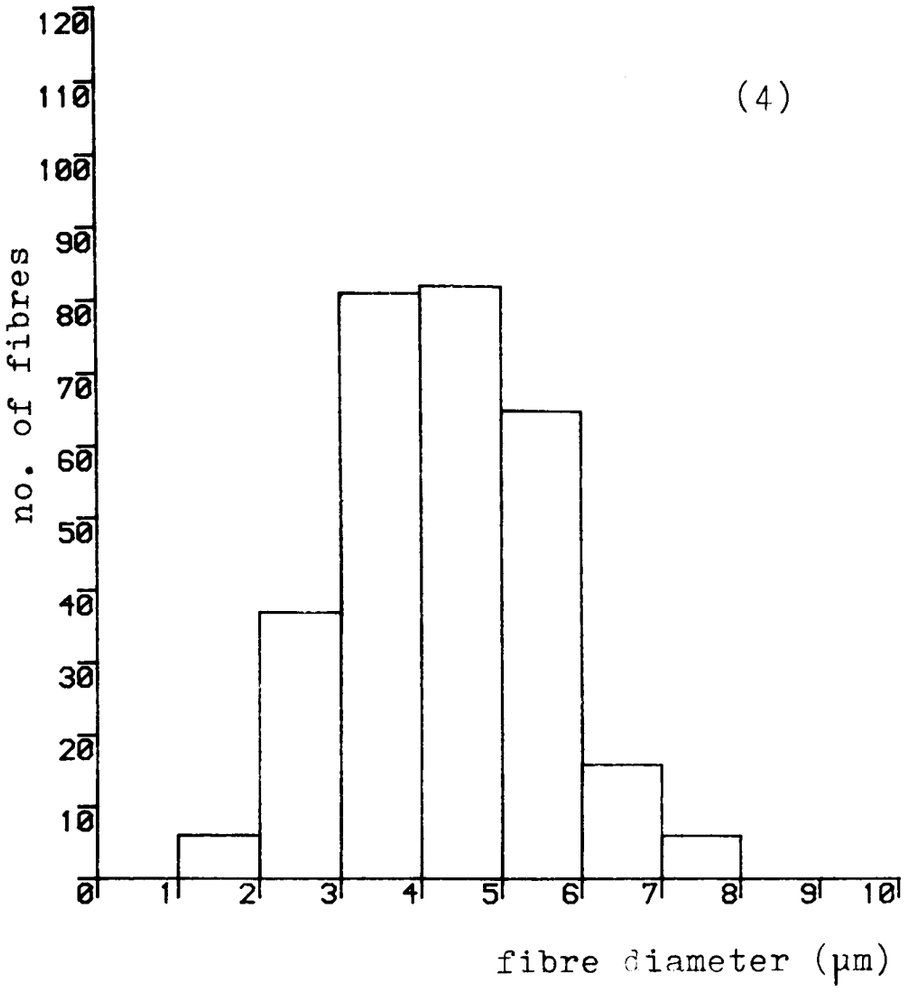
120
110
100
90
80
70
60
50
40
30
20
10
0
no. of fibres
1
2
3
4
5
6
7
8
9
10
fibre diameter (μm)

(5)

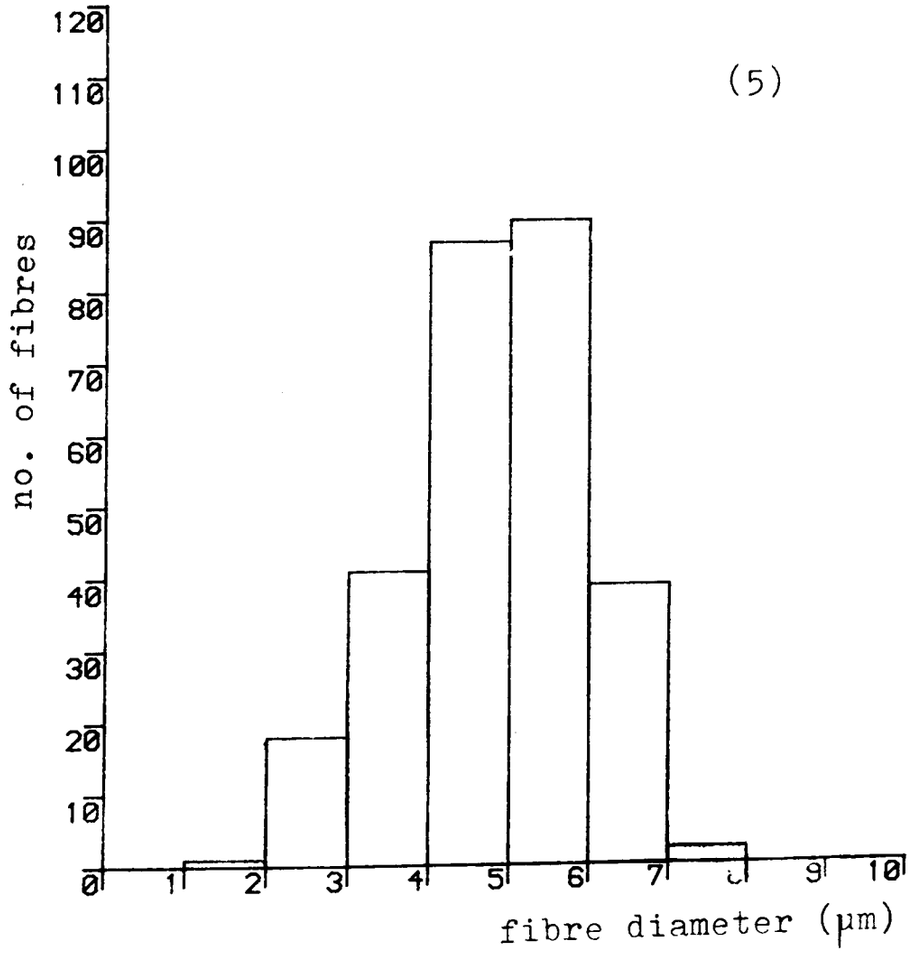
120
110
100
90
80
70
60
50
40
30
20
10
0
no. of fibres
1
2
3
4
5
6
7
9
10
fibre diameter (μm)

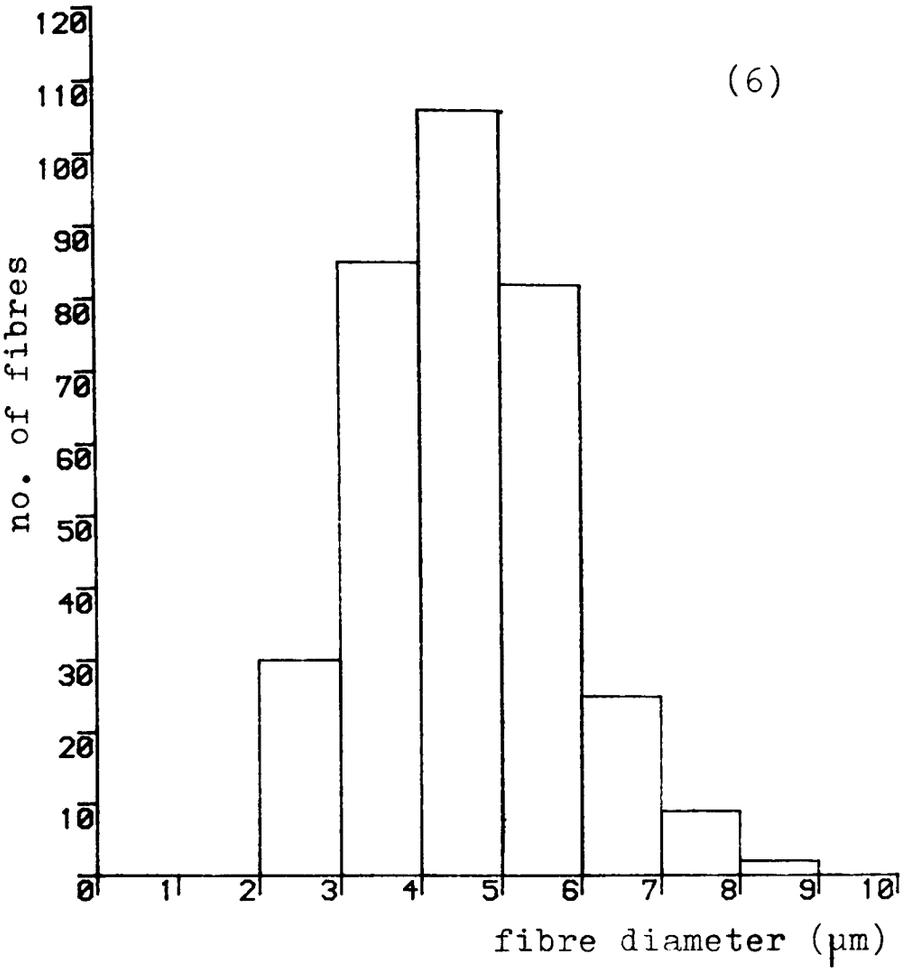
(6)
no. of fibres
0
10
20
30
40
50
60
70
80
90
100
110
120
1
2
3
4
5
6
7
8
9
10
fibre diameter (μm)

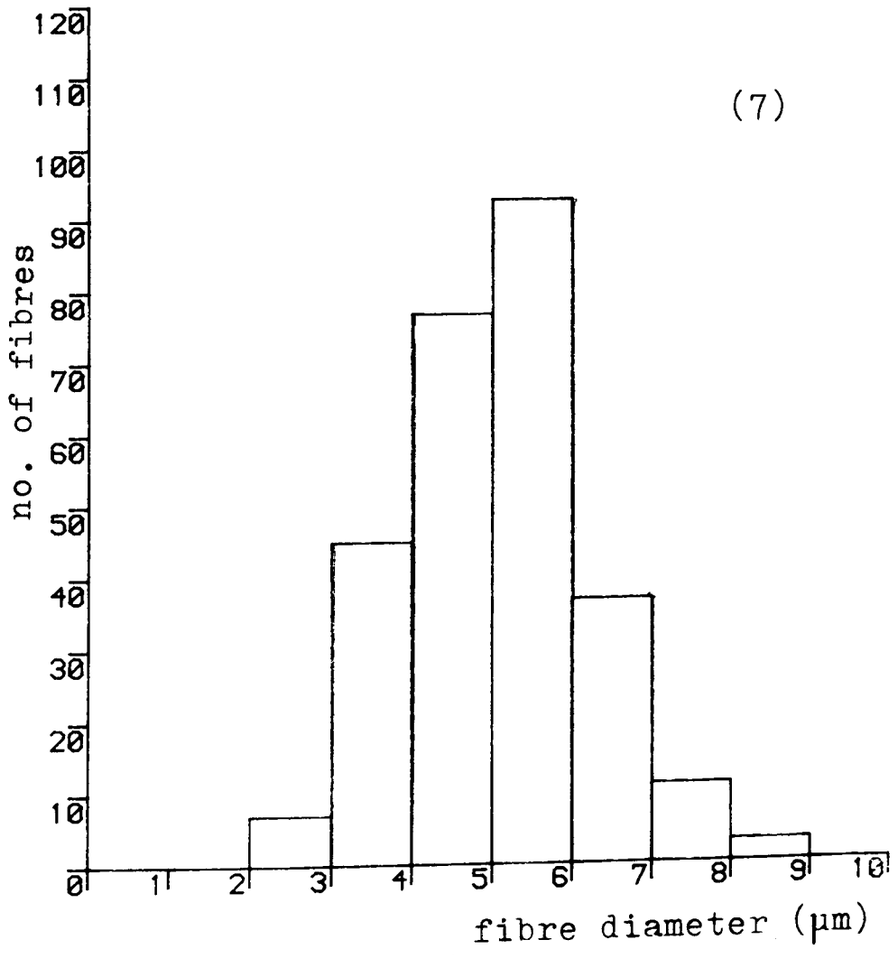
(7)
no. of fibres
0
10
20
30
40
50
60
70
80
90
100
110
120
1
2
3
4
5
6
7
8
9
10
fibre diameter (μm)

APPENDIX 7

PROGRAMMING ASPECTS OF DIGITAL SIMULATION PROGRAM FOR THRESHOLD CURRENT PREDICTION

A flowchart for the simulation program is shown in Figure A7.1. The explanation notes are :

(1) The inputs for the simulation program are

* fibre diameter (μm)
* pulse duration (ms)
* external field per mA of stimulus current (mV/mA)
* total simulation time (ms)
* estimated threshold current (mA)
* terminals of the fibre model
* nodal 'flag' for the type of analysis for each node

(2) In the first time, the applied current will be the estimated current from the input. Afterwards, the actual value of the current will vary depending on the iterative routine.

(3) Ionic current Ii for individual node is calculated either by linear or non-linear (F-H) equations. The latter set of equations are given in Appendix 13.

(4) In general, total simulation time is equal to pulse duration PLUS 0.6ms. This is necessary because, for the near threshold level, membrane depolarisation may drop after the switching off of the applied pulse, for, say 10μs, and it will then rise again to become active.

Figure A7.2 shows two examples output of threshold current prediction.

line (1) : 'IS' is applied current used for that particular testing routine.

line (2) : The integer '1' under 'THRESHOLD' means that the corresponding IS exceeds threshold level.

lines (13-23) : output information

line (20) '1' indicates which node is active under the applied current of -15.6mA. It can be seen that, for this particular field, 5 nodes are excited simultaneously.

lines (22)-(23) : the actual external potential corresponding to the nodes of Ranvier.

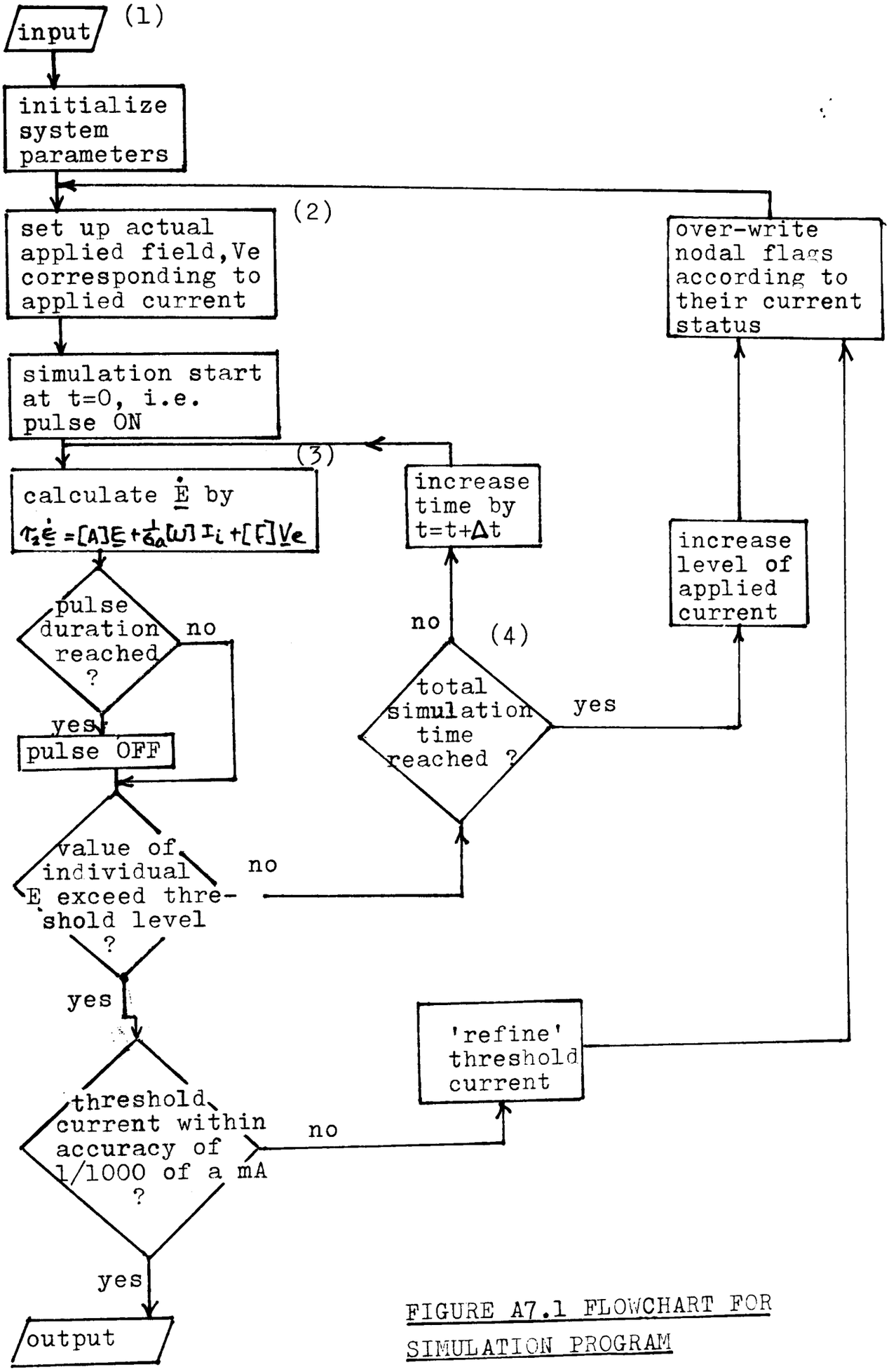

FIGURE A7.1 FLOWCHART FOR SIMULATION PROGRAM

```
1                PROGRAM SEVEN(INPUT,OUTPUT,TAPE5=INPUT,TAPE6=OUTPUT)
 *
```

```
                    IS    THRESHOLD  <-- line (1)
                -20.000       1
                -10.000       0      <-- line (2)
                -11.000       0
                -12.000       0
                -13.000       0
                -14.000       0
                -15.000       0
                -16.000       1
                -15.500       0
                -15.600       1
                -15.550       0

        FIBRE DIAMETER =      7.000 MICRONS   <-- line (13)
DISTANCE FROM ELECTRODE =      .500 MM

      THRESHOLD CURRENT =   -15.600 MA
          PULSE  WIDTH  =     .020 MS
  TOTAL SIMULATION TIME =     .620 MS

     LEFT  TERMINATION =  2
     RIGHT TERMINATION =  1

F-H FLAGS :    0  0  0  0  0  0  1  1  1  1  1  0  0  0  0  0  0  0  0   <-- line (20)

EXTERNAL FIELD (MV) AT EACH NODE
   -205.92      -225.42      -242.60      -280.80      -318.24      -374.40      -455.52      -533.52      -521.24      -533.52
   -452.40      -377.52      -312.00      -262.08      -230.88      -205.92      -187.20      -168.48      -152.10
-------------------------------------------------------------------------------------------------------------------------------
                                                                                                                   <-- line (23)
```

```
                    IS    THRESHOLD
                -20.000       1
                -12.000       0
                -11.000       0
                -12.000       1
                -11.500       1
                -11.400       1
                -11.300       1
                -11.200       1
                -11.100       1
                -11.000       0
                -11.050       1
                -11.040       0

        FIBRE DIAMETER =      7.000 MICRONS
DISTANCE FROM ELECTRODE =      .500 MM

      THRESHOLD CURRENT =   -11.050 MA
          PULSE  WIDTH  =     .030 MS
  TOTAL SIMULATION TIME =     .630 MS

     LEFT  TERMINATION =  2
     RIGHT TERMINATION =  1

F-H FLAGS :    0  0  0  0  0  0  0  1  1  1  0  0  0  0  0  0  0  0  0

EXTERNAL FIELD (MV) AT EACH NODE
   -145.86      -159.67      -176.80      -198.90      -225.42      -265.20      -322.66      -377.91      -418.80      -377.91
   -320.45      -267.41      -221.00      -185.64      -163.54      -145.86      -132.60      -119.34      -107.74
-------------------------------------------------------------------------------------------------------------------------------
```

APPENDIX 8

FIELD DISTORTION ANALYSIS - DESCRIPTION OF FINITE ELEMENT MODEL

8.1 Description of finite element model

A finite element model was designed to investigate the effect of tendon wall on the stimulus field within the nerve bundle.

Figure A8.1 is the schematic diagram of the model. Essentially, it can be divided into five regions.

region 1 : nerve bundles, resistivity values are 138 ohm-cm longitudinal, and 1211 ohm-cm transverse.

region 2 : tendon wall, resistivity values varies between 70-10000 ohm-cm. A range of values is chosen as there is no published data concerning the electrical properties of this tissue.

regions 3-5 : saline bath with resistivity value 70ohm-cm.

The corresponding regions are shown in Figures A8.2-A8.6. The dimensions of the nerve bundle and tendon wall were obtained from histological analysis.

There are, nevertheless, two differences between the finite element model and experimental scheme. The first one was the use of point source in the model. The second was the position of the stimulating indifferent.

Mirror-image modelling technique as described in Figure 2.1(b) also applied.

The model consists of about 2000 nodes and 450 elements.

A8.2 Testing scheme

By varying the position of the electrode and the resistivity of tendon wall, the effects of tendon wall were investigated by plotting the potential profile along the centre line of the bundle (line MN in region 1).

The results can be found in Figure 8.11 of the main text.

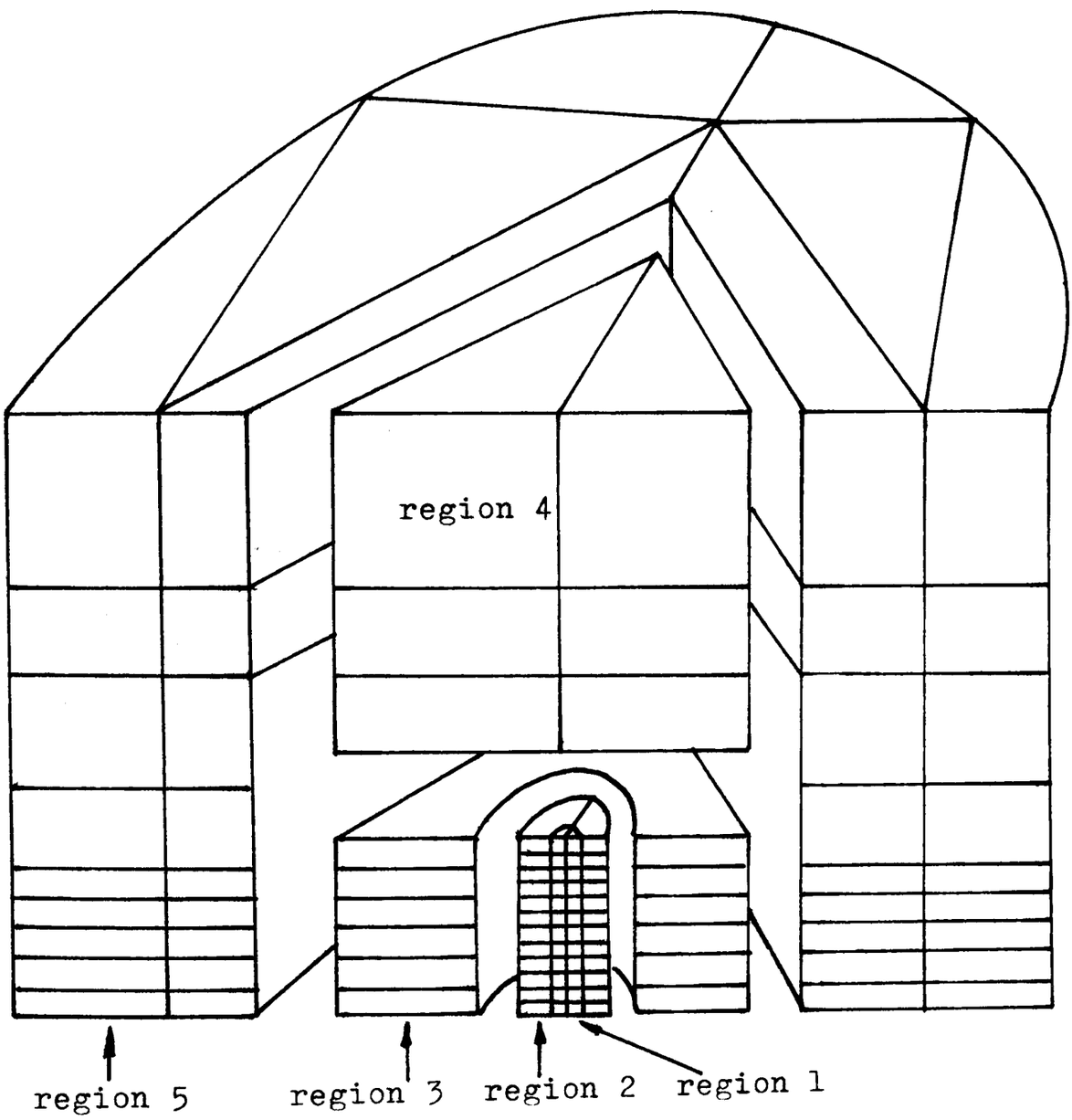

FIGURE A8.1 SCHEMATIC DIAGRAM OF FINITE ELEMENT MODEL FOR FIELD DISTORTION ANALYSIS

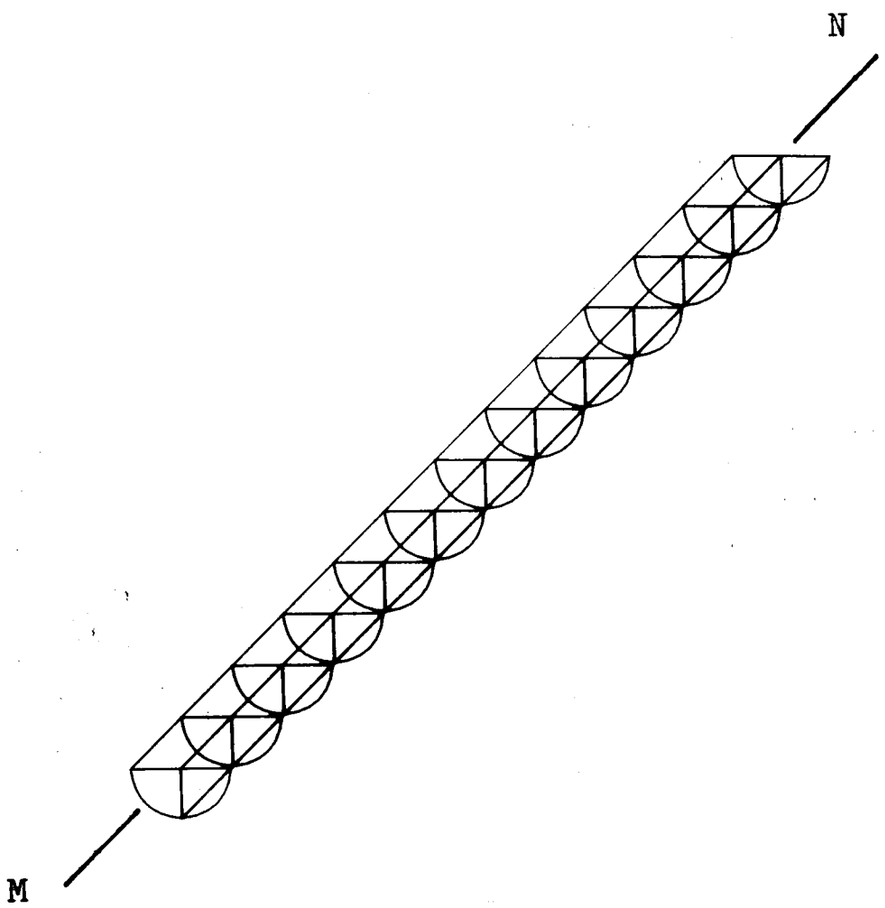

PAFEC 75

VIEW FROM X = .1247
Y = .1247
Z = 1.0000

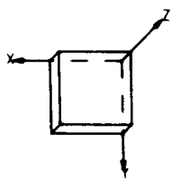

FIGURE A8.2
region 1
nerve bundle

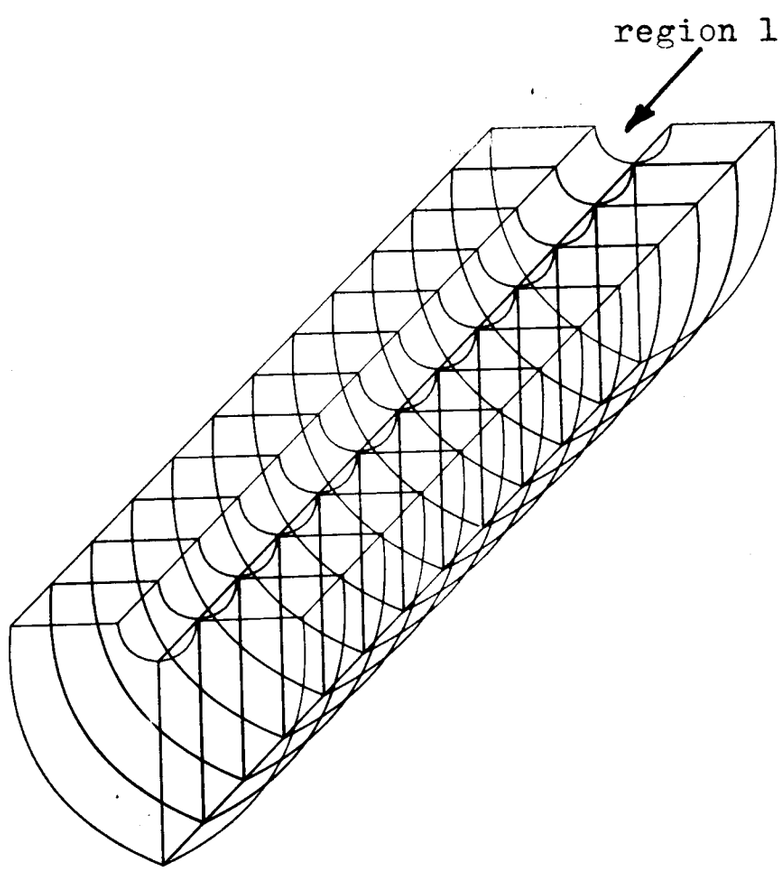

PAFEC 75

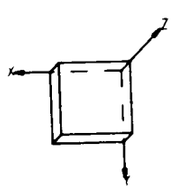

FIGURE A8.3
region 2
tendon wall

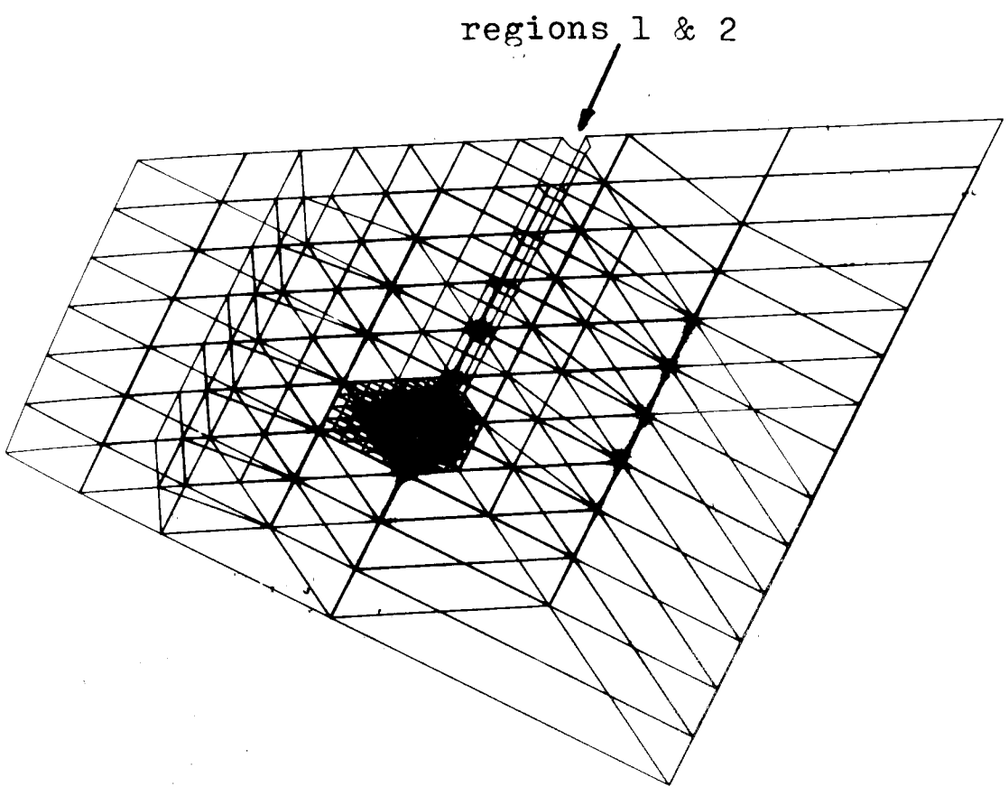

FIGURE A8.4
region 3

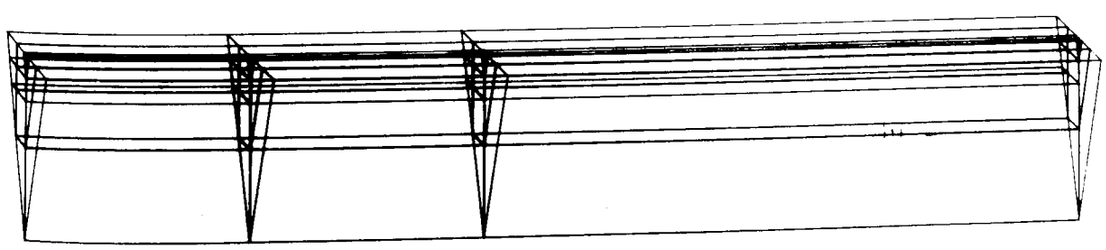

FIGURE A8.5
region 4

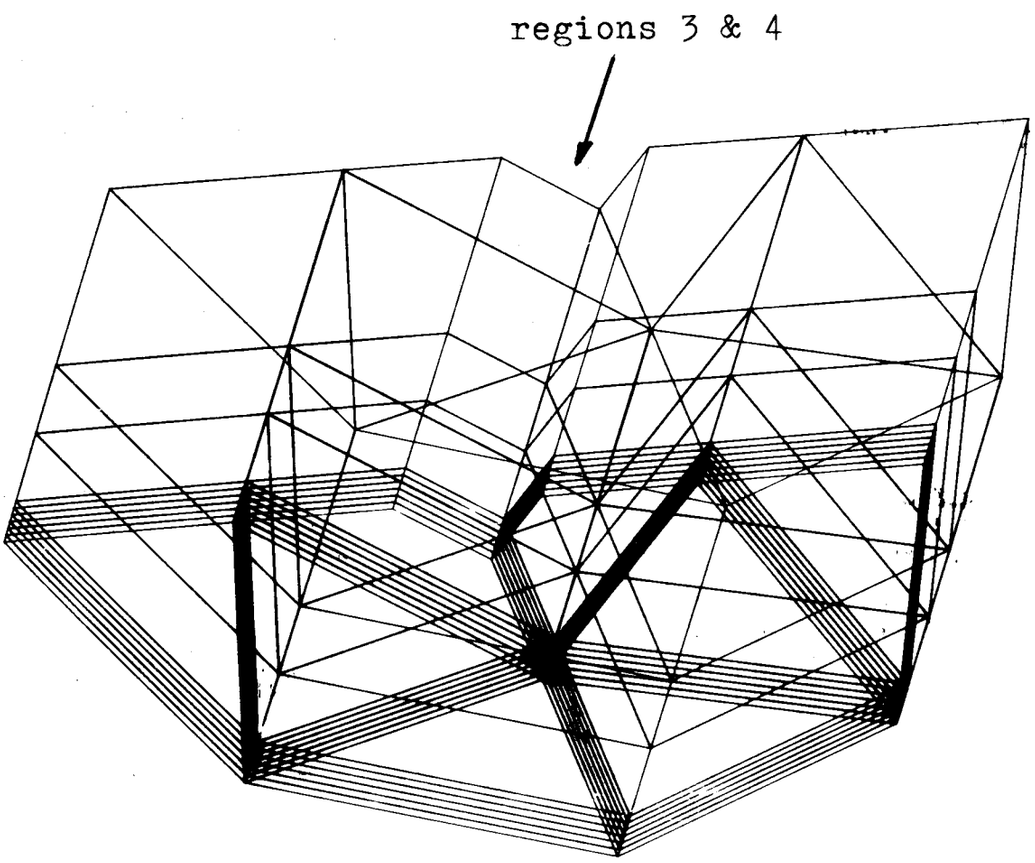

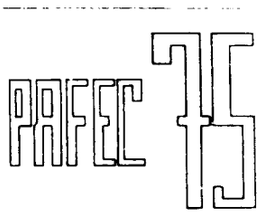

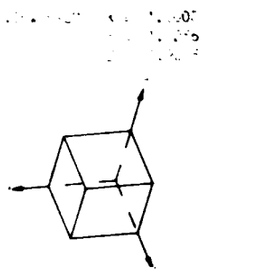

FIGURE A8.6
region 5

APPENDIX 9

DERIVATIONS OF SYSTEM EQUATIONS FOR FIBRE MODEL A

Consider currents at point j with potential Vi,j,

$$I_j = G_a (V_{i,j-1} - 2V_{i,j} + V_{i,j+1})$$

i.e. $$C_m \dot{E}_j + I_{i,j} = G_a (V_{i,j-1} - 2V_{i,j} + V_{i,j+1}) \qquad (A9.1)$$

Similarly, consideration of current at the external pcint with potential Ve,j give

$$C_m \dot{E}_j + I_{i,j} = G_e (-V_{e,j} + 2V_{e,j} - V_{e,j+1}) \qquad (A9.2)$$

Add (A9.1) and (A9.2), and use Vi,j - Ve,j = Ej + Vr.

we have $$\left(\frac{1}{G_a} + \frac{1}{G_e} \right)(C_m \dot{E}_j + I_{i,j}) = E_{j-1} - 2E_j + E_{j+1}$$

i.e. $$C_m \dot{E}_j = \frac{G_a G_e}{G_a + G_e} (E_{j-1} - 2E_j + E_{j+1}) - I_{i,j} \qquad (A9.3)$$

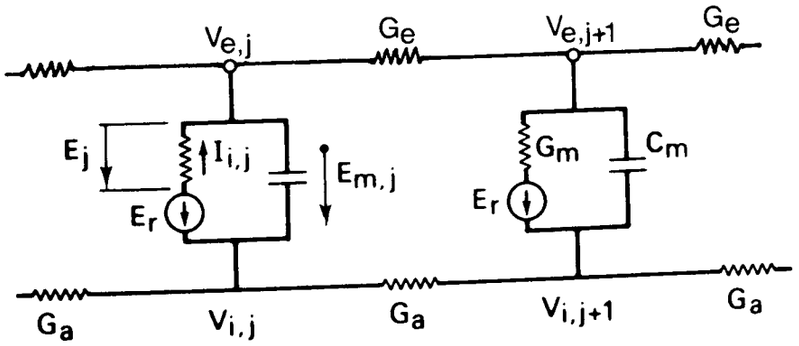

APPENDIX 10 DERIVATION OF SYSTEM EQUATIONS FOR FIBRE MODEL B

10.1 Definition of symbols

$$\tau_2 = \frac{C_m}{G_a}$$

$$\tau_3 = C_m \left\{ \frac{1}{G_a} + \frac{1}{G_e} \right\}$$

$$\tau_4 = 2\tau_3 + K_2 \tau_2$$

$$K_1 = \frac{1}{G_a} + \frac{1}{G_e}$$

$$K_2 = G_s / G_e$$

$$K_3 = 4 + K_2$$

$$K_4 = 6 + 2K_2$$

$$K_5 = 2K_1 + K_2 \frac{1}{G_a}$$

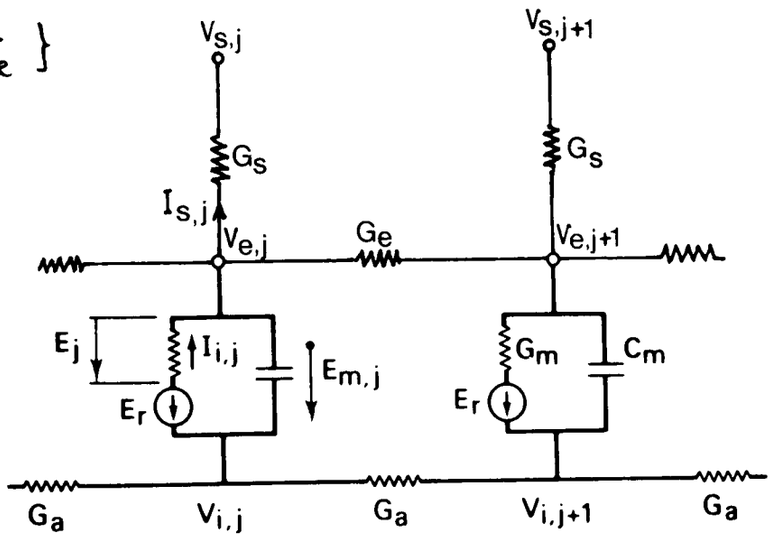

FIGURE A10.1

10.2 Mathematical description of Ve

Consider currents at the external point of node j, where the potential is Ve,j, in Figure A10.1 .

$$C_m \dot{E}_j + I_{i,j} = I_{s,j} - G_e (Ve_{,j-1} - 2Ve_{,j} + Ve_{,j+1})$$

rearrange,

$$\frac{C_m}{G_e} \dot{E}_j + \frac{1}{G_e} I_{i,j} = -(Ve_{,j-1} - 2Ve_{,j} + Ve_{,j+1}) + \frac{I_{s,j}}{G_e} \qquad (A10.1)$$

Similarly, at the internal point where the potential is Vi,j.

$$C_m \dot{E}_j + I_{i,j} = G_a (Vi_{,j-1} - 2Vi_{,j} + Vi_{,j+1})$$

rearrange,

$$\frac{C_m}{G_a}\dot{E}_j + \frac{1}{G_a} I_{i,j} = V_{i,j-1} - 2V_{i,j} + V_{i,j+1} \qquad (A10.2)$$

Adding (A10.1) and (A10.2), and using Vi,j-Ve,j=Ej+Vr, we have

$$\left\{\frac{1}{G_a}+\frac{1}{G_e}\right\}(C_m\dot{E}_j + I_{i,j}) = (E_{j-1} - 2E_j + E_{j+1}) + \frac{I_{s,j}}{G_e}$$

Use Is,j = Gs(Ve,j-Vs,j), where Vs,j is the stimulus field input and the symbols τ_3, K_1 and K_2 defined in 10.1, the above equation becomes

$$\tau_3\dot{E}_j + K_1 I_{i,j} = (E_{j-1} - 2E_j + E_{j+1}) + K_2(V_{e,j} - V_{s,j})$$

Rearrange to give a solution for Ve,j

$$V_{e,j} = \frac{1}{K_2}\left\{\tau_3\dot{E}_j + K_1 I_{i,j} - (E_{j-1} - 2E_j + E_{j+1})\right\} + V_{s,j}$$

(A10.3)

10.3 Formulation of system equations

Substitute Vi,j=Ve,j+Ej+Vr into equation A10.2, get

$$\frac{C_m}{G_a}\dot{E}_j + \frac{1}{G_a} I_{i,j} = (E_{j-1} - 2E_j + E_{j+1}) + (V_{e,j-1} - 2V_{e,j} + V_{e,j+1})$$

(A10.4)

The term $(V_{e,j-1} - 2V_{e,j} + V_{e,j+1})$ can then be substituted by

equation (A10.3). Rearrange equation (A10 4) and use the symbols τ_4, K_3, K_4 and K_5 defined in 10.1, the following equation is obtained :

$$\tau_3 \dot{E}_{j-1} - \tau_4 \dot{E}_j + \tau_3 \dot{E}_{j+1} = (E_{j-2} - K_3 E_{j-1} + K_4 E_j - K_3 E_{j+1} + E_{j+2}) + (-K_1 I_{i,j-1} + K_5 I_{i,j} - K_1 I_{i,j+1}) + (-K_2 V_{s,j-1} + 2K_2 V_{s,j} - K_2 V_{s,j+1}) \quad (A10.5)$$

For a fibre of n nodes, the system equation may be arranged as

$$[M]\underline{\dot{E}} = [N]\underline{E} + [P]\underline{I}i + [L]\underline{V}s \quad (A10.6)$$

where [M], [N], [P] and [L] are nxn matrices and $\underline{\dot{E}}$, $\underline{E}$, $\underline{I}i$ and $\underline{V}s$ are column vectors of dimension n

Neglect the end conditions, the element in the matrices are

$$[M] = \begin{bmatrix} m_{11} & m_{12} & 0 & 0 & 0 & 0 & \cdot \\ \tau_3 & -\tau_4 & \tau_3 & 0 & 0 & \cdot & \cdot \\ \cdot & \tau_3 & -\tau_4 & \tau_3 & 0 & \cdot & \cdot \\ \cdot & \cdot & \cdot & \cdot & \cdot & \cdot & \cdot \\ \cdot & \cdot & 0 & \tau_3 & -\tau_4 & \tau_3 & 0 \\ 0 & \cdot & 0 & 0 & \tau_3 & -\tau_4 & \tau_3 \\ 0 & \cdot & 0 & 0 & 0 & m_{n,n-1} & m_{n,n} \end{bmatrix}$$

$$[N] = \begin{bmatrix} n_{11} & n_{12} & n_{13} & 0 & 0 & \cdots & 0 \\ n_{21} & n_{22} & n_{23} & n_{24} & 0 & \cdots & 0 \\ 1 & -K3 & K_4 & -K_3 & 1 & 0 \cdots & 0 \\ 0 & \cdot & \cdot & \cdot & \cdot & \cdot & \cdot \\ & \cdot & 1 & -K_3 & K_4 & -K_3 & 1 \\ & \cdot & 0 & n_{n-1,n-3} & n_{n-1,n-2} & n_{n-1,n-1} & n_{n-1,n} \\ 0 & 0 & \cdot 0 & 0 & n_{n,n-2} & n_{n,n-1} & n_{n,n} \end{bmatrix}$$

$$[P] = \begin{bmatrix} P_{11} & P_{12} & 0 & & & & \\ -K_1 & K_5 & -K_1 & & & & \\ 0 & -K_1 & K_5 & -K_1 & & & \\ & \cdot & \cdot & \cdot & & & \\ & & & & -K_1 & K_5 & -K_1 \\ & & & & 0 & P_{n,n-1} & P_{n,n} \end{bmatrix}$$

$$[L] = \begin{bmatrix} l_{1,1} & l_{1,2} & 0 & \cdot & & & \\ -K_2 & 2K_2 & -K_2 & 0 & & & \\ & -K_2 & 2K_2 & -K_2 & 0 & & \\ & & \cdot & \cdot & \cdot & & \\ & & & -K_2 & 2K_2 & -K_2 & 0 \\ & & & 0 & -K_2 & 2K_2 & -K_2 \\ & & & & & l_{n,n-1} & l_{n,n} \end{bmatrix}$$

$$\underline{E} = \begin{bmatrix} E_1 \\ E_2 \\ \cdot \\ \cdot \\ \cdot \\ \\ \\ E_n \end{bmatrix} \qquad \underline{V_s} = \begin{bmatrix} V_{s,1} \\ V_{s,2} \\ \cdot \\ \cdot \\ \cdot \\ \\ \\ V_{s,n} \end{bmatrix}$$

APPENDIX 11 TYPES OF TERMINALS FOR FIBRE MODEL B

The following analyses are the end conditions used for the fibre models described in Chapter 9. In general, any of the three end conditions in Appendix 4 can be used.

11.1 Left hand end - symmetry about node 1

Consider the following fibre, where it is symmetrical about node 1. Thus

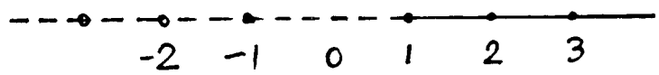

$$\dot{E}_0 = \dot{E}_2 \,, \quad E_0 = E_2$$

$$\dot{E}_{-1} = \dot{E}_3 \,, \quad E_{-1} = E_3$$

etc. etc.

Put j=1 into equation (A10.5).

$$\tau_3\dot{E}_0 - \tau_4\dot{E}_1 + \tau_3\dot{E}_2 = (E_{-1} - K_3E_0 + K_4E_1 - K_3E_2 + E_3) + (-K_1I_{c,0} + K_5I_{c,1} - K_1I_{c,2}) + (-K_2V_{s,0} + 2K_2V_{s,1} - K_2V_{s,2})$$

Use the symmetrical conditions, and collect terms,

$$-\tau_4\dot{E}_1 + 2\tau_3\dot{E}_2 = (K_4E_1 - 2K_3E_2 + 2E_3) + (K_5I_{c,1} - 2K_1I_{c,2}) + (2K_2V_{s,1} - 2K_2V_{s,2}) \qquad (A11.1)$$

Similarly, when j=2,

$$\uparrow_3 \dot{\epsilon}_1 - \uparrow_4 \dot{\epsilon}_2 + \uparrow_3 \dot{\epsilon}_3 = (-K_3\epsilon_1 + (1+K_4)\epsilon_2 - K_3\epsilon_3 + \epsilon_4)$$
$$+(-K_1 I_{i,1} + K_5 I_{i,2} - K_1 I_{i,3})$$
$$+(-K_2 V_{s,1} + 2K_2 V_{s,2} - K_2 V_{s,3})$$

(A11.2)

Thus the first two rows of the matirces are

$$[M] = \begin{bmatrix} -\uparrow_4 & 2\uparrow_3 & 0 & 0 & \cdots \\ \uparrow_3 & -\uparrow_4 & \uparrow_3 & 0 & \cdots \\ \vdots & \vdots & & & \end{bmatrix}$$

$$[N] = \begin{bmatrix} K_4 & -2K_3 & 2 & 0 & \cdots \\ -K_3 & 1+K_4 & -K_3 & 1 & \cdots \\ \vdots & \vdots & \vdots & \vdots & \end{bmatrix}$$

$$[P] = \begin{bmatrix} K_5 & -2K_1 & 0 & 0 & \cdots \\ -K_1 & K_5 & -K_1 & 0 & \cdots \\ \vdots & \vdots & \vdots & \vdots & \end{bmatrix} \quad \text{and}$$

$$[L] = \begin{bmatrix} 2K_2 & -2K_2 & 0 & 0 & \\ -K_2 & 2K_2 & -K_2 & 0 & \\ \vdots & \vdots & \vdots & \vdots & \end{bmatrix}$$

11.2 Right hand end - zero depolarisation

For a fibre of 99 nodes, the 'zero depolarisation' ending and 'zero internal axial current' ending should not make any difference to the general behaviour of other nodes.

The present zero depolarisation condition assumes that any node beyond node 99 has zero depolarisation. Thus $E_{100} = E_{101} = 0 = \dot{E}_{100}$ and $I_{i,100} = 0$.

For simplicity, it is assumed that the external applied field beyond node 99 are constant, i.e. $Vs,_{99} = Vs,_{100}$.

For j=98, equation (A10.5) in Appendix 10 reduces to

$$\tau_3 \dot{E}_{97} - \tau_4 \dot{E}_{98} + \tau_3 \dot{E}_{99} = (E_{96} - K_3 E_{97} + K_4 E_{98} - K_3 E_{99}) + (-K_1 I_{i,97} + K_5 I_{i,98} - K_1 I_{i,99}) + (-K_2 V_{s,97} + 2K_2 V_{s,98} - K_2 V_{s,99})$$

For the end node j=99

$$\tau_3 \dot{E}_{98} - \tau_4 \dot{E}_{99} = (E_{97} - K_3 E_{98} + K_4 E_{99}) + (-K_1 I_{i,98} + K_5 I_{i,99}) + (-K_2 V_{s,98} + K_2 V_{s,99})$$

The last two rows of the matrices are therefore

$$[M] = \begin{bmatrix} \cdots & \cdots & \cdots \\ \cdots & \tau_3 & -\tau_4 & \tau_3 \\ \cdots & 0 & \tau_3 & -\tau_4 \end{bmatrix}$$

$$[N] = \begin{bmatrix} \cdots & \cdots & \cdots \\ \cdots & 1 & -K_3 & K_4 - K_3 \\ \cdots & 1 & -K_3 & K_4 \end{bmatrix}$$

$$[P] = \begin{bmatrix} \cdots & \cdots & \cdots \\ \cdots & 0 & -K_1 & K_5 & -K_1 \\ \cdots & 0 & -K_1 & K_5 \end{bmatrix}$$

$$[L] = \begin{bmatrix} \cdots & \cdots \\ \cdots & 0 & -K_2 & 2K_2 - K_2 \\ & 0 & -K_2 & K_2 \end{bmatrix}$$

APPENDIX 12

EXAMPLES OF EFFECTS OF DIFFERENT APPLIED FIELDS ON PROPAGATING ACTION POTENTIALS

The following 12 cases illustrate the effects of different applied fields on an ongoing action potential with a digital simulation on the nerve fibre Model B. Table A12 summarises all the testing schemes. The effects on action potentials are also shown in Figure A12.

Table A12

case	electrode position	nature of poles(mA)
1	65	+3.5
2	60	+2.0
	65	+2.0
3	60	+2.5
	65	+2.5
4	60	+2.0
	65	+2.0
	70	+2.0
5	60	+2.5
	65	+2.5
	70	+2.5
6	60	+2.0
	65	+2.0
	70	+2.0
	75	+2.0
7	60	+2.5
	65	+2.5
	70	+2.5
	75	+2.5
8	62	+2.0
	65	+2.0
	68	+2.0
	71	+2.0
9	60	-0.5
	65	+1.0
	70	-0.5
10	60	-1.0
	65	+2.0
	70	-1.0
11	65	-0.5
12	65	-1.0

Note that 'electrode position' in the table implies the position of a point source 2mm above the node number

j. The corresponding current is shown in magnitude in the third column. (+) means anode. Note also that the duration of the pulse is infinite long.

Cases (1)-(8) attempted to block the impulse with different anodic configurations and pulse amplitudes.

Cases (9) and (10) were double cathodes-double anodes configurations.

Cases (11) and (12) were cathodic stimulation, purely for illustrative purposes.

Time interval between successive plots with the exception of case 1, is 0.4ms. Case 1 is 0.3ms.

Moreover, assume the 'blocking' pulse is applied at t=0ms, then the time at picture (a), with the exception of case 1, is t=0.4ms. For case 1, t=0.3ms.

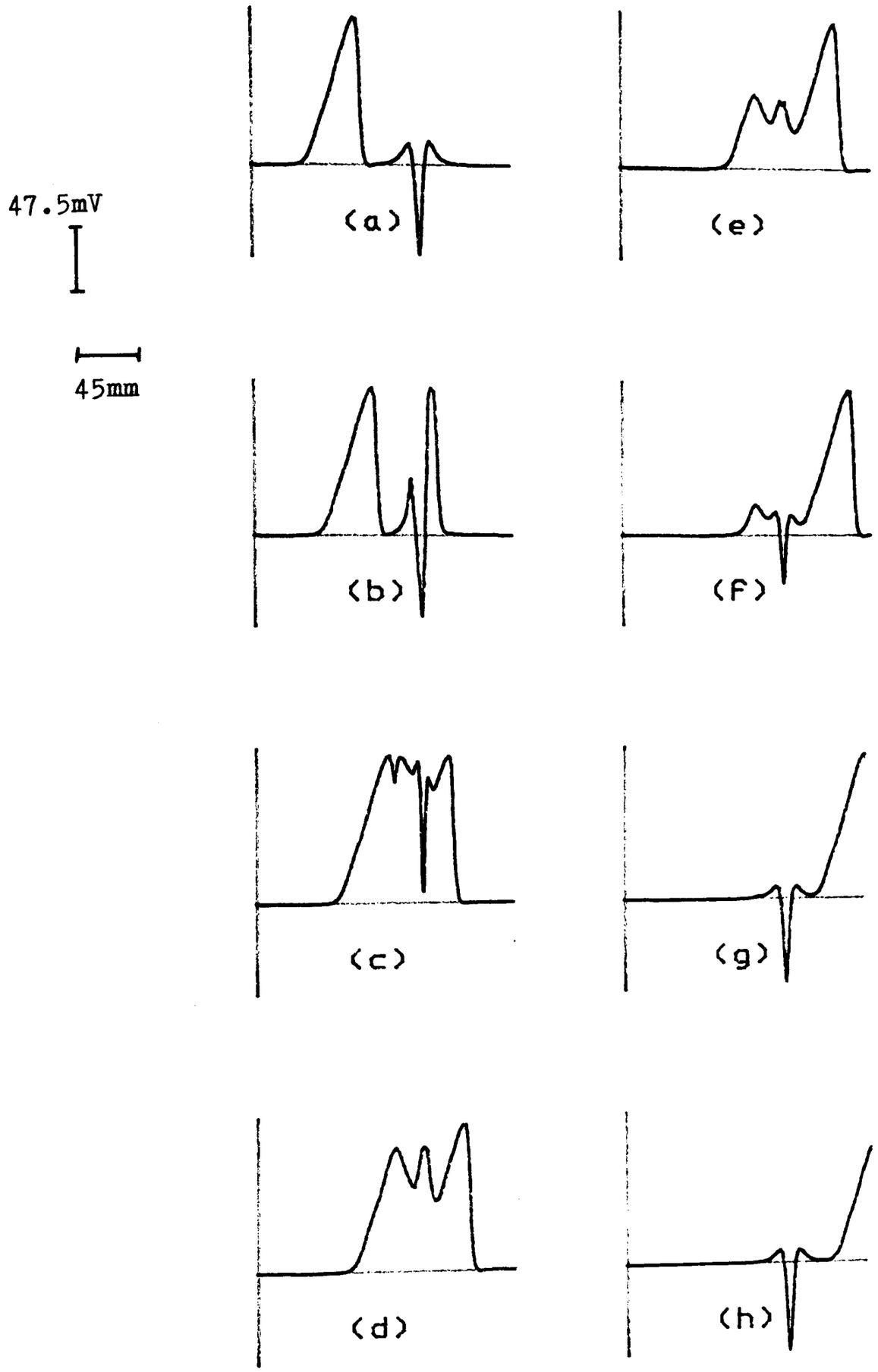

FIGURE A12 : case 1

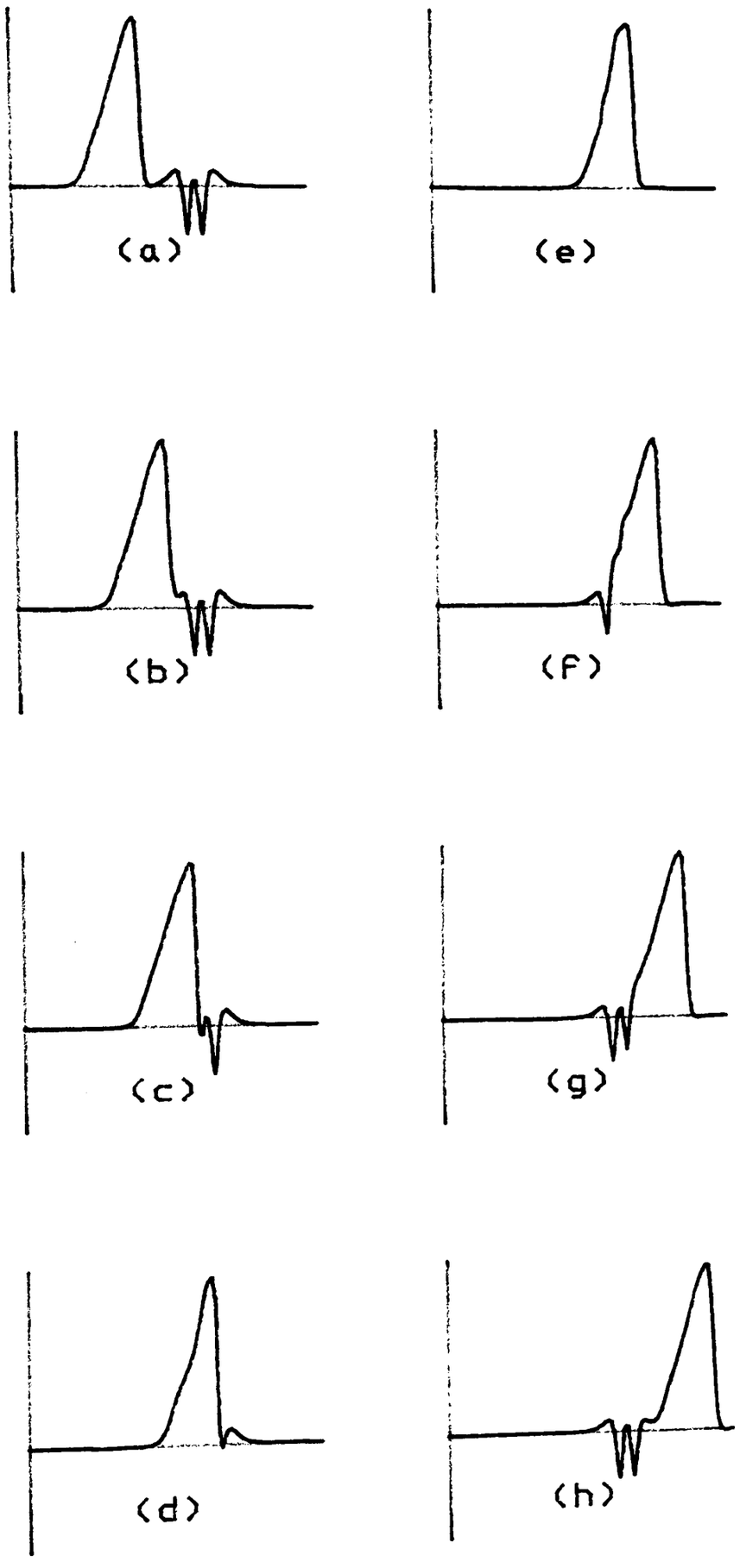

FIGURE A12 : case 2

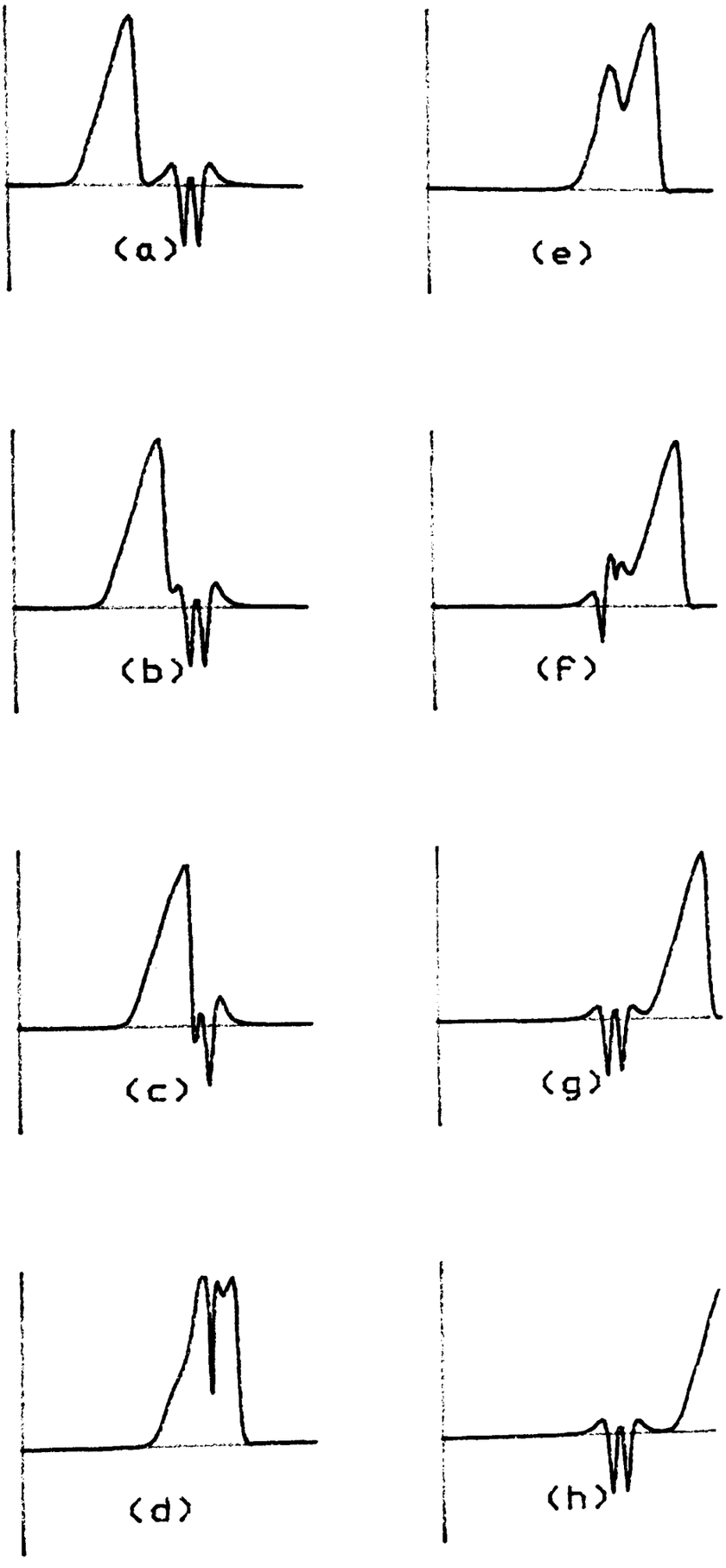

FIGURE A12 : case 3

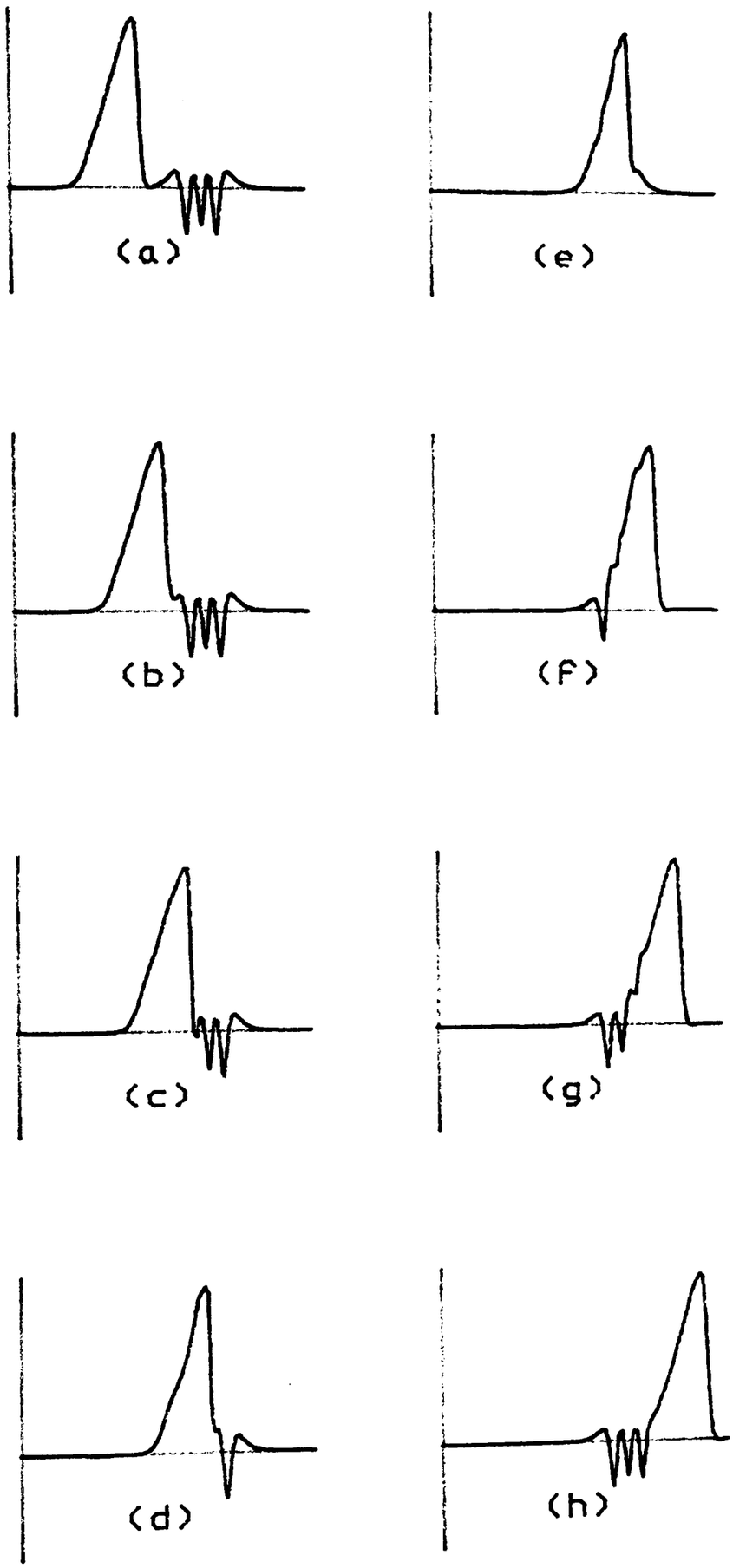

FIGURE A12 : case 4

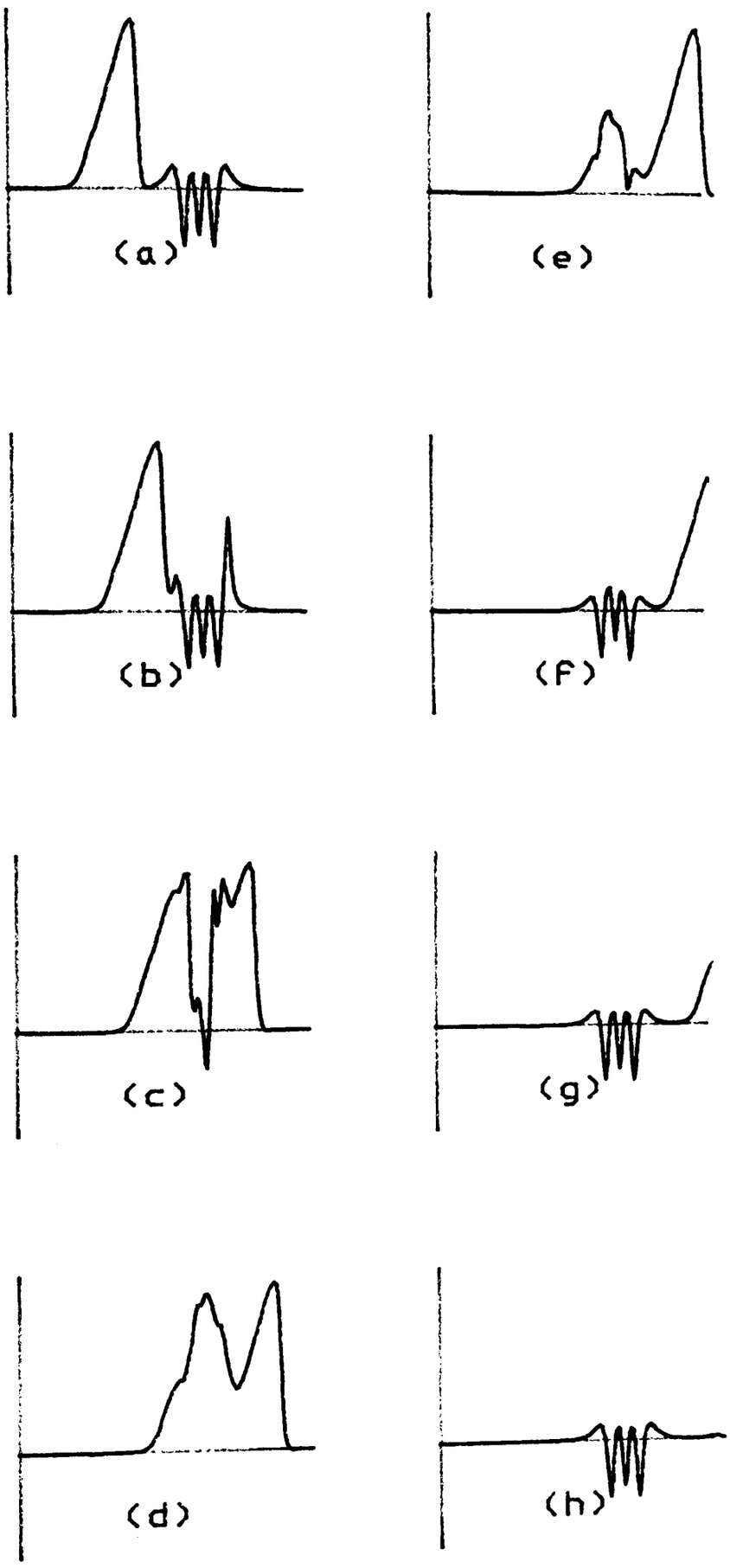

FIGURE A12 : case 5

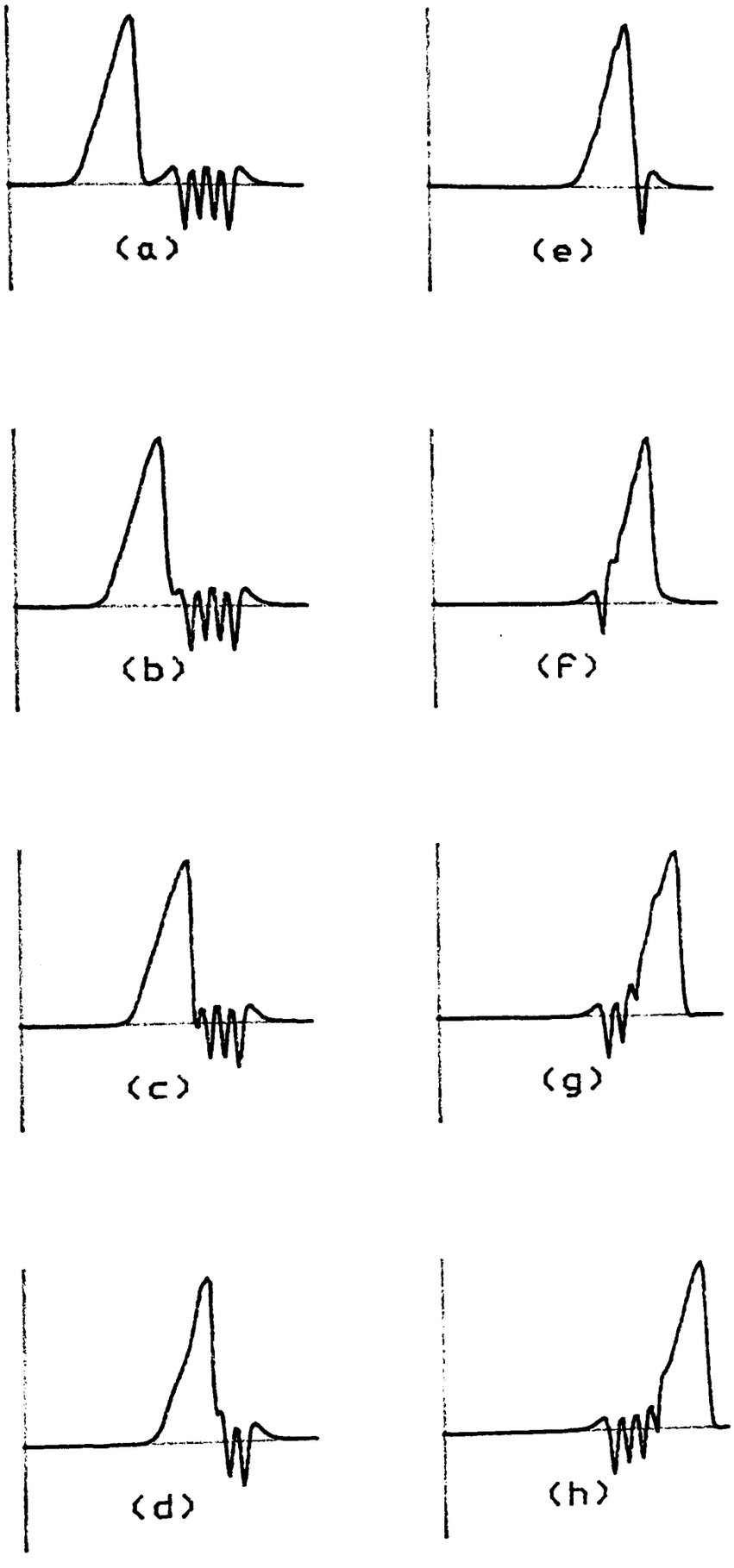

FIGURE A12 : case 6

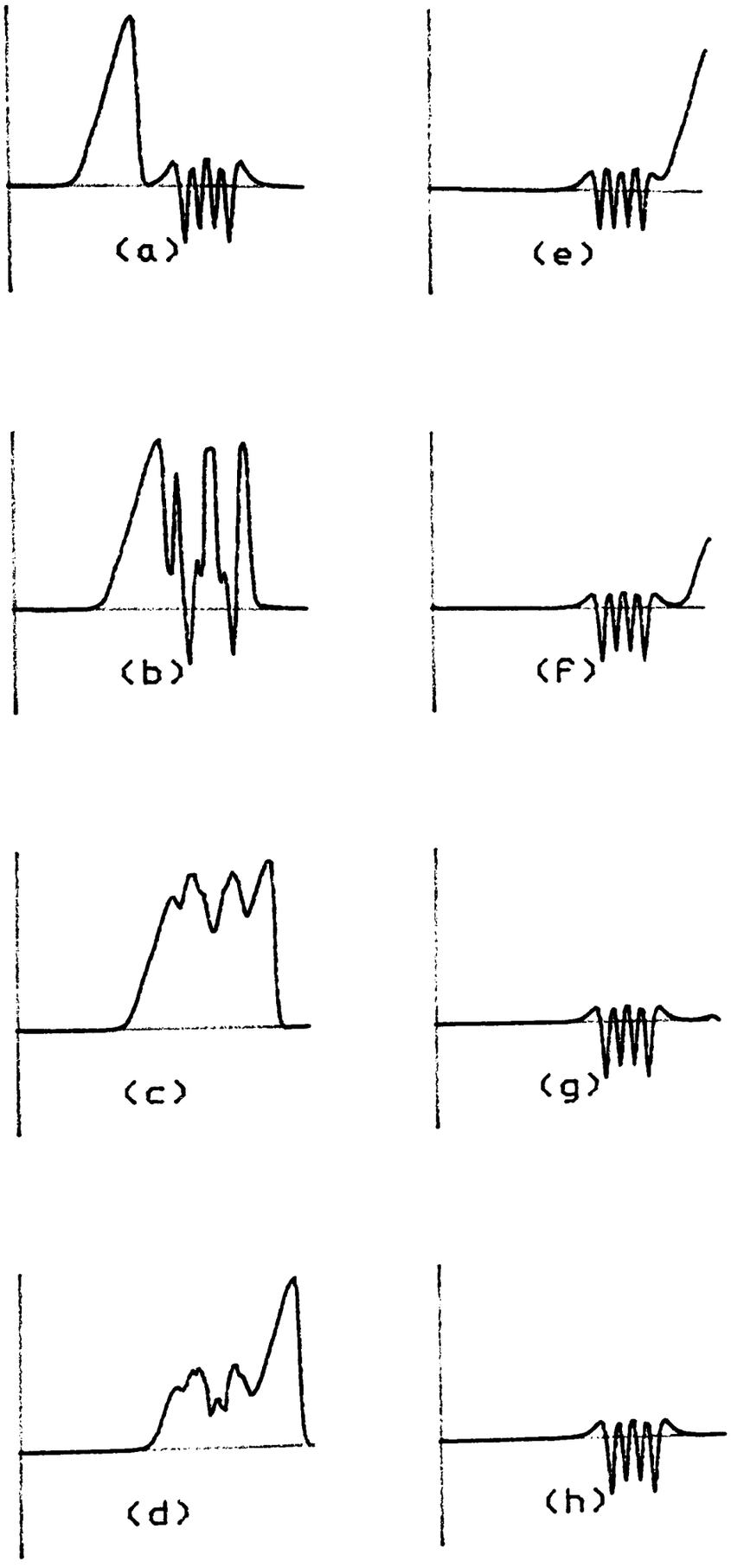

FIGURE A12 : case 7

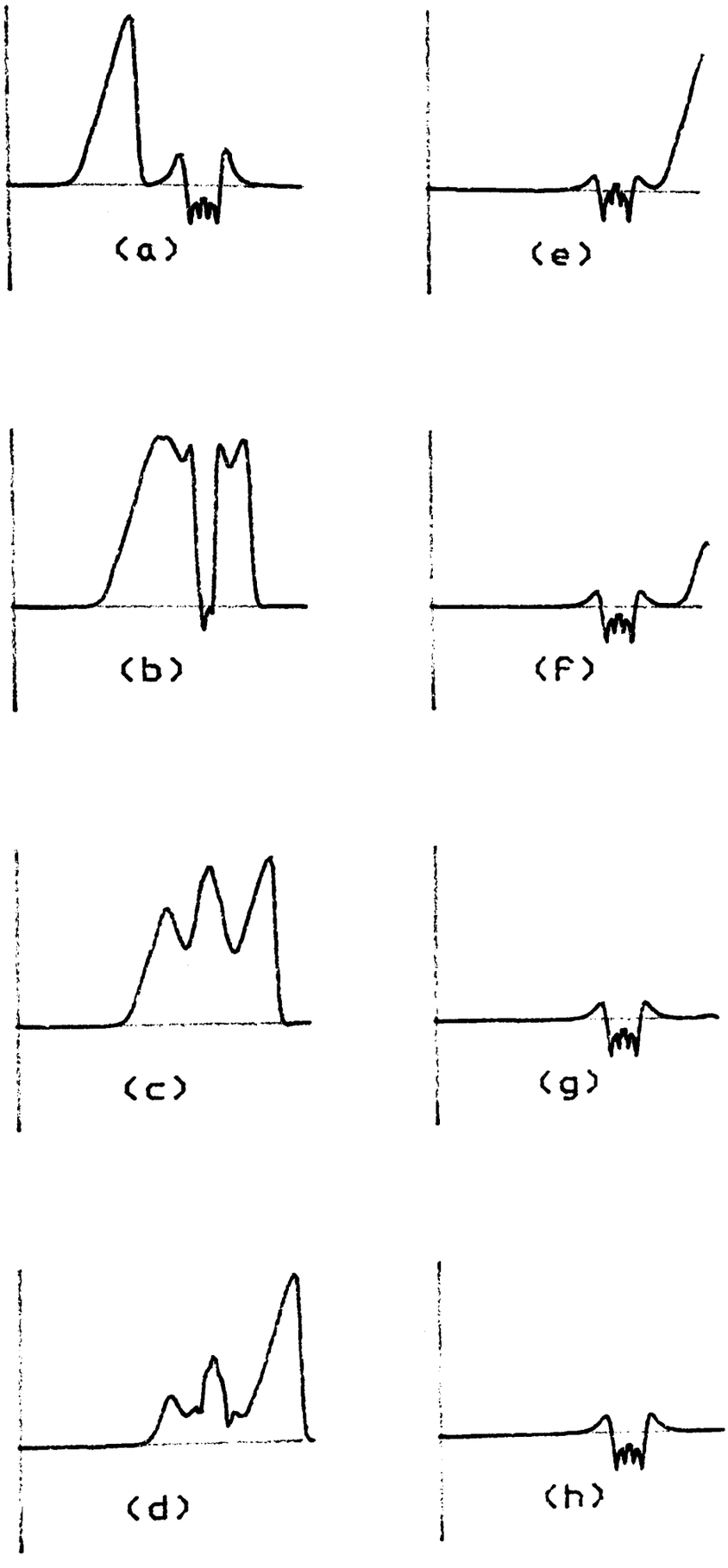

FIGURE A12 : case 8

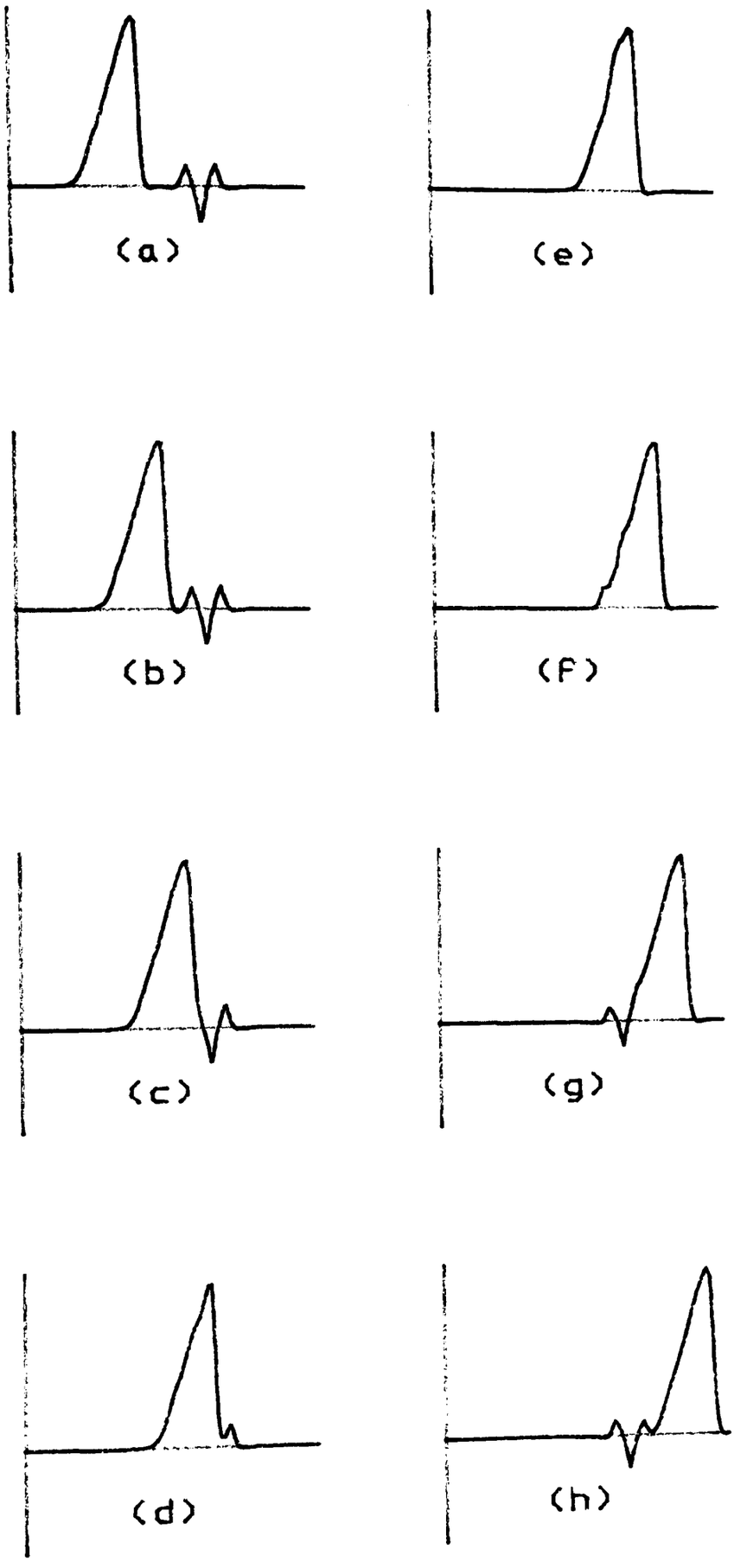

FIGURE A12 : case 9

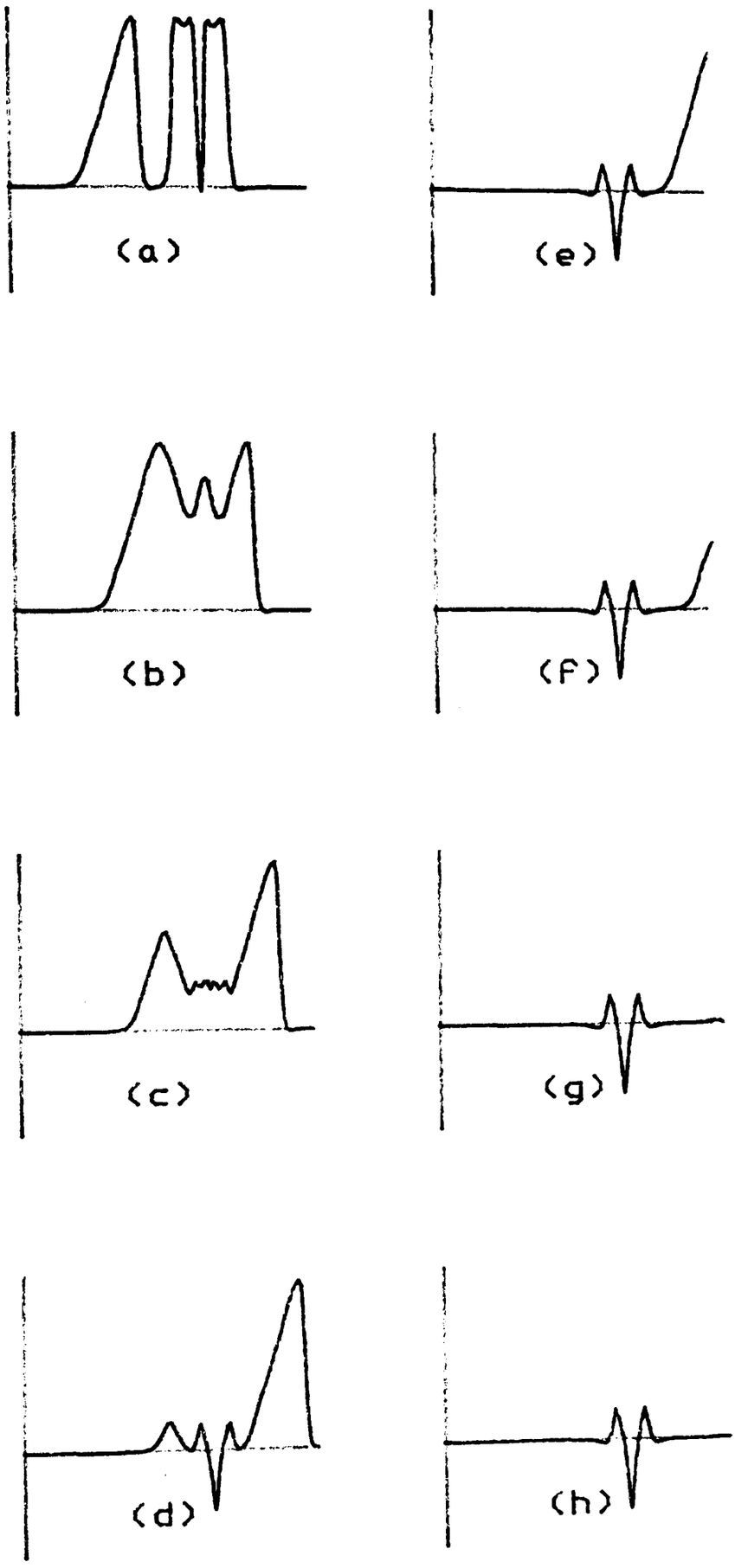

FIGURE A12 : case 10

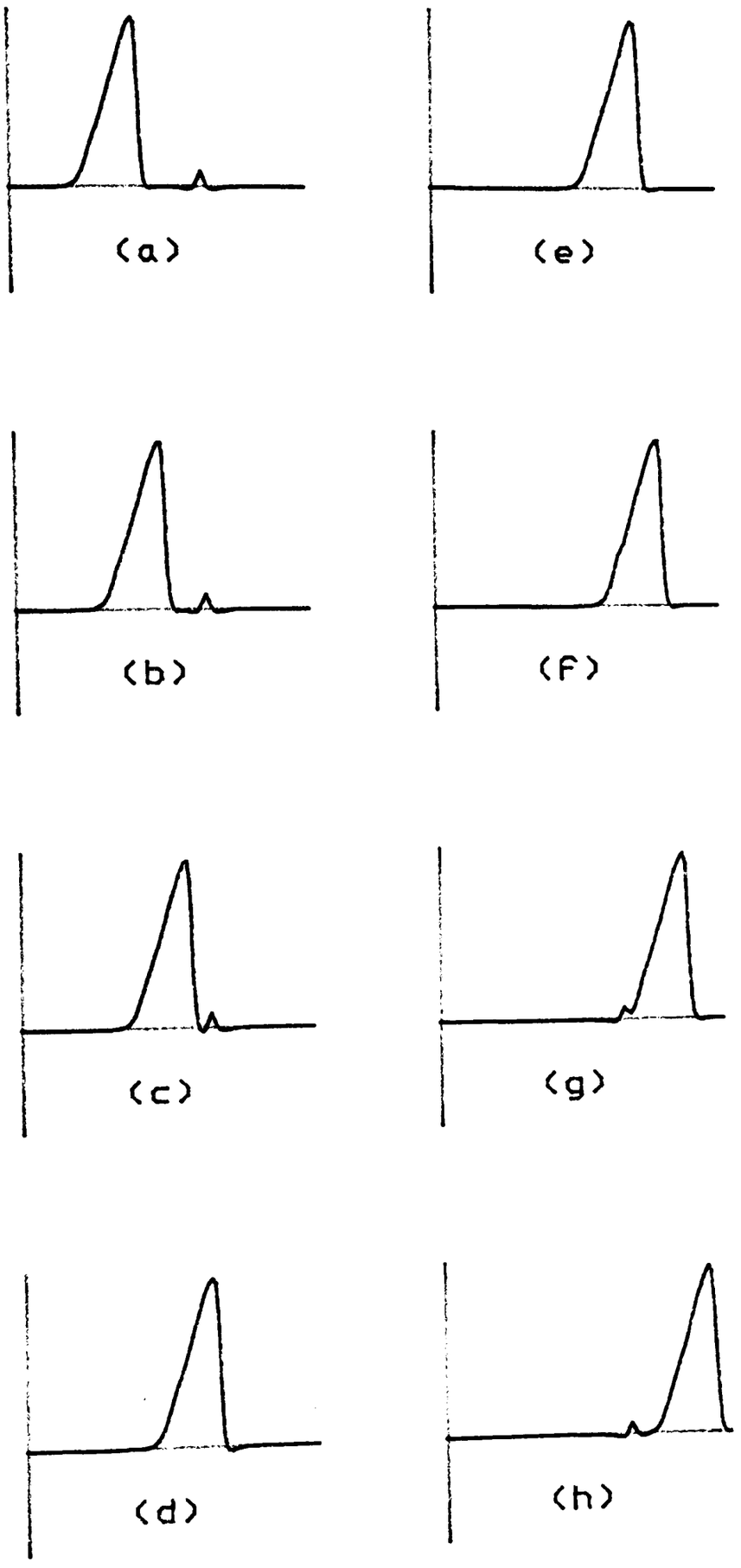

FIGURE A12 : case 11

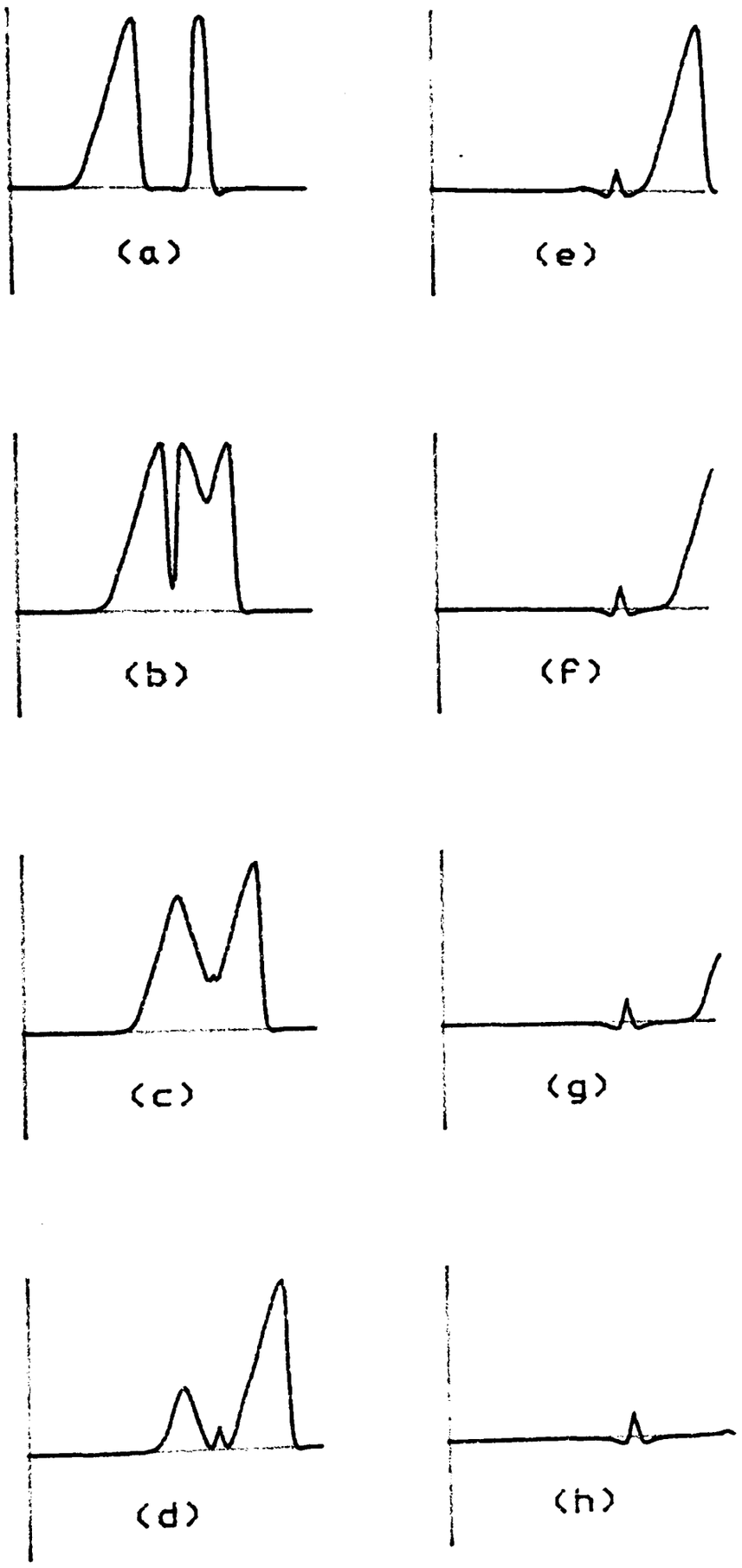

FIGURE A12 : case 12

APPENDIX 13

EQUATIONS DESCRIBING INDIVIDUAL IONIC CURRENT COMPONENTS

$$I_i = \pi d l \, (i_{Na} + i_K + i_p + i_L)$$

$$i_{Na} = \bar{P}_{Na} h m^2 \frac{EF^2}{RT} \frac{(Na)_0 - (Na)_i e^{EF/RT}}{1 - e^{EF/RT}}$$

$$i_K = P'_K n^2 \frac{EF^2}{RT} \frac{(K)_0 - (K)_i e^{EF/RT}}{1 - e^{EF/RT}}$$

$$i_P = \bar{P}_P p^2 \frac{EF^2}{RT} \frac{(Na)_0 - (Na)_i e^{EF/RT}}{1 - e^{EF/RT}}$$

$$i_L = g_L (V - V_L)$$

where

$$E = V + V_r$$

$$dm/dt = \alpha_m (1 - m) - \beta_m m$$

$$dh/dt = \alpha_h (1 - h) - \beta_h h$$

$$dn/dt = \alpha_n (1 - n) - \beta_n n$$

$$dp/dt = \alpha_p (1 - p) - \beta_p p$$

and

$$\alpha_m = 0.36(V - 22) \left[1 - \exp\left(\frac{22 - V}{3} \right) \right]^{-1}$$

$$\beta_m = 0.4(13 - V) \left[1 - \exp\left(\frac{V - 13}{20} \right) \right]^{-1}$$

$$\alpha_h = 0.1(-10 - V) \left[1 - \exp\left(\frac{V + 10}{6} \right) \right]^{-1}$$

$$\beta_h = 4.5 \left[1 + \exp\left(\frac{45 - V}{10} \right) \right]^{-1}$$

$$\alpha_n = 0.02(V - 35) \left[1 - \exp\left(\frac{35 - V}{10} \right) \right]^{-1}$$

$$\beta_n = 0.05(10 - V) \left[1 - \exp\left(\frac{V - 10}{10} \right) \right]^{-1}$$

$$\alpha_p = 0.006(V - 40) \left[1 - \exp\left(\frac{40 - V}{10} \right) \right]^{-1}$$

$$\beta_p = 0.09(-25 - V) \left[1 - \exp\left(\frac{V + 25}{20} \right) \right]^{-1}$$

Note the use of different notation for E and V

E - membrane potential

V - membrane depolarisation

Constants

$\bar{P}_{Na}$	8×10^{-3} cm/s	sodium permeability constant
P'_K	1.2×10^{-3} cm/s	potassium permeability constant
$\bar{P}_P$	0.54×10^{-3} cm/s	nonspecific permeability constant
g_L	30.3 mmho/cm^2	leak conductance
V_L	0.026 mV	leak current equilibrium potential
$(Na)_o$	114.5 mM	external sodium concentration
$(Na)_i$	13.7 mM	internal sodium concentration
$(K)_o$	2.5 mM	external potassium concentration
$(K)_i$	120 mM	internal potassium concentration
F	96 514.0 C/g/mole	Faraday's constant
R	8.3144 J/K/mole	gas constant
T	295.18 K	absolute temperature.

Initial Conditions

$m(0) = 0.0005$
$h(0) = 0.8249$
$n(0) = 0.0268$
$p(0) = 0.0049.$